Triggers, mechanisms and frequency of slope instability processes on mid-Norway's continental margin

Song Jing

Submitted in partial fulfilment of the requirements for the degree of PhD

Cardiff University

School of Earth and Environmental Sciences

March 2022

Abstract

This thesis uses high-quality 3D seismic data from the mid-Norwegian margin to investigate the triggers, mechanisms and frequency of slope instability in the poorly investigated northwestern flank of the Storegga Slide, near the Modgunn Arch, a regional anticline formed by Cenozoic tectonic inversion. Chapters 4, 5 and 6 in this thesis focus on specific aspects of slope failure, from tectonic processes such as uplift and faulting to instability features such as slide blocks and sediment creeping zones. The ultimate aim is to improve the present understanding about distinct aspects of slope failure, investigating at the same time the geological conditions that contribute to recurring submarine landslides. The control of extensional faults and older landslides, or mass-transport complexes (MTCs), on long-term slope instability is also discussed in this thesis, together with other potential preconditioning factors.

Chapter 4 uses a comprehensive seismic and borehole dataset to investigate how fault movement, growth and local uplift were able to precondition slope instability around the South Modgunn Arch. In addition, features leading to fluid migration and accumulation near the sea floor were identified and related to local tectonism. Seismic and borehole data suggest that hydrothermal vents associated with the intrusion of sills have generated a family of radial faults due to differential compaction above the latter intrusions. In parallel, the interpreted data show that a NE-SW oriented compressional stress field generated a family of dense polygonal faults during a phase of uplift of the South Modgunn Arch. A second family of polygonal faults was formed after tectonic uplift ceased, overlapping and partly linking with the first family.

Chapter 5 focuses on characterising the initiation, development and modern slope instability conditions around the South Modgunn Arch. In detail, the recognition of fluid pipes and evidence of fluid migration through faults, together with the sudden deposition of marine deposits on the southern limb of the Modgunn Arch, were considered to be key precondition factors for the long-term slope instability interpreted on seismic data. An interesting aspect verified in this chapter is that density reversal contributed to the evacuation of material on the continental slope, with several evacuation structures being now observed around the Storegga Slide. Furthermore, long-term slope instability was likely preconditioned by multiple weak layers and episodic slope undercutting because

seafloor fractures and scarps were found above slide blocks, as well as interactions between two overlapping intervals with slide blocks.

The influence of weak layers on the behaviour of slide blocks along gentle continental slopes is addressed in Chapter 6. Detailed seismic interpretation and mapping allowed the collection of sinuosity data for multiple lineations on the sea floor, and to gather geometric information about two units with slide blocks. Both the seafloor lineations and the blocks were interpreted as evidence for successive (recurrent) episodes of slope instability, as these lineations and blocks were deformed after they were first formed. The overlapping of two groups of lineations (with distinct sinuosity values) on the modern sea floor suggests important sediment creeping. A numerical simulation (Computational Fluid Dynamics) approach has highlighted the significance of weak layers, pre-existing fractures and MTCs as features capable of preconditioning regions of the continental slope to long-term instability. Consequently, scenarios were modelled to explain the development of both creeping MTCs and sliding blocks around the South Modgunn Arch.

In conclusion, this thesis explores the complex processes leading to long-term slope instability on continental margins. The case study in this thesis, the northwest flank of the Storegga Slide, is a key area to investigate the precondition factors - and triggers – of such long-term instability. This thesis ends by extrapolating its findings - gathered in a thus far poorly studied region of the Storegga Slide - to similar geological environments around the world. Such an extrapolation is important to predict future geological hazards on continental margins.

Author note and status of publications

The results chapter presented in this thesis have been prepared as scientific papers for publication in international journals. Their present status is as follows:

Chapter 4 has been published as Song, J., Alves, T.M., Omosanya, K.O., Hales, T.C., & Ze, T. (2020). Tectonic evolution of strike-slip zones on continental margins and their impact on the development of submarine landslides (Storegga Slide, northeast Atlantic). *GSA Bulletin*, 132(11-12), 2397-2414.

Chapter 5 is under review in *Marine Geology* as Song J., Alves T.M., Omosanya K.O. Styles of slope instability on a Quaternary sub-arctic continental margin: The northwestern flank of the Storegga Slide.

Chapter 6 is under review in *Journal of Geophysical Research: Solid Earth* as Song J., Alves T.M., Omosanya K.O. Critical features and mechanisms marking long-term instability on continental slopes: Evidence from the northern flank of the Storegga Slide, Norway.

Although the articles are jointly co-authored with the project supervisors, the work presented in the publication is that of the lead author, Song Jing. Editorial work was provided by the project supervisors in accordance with a normal thesis chapter.

Acknowledgements

Many people have offered me valuable help, to my thesis and to my PhD journey, including my supervisor, my friends, and my parents.

I would like to give my sincere gratitude to Tiago Alves for all of his support. As my first supervisor, his knowledge and patience have encouraged me to move outside my comfort zone and overcome challenges on research. Thank you for all the editorial work and for so many talks that allow me think and focus clearly. I couldn't have finished this thesis without you.

Thank you also to Gwen Pettigrew for all the help with technical and IT issues during using many new software. I am also grateful for the non-academic conversations with friends in the 3D Seismic Laboratory, including Nick, James, Chantelle, Nathalia, Tao, Roberto, Lilly, Qiang, Duo, Jian Wang, as well as many friends out of school - in particular, Zhi bin, Han ling, Wei xing, Ze yu, Tian yu, Wang shi, Fu bin, Lili, Xiao yi, Xin yi, Zhang rui, Dennis and Freda. Also, thanks to the funding from both the Cardiff University and British Geophysical Association during the Covid-19 pandemic.

I am also very grateful to the Norwegian University of Science and Technology (NTNU) and Norwegian Petroleum Directorate - Schlumberger Petrel Ready Database for the use of the seismic and borehole data presented in this thesis. Many thanks to Kamal'deen O. Omosanya for his support regarding the use of data for this thesis, and multiple revision of manuscripts. I am also thankful to T.C. Hales for this help on improving my first paper.

I would like to thank the many friends outside the UK who still supported me. Many thanks to Wei Li and Nan Wu for multiple online meetings that broaden my horizon and encouraged me further. I am also very grateful to Yu Tian Zhang, who is still in Japan but is graduating at a similar time as me. His knowledge about fluid flow, and the multiple forces acting on continental slopes, allowed me to complete the coding necessary for the scenarios modelled in this thesis.

Finally, but most importantly, I would like to thank my family for their support - both financial and mental. They always show me support and love in time when it's needed. I could not have made this PhD without their support.

Table of Contents

List of Figures

List of Tables

List of Equations

CHAPTER ONE

Introduction and Literature Review

1. Introduction and literature review

1.1 Rationale and aims

1.1.1 Rationale

Slope instability can mobilise large swathes of the sea floor, promoting recurrent phases of deformation in shallow strata, vast (or localised) sediment remobilisation and, in extreme cases, catastrophic tsunamis (Harbitz et al., 2006; Locat and Lee, 2002). The mass-wasting phenomena resulting from slope instability are able to crush submarine pipelines on the ocean floor, damage offshore drilling platforms, as well as compromising infrastructure (and human lives) along shallow coastal areas (Debnath and Hawlader, 2017; Kim et al., 2020). For instance, meter-high waves were generated in the Palu Bay offshore Indonesia (2018) by a submarine landslide triggered by a reactivated strike-slip fault (Pakoksung et al., 2019). Later in the same year, half of Anak Krakatau island failed, producing a broad submarine landslide composed of large megablocks (Hunt et al., 2021). Ancient submarine landslides likely reflecting similar catastrophic events to Anak Krakatau's and Palu Bay's have been interpreted in seismic data. In the South China Sea, the Baiyun-Liwan submarine slide was triggered at about 24 Ma after the strike-slip Red River fault was reactivated to extend for over 250 km, affecting around 40,000 km^2 of the modern and palaeo-seafloor (Zhu et al., 2019). On the mid-Norwegian margin, offshore Norway, the Storegga Slide has evacuated around 3000 km^3 of strata at around 8200 years b.p., affecting approximately 95,000 km^2 of the continental slope (Haflidason et al., 2005) (Fig. 1.1). Within the Storegga Slide per se, multiple pre-Holocene slides have been recognised and sampled, such as a first regional slide that occurred before 1.7 Ma. Such a time span suggests that slope instability on the Mid-Norwegian margin has been occurring for more than a million years (Solheim et al., 2005).

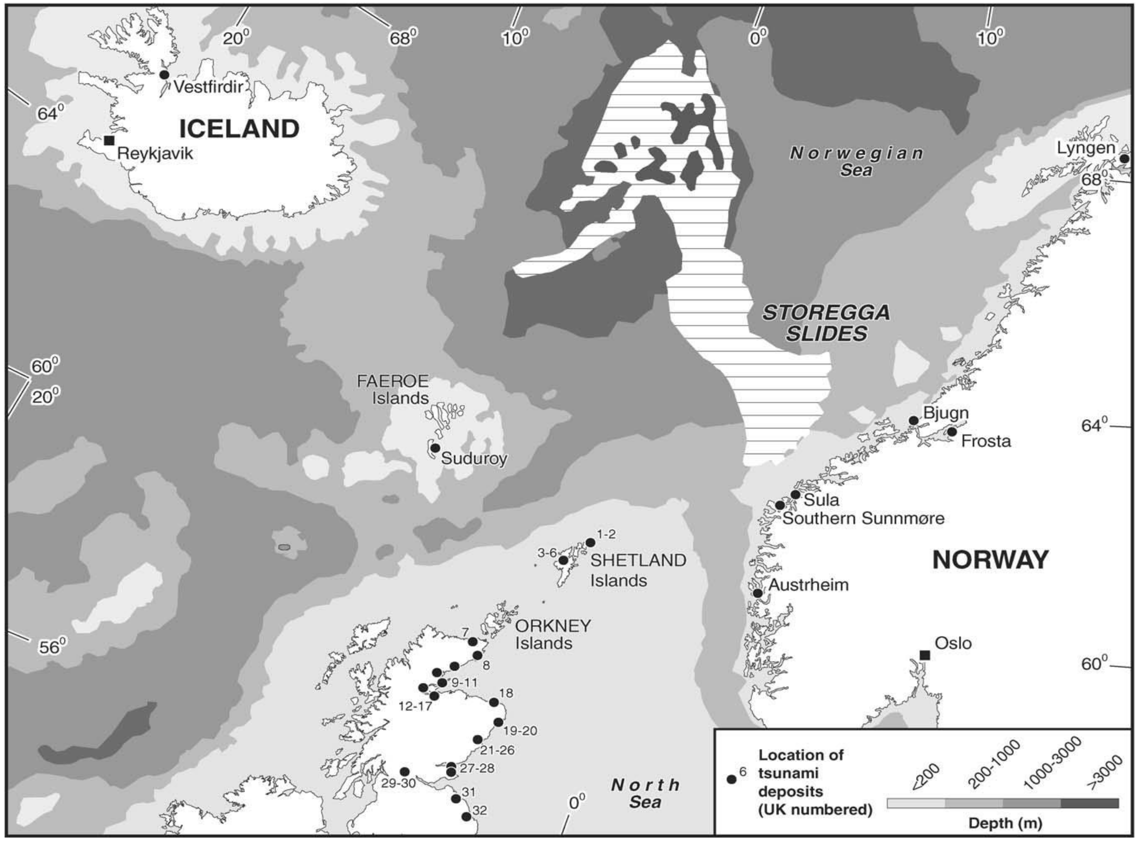

Figure 1.1. Location of the Storegga Slide and sites in which evidence for a Holocene Storegga Slide tsunami has been found. Figure taken from Smith et al. (2004).

Slope instability on continental slopes is often associated with tectonic movements and local earthquakes such as those recorded offshore the ocean islands of Hawaii and Papua New Guinea (Day et al., 2015; Paris et al., 2018), on active margins along the western Caribbean and northern Philippine Seas (Leslie and Mann, 2016; Yamada et al., 2010), and on passive continental margins of the Northeast Atlantic and South China Sea (Li et al., 2015; Smith et al., 2004). Tectonic movements are considered a sudden trigger of slope instability as they can oversteepen continental slopes, generate local faults, deform continental slopes, and increase shear stresses along shallow weakness layers (Cukur et al., 2016b; Kvalstad et al., 2005a; Locat et al., 2016; Urlaub and Centre, 2007). Ultimately, slope instability ensues due to changes in the cohesion and internal repose angles of near-floor sediment (Davies and Clark, 2006; Goldsby and Tullis, 2002; Hamilton, 1979; Hornbach et al., 2015; Kohli and Zoback, 2013; Wiemer et al., 2015). Slope instability can also be triggered by earthquakes, or after slow sediment creeping processes produce large landslide events (Dan et al., 2007; Pope et al., 2017). Ultimately, the way(s) instability processes evolve on continental margins is crucial to understand their potential to generate destructive tsunamis (Macías et al., 2015; Sassa and Takagawa, 2019; Ward, 2001), or affect anthropogenic structures on the sea floor (Hsu et al., 2008).

Extensional faults, specifically polygonal faults formed in strata compacting just below the sea floor, have been widely documented as forming fluid conduits that contribute to increased pore pressures within shallow strata (Cartwright et al., 2003). In the South China Sea, fluid migrating upwards thorough polygonal faults is known to accumulate in, or below, mass-transport deposits or escape through fluid pipes and pockmarks (Sun et al., 2012; 2017). In the lower Congo Basin, the junction of three neighbouring polygonal faults controls the development of gas-charged chimneys (Gay et al., 2006). On the Utgard High of the Norwegian Sea, mass wasting on its crest was partly triggered by episodic fluid dissipation through polygonal faults formed below (Omosanya, 2018). In fact, also on the mid-Norwegian margin, polygonal faults have become a long-term source for fluid since their formation in the Miocene (Berndt et al., 2003). Therefore, understanding the distribution and development of extensional faults, as well as the built-up and preconditions of instability above, are vital for the analysis and prediction of future submarine landslides.

1.1.2 Aims of the research

This work assesses the features and development of submarine landslides identified on the South Modgunn Arch of the mid-Norwegian margin. The aim of this thesis is to understand both the growth histories of fractures in post-breakup strata and the factors contributing to recurrent slope instability in this poorly studied flank of the larger Storegga Slide. High-quality 3D seismic and well-log data allowed a thorough investigation of the northwest flank of the Storegga Slide in terms of the factors preconditioning instability, and their evolution. Hence, this thesis addresses the following hypotheses:

- **Slope instability along the Northwestern flank of the Storegga Slide area was mainly controlled by regional scale tectonics, namely strike-slip faults propagating from oceanic fracture zone - see Chapter 4.** If true, the structural trends of scarps that bound slope instability features will mimic the trend of strike-slip faults below. If false, the trends of strike-slip faults will not be related to the morphology of the landslide deposits above.
- **Apart from the regional strike-slip faults, polygonal fault systems also controlled the development of long-term instability in the study area - see Chapters 4 and 5.** If true, there will be clear evidence for the contribution of polygonal faults to slope instability, such as the presence of pre-existing faults bounding the lateral and headwall scarps of MTCs, and fluid flow features occurring below undeformed strata. If false, the distribution and trends of polygonal faults will be unrelated to the stratigraphic position of MTCs. Also no fluid flow feature will be identified along these same polygonal faults.
- **North Hemisphere Glaciation essentially promoted the development of slope instability in the Storegga Slide - see Chapter 5.** If true, glacial-related features and phenomena - including the presence of glacial deposits and shallow excess pore pressure - will control the recurrence of landslides around the South

Modgunn Arch. If false, there will be no particular concentration of slope instability in glacial depositional intervals.

- **Weak layers, pre-existing fractures and MTCs also contributed to the built-up of long-term slope instability - see Chapters 5 and 6.** If true, features typically associated with long-term instability will be observed such as a evidence for secondary deformation of MTCs and areas with unstable sea floor coinciding with pre-existing faults weak layers. If false, neither regional instability above particular (weak) strata, nor a relationship between present-day instability and pre-existing structures, will be interpreted in seismic data.

1.2 Polygonal faults

Polygonal fault systems (PFS) reflect the formation of multiple sets (or families) of normal faults that are normally limited within specific fine-grained sediments such as claystones, mudstones, hemipelagites and chalk. They are formed at a relatively shallow depth below the sea floor, with adjacent coarse-grained units precluding the growth of these same PFS (Cartwright et al., 2003). The top boundary of PFSs is normally a horizon, or surface, at which the systems became inactive. Some of these faults might propagate to shallower or deeper layers. Classical hexagonal patterns in PFS are developed in areas where sediment thickness and lithology are homogeneous. Importantly, during the development of PFS new faults are formed in the gap between older faults (Cartwright, 2011), and these grow from isolated to hard-linked structures (Cartwright et al., 1995) (Fig. 1.2). The PFS can be identified using time structure maps, horizontal time slices, or attribute data such as amplitude, coherence, and dip (Cartwright et al., 2003; King and Cartwright, 2020; Wrona et al., 2017b). An immature network is marked by unrestricted lateral tips, which are absent in a highly mature system (Fig. 1.2). The maturity of PFS can be defined in the form of a Connectivity Index, which is reflects the relative amounts of 'open' versus 'closed' polygonal faults tip points (Fig. 1.2).

In the Møre and Vøring Basin, polygonal faults occur within the Brygge and Kai formations, which also record throw maxima – thus indicating the first nucleation points for the faults (Neagu et al., 2010a) (Fig. 1.3). In the Ormen Lange area (offshore mid-Norway), PFS comprise syn-sedimentary structures initially generated within pre-breakup strata that were later reactivated after the deposition of post-breakup strata (Stuevold et al., 2003). Two types of polygonal faults were also identified in the Northern North Sea, including listric faults with a 'b-type' displacement-depth profile, and planar faults with a 'c-type'. Planar faults show maximum throws above an Opal A/CT transition, whereas listric polygonal fault cross this same diagenetic front to present two local throw maxima located above and below the Opal A/CT transition (Wrona et al., 2017a) (Fig. 1.4). In the Vøring Basin, biogenic silica (ooze) was affected by diagenesis and the acoustic impedance increases due to rapid porosity reduction on the transition between Opal A to fossilised Opal C/T (Davies and Cartwright, 2002).

Different stratigraphic intervals with polygonal faults normally show distinct fault spacings, orientations and trace shapes (Gay and Berndt, 2007). In the case of polygonal faults, their throws decrease downwards resulting in poorly resolved (and smaller faults) in older strata (Gay et al., 2004) (Fig. 1.5). Sub-seismic faults can, nevertheless, accommodate 25% to 60% of extension (Marrett and Allmendinger, 1992). Thus, in the highly faulted lower interval of PFSs can become less well imaged and connected, in contrast to their shallower upper tips (Gay and Berndt, 2007).

Typically, PFS are formed under stress conditions in which σ_1 is the vertical loading, and σ_2=σ_3 as lateral confining stress in strata (Cartwright, 2011). However, this vertical load is not the direct trigger of PFSs. During diagenesis, along with pore dissolution and recrystallization, widespread losses in particle volume give rise to a decrease of lateral stress that reaches Coulomb frictional failure conditions. This results in the generation of shear fractures and, subsequently, PFSs (Shin et al., 2008). It is worth stressing that, in some areas, σ_2 might be slightly different from σ_3 - such as on gently dipping continental slopes or near submarine channel-levee complexes, to name two examples. In these cases, polygonal faults will tend to be parallel to σ_2, reflecting the influence of the local stress field (Cartwright, 2011).

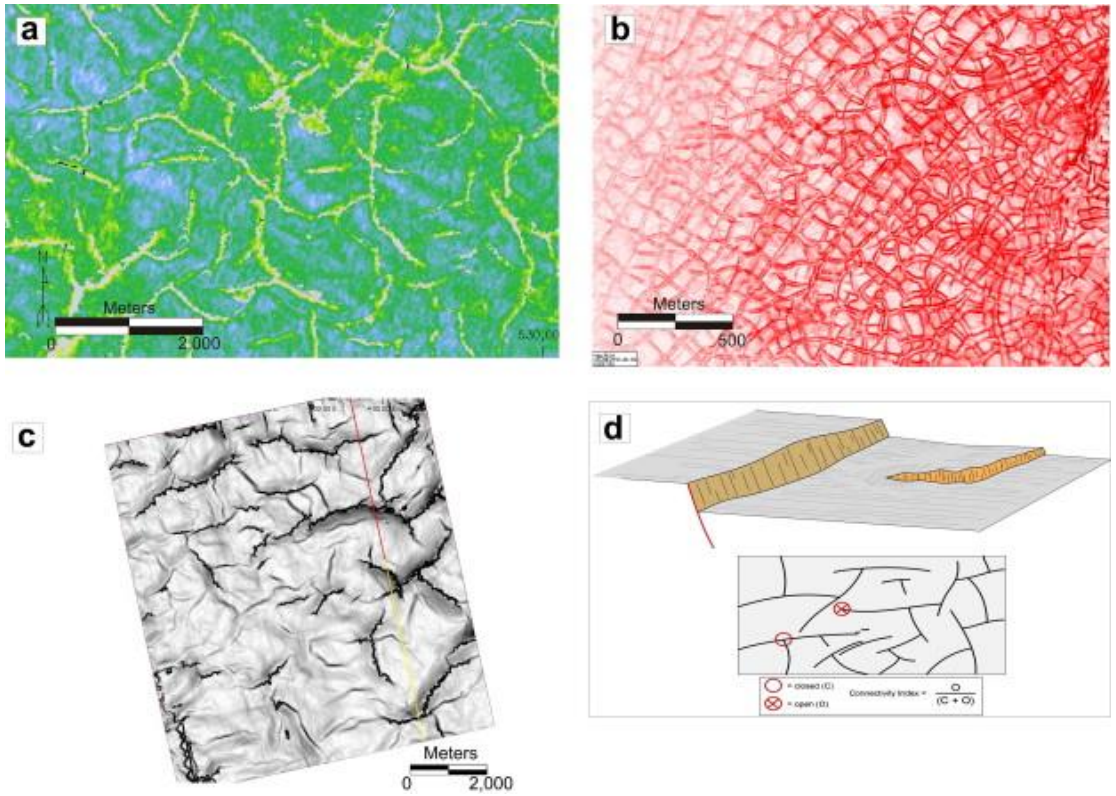

Figure 1.2. Maturity of fault networks in Polygonal Fault Systems (PFS). a) Amplitude map through a polygonal fault system with an open, immature network. b) Coherence time-slice through a highly mature fault system without unrestricted lateral tips. c) Example of an intermediate maturity state between a) and b). d) Sketch explaining the definition of a connectivity index as a measure of PFS maturity. Figure from Cartwright (2011).

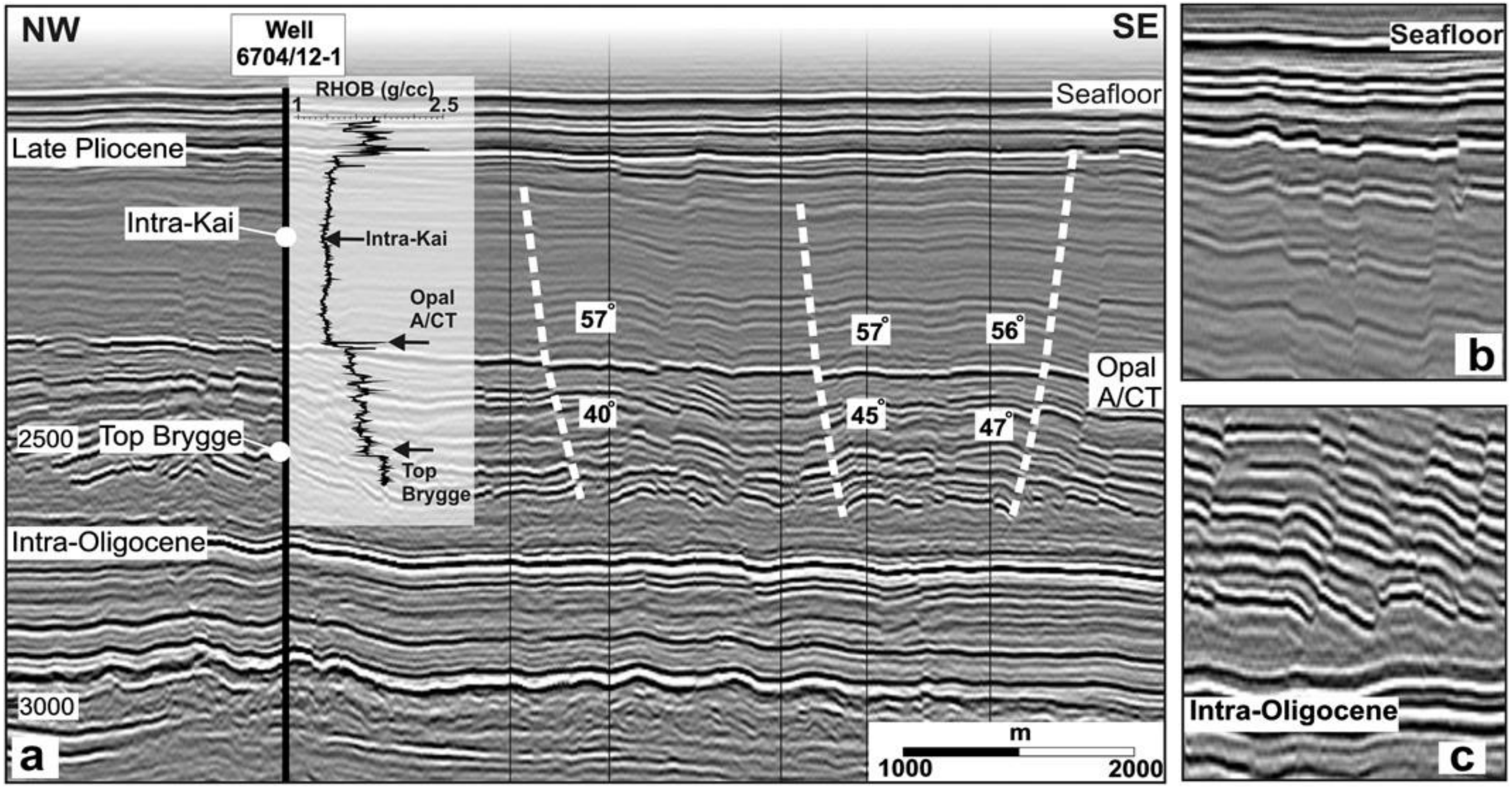

Figure 1.3. a) Composite seismic cross-section from the Gjallar Ridge. Fault planes are marked with white dashed lines. The seismic cross-section profile is orthogonal to each of the fault strikes. b) Close-up of the upper tips of polygonal faults. c) Close-up of the lower tip region of polygonal faults, which is characterised by its low seismic amplitude. Modified from Neagu et al. (2010).

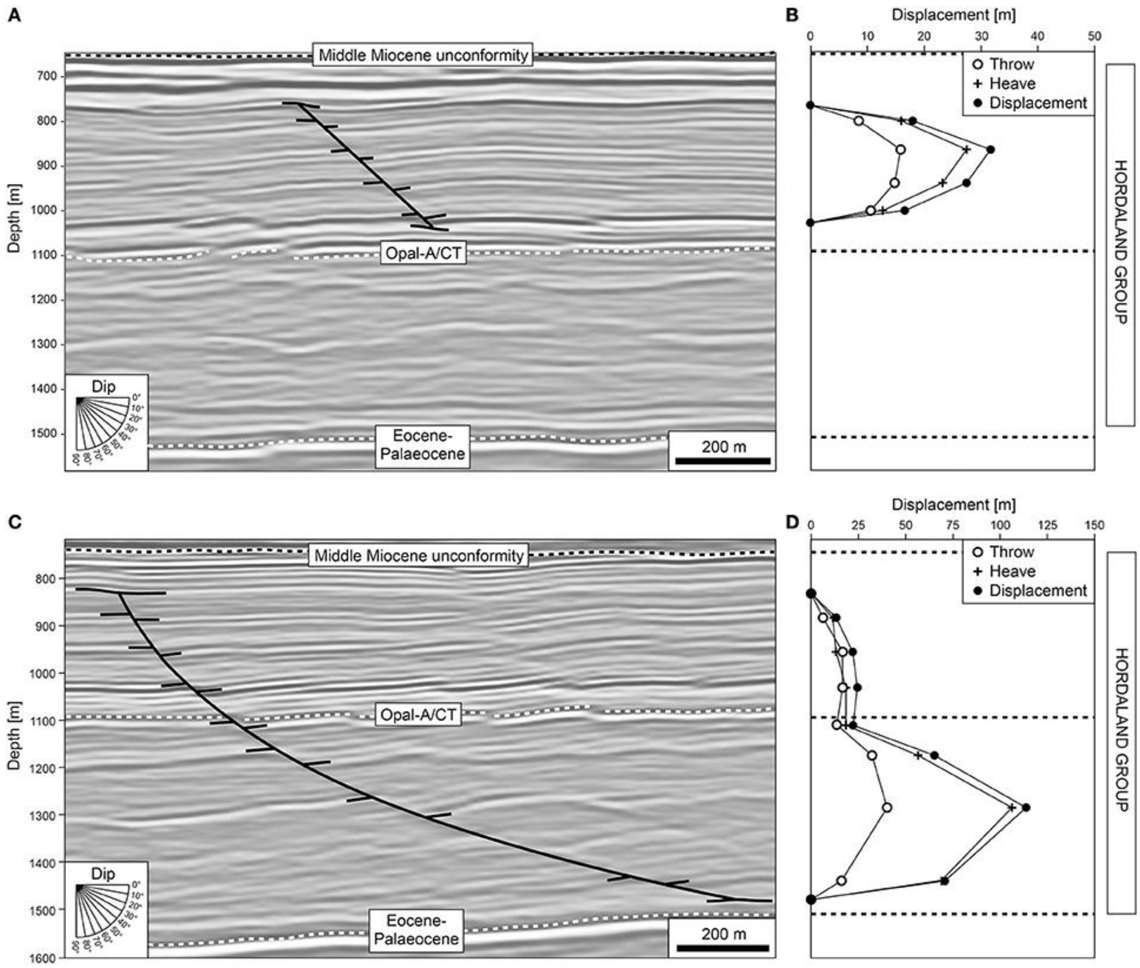

Figure 1.4. Example of a planar polygonal fault: a-b) with c-type displacement-depth profile; c-d) with b-type displacement-depth profile. Figure is modified from Wrona et al. (2017).

In the North Sea, the amount of sediment shrinkage documented in discrete fault tiers appears to increase with decreased grain size (Dewhurst et al., 1999). In parallel, diagenesis and syneresis processes can decrease the coefficients of residual friction on existing slip surfaces, leading to the initiation of faults nucleation and growth (Goulty and Swarbrick, 2005; Wrona et al., 2017b) (Fig. 1.6). Consequently, a sudden unloading event - such as a submarine landslide – can lead to the lead to the cessation of polygonal faults. In the northern Møre Basin, the early slide Y (3.6-1.8Ma) occurred before the most advanced glacial sheet (Lawrence and Cartwright, 2009). Polygonal faults, which propagated onto the palaeo-sea floor at the time, became inactive during or shortly after Slide Y. The arrest of opal A/CT occurred slightly before polygonal fault activity was ceased, spanning the interval from the base of the Brygge Formation to a datum in the Kai Formation (Lawrence and Cartwright, 2009).

1.3 Geological features marking continental slope instability

1.3.1 Submarine landslides

Submarine mass transports were firstly mentioned by Holtedahl in 1971 and subsequently studied by multiple projects including ADFEX (Arctic Delta Failure Experiment, 1989-1992), GLORIA (1984-1991, a side-scan survey of US Exclusive Economic Zone), STEAM (Sediment Transport on European Atlantic Margins, 1993-1996), ENAM II (1996-1999, European North Atlantic Margin), STRATAFORM (1995-2001), Seabed Slope Process in Deep Water Continental Margin (Northwest Gulf of Mexico, 1996-2004), and COSTA (Continental Slope Stability, 2000-2004).

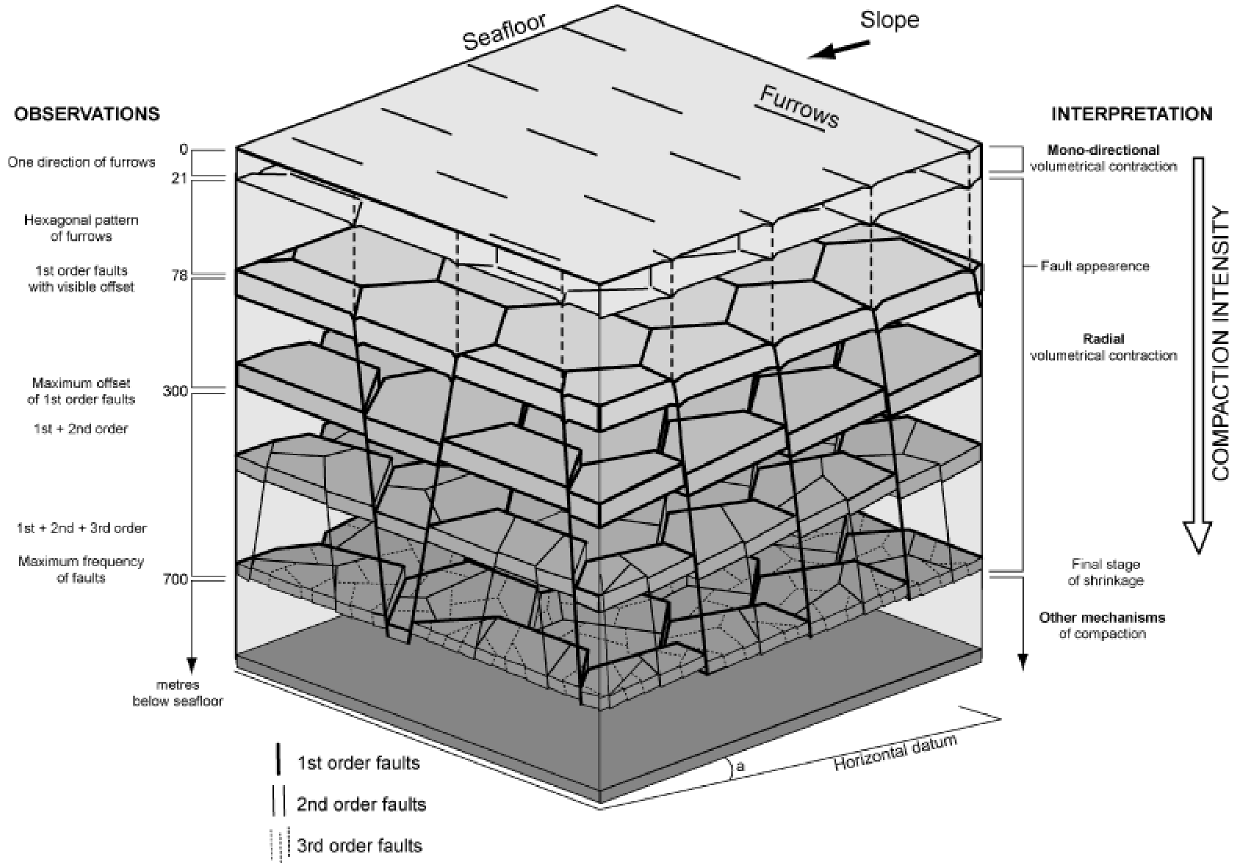

Figure 1.5. Schematic block diagram showing the development of polygonal faults within an imbricated pattern of hexagonal cells during dewatering. Figure modified from Gay et al. (2004).

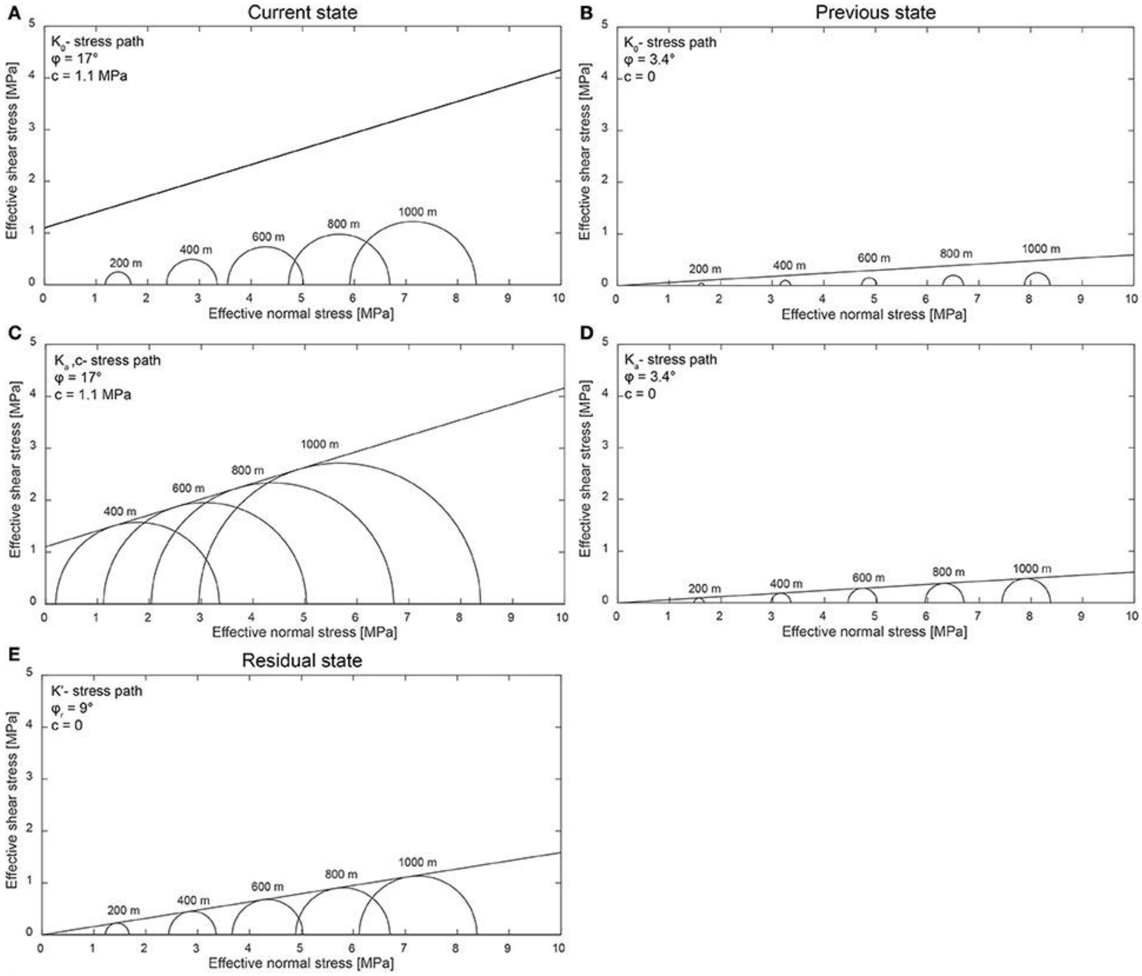

Figure 1.6. a) Mohr circles of the effective stresses affecting the buried Hordaland Group under earth pressure at rest. b) Mohr circles of the effective stresses for shallow-buried weak clays under earth pressure at rest. c) Mohr circles of the effective stresses affecting the buried Hordaland Group under active earth pressures. d) Mohr circles of the effective stresses for shallow-buried weak clays under active earth pressure. e) Mohr circles of the effective stresses for the buried Hordaland Group under earth pressure (K') with low coefficients of residual friction. Figure after Wrona et al. (2017).

Submarine landslides on glaciated margins are unusual at the scale of the globe but common on the Norwegian/Barents Sea and the Southeast Canadian Margin (Hjelstuen et al., 2005). One crucial reason for this particular characteristic is sediment supply. In the case of the Norwegian Margin, glacial-interglacial cycles can be divided into several steps (Fig. 1.7). They included the slow deposition of soft marine clays as weak layers during interglacial periods, and the spreading of ice to the shelf edge (and rapid deposition of glacial sediments) after glacial maxima (Bryn et al., 2005; Haflidason et al., 2004). At the same time, high pore pressure associated with rapid deposition, diagenesis and fluid migration caused the clay-rich layers to weaken and build-up slope instability (Bryn et al., 2003) (Fig. 1.8). For instance, slope failures on the Storfjorden Trough-Mouth Fan of the Barents Sea margin show that water-rich clayey sediments - interbedded with glaciogenic sediments - evolved into weak layers after pore pressure was increased by rapid sediment deposition (Pope et al., 2018).

After slope instability is triggered, usually by earthquakes, the initiation and runout of a submarine landslide can be divided into at least three steps: initial failure that includes sliding blocks and slabs; debris flow as a result of further deformation and liquidation; and finally the turbidity currents after water entrainment (Randolph et al., 2011). In the case of a retrogressive landslide, after the initial failure of its distal area, subsequent unloading and increased shear strain can trigger further instability on the upper slope (Gauer et al., 2005). In areas where strata on the upper slope becomes stronger, this propagation of instability stopped and was followed by the shaping and filling of debris and turbidity channels (Bryn et al., 2005).

In the case of the Storegga Slide, the modern sea floor can be morphologically divided into six areas, or zones, including a zone with an exposed basal failure plane, a zone with in situ sediments, a zone with blocky debris flows, a zone of compression, a zone with semi-disintegrated slide sediments, and a zone of sediment accumulation (Haflidason et al., 2004) (Fig. 1.10). On vertical seismic profiles, it is clear that the slide

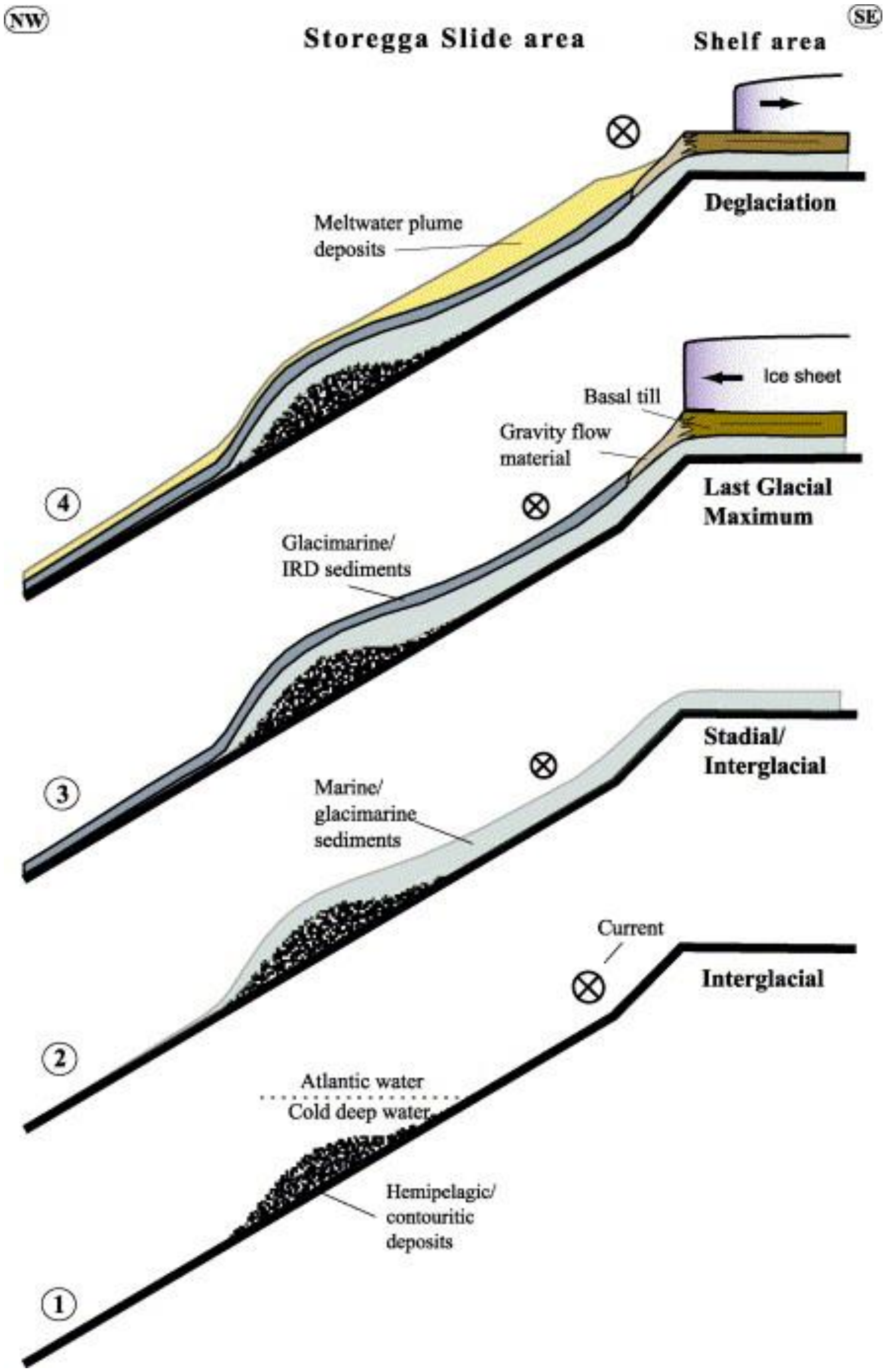

Figure 1.7. Schematic illustration showing the architecture and geological development of the Storegga Slide through one glacial–interglacial cycle. Figure from Haflidason et al. (2004).

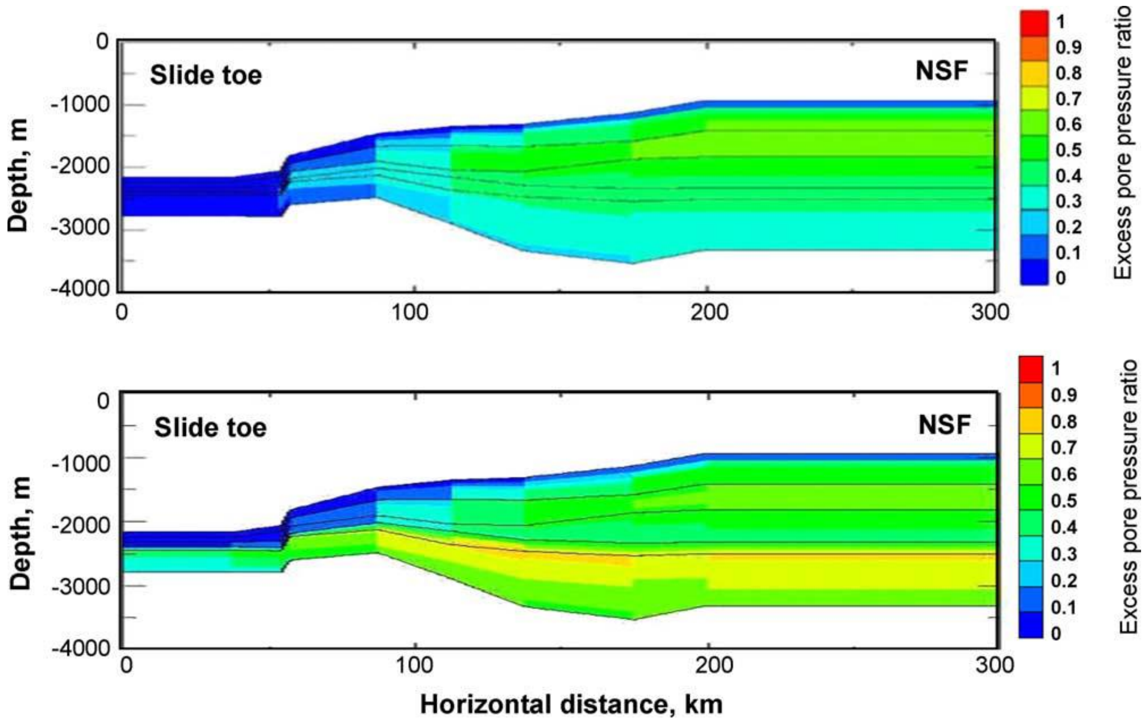

Figure 1.8. Models explaining the excess pore pressure ratio generated during the Storegga Slide, from the North Sea Fan to the toe area. a) In the top figure, vertical permeability is 10 times lower than horizontal permeability. b) In the bottom figure, low permeability marine clays occur over the high permeability Brygge ooze. Figure from Kvalstad et al. (2005).

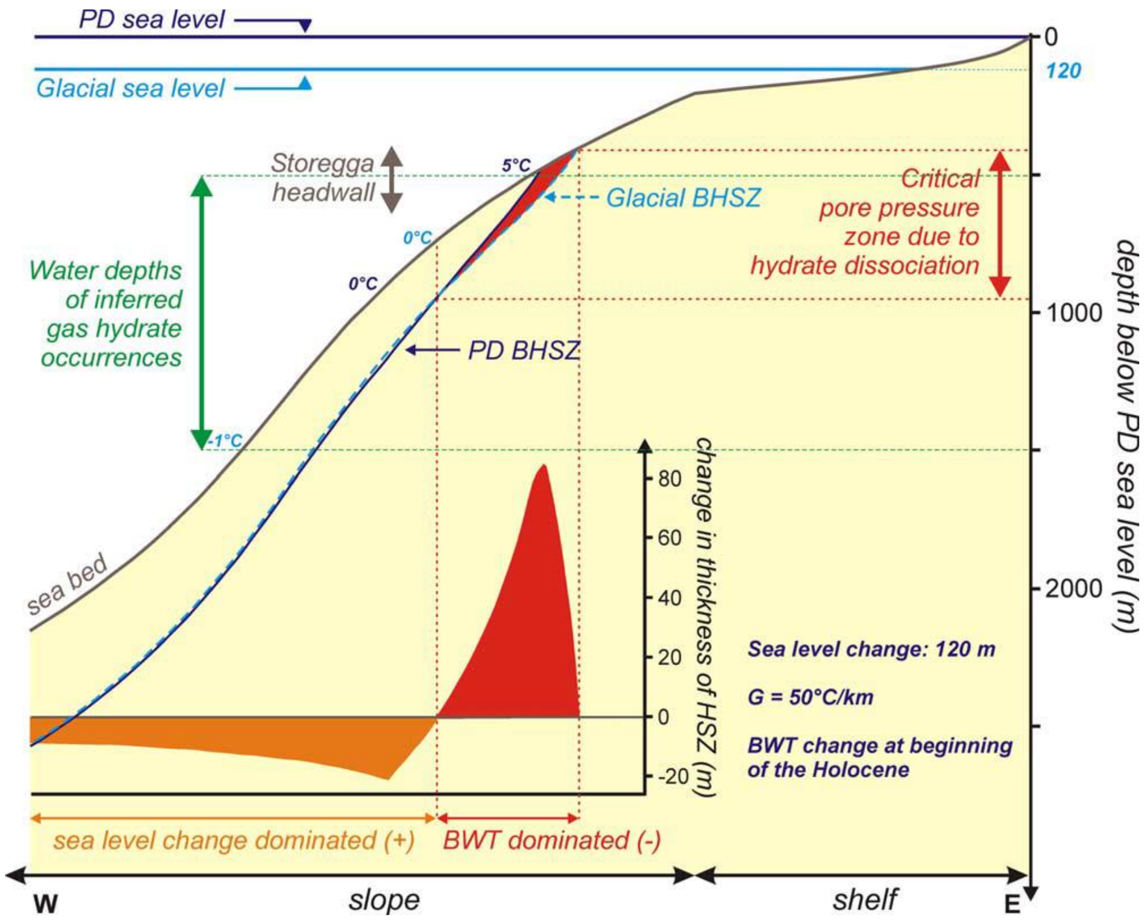

Figure 1.9. Sketch showing the evolution of methane hydrate stability along the mid-Norwegian margin from the last glacial maximum (LGM) (dashed light blue curves) to the present (dark blue), considering the effects of eustatic sea level rise and the bottom water temperature recorded since the Younger Dryas event. There is a weaker hydrate stability zone in the upper slope area (red shading), whereas more stable hydrate conditions occur in the lower slope area (orange shading). Figure after Mienert et al. (2005).

complex comprises several smaller-scale lobes. The lobe at the bottom is assumed to be the oldest and largest, and is followed by younger (and smaller) lobes above. The overlying small-scale slides are recognised as representing the younger phases of what was (and perhaps still is) a major retrogressive slide (Haflidason et al., 2005) (Fig. 1.10).

As one of the many remarkable characteristic of submarine landslides in the study area, lateral spreading of slide blocks occurs close to the headwall scarps and is marked by the presence of parallel to sub-parallel blocks and chasms, oriented perpendicularly to the direction of mass movement (Micallef et al., 2016, 2007a) (Fig. 1.11). Relatively coherent blocks with chasms are interspersed with younger MTCs. Glide planes and weak layers are frequently seen at the base of displaced slide blocks. In seismic data, remnant and rafted blocks are characterised by their relatively high amplitude and lower variance when compared to adjacent MTDs. In fact, debris flows, turbidity channels and other MTDs comprise low coherence strata with chaotic reflections inside (Alves, 2015a) (Fig. 1.12).

1.3.2 Evacuation structures

Multiple evacuation structures are observed in the Storegga area in the form of local topography lows (Lawrence and Cartwright, 2010, 2009; Micallef et al., 2009). In parallel, units with coherent mounds are frequently observed above successive MTC intervals on the lower (downslope) areas of craters (Lawrence and Cartwright, 2010; Riis et al., 2005). These mounds comprise deformed ooze deposits that float on MTCs due to their lower density, reflecting processes occurring during the last phases of slope instability (Omosanya, 2018; Riis et al., 2005). Most of them were formed below Slide W, partly mobilising and evacuating the underlying Oligocene-Miocene ooze (Riis et al., 2005).

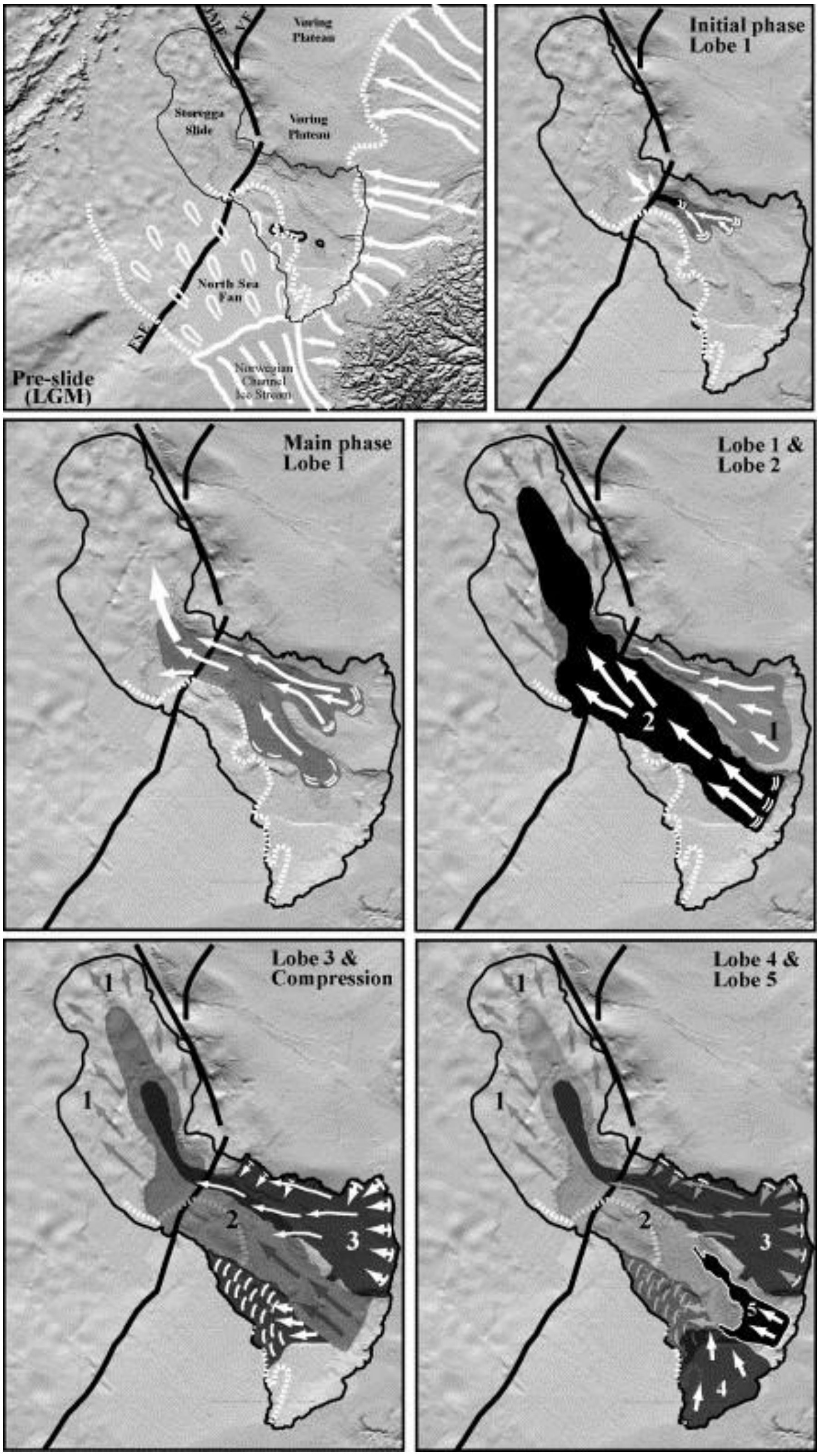

Figure 1.10. Schematic diagram of the Storegga Slide illustrating the step-by-step development of major slide phases, including the initial slide and the pre-slide phase, back to the Last Glacial Maximum (LGM). Figure from Haflidason et al. (2004).

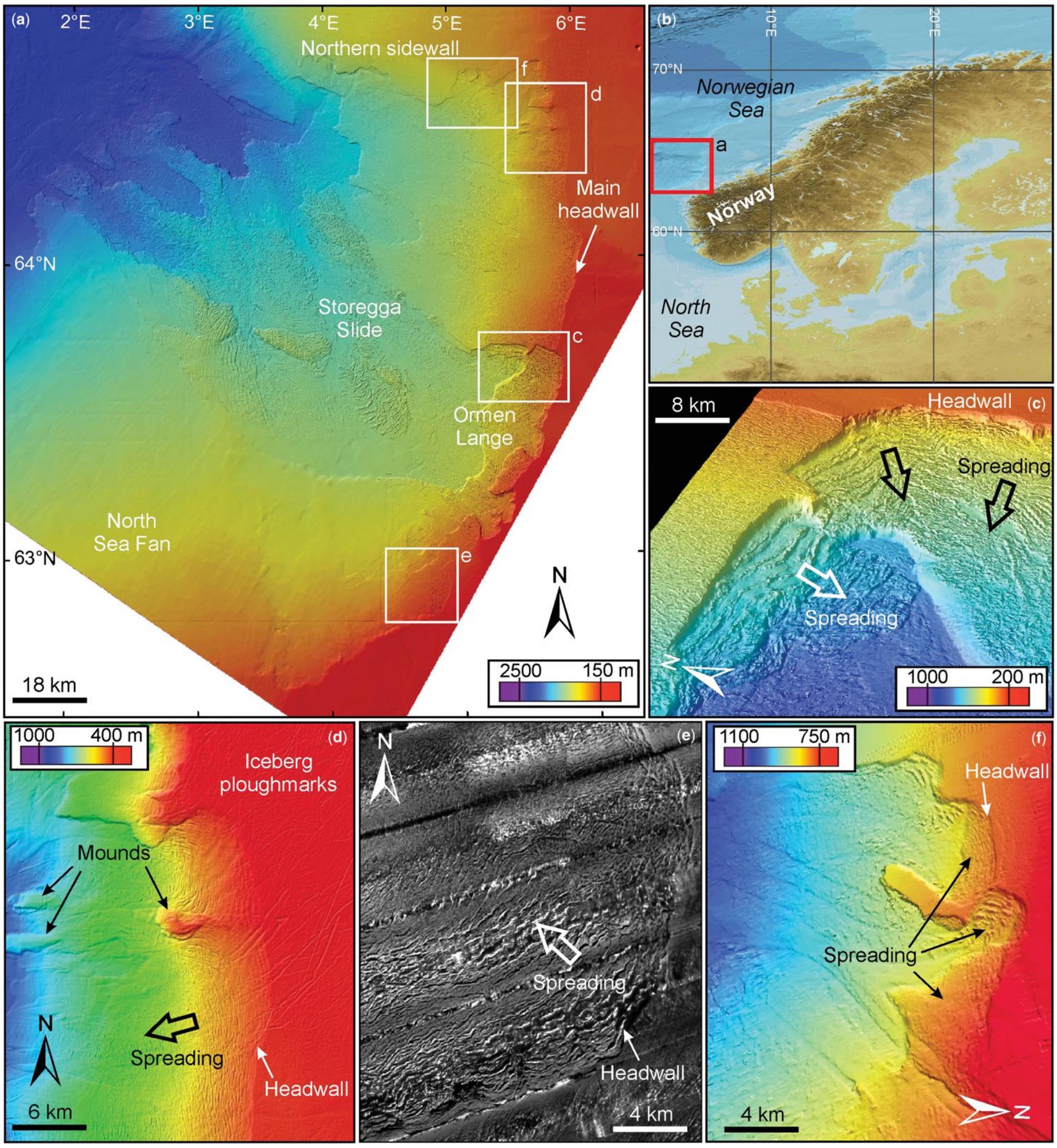

Figure 1.11. Swath-bathymetric and side-scan sonar imagery of laterally spread submarine blocks across the Storegga Slide. Modified from Micallef et al. (2016).

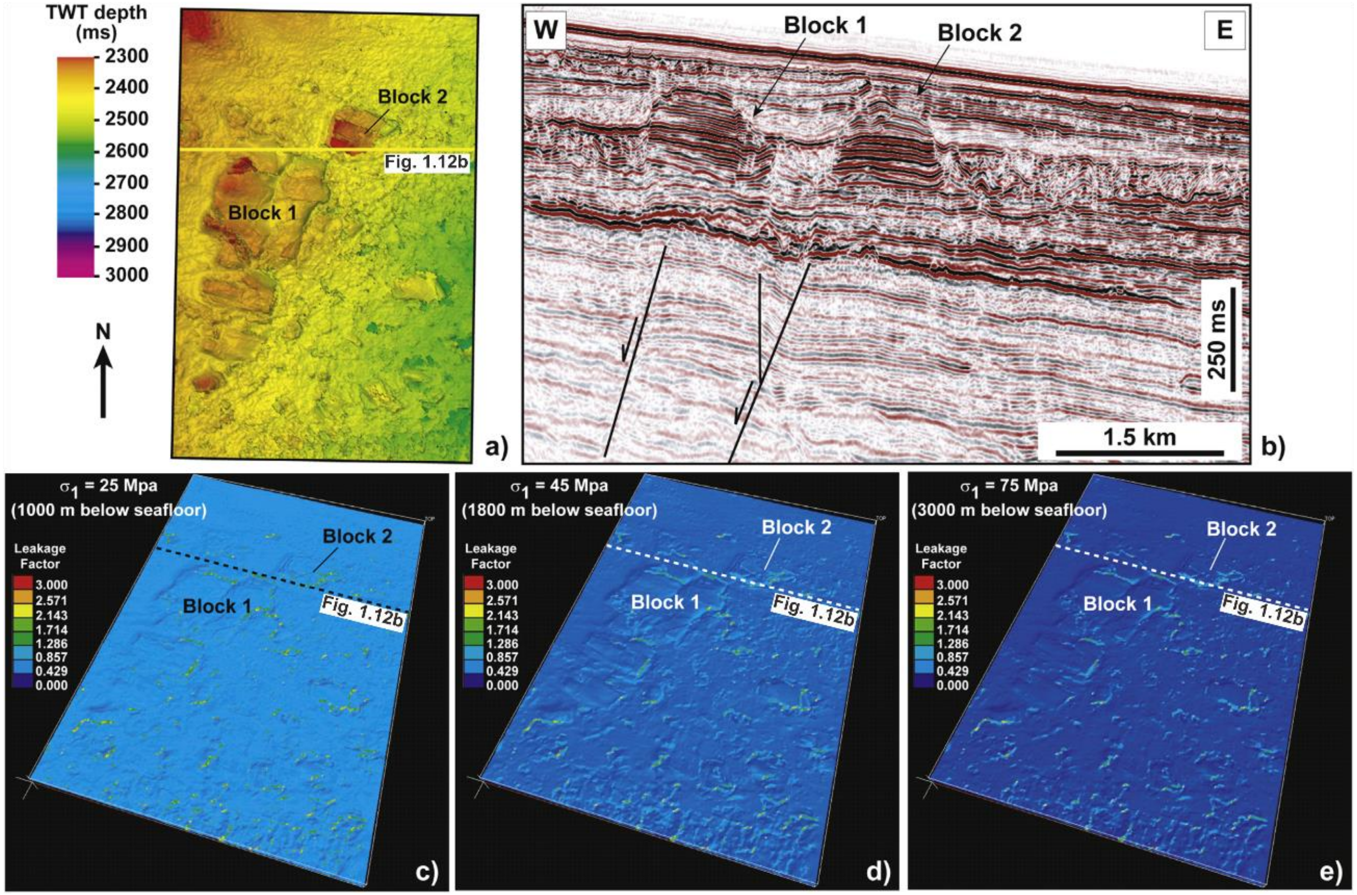

Figure 1.12. a) Relief map of slide blocks from SE Brazil highlighting the presence of internal fault-bounded compartments and chasms. b) Seismic profile showing the local structure of the modelled blocks. c-e) Panels showing leakage factors modelled for the blocks in a) and b). Figure modified from Alves (2015).

Many evacuation features are located on anticline structures (mid-Miocene Domes) above Opal A/CT boundaries (e.g. Havsule structure) and were triggered by mass flows (Slide W) that loaded ooze sediments on the sea floor or at shallow burial depths (Lawrence and Cartwright, 2010). Both seismic interpretation and sediment cores have suggested that those ooze mounds were not liquefied, but rather formed internal faults (Riis et al., 2005). Within the Havsule evacuation structure per se, the sediment fill of this crater-like structure consists of local slides, indicating that ooze evacuation created accommodation space on the palaeo-seafloor (Riis et al., 2005) (Fig. 1.15). Seismically, sediment filling the Havsule structure is divided into two sequences: a) a thicker, tilted and imbricated lower interval, and b) a thin, transparent upper interval. The upper part is interpreted as reflecting the settling of fine material during the last stage of mass flow. The lower part comprises locally-sourced landslides and slump material (Riis et al., 2005). Importantly, excess pore pressure within oozes could be identified below these two sequences in both seismic and well-log data via the identification of an Opal A/CT boundary and fluid conduits (pipes), plus abnormal mud weights when drilling (Berndt, 2005; Berndt et al., 2004; Riis et al., 2005).

There are two models for the development of evacuation structures in the Havsule area. One model suggests the crater was formed after the deposition of overlapping sediment, after which fluid from below was able to drive the oozes onto surface and, subsequently, deform landslide deposits above these oozes (Fig. 1.13). The second model suggests that fluid flow, which exploited hydrothermal vent complexes, was continuous during the deposition and subsequent deformation (sliding) of the Naust formation (Fig. 1.14).

1.3.3 Fluid migration and accumulation

Fluid migration is the movement of gas or liquid through sediment. In parallel with the intrusion of magmatic sills during NE Atlantic continental breakup, extensive (and intensive) fluid migration was recorded by hydrothermal vent complexes on the mid-Norwegian margin (Gernigon et al., 2006b; Roelofse et al., 2021) (Fig. 1.16).

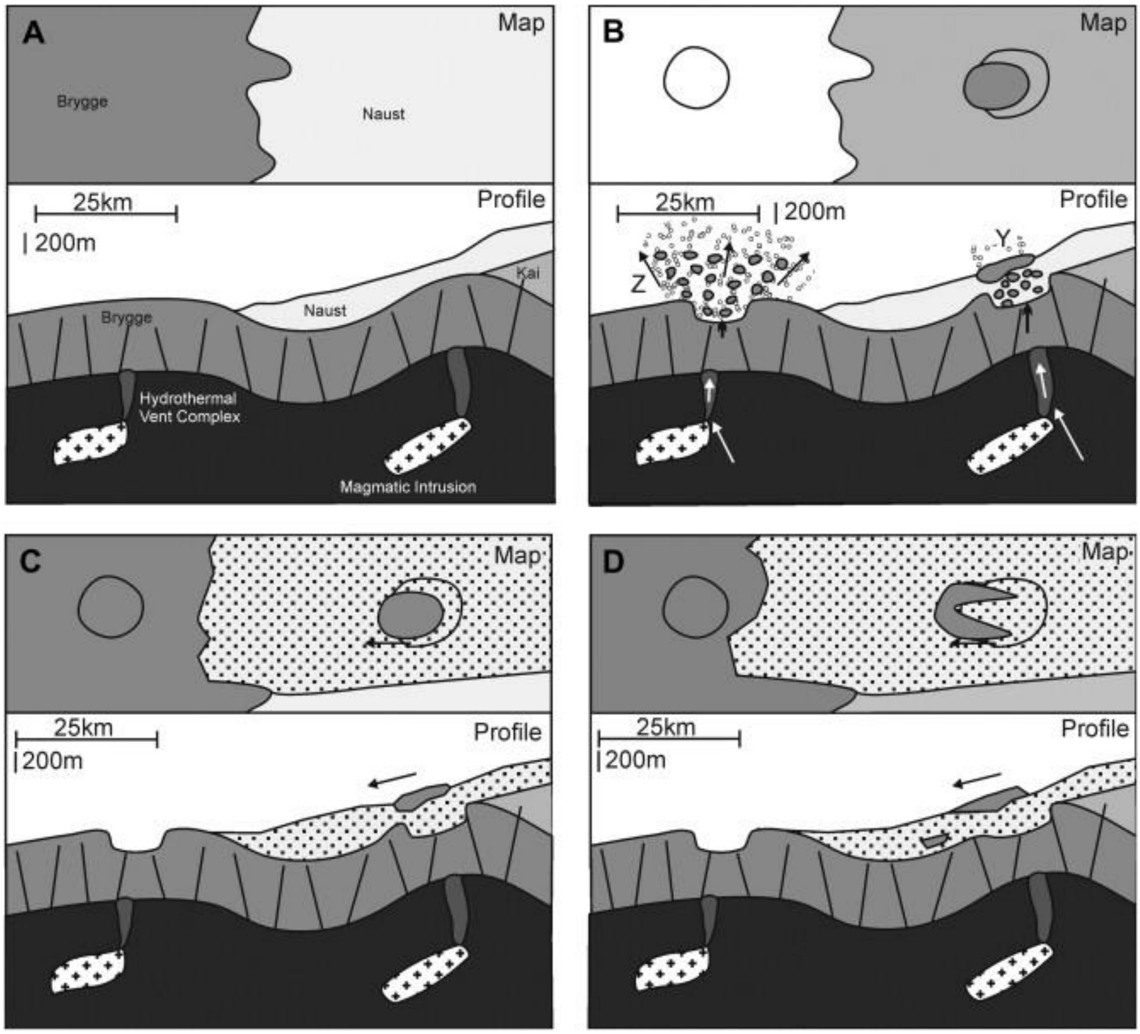

Figure 1.13. Model A: a-b) The oozes located on positive structure are extruded by fluid from beneath and through the overlying Naust sediments. c-d) After the extrusion of ooze to the palaeo-seafloor, slope instability was triggered before the translated strata draped the ooze mounds on the lower slope. Figure is based from Lawrence and Cartwright (2010).

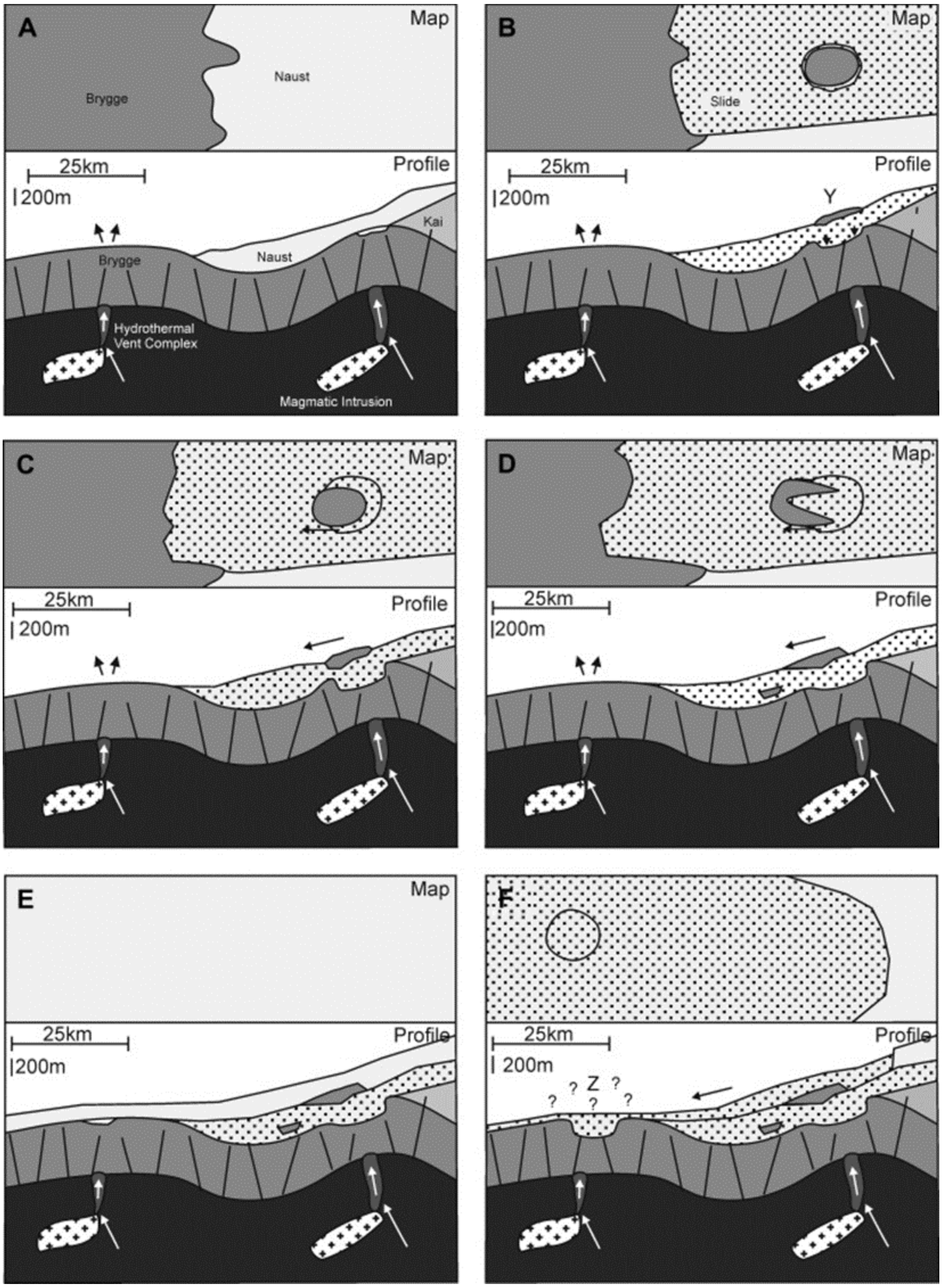

Figure 1.14. Model B: a-b) Low-density oozes occur above an area of important fluid flow and, through sill-intrusion related vents, they are remobilised to ascend to the palaeo-seafloor. c-d) Ooze mounds are further transported downslope within MTDs. e-f) Slope instability above these craters and ooze mounds is enhanced in the long-term. Figure from Lawrence and Cartwright (2010).

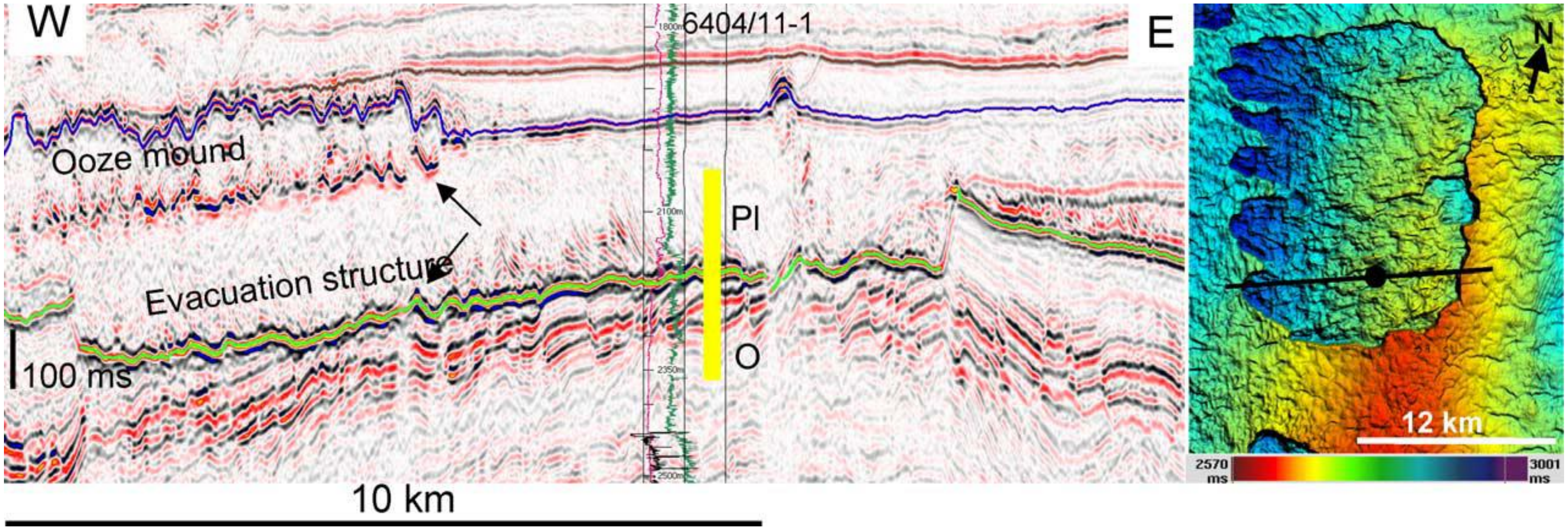

Figure 1.15. Seismic profile across the Havsule structure. The green line indicates the top of the ooze interval, while the blue line marks the top of Intra Naust slide and ooze mounds. Pl=Pleistocene, O=Oligocene. Figure after Riis et al. (2005).

The geomorphology of those hydrothermal vents was influenced by the (local) dynamics of venting, including the density and velocity of seeped fluid, its constancy, activity and dissociation (Ho et al., 2012). In the Vøring and Møre basins, hydrothermal vents are widely observed on the palaeo-seafloor as craters, dome and eye structures (Roelofse et al., 2021). Crater-shaped vents are interpreted to result from the extrusion of shallow unconsolidated sediments. Dome-shaped vents are formed on the sea floor as mud volcanoes with volcanic material inside. Eye-shaped vents are produced by less compacted material that results from high liquid pressures inside the vents themselves (Kjoberg et al., 2017).

Similar to other slope failures on sub-arctic continental margins, the excess pore pressure generated within glacial marine deposits has contributed to a weakening of near-seafloor strata, softening the sensitive marine clays (Leynaud et al., 2007). Climate-controlled hydrate dissociation has been indicated as a key control on the location of the Storegga Slide headwall since the time hydrate stability on the shallow continental slope (estimated to occur at a water depth of 400-800m) decreased by the effect of a warm bottom current during ocean warming (Mienert et al., 2005) (Fig. 1.9). This gas hydrate destabilization could have also enhanced dewatering to drive fluid upwards, further increasing local pore pressure (Suess et al., 1999). Apart from the warm-water inflows, glaciation-related eustatic sea-level changes also controlled the depth and extent of a Gas Hydrate Stability Zone (GHSZ), within which hydrate dissolution efficiently increased pore pressure (Mienert et al., 2005). On the mid-Norwegian margin, isotope testing on benthic foraminifera revealed that a rapid increase of bottom-water temperature has occurred since the end of Younger Dryas (Berstad et al., 2003). Due to its sensitivity to temperature increases, dissociated gas hydrate built up excess pore pressures around the headwall of the Storegga Slide (Sultan et al., 2004b; Xu and Germanovich, 2006). Together with rapid sediment deposition and overloading, gas hydrate dissociation, tectonic tilting, and the dewatering of oozes have all contributed to the migration of fluid to the shallower strata, increasing excess pore pressure as well as the slope instability (Gay and Berndt, 2007; Hustoft et al., 2007). The release of excess pore pressure, following fluid accumulation, has been widely observed in the form of regional pipes and pockmarks (Bünz et al., 2003).

1.3.4. Preconditioning factors and triggering mechanisms

The preconditioning factors and triggering mechanisms of submarine landslides comprise the factors increasing slope instability and eventually leading to slope failure (Leynaud et al., 2009). Preconditioning factors are those that can build-up slope instability in a relatively longer period, such as the deposition of strata with different geomechanical properties, the build-up of excess pore pressure below the sea floor, and past mass-movement history (Laberg et al., 2003). In contrast, triggers of slope failure are those short-term events that initiate deformation on the sea floor and transport the failed material downslope, such as earthquakes and human activity (Sultan et al., 2004a).

The broader definition of mass-transport deposits (MTDs) considers them as comprising four types of deposits: slides, slumps, debrites and turbidites (Herdendorf, 1990). The terms slide and slump represent both the instability process and its corresponding deposits, whereas debrites and turbidites are used to define the deposits accumulated by debris flows and turbidity currents (Herdendorf, 1990).

During the initiation of a submarine landslide, a coherent unit of sediment is frequently observed to move downslope along a glide plane without internal deformation. This coherent mass unit is defined as ‘Slide’, which could end up with hundreds of kilometres runout (Shanmugam and Wang, 2015). Along with a further transport, this ‘Slide’ unit can experience rotational movements, causing internal deformation above a concave-up glide plane, marking the formation of a ‘Slump’ unit. However, the difference between ‘Slides’ and ‘Slumps’ can be hard to recognised as the internal deformation of such deposits is not always resolved in seismic data. Even though the broader Storegga Slide is called a ‘Slide’, many of its constituting MTDs are composed of slumps and debrites (Shanmugam, 2021).

Debris flows and turbidity currents are distinguished by their particular rheology. Debris flows represent sediment flow with an internal cohesion that is capable of supporting gravel and coarse-grained sand during transport (Shanmugam, 1996). In contrast, turbidity currents are Newton fluids that are supported by turbulence without internal coherence, despite the fact that some flows may contain gravel and coarse-grained sand at their base, similarly to debris flows (Shanmugam, 1996).

1.4. Thesis layout

This Thesis contains eight chapters. Chapter 1 introduces the thesis, reviews the published literature concerning extensional faults and slope instability on continental margins. The geological setting of the study area on the mid-Norwegian margin is summarised in Chapter 2. The 3D seismic dataset and key methods used in the thesis are described in detail in Chapter 3. Chapters 4, 5 and 6 address three related themes of importance in slope instability. The structural evolution of the South Modgunn Arch and its relationship with two groups of polygonal faults are investigated in Chapter 4. Chapter 5 focuses on characterising the internal character of multiple landslides around the South Modgunn Arch, including regional slides investigated in previous work and three newly identified landslides. Chapter 6 considers the development of long-term instability around the South Modgunn Arch by investigating the degree (and styles) of deformation within mass-transport complexes and by modelling the propagation of instability around the Storegga Slide. Chapter 7 discusses the control of extensional faults on slope instability and the effect multiple factors (and triggers) have on this same instability. Final conclusions are provided in Chapter 8.

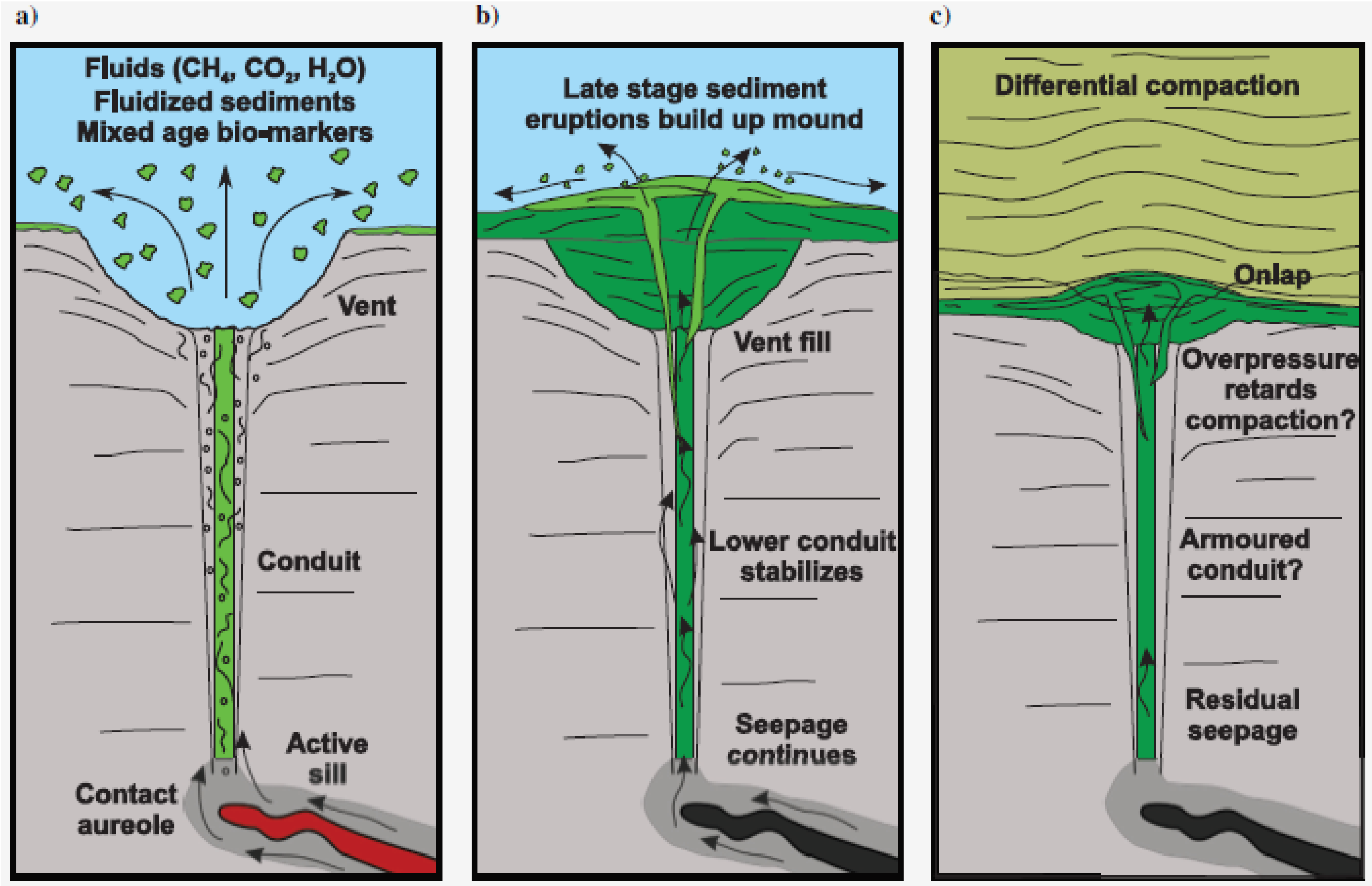

Figure 1.16. Schematic model displaying the key development stages occurring during hydrothermal vent formation. Figure modified from Kjoberg et al. (2017).

CHAPTER TWO

Geological Setting

2. Geological Setting

2.1 Introduction

This chapter reviews the geological setting of the northwest flank of the Storegga Slide on the mid-Norwegian margin, including the formation of this same continental margin, the northern hemisphere glaciation that characterises its most recent geological evolution, and the nature of post-breakup deposits.

2.2 The formation of the mid-Norwegian margin

2.2.1 Lithospheric break-up and onset of seafloor spreading

Three main provinces are recognised along the Norwegian continental shelf: the North Sea, the Mid-Norwegian continental margin and the Western Barents Sea. These provinces formed an epicontinental sea before lithospheric break-up and seafloor spreading, as their stratigraphy are similar for that period (Faleide et al., 2015). The rifted mid-Norway margin is located between 62-70°N, and is bounded to the north by the Western Barents Sea and to the south by the North Sea. The mid-Norwegian margin per se contains three segments, the Møre, Vøring and Lofoten-Vesteralen segments, which are separated by the East Jan Mayen Fracture Zone and Bivrost Lineament/transfer zone (Tsikalas et al., 2005). In parallel, the Norwegian continental Shelf and adjacent area record the effect of three main tectonic episodes: Late Palaeozoic, Late Jurassic-Early Cretaceous, and Late Cretaceous-Paleocene (Faleide et al., 2008) (Fig. 2.1).

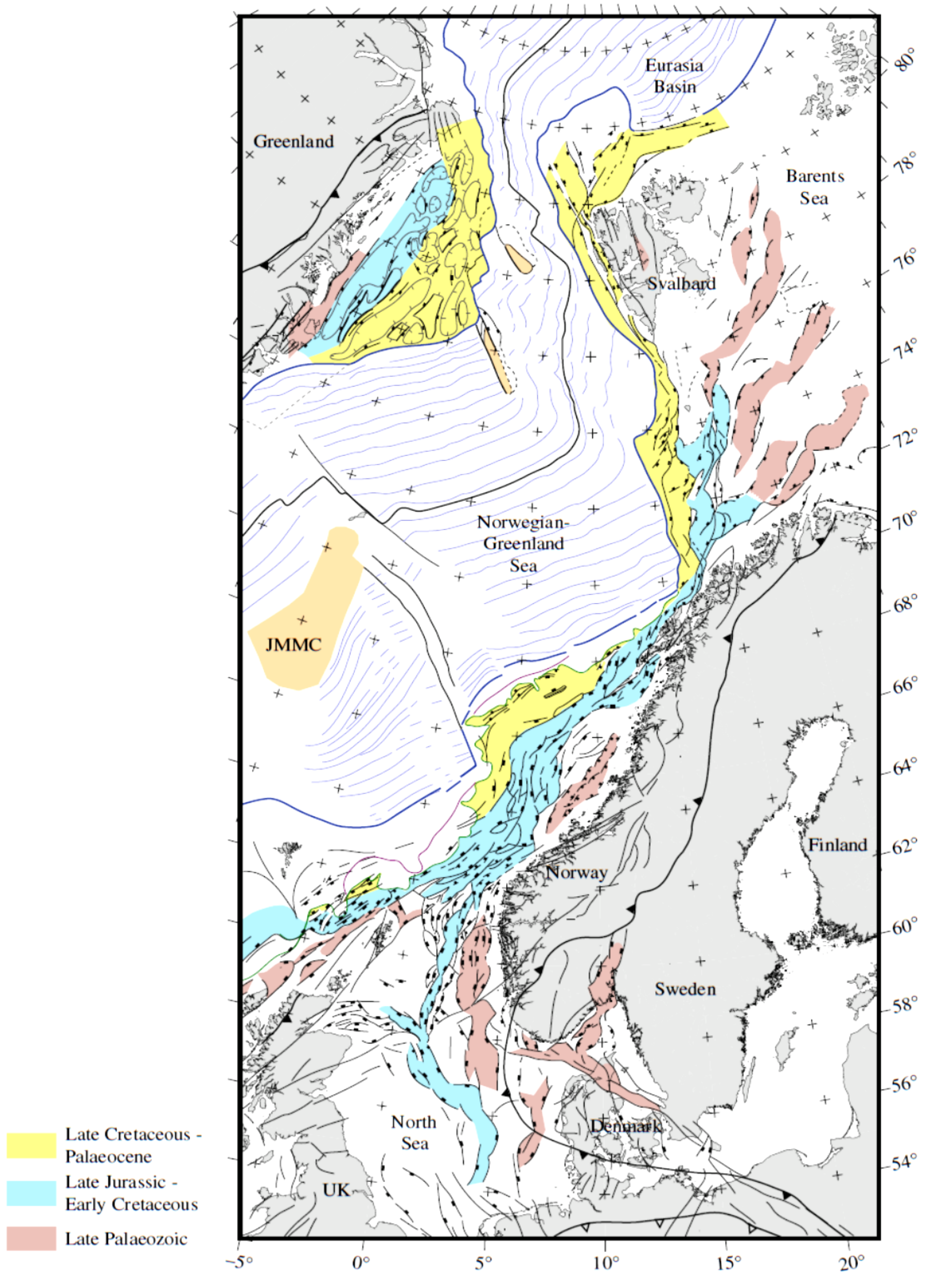

Figure 2.1. Main structural elements of the Norwegian Continental Shelf and adjacent areas that are associated with the three rift phases affecting the NE Atlantic region. Figure modified after Faleide et al. (2015).

The Late Palaeozoic rift basins of the Norway continental shelf were formed during three main Late Palaeozoic- Early Mesozoic rifting episodes, which took place in mid-Carboniferous, Carboniferous-Permian and Permian-Early Triassic times (Doré, 1991). Many of the tectonic movements and relative sedimentation of Late Palaeozoic are still unclear, due to overprint by younger tectonism and burial of older basins by thick strata (Faleide et al., 2008). Nevertheless, a major phase of faulting onshore East Greenland suggests Permian-Triassic extension to have comprised the most intense of the three rifting episodes (Surlyk, 1990). Soon after, Triassic basins became dominated by gentle, regional subsidence. During the Lower-Middle Jurassic, deposition occurred mainly in shallow marine environments.

During Late Jurassic-Earliest Cretaceous, NW-SE rifting associated with the northward propagation of Atlantic rifting led to the extension and thinning of continental crust in the study area (Faleide et al., 1993). In parallel, major Cretaceous sub-basins and highs were formed off mid-Norway accompanying the rapid differential subsidence and segmentation of the crust (Faleide et al., 1993). As a result of about 60 km of crustal stretching, intra-basin highs and basins were formed off mid-Norway and available accommodation space - such as Møre and Vøring basins - was filled by mid-Cretaceous fine-grained clastic sediments (Faleide et al., 2015; Skogseid et al., 2000).

Late Cretaceous-Paleocene lithospheric extension resulted in continental break-up and is associated with 140 km of stretching between Greenland and Eurasia (Skogseid et al., 2000). A ~150 km wide area of extension area was also generated on the Vøring Margin, and was bounded by the Fles Fault Complex and the Utgard High on the east (Faleide et al., 2008).

During the Campanian, plate separation occurred not only in the Labrador Sea (NW Atlantic) and Baffin Bay further NW (Srivastava and Roest, 1999), but also between NW Europe and Greenland, resulting in low-angle detachment structures that uplifted a thick Cretaceous sequence (Faleide et al., 2015). As a result, Paleocene sediments filling the Møre and Vøring basins derived from the uplifted Vøring marginal high and were deposited in a deep-water environment (Hjelstuen et al., 1999).

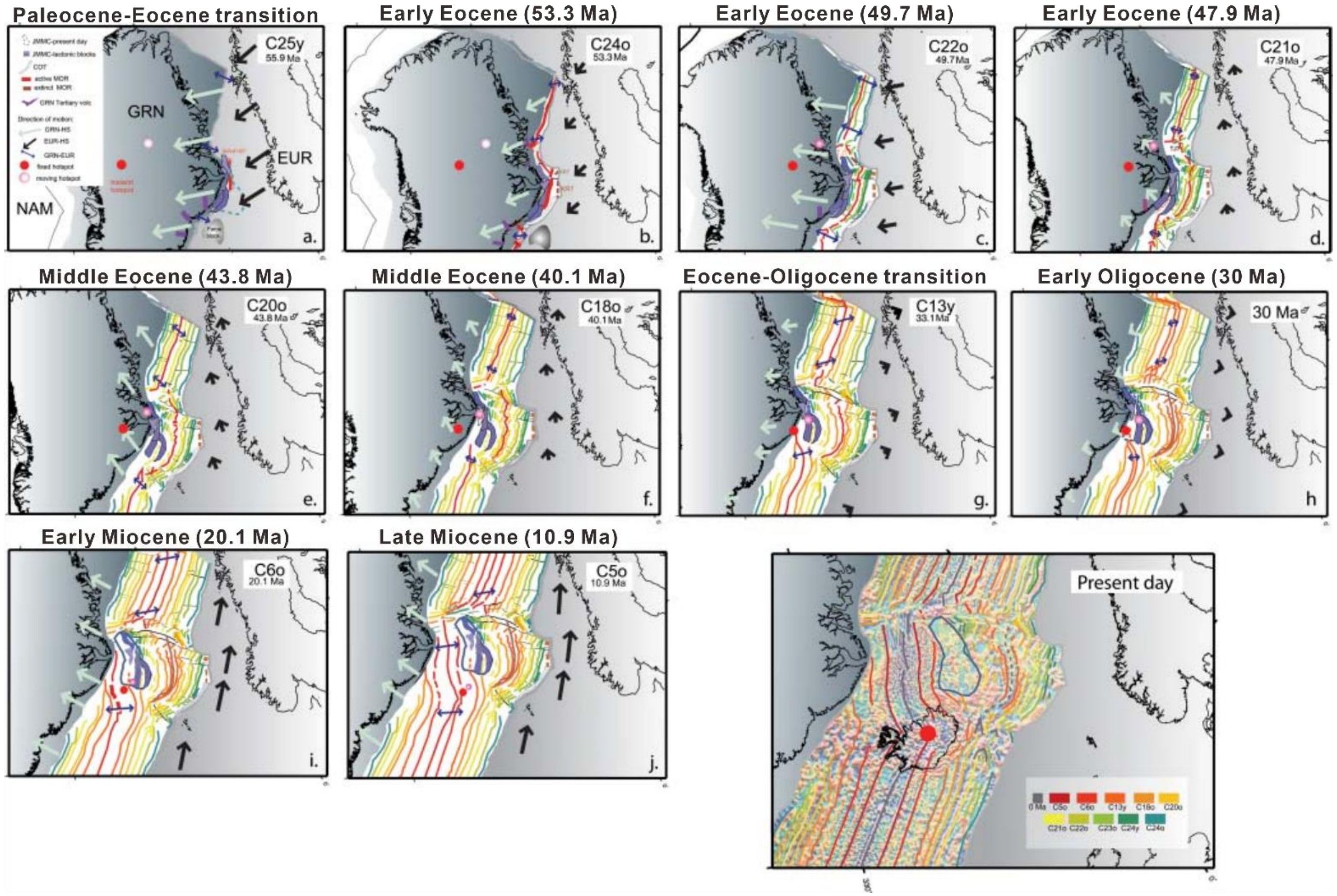

Figure 2.2. Evolution of plate boundaries in the NE Atlantic and kinematic evolution of the Jan Mayen microcontinent illustrated by a series of tectonic reconstructions in an absolute reference frame (centred on hotspot). Figure after Gaina et al. (2009).

Oceanic spreading was triggered between Greenland and Eurasia at the Paleocene-Eocene transition (Gaina et al., 2009) (Fig. 2.2). On the outer continental margin off Norway, thick seaward-dipping reflector (SRD) sequences were developed at this time and interpreted to result from the eruption of lavas onto the newly split continental margin and new oceanic crust (Tsikalas et al., 2005). At the same time, sills intruded into thick organic-rich Cretaceous strata, promoting the rapid maturation of source rocks and the production of fluid through hydrothermal vent complexes (Planke et al., 2005; Roelofse et al., 2021).

Contrasting with the extension dominated regime recorded until then, the middle Eocene witnessed the development of multiple compressional structures on the mid-Norwegian margin, such as the Ormen Lange Dome and the Helland-Hansen Arch (Lundin and Doré, 2002). The mechanism behind this compression and local uplift process is still unclear, but was probably controlled by the structural 'fabric' of Early Cretaceous crustal hyperextended rifts (Lundin and Doré, 2011) (Fig. 2.3). Apart from the early generation of compressional structures, the mid-Norwegian margin experienced regional subsidence and relatively moderate sedimentation rates at this time (Faleide et al., 2008).

Near the Eocene-Oligocene boundary, the main ocean-spreading ridge of the NE Atlantic jumped from the Norway Basin to the eastern margin of Greenland, leading to the formation and northward propagation of the Kolbeinsey Ridge. The Reykjanes and Mohns Ridges became, at this time, linked by this same Kolbeinsey Ridge, and the Jan Mayen microcontinent became completely isolated from the Greenland margin at about 20 Ma. This followed the final extinction of Aegir Ridge at ~30 Ma (Gaina et al., 2009). Another important change was the change in the direction of seafloor spreading between Greenland and Eurasia from NW-SE to NE-SW (Talwani and Eldholm, 1977). In parallel, the onset of volcanism over the Iceland mantle plume correlates with the cessation of seafloor spreading in the Labrador Sea (Nielsen et al., 2002).

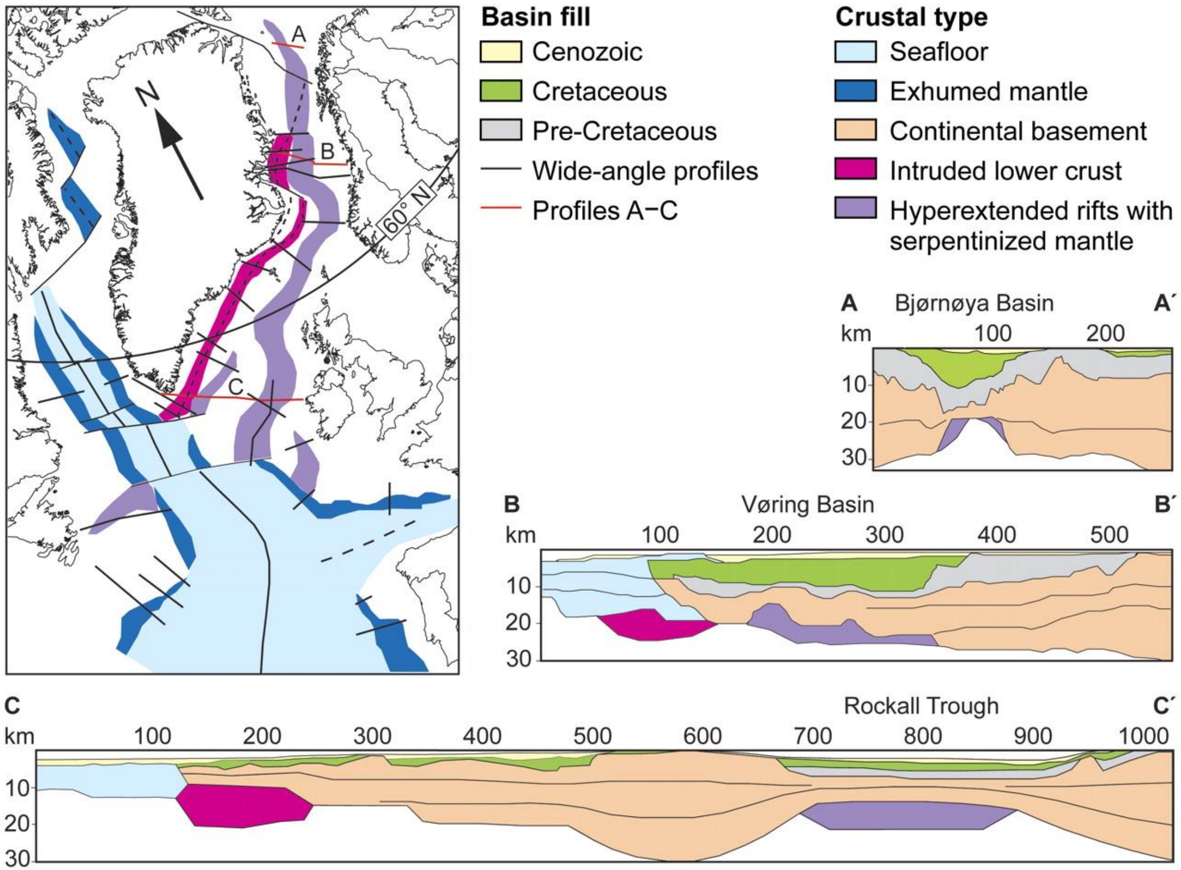

Figure 2.3. Plate reconstruction of the Northeast Atlantic in the Early Eocene (ca. 53 Ma) revealing a chain of hyperextended Early Cretaceous rift basins, oblique continental breakup and associated underplated areas. Examples of crustal profiles are also shown. Figure modified from Lundin and Doré (2011).

2.2.2 Uplift and subsidence of continents and margins

Co-seismic uplift and subduction can be identified on the stratigraphic record by major changes such as the presence of coarse-grain tectonic sequences, the sudden appearance of shallow-marine deposits and marshes, and deposits associated with tsunami inundation (Hemphill-Haley, 1996). Comparing stratigraphic records at different locations can demonstrate the influence of earthquakes in the local stratigraphy, and can provide scientists with quantifiable rates of tectonic uplift and subsidence, e.g. the types of microfossils (diatoms, foraminifera, ostracods, etc.) in a sequence can be used to deduce local sea-level transgressions or regressions, so to interpret the co-seismic subsidence or uplift (Dura et al., 2017).

In the Paleocene-early Eocene, the North Atlantic Igneous Province (NAIP) recorded large-scale tectonic compression with surface uplift affecting many areas: East Greenland, northern Scotland, the East Shetland Platform and SE Ireland (Saunders et al., 2007). At the same time, uplift of Norway and its continental margin occurred due to the thermal (uplift) effect of the Iceland plume and associated continental break-up to the west of the study area (Ren et al., 2003).

During the Late Eocene- Early Oligocene, both the coasts of Greenland and Norwegian margin were uplifted due to the slowing of (and eventually cessation of) oceanic spreading in the Labrador Sea, and the jump in the ocean spreading ridge from the Aejir to the Kolbeinsey Ridge (Anell et al., 2009). The latest Oligocene-earliest Miocene is marked by the final separation of the Jan Mayen island from Greenland (Anell et al., 2009). The Fennoscandian mainland was also uplifted during the late Oligocene leading to the deposition of widespread, prograding sediment wedges offshore South Norway (Clausen et al., 1999).

In the Miocene, a series of dome structures were formed on the Norwegian margin due to the effect of a mid-Miocene compressional phase, which is particularly well documented in southern Norway, the northern North Sea, the Faroe Islands, and in the Greenland-Scotland ridge (Anell et al., 2009). During the Plio-Pleistocene, the Norwegian mainland experienced another uplift episode that resulted from isostatic adjustment to glacial erosion at around 4 Ma (Huuse, 2002; Japsen et al., 2007a).

2.2.3 Mid Miocene domes

A series of positive-relief structures was formed on the mid-Norwegian margin during the Miocene: the South Modgunn Arch, the Havsule Dome, the Orman Lange Dome, the Helland Hansen Arch, the Vema Dome, the Hedda Dome and the Naglfar Dome (Doré et al., 2008a; Lundin and Doré, 2002) (Fig. 2.4). The timing of their formation can be inferred from analysing (and dating) syn-tectonic sediments, and by dating the subtle unconformities formed on the flanks of such structures where younger sediments onlap or drape the domes (Løseth and Henriksen, 2005). The South-Modgunn Arch, the Havsule Dome and the Ormen Lange Dome are located along the Jan Mayen structural corridor, whereas most of the other domes are distributed through the Voring Basin, located to the north of the latter corridor (Fig. 2.4). The mechanism behind the uplift and deformation of the domes is still not well understood, but it is likely associated with mild compression (2-3% shortening) of the Norwegian margin from a mid-Northeast Atlantic tectonic source or in association with the Alpine orogeny (Vågnes et al., 1998). Due to their broader scale, showing lengths of tens of kilometres, these positive structures were not triggered by overburden deformation locally, which is also recorded on the mid-Norwegian margin as a result of sill intrusion during the opening of the NE Atlantic (Schmiedel et al., 2017). Mafic underplating during continental break-up (Early Eocene) also led to local magma-tectonic processes, including the uplift of the upper crust and the formation of listric faults (Gernigon et al., 2003). In general, the formation of positive structures on the mid-Norwegian margin can be associated with two distinct events: a) the first and earlier event is associated with mafic underplating during continental breakup stage, and b) a second event is associated with 'compressional-compactional' phenomena that post-date continental breakup (Doré et al., 2008a).

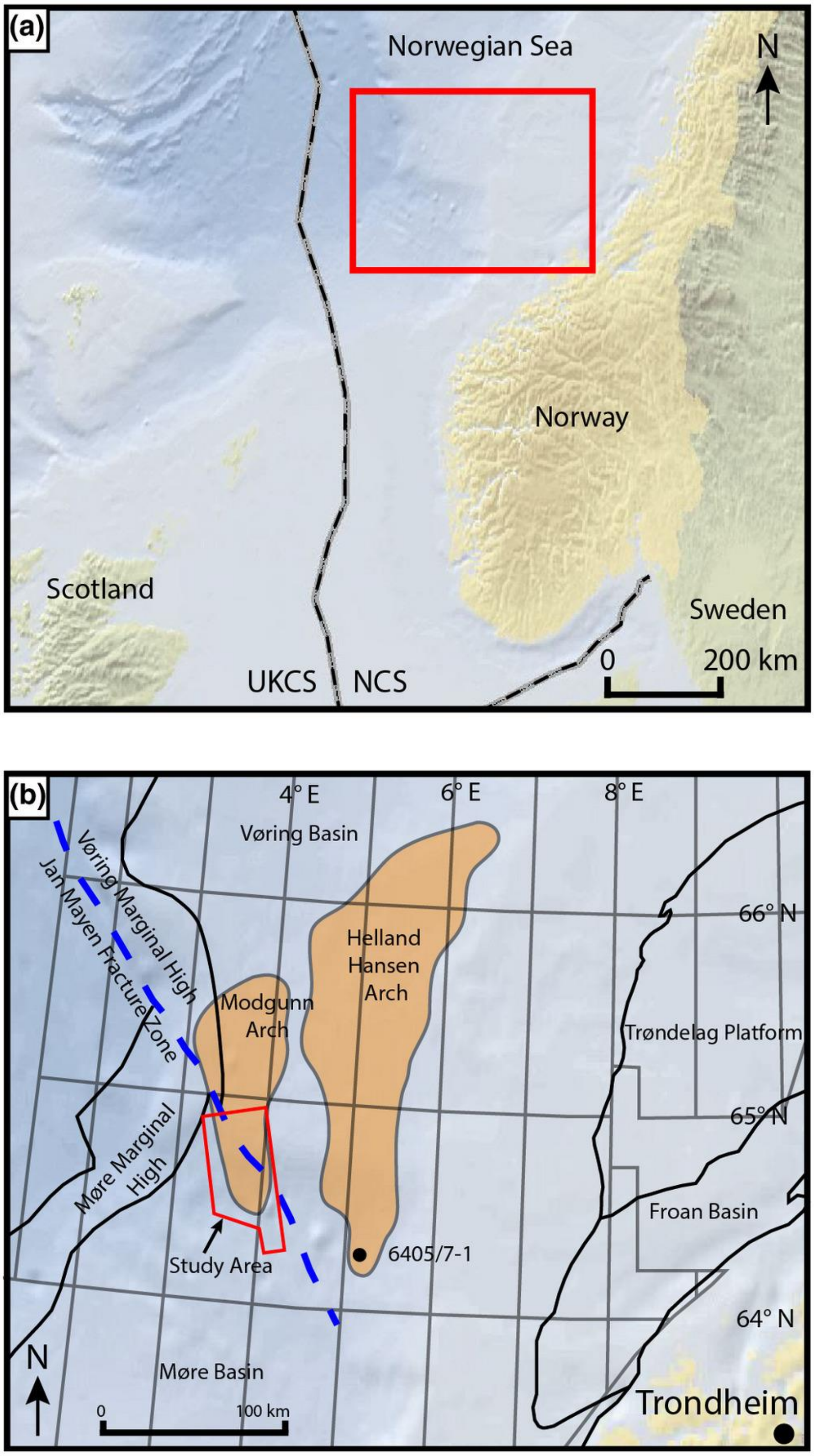

Figure 2.4. (a) Map of the Norwegian Sea. (b) Location of study area in the southern part of the Modgunn Arch highlighting main structural elements in the Vøring and Møre Basins. Figure modified from Roelofse et al. (2020).

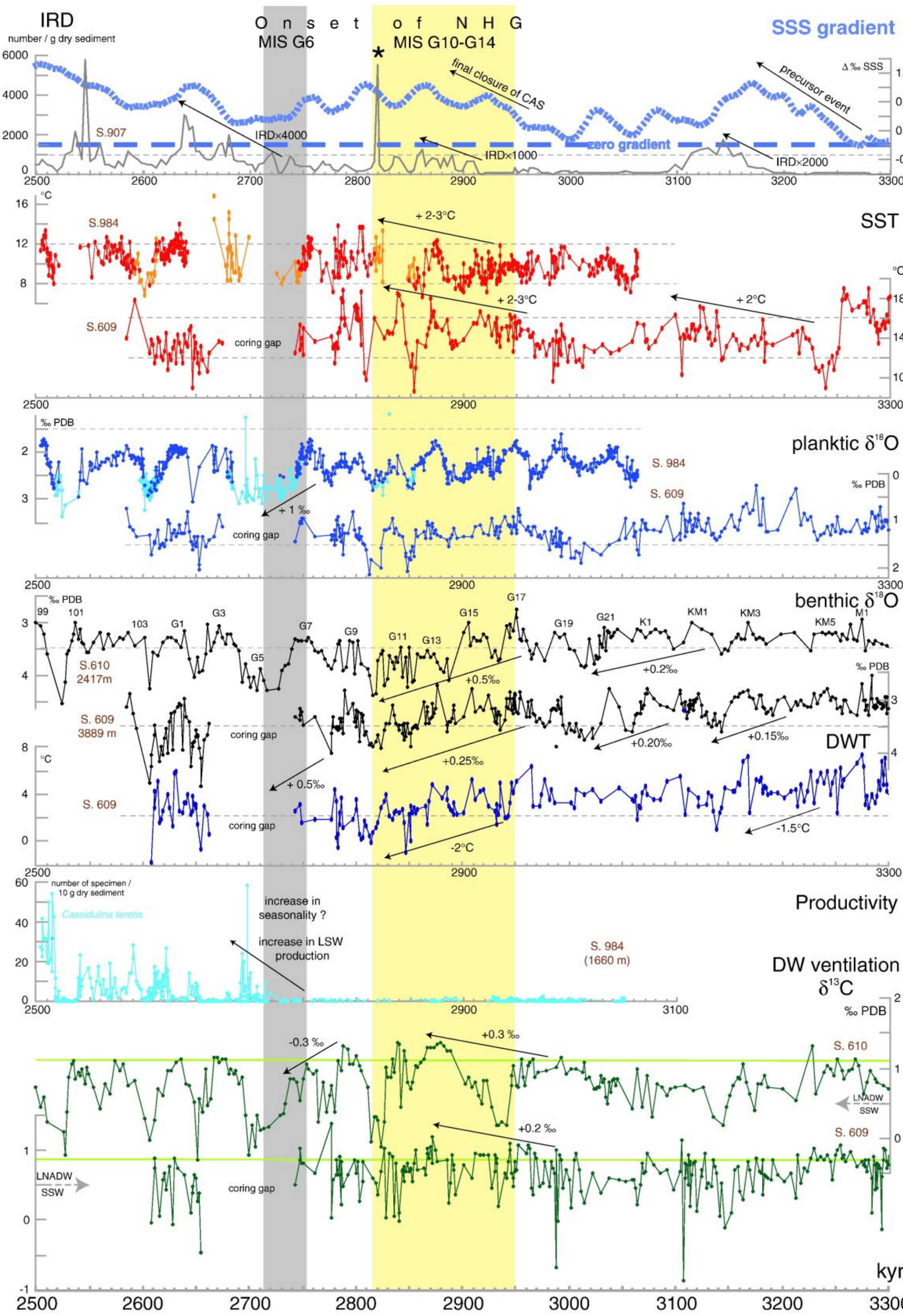

Figure 2.5. Palaeoclimatic records for the Pliocene North Atlantic. Figure after Bartoli et al. (2005).

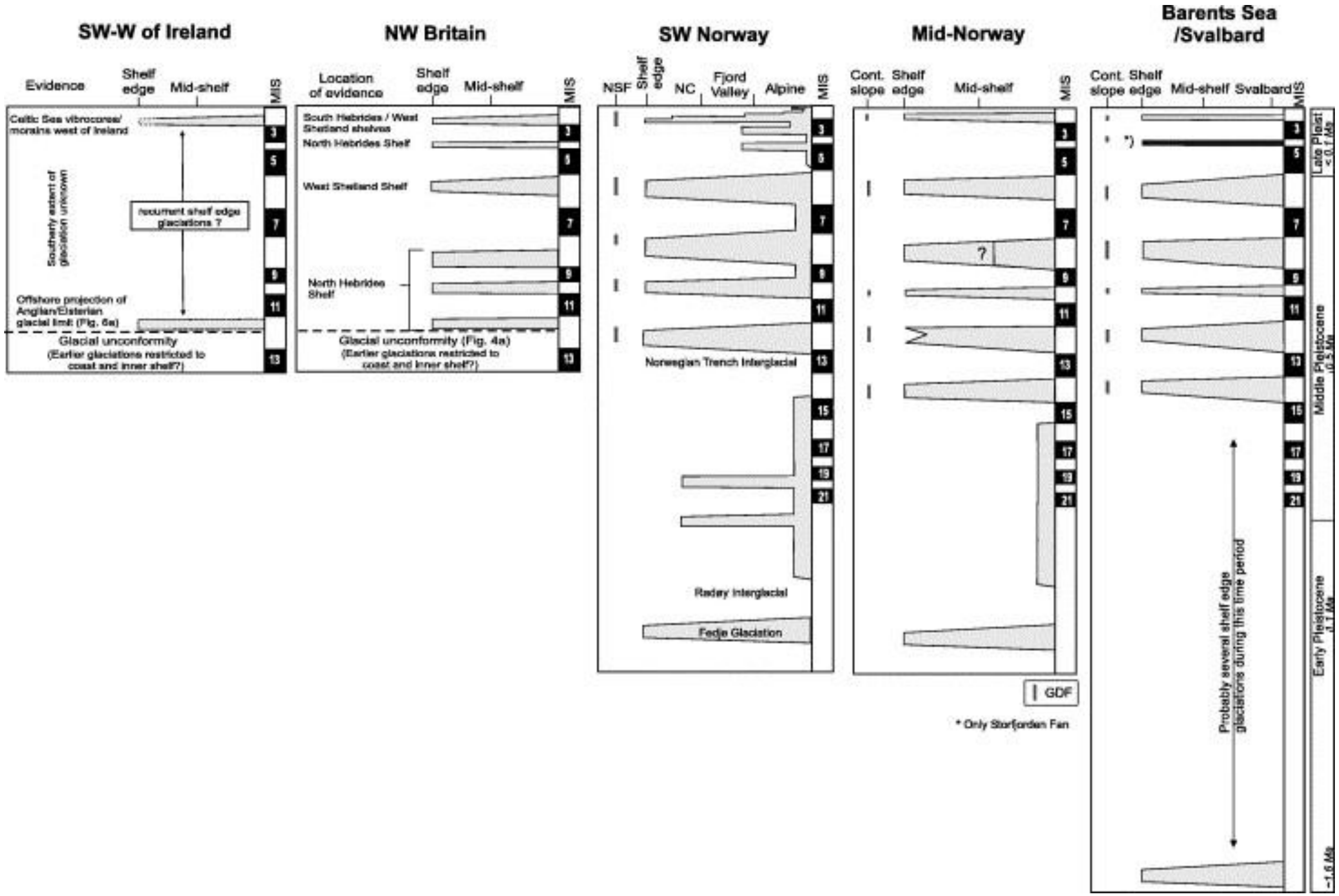

Figure 2.6. Glaciation curves for the Ireland-Svalbard margin segment. Figure from Sejrup et al. (2005).

2.3 Northern hemisphere glaciation

2.3.1 The development of the northern hemisphere glaciation

Due to the final closure of Panama and associated strengthening of North Atlantic Thermohaline Circulation, warm water was brought in larger volumes to northern high latitudes at ~2.75 Ma. This water was stored in NE Europe in the form of ice sheets, leading to the initiation of the Northern Hemisphere Glaciation, or NHG (Bartoli et al., 2005) (Fig. 2.5). In parallel with these phenomena, sea surface temperatures, thermohaline circulation, the Antarctic glacial history and climate in low latitudes were changed as recorded by the varying oxygen isotope ratios in both oceanic sediments and ice sequences (Raymo, 1994). Milankovitch cycles controlled the frequency of glacial-interglacial cycles - between the onset of the NHG to about 900 ka, the weaker 41 kyr obliquity cycle controlled sedimentation with a minor influence from the 100 kyr eccentricity cycle (Zachos et al., 2001). As a result of the effect of these cycles on sedimentation, there is an obvious section of downlapping unconformities formed at this time on the NE Atlantic shelf (Faleide et al., 2015). After the NHG started, the Fennoscandian ice sheet grew and covered the NW European continental shelf until around 1.1 Ma, the time when the Fedje Glaciation till was deposited on Scandinavia. This ice sheet repeatedly reached the shelf break after 0.5 Ma, up to ~10 ka (Sejrup et al., 2005, 2000) (Fig. 2.6).

Glacial-interglacial cycles could efficiently change local sedimentary processes. During maximum glacial coverage – which lasts for a small period – a large volume of glacial sediments (mainly diamictic till and debris flow) were deposited in front of ice streams on the outermost shelf and upper continental slope. These sequences of till and debris flows materialise high sedimentation rates and overlie fine-grained drift deposits on the shelf and upper slope areas of mid Norway. In interglacial periods, the ice front retreated and glacial marine sediment becomes predominant on the margin. At the same time, current-driven contourite drift deposits were (and are presently) deposited on the mid to lower continental slope. Some of these contourite deposits are thick enough to fill older landslide scars (Henrich et al., 1989; Henrich and Baumann, 1994; Solheim et al., 2005).

The glacial-interglacial cycle impacted the development of slope instability on the mid-Norwegian margin. In the Storegga Slide, submarine landslides occurred more frequently after 1.1 Ma, with a peak in activity at ~0.5 Ma, correlating with a phase of glacial advance (Haflidason et al., 2004). The development of the Storegga Slide can therefore be divided into four distinct phases: 1) an interglacial phase, when thick fine-grained sediment was transported and deposited by currents; 2) after the later interglacial phase, ice sheets moved basal till from the inner continental shelf onto its edge; 3) a deglaciation phase followed, and meltwater plume deposited sediment on the continental slope; 4) following this deglaciation period, submarine landslides were triggered by regional isostatic rebound, sea-level change, by the generation of excess pore pressure in near-seafloor sediment, and also by local earthquakes (Haflidason et al., 2004).

2.3.2 Glacial marine deposition

From 2.6 Ma to 1.0 Ma, the response of the Norwegian Sea to climate change was weak and, as a result, relatively small ice caps and short glacial periods are recorded during this period. From 1.0 Ma to 0.6 Ma, the broader difference between glacial and interglacial periods strengthened the Norwegian current. In the last 0.6 Ma, within a warm interglacial period, fine-grained sediments have been transported by the North Atlantic current and deposited on the mid-Norwegian margin as the result of regional embayment, i.e. sediment is deposited in response to decreased current velocities (Henrich and Baumann, 1994).

The depositional model during glacial/interglacial cycles is divided into two stages (Berg et al., 2005):

Stage 1 (10%): Periods of peak glaciation. Icecaps reach the shelf break and transport basal tills. Thus, sediments in front of the ice stream become unstable and lead to slope failure and frequent debris flows on the continental slope. Glacial sediments are also deposited in the deeper parts of the continental slope and rise.

Stage 2 (90%): Periods recording a retreat of the ice front. Fine-grained clays with ice-rafted detritus (IRD) and biogenic components are deposited on the continental margin. The IRD record peak depositional rates when ice starts to retreat. At the same time, contour currents deposit sediment drift, which are the thickest in older slide scars. Regional submarine landslides might occur early in this stage (Solheim et al., 2005).

The clay and water-rich sediments below glacial material form weak layers and lead to slope failure on the mid-Norwegian margin. However, in the Storegga Slide the period between the largest, regional submarine landslides correlates with multiple periods of ice advance (Solheim et al., 2005), suggesting that some of this ice did not reach the shelf edge or supply enough sediment to the continental slope generating, instead, a slope with increasing instability (Sejrup et al., 2005).

2.4 Main depositional sequences

2.4.1 Pre-Breakup strata

Before the breakup of the NE Atlantic, Cretaceous-Paleocene strata were deposited on the mid-Norwegian margin. This pre-breakup phase of deposition ended with the Tang Formation, which marks the youngest sediments imaged in the study area before continental breakup ensued (Jongepier et al., 1996; Kjoberg et al., 2017) (Fig. 2.7). Upper Cretaceous strata composed of sandstone, carbonate, mudstone, as well as several potential hydrocarbon reservoirs that led to the drilling of Well 6403/6-1 (Dalland, 1988; Knaust, 2009; Lien, 2005). During the deposition of the Paleocene Tang Formation, the Møre Basin was part of a volcanic rifted margin, and sill intrusion and related hydrothermal vent complexes affected this same stratigraphic unit (Planke et al., 2005; Roelofse et al., 2021; Svensen et al., 2003).

2.4.2 Tare Formation (lower Eocene)

Above the Tang Formation, the Tare Formation was deposited as a continental breakup sequence sensu Soares et al. (2012) and Alves et al. (2020) (Fig. 2.7). This unit

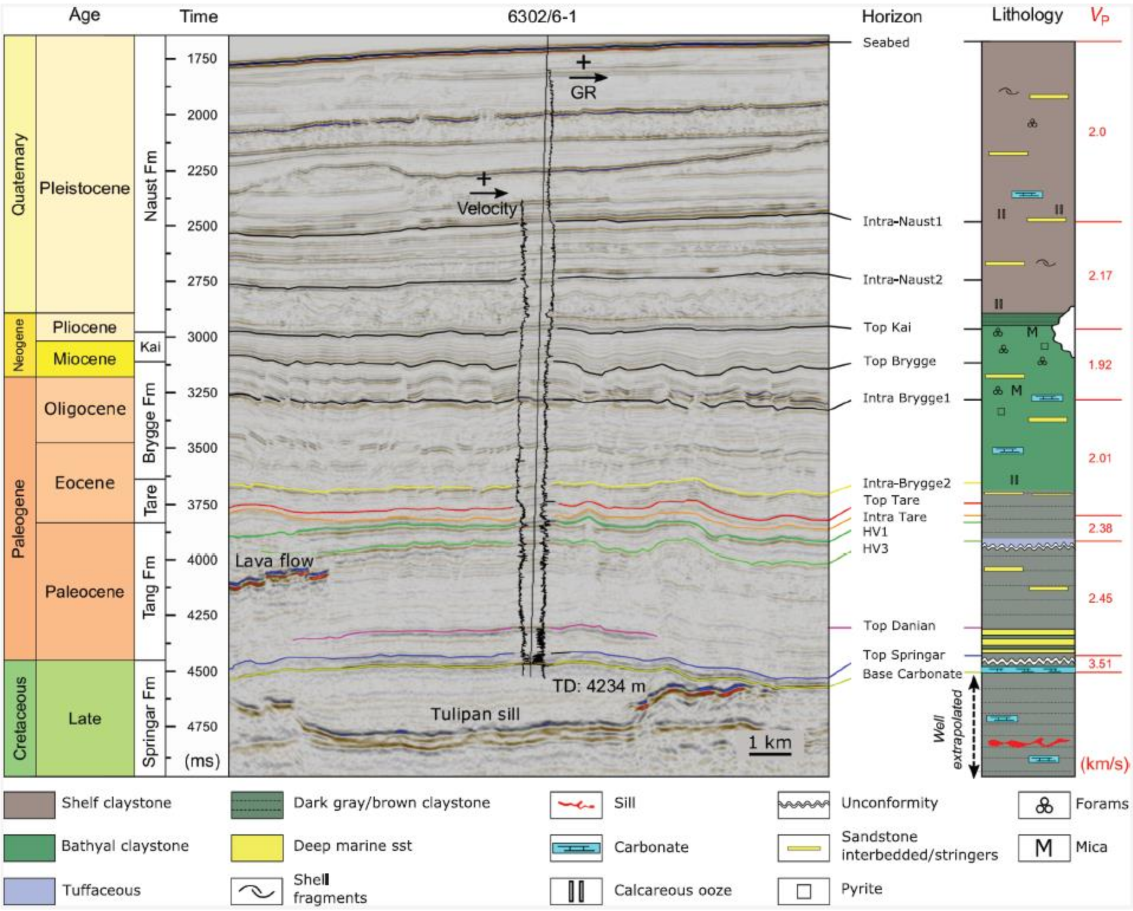

Figure 2.7. Summary diagram showing the key seismic horizons interpreted in this thesis and a synthesis of lithostratigraphic data in exploration well 6302/6-1. Figure modified from Kjoberg et al. (2017).

was deposited in a deep-marine environment, consisting of dark grey, green or brown claystone interbedded with thin sandstone intervals (Dalland, 1988). The base of this formation is defined by an increase in tuff content (Kjoberg et al., 2017).

2.4.3 Brygge Formation (upper Eocene to lower Miocene)

Previous research has suggested that the Brygge Formation is composed of marine claystone with intervals of sandstone, siltstone, limestone and marl, recording a density of 1.85 g/cm3 at the centre of the Møre Basin (Dalland, 1988; Lawrence and Cartwright, 2010). This ooze-rich and multi-component unit can be subdivided into several seismic-stratigraphic packages (Lawrence and Cartwright, 2010; Riis et al., 2005) (Fig. 2.7):

Unit I: Showing moderate amplitude in seismic data, it is bounded on its top by a high-amplitude ‘positive’ reflector (same with seafloor). Early Eocene in age

Unit II: A seismically transparent interval. Bounded above by a low-amplitude ‘negative’ seismic reflector. Early Eocene to Oligocene in age.

Unit III: Moderate amplitude. It is bounded by a low-amplitude ‘negative’ reflector on its top. Late Oligocene in age.

2.4.4 Kai Formation (lower Miocene to upper Pliocene)

The Kai Formation is composed of fine-grained hemipelagic sediments with abundant oozes. It is rich in smectite with a density of 1.9-2.25 g/cm^3 at the centre of the Møre Basin (Dalland, 1988; Forsberg and Locat, 2005; Lawrence and Cartwright, 2010). Fine-grained contourite drifts were formed in its interior by northward-flowing marine currents, which were established in the Miocene and limited by a strong thermocline to a depth between 500 m and 700 m (Alendal et al., 2005a; Bryn et al., 2005b; Krokmyrdal, 2017; Thiede and Myhre, 1996). Both the Kai Formation and its lateral equivalent (Molo Formations) were deposited on the mid-Norwegian margin at the same time but in different environments. The Kai formation was deposited on distal and deeper marine environments, whereas the Molo formation was deposited on proximal marine areas via the progradation of coastal deposits as a result of the uplift of the landward side of the margin. There is a recognised sediment bypass zone between the Molo and the Kai formations (Eidvin et al., 2007).

2.4.5 Naust Formation (upper Pliocene-Quaternary)

The Naust Formation, comprising the youngest marine deposits in the study area, comprises interbedded claystone, siltstone and sandstone, occasionally with very coarse glacio-marine clastics in its upper part. Even though the Naust Formation is rich in soft clay, the relatively large silt component in this unit prevented the onset of widespread syneresis and subsequent formation of polygonal faults in its interior (Gay and Berndt, 2007). The unit records a density of 2.3 g/cm^3 in the east Møre Basin. These glaciomarine deposits can be divided into several packages reflecting distinct glaciation episodes (Berg et al., 2005; Dalland, 1988; King et al. 1996; Lawrence and Cartwright, 2010) (Table 2.1).

Fm.	Unit	Sub-unit	Hor.	Seismic facies	Lithology	Phys. Props.	Dep. Env.	Age (ka)
Naust	O	O1–O2	INO2	Generally transparent, occasional weak internal reflections. Largely removed by Storegga Slide. Present and but displaced and partly disturbed at Site 22	Unsorted silty, sandy, gravely clay (Diamicton), with shell fragments	Clay: 20–40%, S&G: 10–25%, Wc: 14–27%, UW: 19.7–21.1 g/cm^3, Ip: 16–34%	Basal till and/or deformation till, deposited beneath fast-flowing ice stream	30–15 (MIS 1–2)
		O3	INO3	Stratified, Mounded, climbing character on the slope, with thickness increase down-slope. Largely eroded on the shelf	Silty clay with sand, scattered gravel and shell fragments. Increasing clay content in lower part of the sub-unit	Clay: 40–65%, S&G: 5–15%, Wc: 30–34%, UW: 18.5–19 g/cm^3, Ip: 30–32%	Major part is glacial marine, variable glacial proximity. Lower 5–10 m represent interglacial marine hemipelagic deposits. Contouritic deposition	130–30 (MIS 5e–3) (Lower part is Eemian)
		O4–O7	TNR	Homogeneous, transparent, w/ some discontinuous reflections. Fan-shaped distribution on the slope, cut by the Storegga Slide. Some internal high relief formed by INO5	Diamicton with shell fragments and variable content of gravel and larger clasts. In general a upwards-fining character of O4	Clay: 20–40%, S&G: 10–25%, Wc: 13–20%, UW: 20.8–22.2 g/cm^3, Ip: 15–20%	Primarily glacial. Tills on the shelf, debris flows on the slope. O4 is transitional in character	200–130 (MIS 6)
	R	R1–R2	INR2	Stratified, with partly mounded, climbing character (R2) filling in underlying topography. R1 only limited extent as a wedge–shaped deposit near Site 99. TNR is a main horizon and forms a main failure plane for the Storegga Slide	Silty clay (~60% clay) w/ little sand and gravel. Lower part of R2 shows gradual change to the more diamictic R3 unit	Clay: 35–70%, S&G: 3–20%, Wc: 20–31%, UW: 18.9–21.5 g/cm^3, Ip: 27–31%	Glacial marine to normal marine conditions, in an ice-distal to interglacial setting. Largely affected by contour currents, i.e. contouritic deposition	330–200 (MIS 9–7)
		R3	TNS	Less stratified than R2, but some internal reflections of variable strength	Increasing sand and gravel compared to R2	Clay: 31–66%, S&G: 4–40%, Wc: 16–18%, UW: 21.4–22.0/cm^3, Ip: 19–20%, (Poorly sampled)	Primarily glacial marine, but more ice-proximal than R2. Probably also some glacial debris flow deposits on the slope	380–330 (MIS 10)
	S	S1–S2	INS2	Stratified, partly mounded, contouritic, filling in old slide scars in the INS2 surface	Poorly sampled. Silty clays with variable sand, gravel and shell fragments. Primarily fine grained, as also supported by downhole logs	Clay: 26–66%, S&G: 2–30%, Wc: 30–40%, UW: 18.1–19.8 g/cm^3, Ip: 25–45%	Distal glacial marine to normal marine, hemipelagic deposition	420–380 (MIS 11)
		S3–S6	TNU	Varies between homogeneous, chaotic and stratified. S5 and S6 have an opaque character and limited lateral extent. S4 partly stratified and mounded	Poorly sampled. Silty clays with variable content of sand, gravel and shell fragments. Thin sand layers. Increased content of coarse components relative to Unit R	Clay: 30–60%, S&G: 3–20%, Wc: 17–30%, UW: 19.3–21.5 g/cm^3, Ip: 20–28%	Glacial marine deposits, deposited under variable glacial conditions. The sequence represents one or more glaciations	S3–S5: 550–420 (MIS 14–12), S6: 1000–550(?)
	U	U1–U2	TNW	Present under the entire Ormen Lange license area. Mainly homogeneous, but with some stratification in distal parts	Unsampled	Clay: S&G: Wc: UW: Ip:	U1 represnts distal glacial marine to normal marine deposits from initial glacial advance ('Fedje glaciation'). U2 is probably debris flow or slump deposits	~1700–1100
	W	W1–W3	BNa-ust	Present under the entire Ormen Lange license area. Massive, transparent character. Strong contrast to the underlying stratified, faulted biogenic Kai Fm. Deposits	Undiffentiated Unit W sampled sparsely at Storegga North Flank (Site 28); Silty clay with relatively high biogenic content (foraminifera)	Clay: S&G: Wc: UW: Ip:	Mainly normal marine, hemipelagic deposits, but with some IRD from mainly land-based glaciers	~2600–1700

Table 2.1: Summary table for the Naust Formation based on data from the Ormen Lange area, near the headwall of the Storegga Slide. Modified from Berg et al. (2005).

CHAPTER THREE

Data and Methods

3. Data and methods

3.1 Introduction

Three-dimensional (3D) seismic volumes are widely used in the petroleum industry to interpret subsurface geological structures such as domes, faults and landslides. This chapter briefly introduces the 3D seismic dataset used in this thesis and outlines how seismic data is acquired, processed and interpreted. The data in this study was shot for petroleum exploration and development and are used in several research projects in Cardiff University's 3D Seismic Laboratory. The methodology adopted in this thesis when interpreting the seismic data, including attribute mapping and fault ant-tracking, is summarised in next sections (3.2-3.3). The main concepts explaining the numerical modelling completed for this thesis are described in 3.4.

3.2 Seismic data

Three-dimensional (3D) seismic data and corresponding seismic interpretation is one of the most primary tools for the investigation of geological features associated with submarine structures, especially when exploring deep-water depositional systems (Bull et al., 2009a; Yilmaz, 2001). In addition, regional tectonics, fault systems, mass-transport deposits and fluid migration and accumulation can also be characterised by using 3D seismic data. In comparison to 2D seismic data, which can only produce a cross-section of the subsurface, 3D seismic data consist of multiple closely spaced profiles that provide a complete image of geological structure without spatial aliasing problems (Davies et al., 2004).

3.2.1. Seismic acquisition

The acquisition of seismic data is based on the production of sound waves and later reception (acquisition) of their reflections after they travelled through subsurface strata. Each of these reflections record strata with distinct wave impedances (Equation 3.1). Offshore seismic acquisition often uses offshore survey vessels to produce the acoustic (sound) pulse, which is then received by data receivers as seismic wave signals from reflectors below the sea floor. On a seismic volume, the direction of inline coincides with ship track and varies in spacing from around 12.5 to 25 m. Crosslines are acquired in a direction perpendicular to the inlines, and their spacing varies from 25 to 50 m (Yilmaz, 2001).

After an acoustic pulse, or P-wave, is generated by a vessel, this wave penetrates the sea floor and propagates through the subsurface strata below. In strata presenting changes in their physical properties with depth, P-waves are propagating as a transmitted P-wave until they are partly reflected (Gluyas and Swarbrick, 2021; Sheriff and Geldart, 1995). The reflected wave is recorded by hydrophones before being compiled in a coherent seismic profile, or volume. The time between the initial production (shot) of a seismic wave from a vessel and the time when is received by the hydrophones is measured as two-way travel (TWT) time in seconds or milliseconds.

The polarity and magnitude of the detected wave reflects the difference of impedance between rocks on both sides of an interface, or seismic reflector. The velocity of a seismic wave depends on the composition, texture, porosity, fluid content and elastic module of the strata crossed by this same seismic wave (Kearey et al., 2002). Hence, seismic velocity normally increases with depth due to the increasing degree of compaction and cementation in strata (Kearey et al., 2002). The relationship between velocity (v), density (ρ) and acoustic impedance (Z) is expressed as:

$$Z = \rho * v$$

Equation 3.1

The impedance (Z) represents the intrinsic properties of geological interfaces affected by the partition of energy between transmitted and reflected P-waves (Lowrie and Fichtner, 2020). In this study, seismic data is displayed in ‘SEG (Society of Exploration Geophysicists) European polarity classification’ (Sanderson, 1991). A positive amplitude (peak) indicates an increase in acoustic impedance with depth, and is represented by a red coloured reflection on seismic profiles (Fig. 3.4c).

3.2.2 Seismic resolution

The resolution of seismic data is one of the key parameters used to measure the quality of seismic data. It relates to the detection and distinction of two points that are close to each other and represent different geological features (Kearey et al., 2002; Sanderson, 1991). Based on the relative position of these ‘two points’, the seismic resolution can be discriminated between vertical resolution and horizontal resolution. The vertical resolution of a seismic dataset is determined along the direction of wave propagation by the seismic source signal and the wavelength of the seismic waves. This wavelength (λ) is defined as a function of velocity (v) and frequency (f) (Sanderson, 1991):

$$\lambda = v/f$$

Equation 3.2

An important aspect is that wavelength tends to increase as the velocity of a seismic wave becomes higher with depth due to the effect of sediment compaction (Kearey et al., 2002). The maximum possible resolution of a single wavelet thus varies between one-quarter ($\lambda/4$) to one-eight ($\lambda/8$) of the dominant wavelength of the original seismic pulse (Sheriff and Geldart, 1995), though geological features at $\lambda/32$ of the dominant wavelength are not uncommon at shallow depths (Chopra et al., 2006). Consequently, the detectable size of geological features in seismic data is often an order of magnitude larger than that observed at outcrop (Kearey et al., 2002). The higher frequency spectrum of emitted waves are absorbed with the increasing propagation of seismic waves. Therefore, vertical resolution decreases with increasing wavelength in deep-buried sediment.

Compared to vertical resolution, the horizontal resolution of a seismic survey is controlled not only by the physical process of reflection but also by the spacing of the receivers (hydrophones) towed behind a vessel (Kearey et al., 2002) . The detector spacing, as illustrated in Fig. 3.1, is double the length of the reflector. By spacing the receivers closely, the horizontal resolution could be correspondingly increased. However, similar to the vertical resolution, the horizontal resolution also decreases with depth with increasing wavelength (λ) and by the progressive loss of the higher frequency signal. Specifically, horizontal resolution is expressed by the concept of a *Fresnel Zone* (Bacon et al., 2007) (Fig. 3.2), which represents the coverage zone (W) of a seismic reflector:

$$\mathrm{W} = \sqrt{2z\lambda}$$

Equation 3.3

During seismic data processing, by collecting the reflection events that fall into the same area with a common midpoint (CMP), the horizontal resolution can be further increased to one-quarter of the wavelength.

3.3. 3D seismic dataset and interpretations in this study

3.3.1 3D seismic dataset

A high-resolution 3D Seismic data from the northwest flank of the Storegga Slide has been interpreted in this study. The survey also images one of the Cenozoic domes that are typically observed on the mid-Norwegian margin - the South Modgunn Arch (SMA) – and covers an area of 2635 km^2. It was acquired by PGS in 2002 and named as MC3DDMGS2002 (Fig. 3.3). The seismic data were processed and displayed in zero-phase, European polarity of which a red positive wave peak represents an increase in acoustic impedance with depth, whereas troughs are blue (or black) negative reflectors. Inlines and perpendicular crosslines are oriented NNW and WSW, respectively, with a

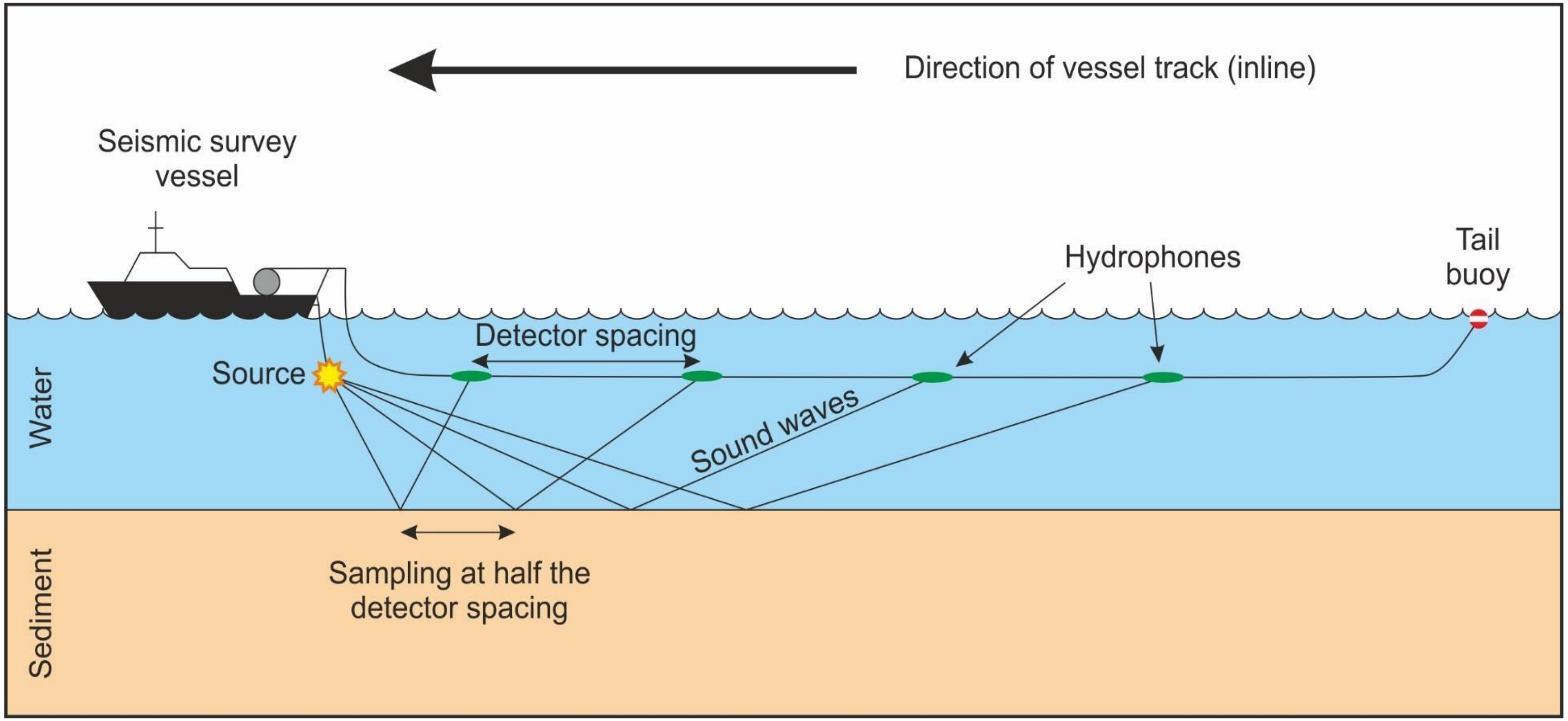

Figure 3.1. Cartoon illustrating the method behind the acquisition of 3D seismic data. The seismic vessel tows an acoustic source near the surface, which emits a loud soundwave. These waves travel through the water and into the sediment layer, reflecting back to the receiver (hydrophones). Figure after Bacon et al. (2007).

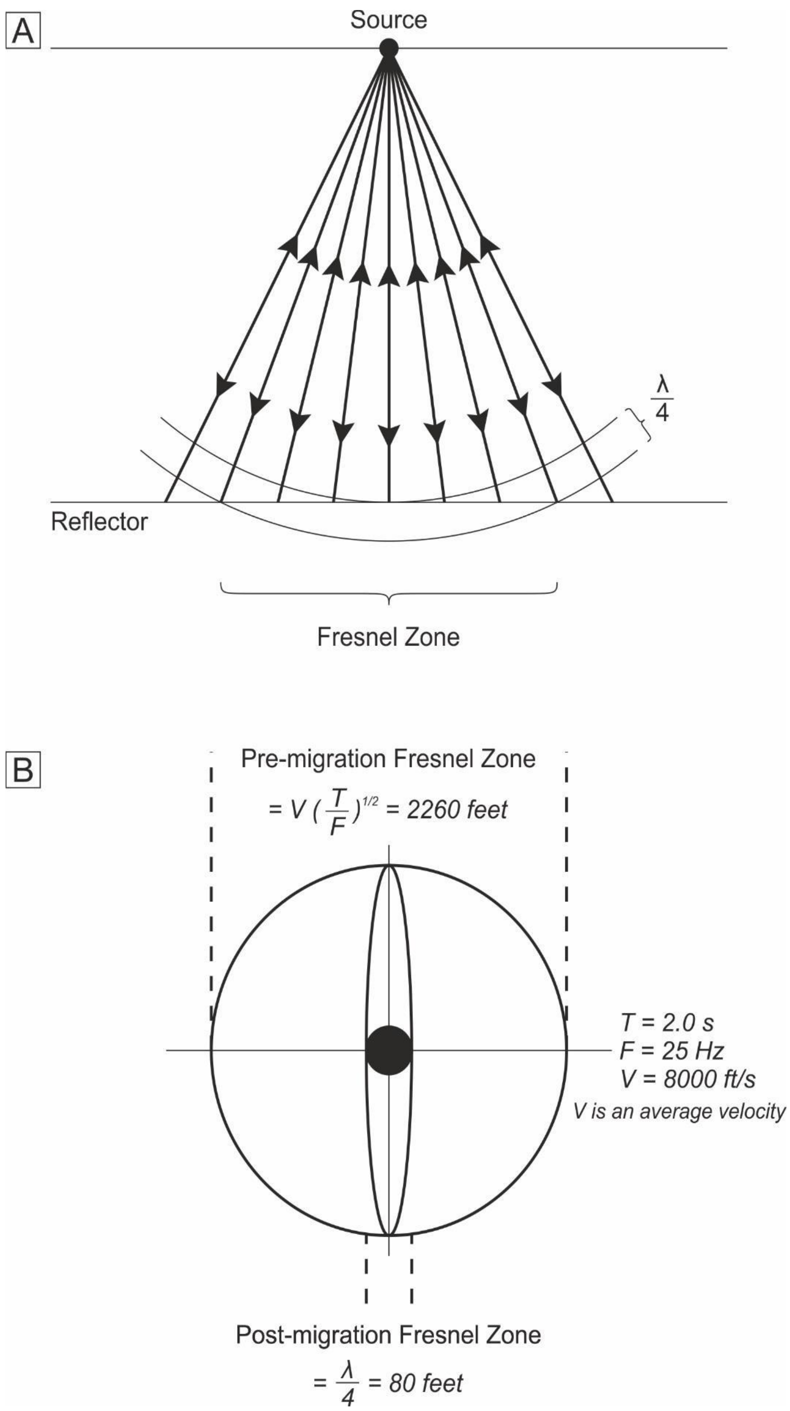

Figure 3.2. a) A simplified scenario of a flat reflector on which seismic energy is returned (reflected) in the direction of the source (and thus acquired by a receiver). The Fresnel Zone is the horizontal region of the reflector where all the energy is returned within half a wavelength of the initial reflected arrival. The energy from within this zone contributes constructively to the seismic signal at this point in space. Figure is modified from Kearey et al. (2002). b) Schematic diagram showing the reduction of the Fresnel Zone after signal migration to λ/4, with values provided as an example. Figure from Brown (2004).

bin spacing of 12.5m. This survey is presented in two-way travel (TWT) time with a vertical sampling rate of 4 ms TWT. One exploration well (6403/6-1) was drilled in the centre of the South Modgunn Arch in 2002, indicating a vertical resolution of 8 m for post-breakup strata in the interpreted survey.

3.3.2 Seismic interpretation

The seismic interpretation in this thesis was completed on Schlumberger Petrel 2019, including structure and stratigraphic analyses to describe the character of sub-surface geological bodies. A combination of 3D visualisation techniques, mapping and construction of seismic attributes maps was applied to the interpretation workflow in this thesis. Attribute data frequently used were amplitude, root mean square (RMS) amplitude, and variance (coherence) maps and slices (Fig. 3.4).

During the interpretation of key seismic horizons, the seeded 3D auto-tracking tool was used to automatically track reflections that have a similar energy, phase and amplitude. The 3D auto-tracking is occasionally interrupted by changes in seismic attributes, which could be a result of faults, fluid flow and stratigraphic unconformities.

The amplitude of seismic reflections depends on differences in acoustic impedance, which are related to the density and velocity of strata and suggest changes in the properties of strata crossed by the seismic waves, i.e. lithology, porosity and fluid content. It is recorded as either positive or negative value, depending on the change of acoustic impedance through the seismic reflector. Based on the analysis of amplitude changes, RMS amplitude can compute the square root of the sum of squared amplitude values divided by the number of samples within the specified window (i =1 to n in Equation 3.4) and usually be used to highlight the presence of fluid and faults in a volume of rock (Koson et al., 2014).

$$x_{RMS} = \sqrt{\frac{1}{n}\sum_{i=1}^{n} x_i^2}$$

Equation 3.4

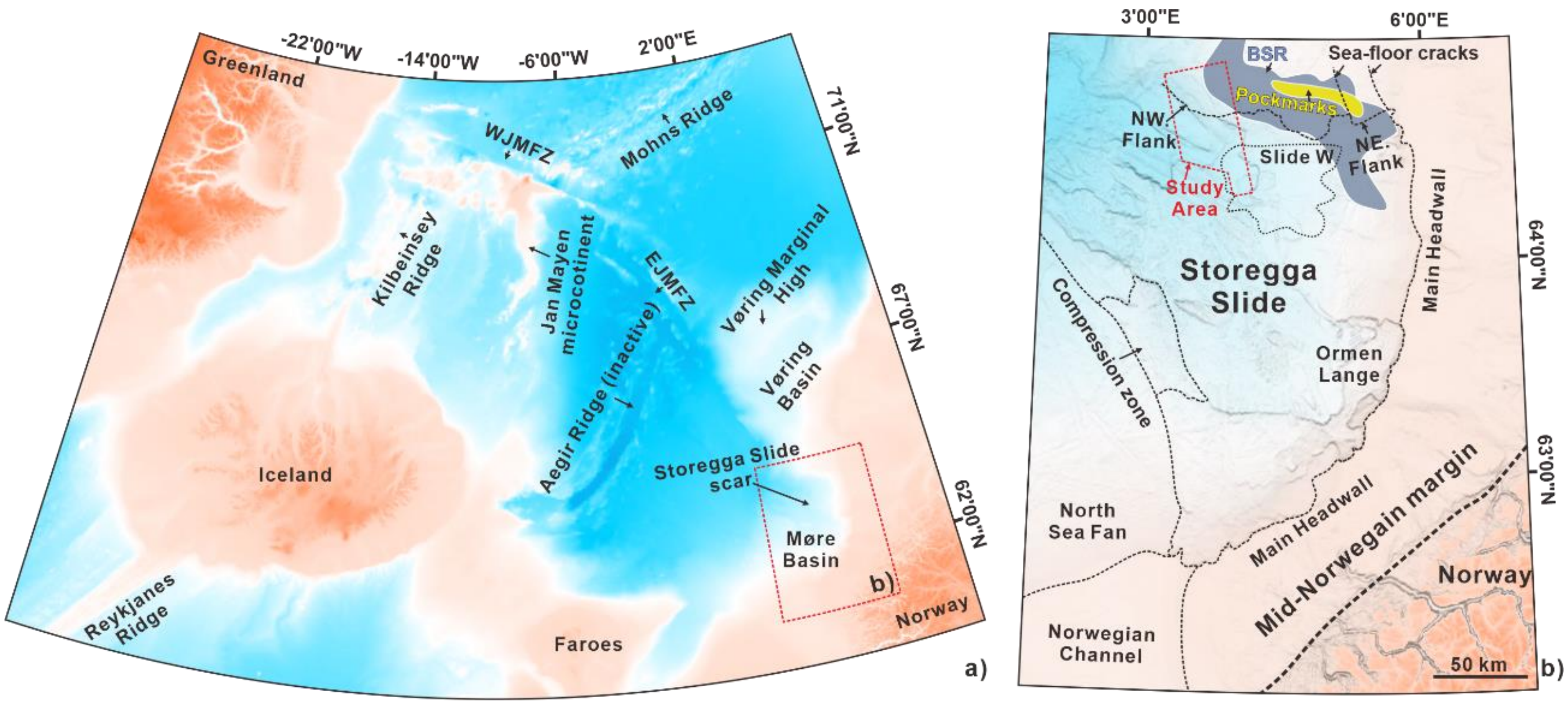

Figure 3.3. Location of study area on the mid-Norwegian margin, NE Atlantic Ocean.

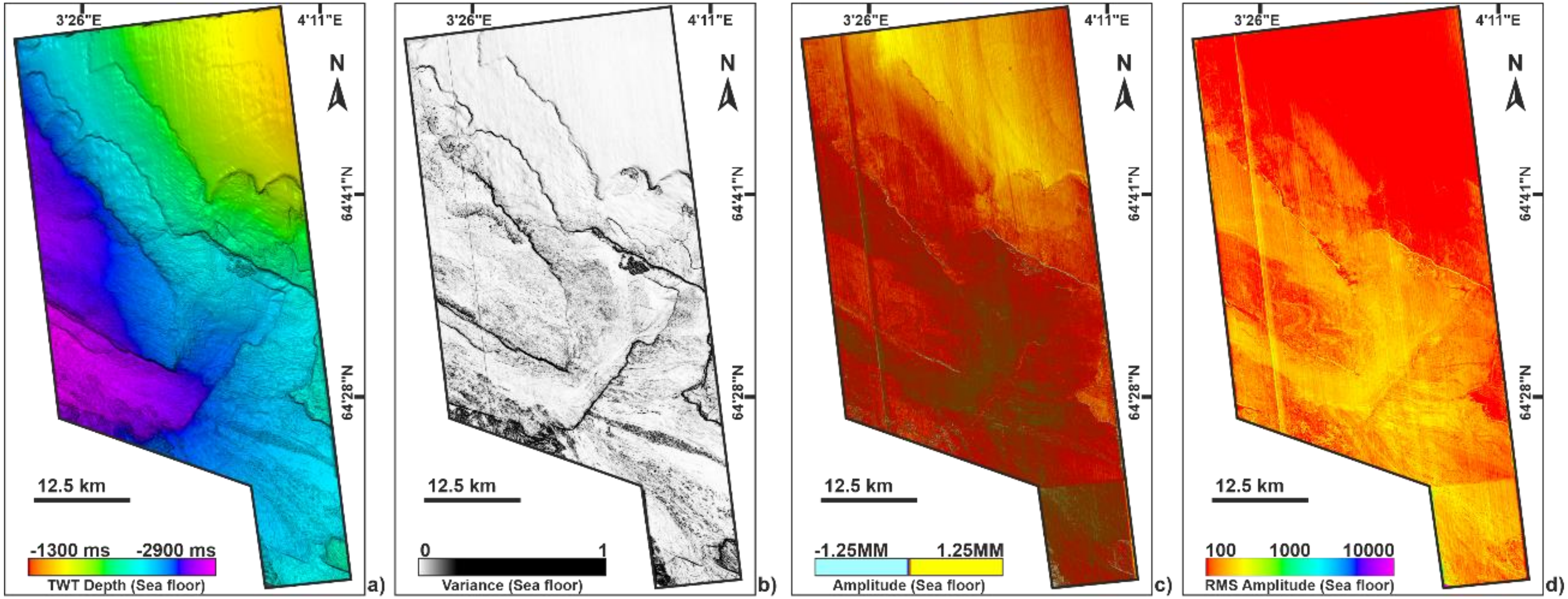

Figure 3.4. Examples of different structural maps and seismic attributes used in the interpretation of the 3D seismic data volumes in this thesis: a) two-way time structural map; b) variance; c) amplitude; d) root-mean-square amplitude.

Variance (coherence) implies the squares of deviations from an average value of waveforms over a given lateral and/or vertical windows, suggesting the contrast between adjacent seismic reflections (Koson et al., 2014). When there is a fault or unconformity, features with different amplitude and continuity from the surrounding strata, the variance values increase (Pigott et al., 2013). In contrast, variance values are lower in continuous layers. Based on this same response, the variance attribute is used to map unconformities, faults, fractures, pockmarks, submarine channels, etc.

3.3.3 Fault analyses

In this thesis, variations in fault throw vs. depth (T-Z plots) are used to understand the depth of nucleation and development of faults (see Tao and Alves, 2019). The height of faults is measured as the vertical distance between the top and bottom tips on a seismic section. To complement the T-Z fault interpretations commonly used in the literature, a combination of 3D visualisation techniques, structural and attribute maps was applied when analysing the fault systems in the study area. Attributes of interest included thickness calculation, variance, trace AGC, structural smoothing, chaos, ant-tracking, and automatic fault extraction. Relief maps were based on the seismic interpretation of several horizons, which were then compiled into a 3D surface to highlight changes in structural depth. The location of faults in different horizons was shown by flattened variance maps displaying the horizontal relationship between faults and associated structures, i.e. evacuation structures, the SMA and adjacent submarine landslides. The thickness of several intervals was calculated as the TWT difference between two seismic reflections.

Automatic fault extraction was performed and quality-controlled on seismic profiles and variance slides. The automatic fault extraction works in tandem with the ant-tracking seismic attribute, which is based on trace AGC, structural smoothing and chaos seismic cubes. The trace AGC (Amplitude Gain Control) normalises RMS amplitude over a specified window. As a result, the existence of faults in strata with low amplitude becomes more obvious. Structure smoothing is available to smooth the perturbation of seismic facies and sharpen fault-related discontinuities. The chaos seismic cube highlights the lack of organization (discontinuities) in seismic volumes, which is often a result of faulting and mass-wasting (deformation) of near-seafloor strata. Eventually, the ant-tracking function can extract faults by searching any marked discontinuities and exporting correlating path as fault planes (Ngeri et al., 2015).

Based on fault analyses, the stress field during the different periods could be deduced by stress inversions. As a stress field could create a specific type and direction of faults, the strike of faults can supply the necessary data to estimate palaeo-stresses. Rose diagrams and stereographic projection were also used in the estimate of the faults' strikes and in palaeo-stress analysis.

3.4 Evolution models of slope instability

As one of the major offshore geohazards, submarine landslides comprise failed soil masses recording internal softening and liquefaction before evolving into debris and turbidity flows during their transport. In this study, a computational fluid dynamics (CFD) approach is used in ANSYS FLUENT in the numerical simulation of slide blocks and associated glide-plane propagation. The soft clay-rich Naust formation, including weak layers, was modelled as non-Newtonian fluid. Due to the location of the study area on the northwest flank of the Storegga Slide, the numerical simulation focuses on the initial phases of slope failure. The existence of slope undercutting was revealed in seismic data by the presence of multiple scarps on a slope that records, for almost its entire length, a gradient $<1^{o}$ below Slides S and R. Thus, the models in this chapter consider the existence of weak layers and the pre-existence of scarps as important features controlling the style and development of submarine landslide in the study area.

During the CFD approach, the strata (non-newton fluid) was modelled as an Eulerian material where a finite-volume technique is used. At the same time, the momentum and mass transfer processes were modelled by solving the Navier-Stokes equations and additional transport equations. In FLUENT, the models were set as a 2D planar models with laminar flow.

The initial geometry of the models completed in this thesis is shown in Fig. 6.8, where the existence of a weak layer is defined as an 8m thick marine clay with lower shear strength at the bottom. A submerged density of 900 kg/m^3 is assigned to both ‘block’ and weak layer intervals. The physical properties of air are set by default. Both strata and air are modelled as multiphase Eulerian materials. All boundaries between the walls of the landslide and this latter are defined using a no-slip boundary condition.

In this study, the reduction of shear strength (τ_y) during initial sliding and run-out is modelled as a function of the accumulated plastic shear strain (ξ). The strain-softening process is expressed as (De Blasio et al., 2005; Dutta et al., 2018; Einav and Randolph, 2005) (Fig. 3.5):

$$\tau_y = \begin{cases} \left[\frac{1}{S_t} + \left(1 - \frac{1}{S_t}\right) * e^{-3\xi/\xi_{95}}\right] * S_{up}; & \boldsymbol{if}\ \xi \le \xi_{95} \\ \left[S_{u95} - \frac{\left(S_{u95} - \tau_{y(ld)}\right)(\xi - \xi_{95})}{\xi_{ld} - \xi_{95}}\right]; & \boldsymbol{if}\ \xi_{95} < \xi \le \xi_{ld} \\ \tau_{y(ld)}; & \boldsymbol{if}\ \xi > \xi_{ld} \end{cases}$$

Equation 3.5

τ_y: Mobilised shear strength;

S_t: Sensitivity. The ratio of intact undrained shear strength to remolded undrained shear strength;

ξ: Accumulated plastic shear strain;

ξ_{95}: Value of accumulated shear strain where 95% of soil strength is reduced;

S_{up}: Peak undrained shear strength of soil;

S_{u95}: Undrained shear strength of soil at ξ_{95};

$\tau_{y(ld)}$: Large-strain shear strength with shear wetting

ξ_{ld}: Shear wetting parameter

However, FLUENT does not have any direct option to pre-define the accumulated strain (ξ) a parameter further controlling decreases in the shear strength of failed material (Equation 3.5). In order to set an initial shear strength that increases with depth (Gauer et al., 2005), and thus track the accumulated strain during downslope sliding, additional transport equations were included in the modelling workflow (Dutta and Hawlader, 2019):

$$\frac{\partial}{\partial \mathrm{t}}(\rho\phi) + div(\rho\phi\boldsymbol{u}) = div(\Gamma gard\phi) + S_{\phi}$$

Equation 3.6

where ρ is the density of the flowing material, assumed to be the density of strata in this study, $\boldsymbol{u}$ is the velocity vector, Γ is the diffusion coefficient, which has been set as zero as the diffusivity of strain is neglected in this study. The parameter S_{ϕ} is a source term equal to the increase of strain in each time step. In Equation 3.6, the first term represents the rate of change of a variable of the flowing material in the control volume. The second term represents changes due to advection, while the third term reflects sediment transport due to variations in porosity (ϕ) from point to point. The initial shear strength is defined, in this thesis, as 25 kPa at the sea floor, increasing linearly with depth in the order of 2.4 kPa/m (Gauer et al., 2005).

The shear behaviour of homogeneous multiphase Eulerian materials was defined using the dynamic viscosity (μ_d). Except for the air with its default settings, the strata were modelled as a visco-plastic non-newton fluid with μ_d defined as $S_u/\dot{\gamma}$, where $\dot{\gamma}$ is the strain rate; and S_u represent the shear strength calculated from Equation 3.5 (Dutta et al., 2018). To ensure the numerical stability of the models during very small deformation rates, the minimum value of $\dot{\gamma}$ in this study was set at 0.0001. Further discussions regarding this modelling approach are available in Debnath (2018), Dutta et al. (2018) and Dutta and Hawlader (2019).

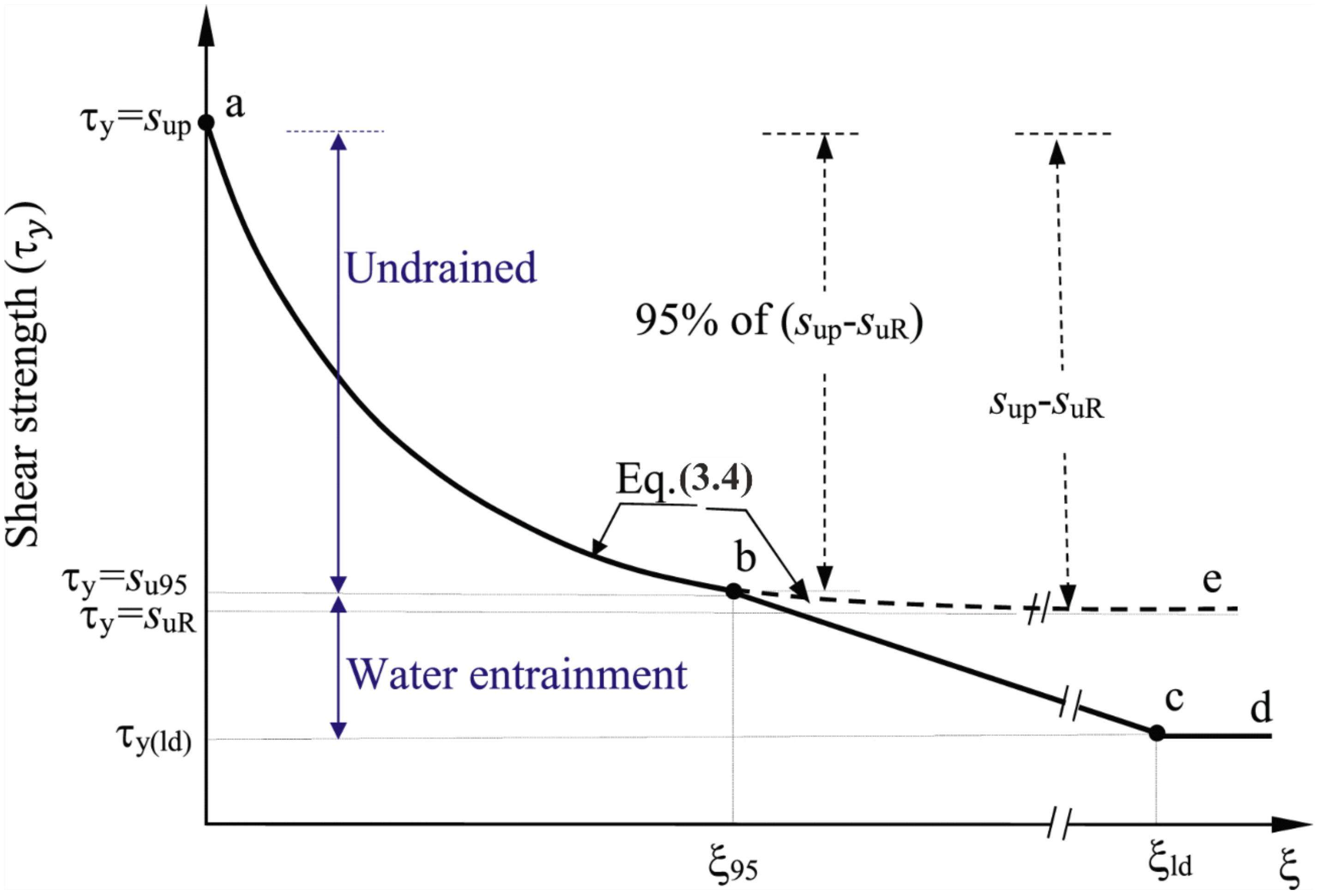

Figure 3.5. Strain-softening process. The shear strength decreases with accumulated strain. Figure modified from Dutta et al. (2018).

CHAPTER FOUR

Tectonic evolution of strike-slip zones on continental margins and their impact on the development of submarine landslides

4. Tectonic evolution of strike-slip zones on continental margins and their impact on the development of submarine landslides (Storegga Slide, Northeast Atlantic)

4.1 Abstract

Submarine landslides have affected the mid-Norwegian margin since the last glacial maximum. However, the role of tectonic movements, and most especially fault reactivation, in generating landslides offshore Norway is largely unconstrained. This study uses high-quality 3D seismic and borehole data to understand how landslide development was partly controlled by faults propagating within the uplifted South Modgunn Arch. Variance and structural maps above the South Modgunn Arch show that: a) local scarps of recurrent landslides were formed close to the largest faults, and mainly above strike-slip faults. b) distinct periods of fault generation were associated with tectonic events, including the breakup of the Northeast Atlantic Ocean, and those events forming the South Modgunn Arch. c) important fluid-flow features coincide with faults and sill intrusions. A total of 177 faults were analysed to demonstrate that fault throw-values vary from 10 ms to 115 ms two-way travel time (8 m to 92 m). It is proposed that the long-term activity of faults in the study area has contributed to fluid migration, weakened post-breakup strata and controlled the development of submarine slope instability. In particular, strike-slip faults coincide with the location of several Quaternary landslide scars near the modern sea floor. Similar processes to those documented in Norway may explain the onset of large-scale landslides on continental margins.

4.2 Introduction

The role of tectonic reactivation and uplift is recognised as one of the main triggers of submarine slope instability on continental margins. Multiple examples of the importance of tectonic events in triggering submarine landslides are known in the literature, from the Grand Banks 1929 earthquake, associated landslide and turbidity current (Løvholt et al., 2019; Piper et al., 1999; Schulten et al., 2018), to widespread slope creeping and instability in the South China Sea (He et al., 2014; Li et al., 2015), tectonically active areas of Japan (Kawamura et al., 2014, 2012; Laberg et al., 2017; Yamada et al., 2010), East Korea (Cukur et al., 2016a), Indonesia and Australasia (Day et al., 2015; Pope et al., 2017), as well as West Africa (Gee et al., 2006).

Located on the mid-Norwegian margin (Northeast Atlantic), the position of the headwall of the Storegga Slide was controlled by lateral changes in lithology and tectonic stresses (Bryn et al., 2005a). The Storegga Slide is one of the largest submarine landslides on Earth, having displaced thousands of cubic kilometres of sediment during the Quaternary. Yet, the importance of far-field tectonic stresses and local crustal deformation on the Storegga Slide's evolution is still poorly understood. Part of this limited knowledge results from the fact that strike-slip faults indicating significant tectonic movements offshore Norway have yet to be recognised as forming landslide scars in the Storegga Slide. Slope instability commonly erodes such scars during landslide development (Bull et al., 2009).

In the study area first-order tectonic structures, which crucially affected the long-term development of the South Modgunn Arch (SMA), comprise the Jan Mayen Fault Zone (JMFZ) in oceanic crust and its prolongation to the east, the Jan Mayen Fracture Corridor (JMFC) (Fig. 4.1a). The JMFC was formed as a deep-seated strike-slip fault zone during the Mesozoic onset of continental rifting (Surlyk et al., 1981). Later, it formed a deep conduit of magma and volatiles ascending in what was a zone of structural weakness during early Eocene continental breakup (Torske and Prestvik, 1991), which has spanned 3-6 m.y. (Faleide et al., 2008). Due to its thinner crust and minor degree of compaction, gravity anomalies are clearly of lower amplitude along the JMFC and continue towards the continental crust of mid Norway (Berndt et al., 2001; Maystrenko and Scheck-Wenderoth, 2009). Furthermore, the JMFC offsets lower crustal eclogites formed during the Caledonian Orogeny (Gernigon et al., 2006a), and relates to a broad zone of hyperextension on the Norwegian Margin (Mohn et al., 2012; Nirrengarten et al., 2014; Sutra et al., 2013).

Tectonic uplift of the Modgunn Arch during the Late Cenozoic led to secondary (local) faulting in the study area (Fig. 4.1c). In fact, regional seismic data documents several episodes of Miocene tectonic uplift on the Norwegian Margin (Anell et al., 2009; Doré et al., 2008b; Døssing et al., 2016; Kimbell et al., 2017; Omosanya et al., 2017). The mechanisms behind these uplift episodes are still poorly understood and may include: a) enhanced dynamic support from a hot pulse around the Iceland plume (Koptev et al., 2017), b) changes in intraplate stresses related to regional tectonics (Døssing et al., 2016), or c) mid-ocean ridge push (Doré et al., 2008b). Resulting compressional structures on the Norwegian Margin, or 'arches', comprise elongate anticlines with 4-way closures (Fig. 4.1c). On seismic profiles, regional folds such as the Modgunn Arch are onlapped by relatively young sediment and show some degree of erosion on their tops (Fig. 4.1c). The main period of uplift of the Modgunn Arch is suggested as early-middle Miocene based on precise datings from the Ormen Lange Dome (Vågnes et al., 1998).

In order to achieve the aims of this chapter, high-quality 3D seismic data from the Southern flank of the Modgunn Arch (SMA) are interpreted in great detail. The significance of faults crossing the SMA is assessed in order to understand their control on local slope instability processes. The study area is important as it coincides with the northern flank of the Storegga Slide (Fig. 4.1). In parallel, the activity of different faults are compared for different periods, the geometry of submarine slides is mapped, the seismic character of post-breakup strata is interpreted, and the mechanisms behind the uplift and folding of the SMA are analysed. Hence, this chapter aims to address the following research questions:

a) How does the growth history of faults on the SMA relate to discrete tectonic episodes?

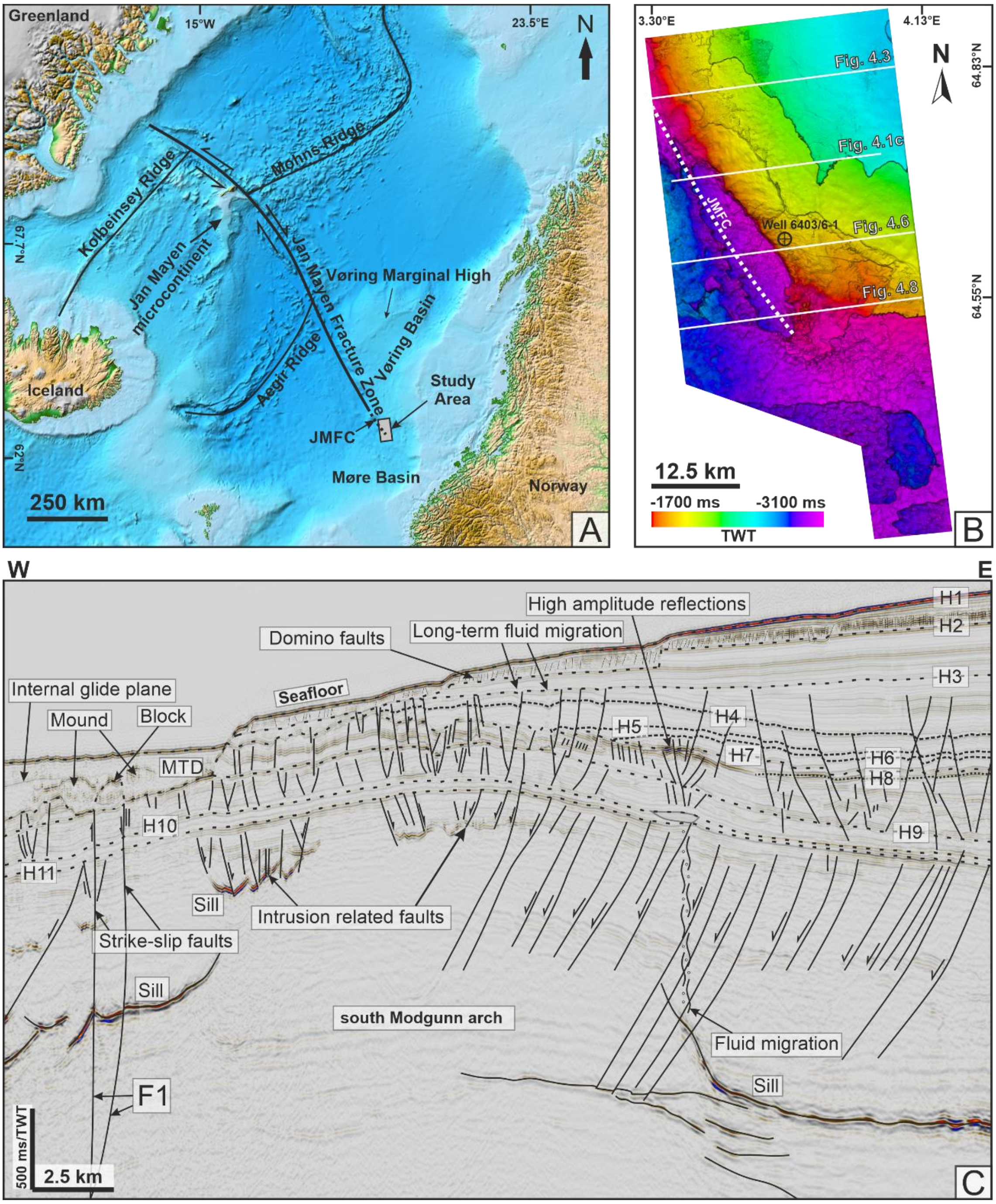

Figure 4.1. a) Location of the study area in the wider context of the NE Atlantic Ocean. b) Interpreted two-way time-structure map of the bottom glide plane of multiple submarine landslides. The seismic survey interpreted in this thesis is shown by the rectangle in a). The locations of seismic profiles are shown by the white lines in b). c) Interpreted seismic profile highlighting the geometry of the South Modgunn Arch, associated faults, magmatic and fluid-flow features. The relief map in Fig. 4.1a was modified from the National Centre for Environmental Information (NCEI).

b) How faults affected fluid migration and triggered submarine slope instability in post-breakup strata of the SMA?

c) How do the mapped fault families relate to slope instability and the present-day geometry of the Storegga Slide?

4.3 Data and Methods

This chapter uses time and depth migrated 3D data from the Central Norwegian Continental Shelf, together with information from one exploration well (Well 6403/6-1; Figs. 4.1b and 4.2). The interpreted seismic volume covers 263 km^2 of the northern headwall of the Storegga Slide (Fig. 4.1b). Inlines (strike) and crosslines (dip) are respectively oriented in a North-northwest and South-southwest direction, and are spaced 12.5 m. The seismic cube acquired information to a maximum two-way time (TWT) depth of 8.2 s and was processed with a vertical sampling rate of 4 ms.

The central part of the SMA was drilled by well 6403/6-1, which provided gamma-ray, bulk density, neutron porosity, sonic (Vp) and resistivity data (Fig. 4.2). Based on well-seismic correlations, the vertical seismic resolution of the seismic dataset is ~11 m in the Brygge to Naust Formations (post-breakup strata, upper Eocene to Quaternary), and ~19 m in the Tare Formation (lower Eocene). Relative dates for seismic-stratigraphic units are based on seismic-well ties and published information from the Norwegian Sea (Berg et al., 2005; Bryn et al., 2005a; Dalland et al., 1988; Forsberg and Locat, 2005; Kjoberg et al., 2017).

Seismic interpretation used Schlumberger Petrel® and included local structural and stratigraphic analyses to describe the character of sub-surface geological bodies. In detail, eleven discrete horizons (H1 to H11) were identified and mapped including the tops of the Tang, Tare, Brygge and Kai Formations (Figs. 4.2, 4.4, 4.5 and 4.7). Several arbitrary horizons marking important tectonic events, magmatic sills, hydrothermal vent complexes, unconformities and faults, were also mapped in detail.

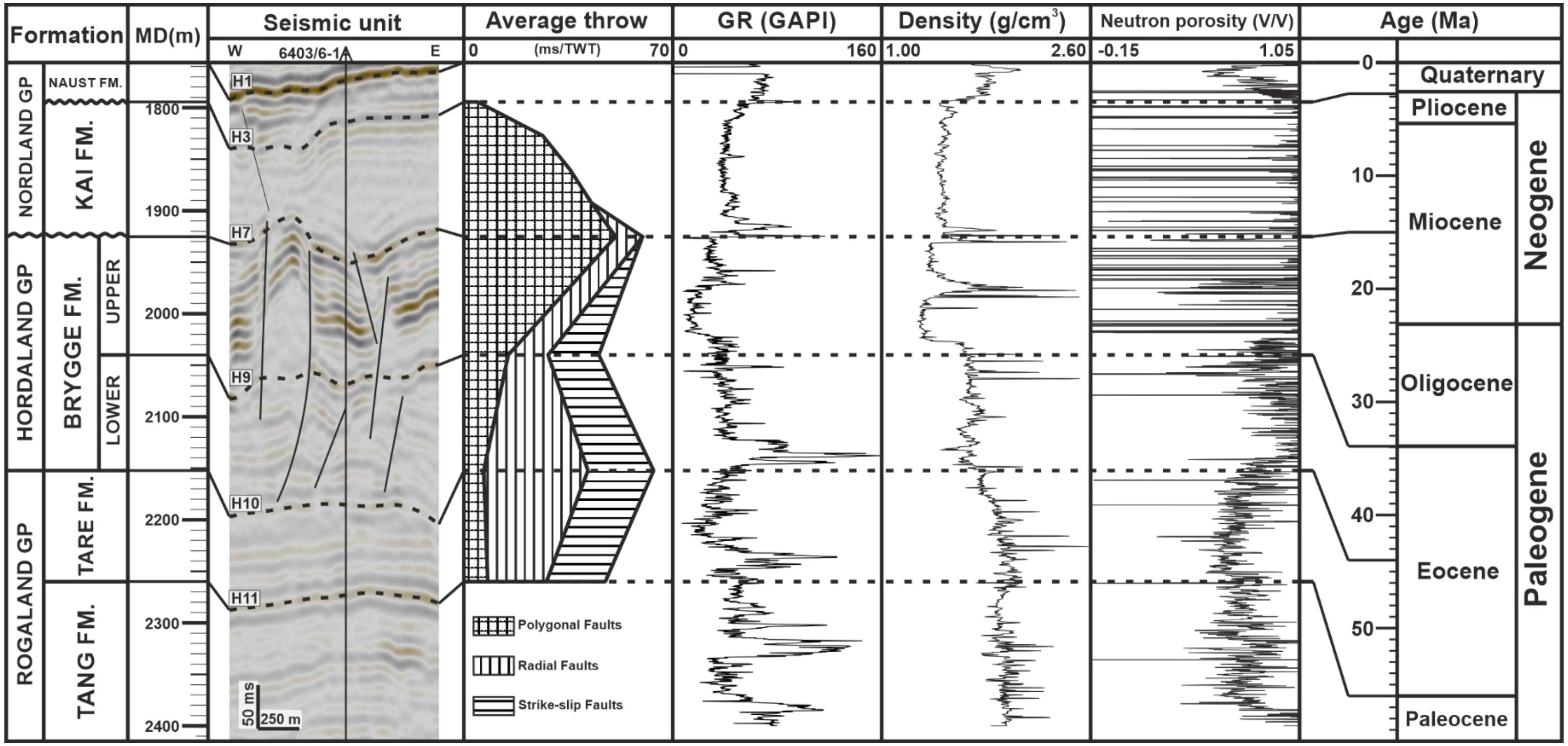

Figure 4.2. Summary diagram showing the position of seismic-stratigraphic horizons H1 to H11 and a synthesis of wireline data from well 6403/6-1. The ages of horizons are taken from Forsberg (2005), Loseth et al. (2005), Rise et al. (2006) and Kjoberg et al. (2017). H1: Sea floor; H3: Top Kai Formation; H7: Top Brygge Formation; H9: Mid Brygge Formation; H10: Top Tare Formation; H11: Top Tang Formation.

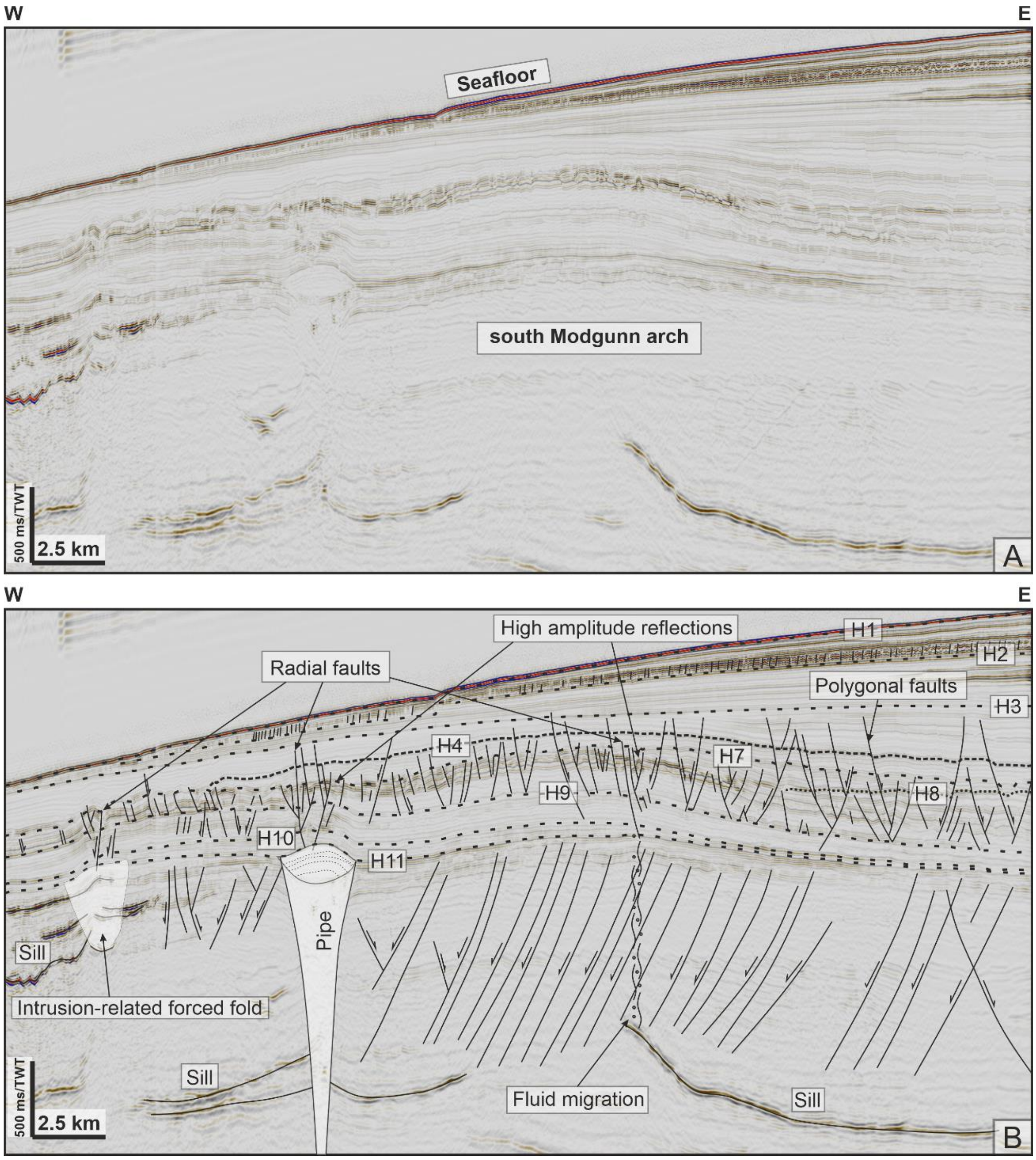

Figure 4.3. East-west seismic profile across the Modgunn Arch. The location of the seismic profile is shown in Fig. 4.1b. This profile images a pipe structure on the northern flank of the South Modgunn Arch (SMA). The pipe ends up as an eye-shaped hydrothermal vent at its top from the release of overpressured fluid derived from heated organic carbon around magmatic intrusions. Polygonal faults, radial faults and high amplitude reflections are also observed in this seismic profile. H1: Sea floor; H2: Bottom glide plane of landslides; H3: Top Kai Formation; H4: Unconformity 1; H7: Top Brygge Formation; H8: Boundary of opal A/CT; H9: Mid Brygge Formation; H10: Top Tare Formation; H11: Top Tang Formation.

The recognition of magmatic intrusions on seismic data is based on the mapping of their typical concave geometry (mainly saucer-shaped in study area), relatively high acoustic impedance, and seismic stratigraphic character of abrupt terminations within their host strata (Fig. 4.3). Hence, in the study area, magmatic intrusions form positive high-amplitude seismic anomalies (Alves et al., 2015; Planke et al., 2005; Smallwood and Maresh, 2002). Along the Northeast Atlantic, including the study area, intrusion-related pipes and vents are broadly recognised at palaeo-seafloors by their eye-, crater- or dome-shaped upper vents, accompanying low-amplitude reflections below that materialise poor acoustic impedances in pipe structures (Møller Hansen, 2006; Omosanya et al., 2018; Planke et al., 2005) (Figs. 4.1c and 4.3).

Variations in fault throw vs. depth (T-Z plots) are used to understand the initiation and development of distinct fault families (Tao and Alves, 2019). The height of faults is measured as the vertical distance between their upper and lower tips in seismic sections orthogonal to the fault strike, thus imaging the maximum fault throw. A combination of 3D visualisation techniques were applied to better show the spatial distribution of subsurface and faults in strata; structural and attribute maps, which provide structural information including the presence of faults, vents, scarps, etc., and automatic fault extraction to complement seismic attribute techniques such as trace Amplitude Gain Control (AGC), structural smoothing, chaos and ant tracking (Fig. 4.12). The geometry of faults on different seismic-stratigraphic horizons is shown in flattened variance maps. These same maps also show the spatial relationship between faults and associated structures, submarine landslides and overhanging evacuation structures, which were observed on the SMA. The thickness of several intervals are calculated by the difference of TWT between two seismic reflections.

Automatic fault extraction was performed in Schlumberger Petrel®, and quality-controlled by seismic profiles and variance slices. The automatic fault extraction works in tandem with the ant tracking seismic attribute, which is based on trace AGC, structural smoothing and chaos attribute seismic cubes. The trace AGC normalises root mean square (RMS) amplitude over a specified window. Accordingly, discontinuities in seismic reflections become more obvious and increase the accuracy of seismic interpretations.

Structural smoothing is available to enhance coherent events in seismic data by reducing noise. In addition, the chaos attribute is defined as a measure of the organisation in seismic reflections, or in the seismic signal (Koson et al., 2014). In seismic data, discontinuities are obvious around fault planes, scarps and inside mass-transport deposits (MTDs). Consequently, the chaos attribute seismic cube helps the process of automatic fault extraction, highlighting the presence of any faults in a seismic cube.

4.4 Geological Setting

4.4.1 Tectonic activity and sedimentation along the Norwegian Shelf

The study area is located on the Mid-Norwegian continental margin, between 62˚N and 70˚N, close to the large Vøring and Møre Basins (Fig. 4.1a). These two Cretaceous basins are separated by the East JMFZ and JMFC, which continue to the Southeast underneath the study area. Based on the effect of distinct rift phases, the evolution of the Norwegian Margin can be divided into three periods: Late Paleozoic, Late Jurassic-Early Cretaceous and Late Cretaceous-Paleogene (Faleide et al., 2008).

The pre-breakup stratigraphy of the study area is similar to other provinces of the Norwegian continental shelf, as they were all part of a vast epicontinental sea (Faleide et al., 2010). The rift basins of Norway's continental margin were formed during three Late Paleozoic-Early Mesozoic rift episodes (Doré, 1991). These episodes ended with a major phase of Permian-Triassic extension onshore East Greenland (Osmundsen et al., 2002). During Late Middle Jurassic-earliest Cretaceous rifting, a Northwest-Southeast shift in the extensional stress field, associated with the northward propagation of Atlantic rifting, led to widespread crustal extension and thinning, creating major sedimentary basins offshore mid-Norway (Faleide et al., 1993). As a result of ~60 km of crustal stretching, intrabasinal highs and associated basins such as the Vøring and Møre Basins were generated and filled with thick Lower Cretaceous strata, which are mainly composed of fine-grained clastics, derived from uplifted continental sources (Faleide et al., 2010; Scheck-Wenderoth et al., 2007; Skogseid et al., 2000).

A final episode of Late Cretaceous-Paleogene lithospheric extension led to continental breakup, as documented by the ~140 km of crustal stretching between Greenland and Eurasia (Skogseid et al., 2000) and the ~150 km wide extension at the Vøring Margin recorded at this time (Faleide et al., 2008). Continental breakup was preceded by a final episode of rifting around the Campanian-Maastrichtian boundary, followed by significant magmatic activity until continental breakup was fully achieved. A breakup sequence *sensu* Soares et al. (2012) on the mid-Norwegian margin was mainly sourced from the east and precedes thermal cooling and sediment loading as the main drivers of subsidence (Hjelstuen et al., 1999). These sequences consist of fine-grained hemipelagites with variable amounts of sand and tuffaceous material (Dalland et al., 1988).

In the Middle Eocene transition, ocean spreading was clearly established between Greenland and Eurasia. The formation of ocean crust was accompanied by several changes in Northeast Atlantic plate boundaries (Faleide et al., 2008; Gaina et al., 2009). At the same time, basaltic rocks intruded into thick Cretaceous sediment and released methane through hydrothermal vents by heating organic carbon beyond the gas window (Aarnes et al., 2014; Berndt et al., 2000; Svensen et al., 2004; Tsikalas et al., 2008). During the Middle Eocene, compressional anticlines such as the Ormen Lange Dome and Helland-Hansen Arch (Lundin and Doré, 2002) started developing offshore Mid-Norway above the Early Cretaceous hyperextended rifts (Lundin and Doré, 2011).

During the early Oligocene, as a result of the magma supply from the Iceland plume, the Northeast Atlantic spreading ridge relocated westwards from the Norway Basin to the eastern margin of Greenland, leading to: a) the formation and northward propagation of the Kolbeinsey Ridge, b) the final abandonment of the Aegir Ridge at 30 Ma, and c) the generation of the isolated Jan Mayen microcontinent at ~20 Ma (Fig. 4.1a). This latter event has also been associated with the linkage of the Reykjanes and Mohns Ridges by the Kolbeinsey Ridge (Gaina et al., 2009). Another remarkable event is the change in spreading direction between Greenland and Eurasia, from Northwest-Southeast to Northeast-Southwest (Talwani and Eldholm, 1977). The formation of the Iceland mantle plume is, at a regional scale, correlated with the cessation of seafloor spreading in the Labrador Sea (Nielsen et al., 2002) (Fig. 4.1a).

Multiple anticlinal compressional structures of Miocene age are thus identified on the Norwegian Margin (Anell et al., 2009), including the SMA investigated in this study (Figs. 4.1a and 4.1c) and other anticlines along the JMFC. Throughout the Plio-Pleistocene, the Norwegian mainland experienced marked tectonic uplift is association with important isostatic adjustments from ~4 Ma to the present day due to ice-cap melting (Huuse, 2002; Japsen et al., 2007b).

Since the onset of shelf glaciations at 0.5 Ma, corresponding to climatic cyclicity, several submarine landslides have occurred on the mid-Norwegian margin (Bryn et al., 2005a, 2003). Predisposing factors of submarine slope instability are varied offshore Norway and relate to long-term preconditioning factors such as buried contourite drifts, fluid migration, gas hydrate dissociation, high sedimentation rates and pore pressure build-up (Leynaud et al., 2009; Miramontes et al., 2018; Omosanya, 2018; Solheim et al., 2005). In the study area, common short-term triggers of submarine slope instability are frequent earthquakes associated with the Quaternary glacio-isostatic rebound of the Norwegian Margin (Bryn et al., 2003).

4.4.2 Vøring Basin, Møre Basin and the South Modgunn Arch

The Vøring and Møre margin segments are both around 400-500 km long and separated by the Jan Mayen Fracture Zone and corresponding Fracture Corridor (Fig. 4.1a). They are characterised by thick Cretaceous deposits, which are locally up to 13 km thick (Gernigon et al., 2003). During continental breakup, kilometre-thick basaltic complexes were formed close to the continent-ocean boundary (Brekke, 2000). At the same time, massive igneous intrusions were emplaced in adjacent sedimentary basins as dykes and sills. As a result, hydrothermal vents and associated structures - including faults and pockmarks - were generated in shallow strata near and at the sea floor (Planke et al., 2015, 2005).

The SMA is located on the JMFC, separating the Vøring and Møre Basins (Figs. 4.1a and 4.1c). It is around 45 km long, 25 km wide and reaches a maximum amplitude of 600 m in study area, with a large field of hydrothermal vents located on its northern flank. The Vøring and Møre basins have developed extensive swathes of polygonal faults since the Miocene, chiefly in the uppermost Brygge and Kai Formations (Berndt et al., 2003). These polygonal faults are thought to relate to modern fluid migration paths and are potentially a long-term preconditioning trigger of submarine landslides in Pleistocene strata (Chand et al., 2011; Hustoft et al., 2007).

4.5 Stratigraphy

As recorded in Well 6403/6-1, the lithostratigrapy of the study area spans from the Cretaceous Lysing Formation to the Quaternary Naust Formation, and four units were interpreted and correlated with borehole data (Fig. 4.2). Furthermore, there are traces of migrated hydrocarbons in core samples from Cretaceous strata, as confirmed by geochemical analyses (Geochemical Information in well 6403/6-1). A detailed description of the interpreted seismic units is provided below.

4.5.1. Pre-Breakup strata (Cretaceous to Paleocene)

Before continental breakup, several drilled formations were deposited on the mid-Norwegian margin from the Cretaceous to the Paleocene (Jongepier et al., 1996; Kjoberg et al., 2017) (Fig. 4.1c, beneath H11). The Upper Cretaceous formations contain sandstone, carbonate, mudstone, and potential Campanian hydrocarbon reservoirs that led to the drilling of Well 6403/6-1 (Dalland et al., 1988; Knaust, 2009; Lien, 2005) (Fig. 4.2). The Møre Basin was part of a volcanic rifted margin during the deposition of the

Paleocene Tang Formation, associated magmatic sills and dykes generated large hydrothermal vent complexes and contributed to fluid migration (Planke et al., 2005; Svensen et al., 2004) (Fig. 4.3). In the study area, the Tang Formation is around 180 m-thick and bounded by a high amplitude positive reflection at its top (Fig. 4.2, H11).

4.5.2 Tare Formation (lower Eocene Breakup Sequence)

Above the Tang Formation is the Tare Formation, a unit deposited in a deep-marine environment during the progressive opening of Norwegian-Greenland Sea (Fig. 4.2). It consists of dark grey, green or brown claystone with thin sandstone intervals recording a variable amount of volcanic tuff (Dalland et al., 1988). The base of the formation is defined by a relative increase in tuff content (Kjoberg et al., 2017). Based on the interpretated seismic data, the Tare Formation is bounded by positive reflections at both its base (H11) and top (H10) (Figs. 4.2 and 4.3), and its thickness is ~100m on average. However, due to differential compaction (Kjoberg et al., 2017), it becomes thinner over intrusion-related structures, especially on the eastern flank of the SMA where a ~400 km^2 sill in pre-breakup strata was blanketed by only ~25 m of the Tare Formation (Fig. 4.3). Seismic reflections inside this unit have moderate amplitude and good continuity, showing it is relatively less faulted (Figs. 4.1c and 4.3).

4.5.3 Brygge Formation (upper Eocene to lower Miocene)

Based on previous research, the Brygge Formation is chiefly composed of marine claystone with intervals of sandstone, siltstone, limestone and marl, recording a density of 1.85 g/cm3 at the centre of the Møre Basin (Dalland et al., 1988; Lawrence and Cartwright, 2010). Biogenic oozes may also occur in significant volumes in this unit (Riis et al., 2005). This multi-component unit, bounded by a high-amplitude positive reflection at its top, can be subdivided into several seismic-stratigraphic packages (Lawrence and

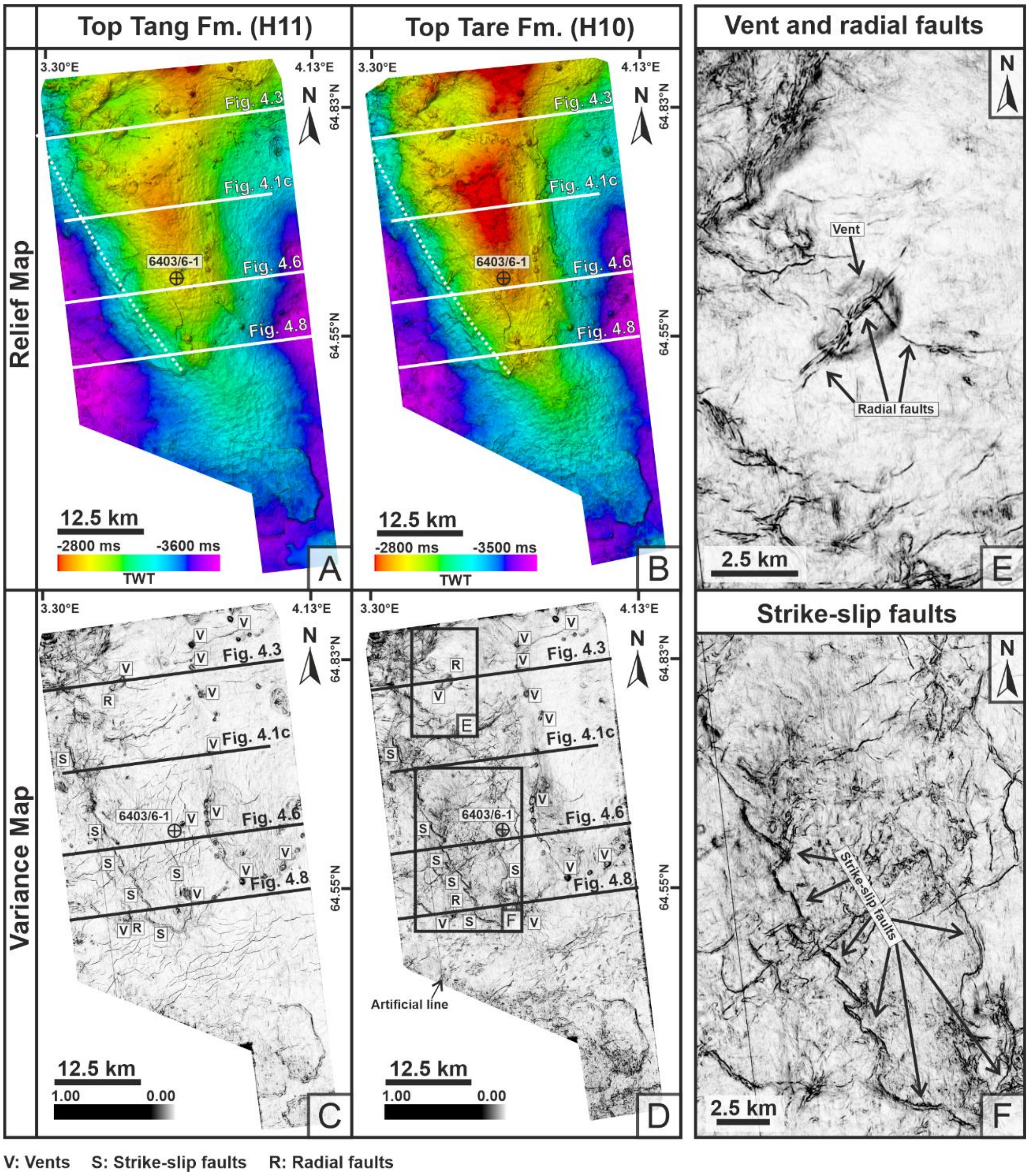

Figure 4.4. a) and b) Time-structure maps of the Top Tang (H11) and Top Tare (H10) formations highlighting the subsurface structure of these units on the SMA. The variance maps in c) and d) indicate the location of vents (V), faults (S: Strike-slip faults; R: Radial faults), and the geometric relationships between them. The detailed maps of strike-slip faults, radial faults and vents are shown in e) and f). Radial faults form perpendicular strands over the magmatic vents. Strike-slip faults are shown as a combination of several small fault segments, or strands, with a predominant northwest strike.

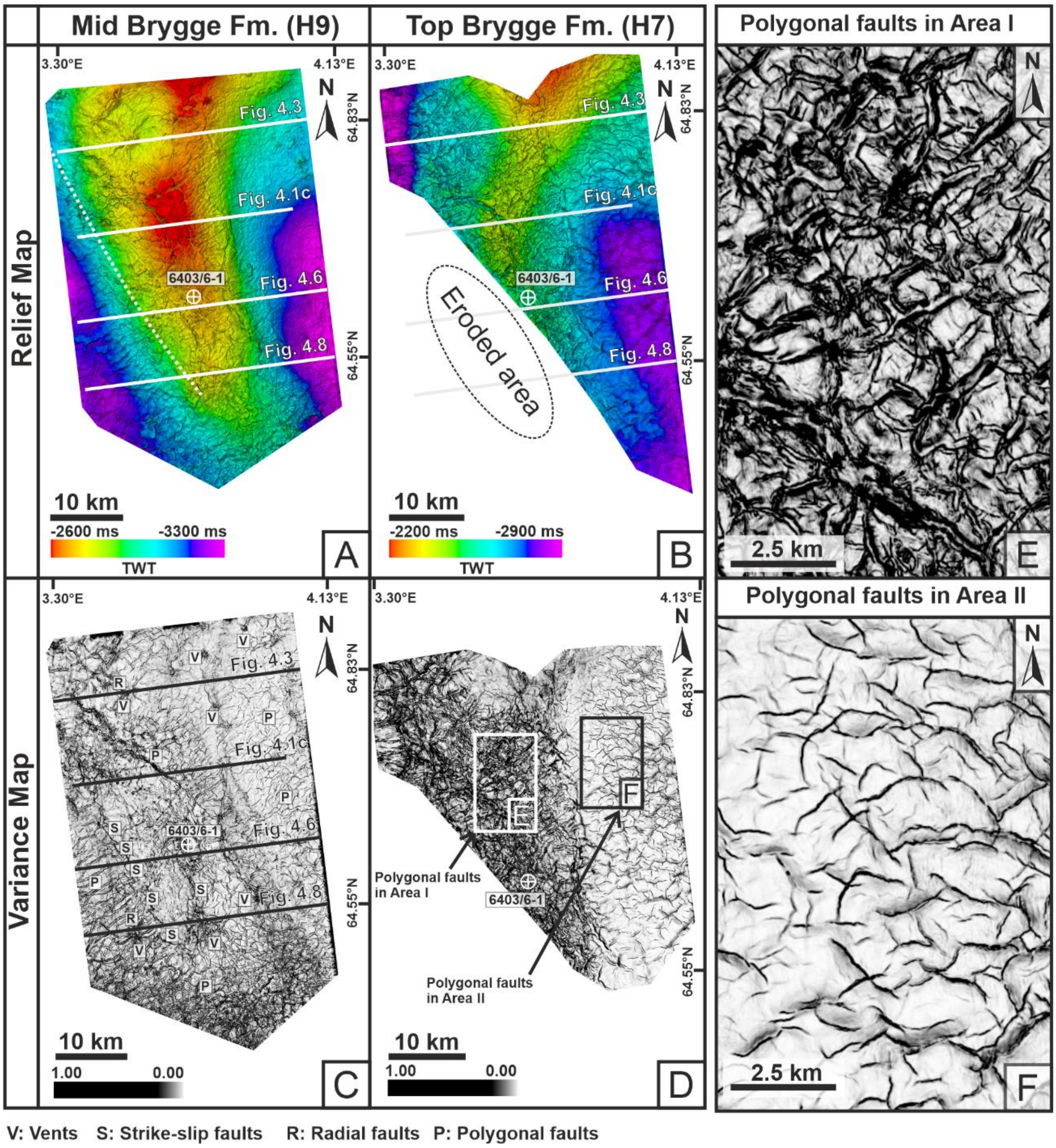

Figure 4.5. a) and b) Time-structure maps on the mid Brygge (H9) and Top Brygge (H7) formations revealing tectonically uplifted and eroded parts of the SMA. The variance maps indicate the location of vents (V), faults (S: Strike-slip faults; R: Radial faults; P: Polygonal faults). The distribution and character of Group II polygonal faults are shown in d) and further detailed in e) and f). Relatively greater throw values in Area I relate to the long-term activity of faults. The top Brygge Formation (H7) was eroded by landslides to the west. The difference between polygonal faults at the level of H7 and H9 is discussed in the text.

Cartwright, 2010). Two seismic packages can be defined in seismic data; they are separated by a positive ‘Mid Brygge’ reflection with moderate continuity and amplitude (Horizon H9; Fig. 4.1c).

The lower Brygge Formation shows low-amplitude and low-continuity internal reflections crossed by polygonal faults (Fig. 4.3). Similarly to the Tare Formation, the lower Brygge unit is thinner above intrusion-related forced folds and vents (Kjoberg et al., 2017) (Fig. 4.6). The upper Brygge strata was eroded during the Miocene doming process by Quaternary submarine landslides (Figs. 4.1c and 4.5b). At the top of the Upper Brygge interval, a high amplitude positive reflection suggests the presence of an unconformity (H7) marking the start of the doming of the SMA in the Miocene.

The migration and accumulation of fluids along polygonal faults (Berndt et al., 2003), are shown as local increases in seismic amplitude (Fig. 4.3). Additionally, an Opal A/CT boundary (H8) inside the Upper Brygge strata crosses multiple stratigraphic boundaries on the eastern flank of the SMA (Fig, 4.1c). This suggests a fossilisation of this diagenetic boundary in association with polygonal faulting, regional folding and differential compaction (Lawrence and Cartwright, 2010; Neagu et al., 2010b).

4.5.4. Kai Formation (upper Miocene to upper Pliocene)

The Kai Formation is composed of fine-grained hemipelagic sediments with abundant calcareous and siliceous fossils. It is rich in smectite with a density of 1.9-2.25 g/cm^3 at the centre of the Møre Basin (Dalland et al., 1988; Forsberg and Locat, 2005; Lawrence and Cartwright, 2010). During the deposition of the this unit, fine-grained contourite drifts were formed by northward-flowing marine currents on the mid-Norwegian margin (Bryn et al., 2005b). This sedimentary process was established in the Miocene and limited to a depth between 500 m and 700 m by a strong thermocline (Alendal et al., 2005b; Krokmyrdal, 2017; Thiede and Myhre, 1996).

The Kai Formation onlaps the Brygge Formation on the flanks of the SMA (Fig. 4.1c), and is composed of continuous internal reflections, including low-amplitude strata interbedded with a few high (and positive) amplitude unconformities (Fig. 4.2; Horizons H4-H6). Based on log data from Well 6403/6-1, the Kai Formation has a density of 1.5 g/cm^3; higher than the Upper Brygge Formation (1.4 g/cm^3) and lower than the Naust Formation (1.85 g/cm^3) (see the density column in Fig. 4.2).

4.5.5 Naust Formation (upper Pliocene-Quaternary)

The Naust Formation, the youngest marine unit in the study area, consists of interbedded claystone, siltstone and sandstone, occasionally with very coarse glaciomarine clastics in its upper part. It shows a density of 2.3 g/cm^3 in the east Møre Basin and 1.85g/cm^3 in the study area (Fig. 4.2). These glaciomarine deposits can be divided into several packages that reflect different glaciation episodes (Berg et al., 2005; Dalland et al., 1988; Lawrence and Cartwright, 2010). As a result of frequent slope instability, the original thickness of the Naust Formation is unaccountable (Figs. 4.1c and 4.8). Between the high amplitude, positive seabed reflector (H1) and the high amplitude negative Horizon H2, a chaotic MTD reveals a marked basal scar on both the TWT structural and variance maps in Figs. 4.7c and 4.7f.

4.6 Results

Within the mapped 3D seismic survey were interpreted one compressional structure (SMA) and eleven seismic horizons (H1 to H11), including the tops of the Kai, Brygge, Tang, Tare Formation and other horizons (Figs. 4.1c and 4.6). The axial plane of the SMA is vertical, but its hinge line trends 0.5° to the South-Southeast. Folded intervals include the Kai, Brygge and Tare Formations, Cretaceous and older strata with magmatic intrusions. In the study area, there is an evacuation structure over the west flank of the SMA (Fig. 4.7e). It has a crater-like relief with a vertically jagged boundary and a rugged bottom glide plane (Figs. 4.1c, 4.6, 4.7b, 4.7e and 4.8). The major and minor axes of this

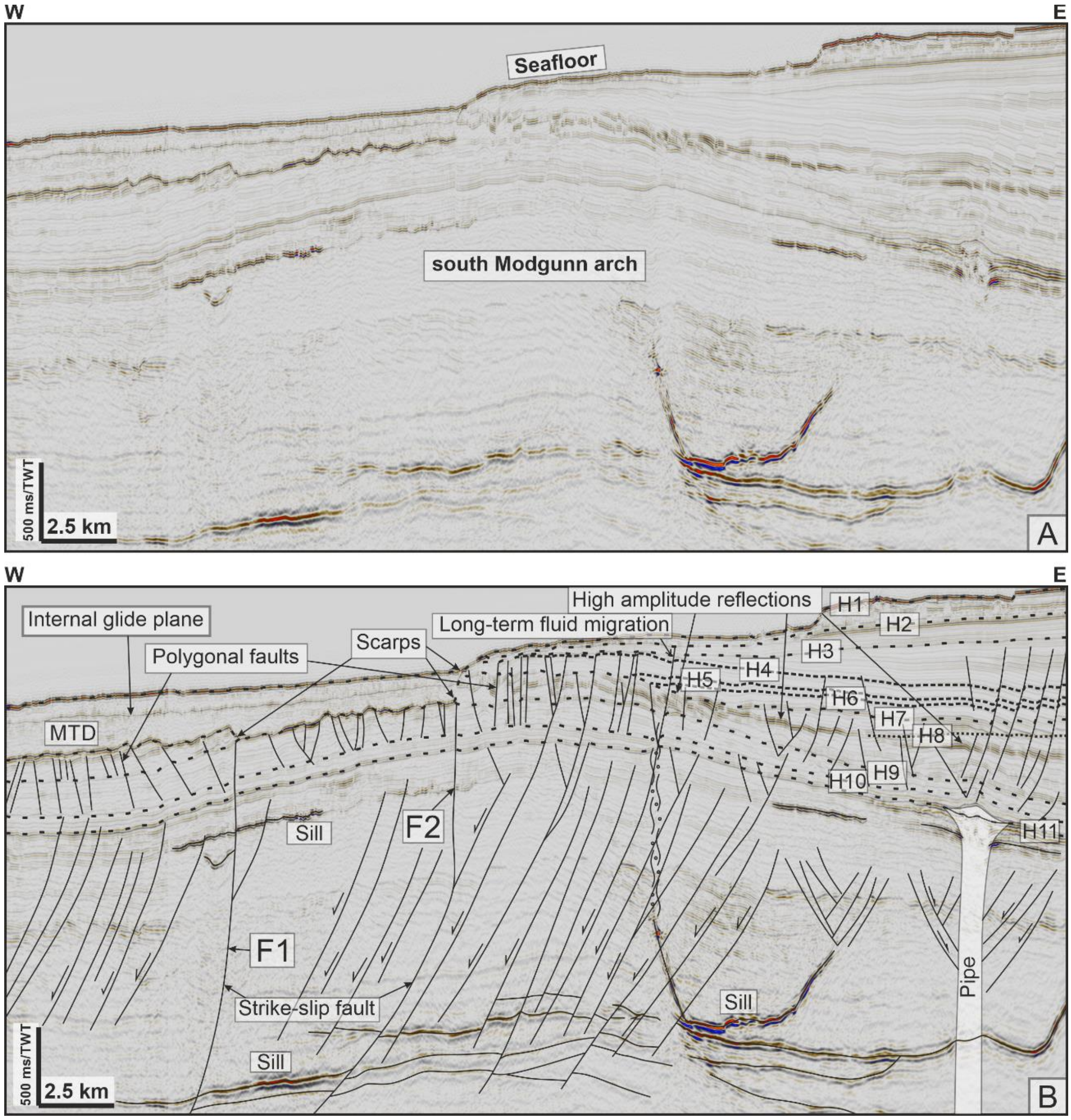

Figure 4.6. East-west seismic profile across the study area. Its location is shown in Fig. 4.1b. Magma intrusions formed during the break-up of the NE Atlantic gave rise to the migration of fluid via faults and pipes. Trapped fluid is revealed in the form of high-amplitude reflections above pipes and around faults. H1: Sea floor; H2: Bottom glide plane of landslides; H3: Top Kai Formation; H4: Unconformity 1; H5: Unconformity 2; H6: Unconformity 3; H7: Top Brygge Formation; H8: Boundary of opal A/CT; H9: Mid Brygge Formation; H10: Top Tare Formation; H11: Top Tang Formation.

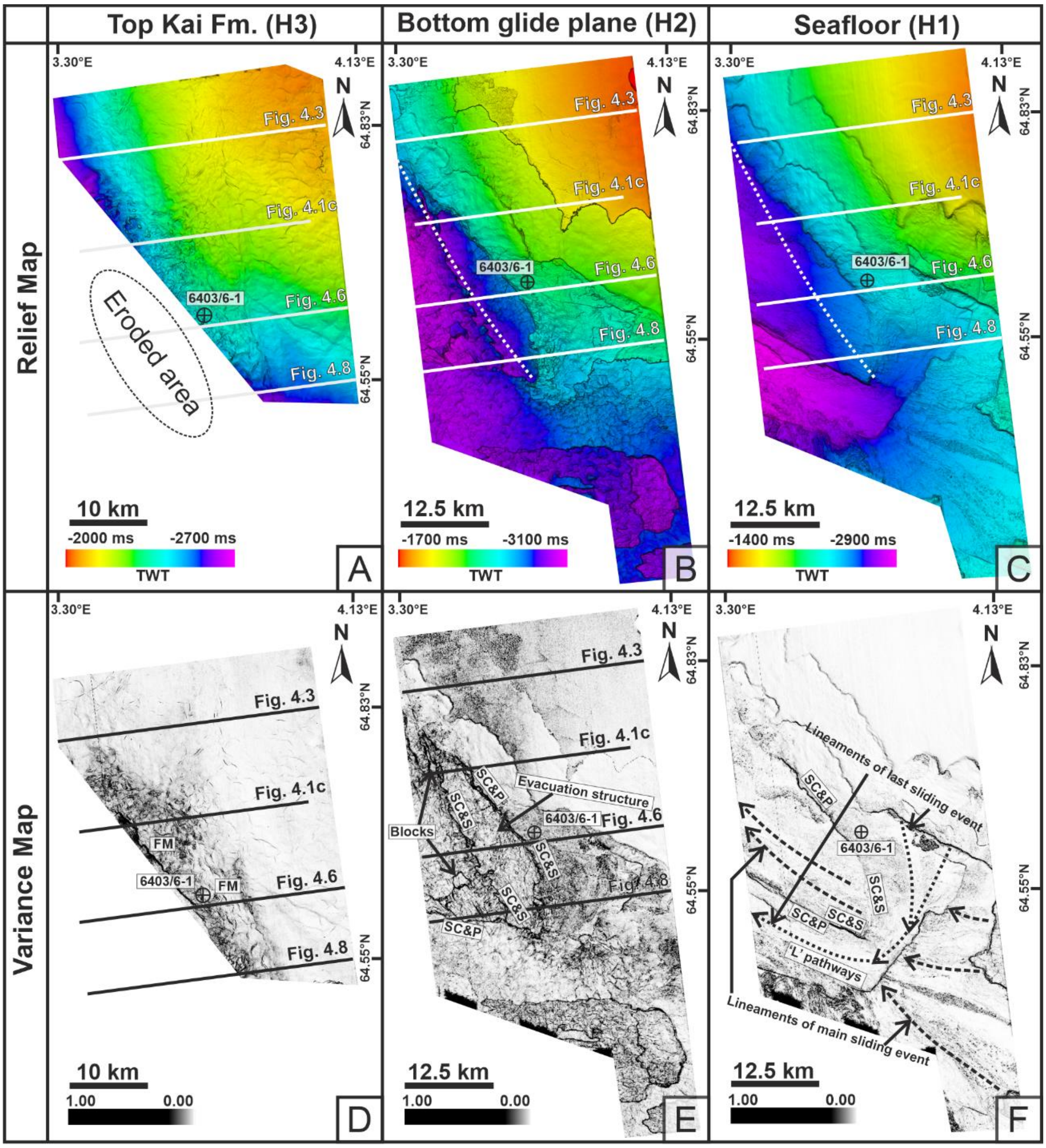

Figure 4.7. Time-structure maps of the (a) top Kai Formation, (b) bottom glide plane and (c) sea floor, accompanied by their corresponding variance maps, highlighting the influence of faults on landslide location and the formation of headwall scarps and blocks. The ‘L-shaped pathways’ in f) suggest the southwestward movement of the last landslide event before turning to the northwest.

structure are ~2.2 km and ~0.6 km, respectively (Fig. 4.1b). In addition, there are at least three unconformities in the Kai Formation, each one resulting from seafloor erosion during tectonic reactivation and representing a distinct episode of uplift in the SMA (H4-6, Figs. 4.1c and 4.6). Finally, there are three types of faults around the SMA, including polygonal faults, radial faults and strike-slip faults.

4.6.1 Geometry of mass-transport deposits

As a retrogressive large-scale landslide, the Storegga Slide was triggered by a first collapse event on the lower continental slope, which itself triggered recurrent failure events during the Quaternary. This recurrence is documented in the form of multiple basal glide zones and scarps (Bryn et al., 2005; Gauer et al., 2005; Haflidason et al., 2004). In the study area, resulting mass-transport deposits (MTDs) can be divided in two types. The first type is located on upper continental slope, where strata maintained its inner structure but are highly faulted by oceanward-dipping domino faults (Fig. 4.1c). The second type was accumulated further downslope from Type 1 and includes MTDs in an evacuation structure - where strata were significantly remobilised (Fig. 4.1c). Both types of MTDs are bounded by composite (and multiple) basal glide zones, which can truncate each other to indicate recurrent sliding events (Figs. 4.6 and 4.8). Vertical changes in the geometry of the basal glide planes suggest the presence of multiple headwall scarps (Figs. 4.6, 4.7b and 4.7c). Lineaments (striations and grooves) on the sea floor, inside the landslide evacuation area and in other part around, reveal local Southwest and regional Northwest directions for downslope movement in the form of an intricate 'L' pathway for MTDs (Figs. 4.7c and 4.7f). This L-shaped pathway starts as a series of southwest-striking grooves in the shallower part of the study area, and then changes to a northwest orientation. Such a feature suggests debris flows formed after the main instability phase of the Storegga Slide, creating the 'L' pathway by eroding the basal glide planes of older MTDs.

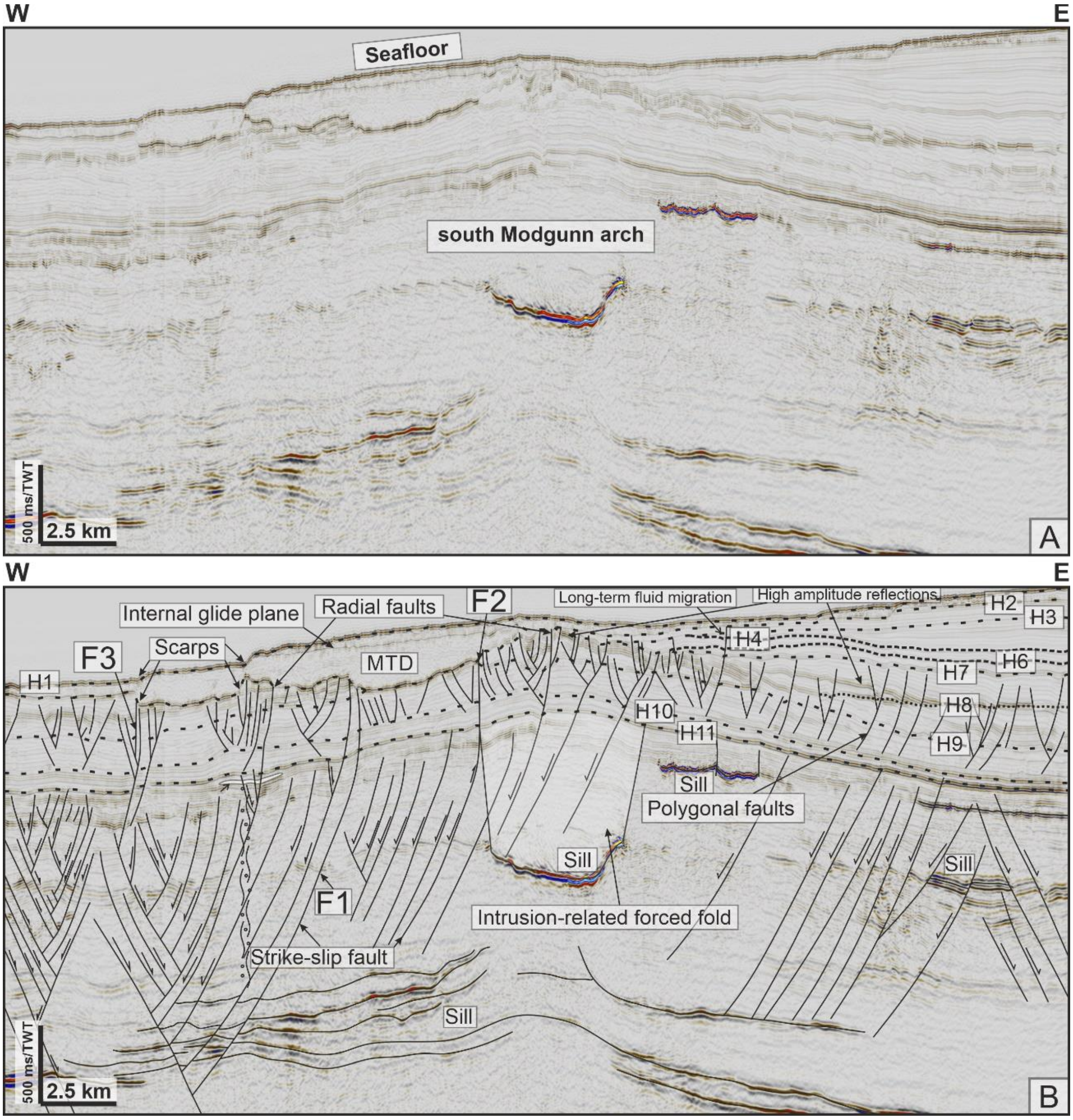

Figure 4.8. East-west seismic profile across the southern flank of the SMA. Its location is shown in Fig. 4.1b. The control of faults on landslide scarps is revealed by F1, F2, F3 and other faults, including polygonal faults, radial faults and strike-slip faults. Radial faults occur above intrusion- related structures, local folds and vents. H1: Sea floor; H2: Bottom glide plane of landslides; H3: Top Kai Formation; H4: Unconformity 1; H5: Unconformity 2; H6: Unconformity 3; H7: Top Brygge Formation; H8: Boundary of opal A/CT; H9: Mid Brygge Formation; H10: Top Tare Formation; H11: Top Tang Formation.

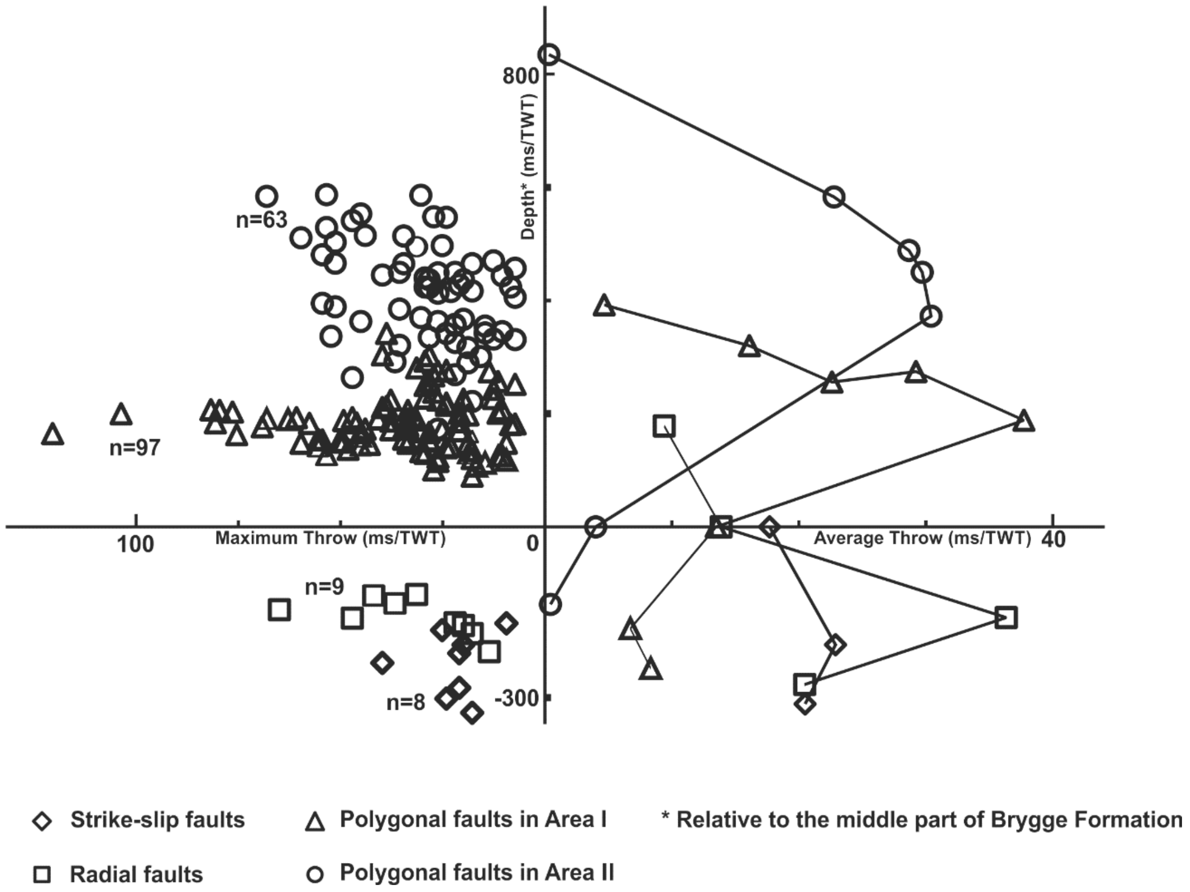

Figure 4.9. Maximum and average throw-depth diagrams. Four types of faults are interpreted in the study area, as plotted in the graph in this figure. All depths are plotted relative to the mid Brygge Formation (H9) in order to compare the development of faults on the evolving SMA.

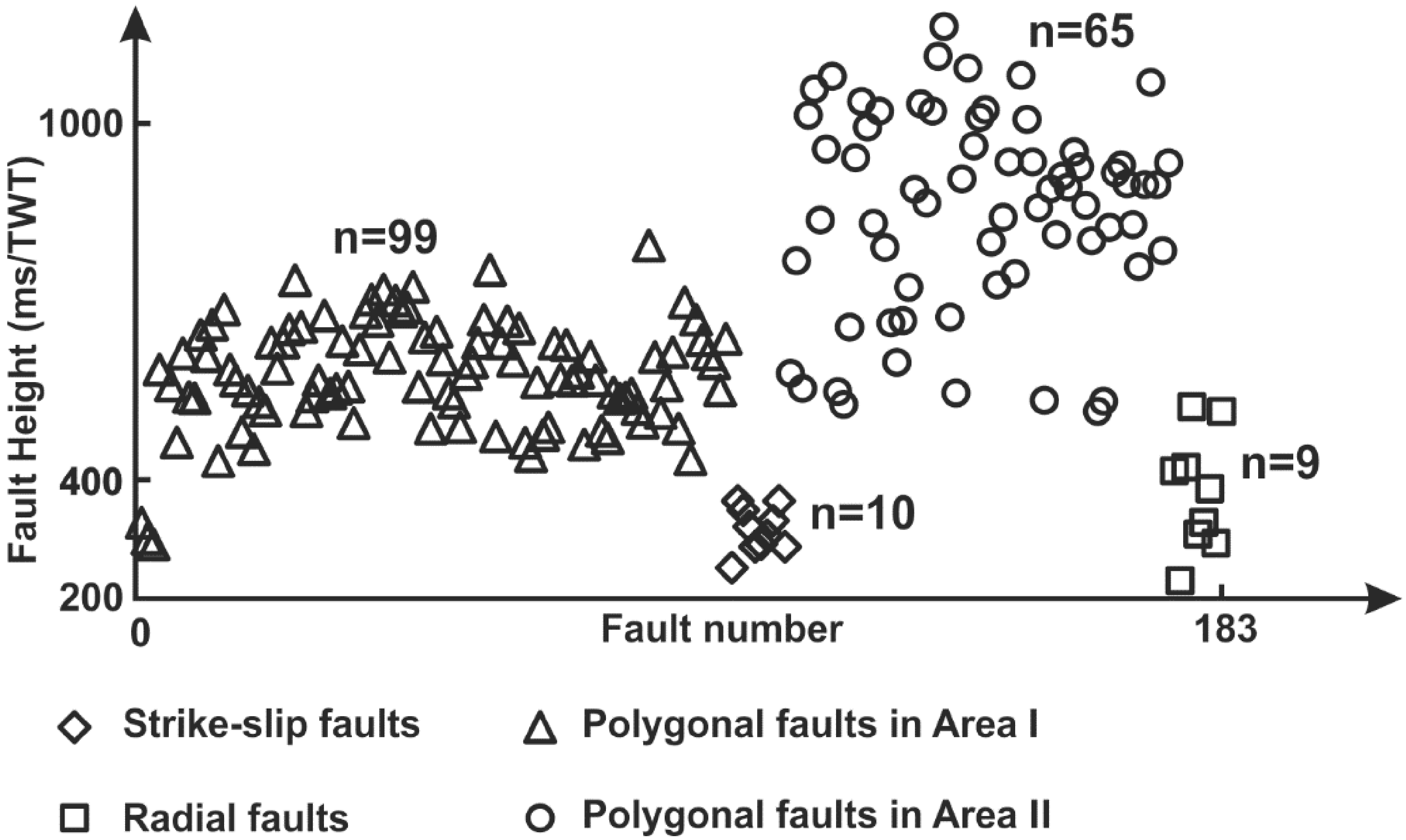

Figure 4.10. Fault height (ms/TWT) data for all interpreted faults.

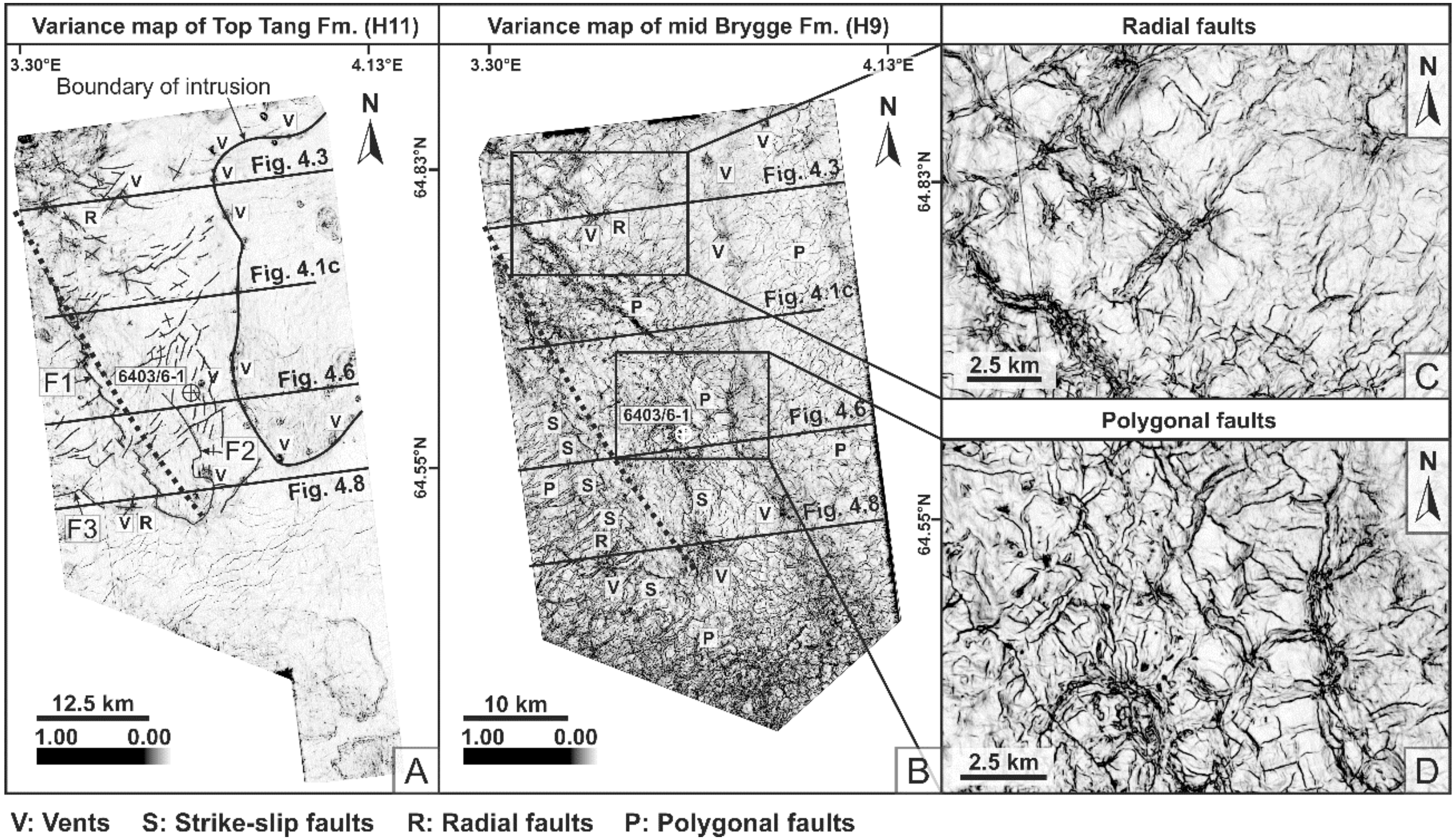

Figure 4.11. Variance map of the Top Tang (H11) and Top Brygge (H7) formations. a) Vent structure showing radial faults above them. Local differential compaction over intrusion-related structures led to the development of the radial faults in c), which have a central cross-shape and differ from the polygonal faults around them, as shown in d). The dotted black lines indicate the location of the Jan Mayen Fracture Corridor.

4.6.2 Fault systems

4.6.2.1 Polygonal faults

Based on previous research work, the preferential strike directions in polygonal faults are related to their reactivation under different stress fields (Cartwright et al., 2003; Gay and Berndt, 2007). In post-breakup strata there are two groups of polygonal faults with a narrow interaction zone between them, at around -2970 ms TWT (Fig. 4.12). Group I polygonal faults occur deeper than their Group II counterparts and have a predominant Northeast-Southwest (40-65°) strike, perpendicular to the strike of the SMA. This narrow interaction zone is most obvious where strata were less deformed during uplift of the SMA (see Fig. 4.12, showing the distribution of the two groups of polygonal faults in the third 3D relief map). The narrow interaction zone becomes less clear on the flanks of the SMA to disappear at its axis where all the polygonal faults are shallower than the interaction zone (Fig. 4.12). In contrast to the interaction zone, which occurs at a specific depth, the bottom boundary of Group I polygonal faults is the top Tare Formation, which was uplifted together with the Brygge Formation during the middle Miocene and was broadly folded. In contrast, Group II polygonal faults have a dominant Northwest (110-135°) strike, parallel to the JMFC (Figs. 4.1b and 4.12). There is not a specific top boundary for Group II polygonal faults, which mainly tip out around the top Kai Formation.

Even though the upper tips of polygonal faults usually limit the earliest time when they stopped propagating, the history of faulting around the SMA is still not fully addressed. The interaction zone between the two groups of polygonal faults crosses the broadly folded Brygge Formation, which was deposited from Oligocene to early Miocene. The SMA itself was formed in the middle Miocene under Northeast-Southwest shorting, correlating with the dominant Northeast-Southwest strike of Group I polygonal faults. Furthermore, the distribution of Group I polygonal faults surrounding the SMA suggests they were subject to a similar stress field to that originating the arch (see Fig. 4.12, showing the distribution of Group I polygonal faults). Similarly, the top boundary of Group II polygonal faults indicates that it was formed before or during the Quaternary under a Northwest-Southeast oriented stress field, in which the main compressional stress is perpendicular to the mid-ocean ridge and similar to the present-day stress.

The different distribution of the two groups of polygonal faults is shown in Figs. 4.5c, 4.5d and 4.12, in which Group I is included in the variance map of the mid Brygge Formation (Fig. 4.5c), and Group II in the top Brygge Formation (Fig. 4.5d). The broadly folded axis of the SMA is marked as 'Area I', distinct from the surrounding less deformed 'Area II' (Figs. 4.5e and 4.5f). Based on the analysis in this work, polygonal faults in Area I show smaller heights, larger maximum throws, larger average throw, and are closer to Horizon H9, when compared with Area II (Figs. 4.9 and 4.10).

4.6.2.2 Radial faults and igneous intrusions

Radial faults have been frequently observed and related to the existence of positive structures and differential compaction (Ho et al., 2019; Kjoberg et al., 2017; Mattos et al., 2016; Stewart, 2006; Waghorn et al., 2018). Along the east margin of the Northeast Atlantic, there are at least two types of magmatic intrusion with related positive structures, including: 1) intrusion-related forced folds, a result of vertical displacement, elastic bending or differential compaction (Hansen and Cartwright, 2006; Schmiedel et al., 2017), and 2) intrusion-related vent structures are also observed (Hansen and Cartwright, 2006; Ligtenberg, 2005; Omosanya, 2018).

In the vertical seismic profile in Fig. 4.3, radial faults in post-breakup strata have similar geometries to polygonal faults, but only occur above igneous intrusion related folds and vents (Fig. 4.3). Fault analyses show that their maximum throws occur in the Tare Formation (lower Eocene), where they reach ~ 36 ms on average (Fig. 4.9). Most radial faults stopped propagating upward at the level of Horizon H7, and down to H11, occasionally crossing the Tare Formation and linking with pre-breakup faults (Figs. 4.2 and 9). As interpreted in seismic data, two intrusion-related forced folds are observed as positive structures formed beneath radial faults. The structure in Fig. 4.3 shows at least five sill intrusions. The one in Fig. 4.8 is located at the axis of the SMA, a broad fold, with only one large sill underneath. The thickness of Tare Formation is similar above the SMA, but the Brygge Formation becomes thinner above this same structure.

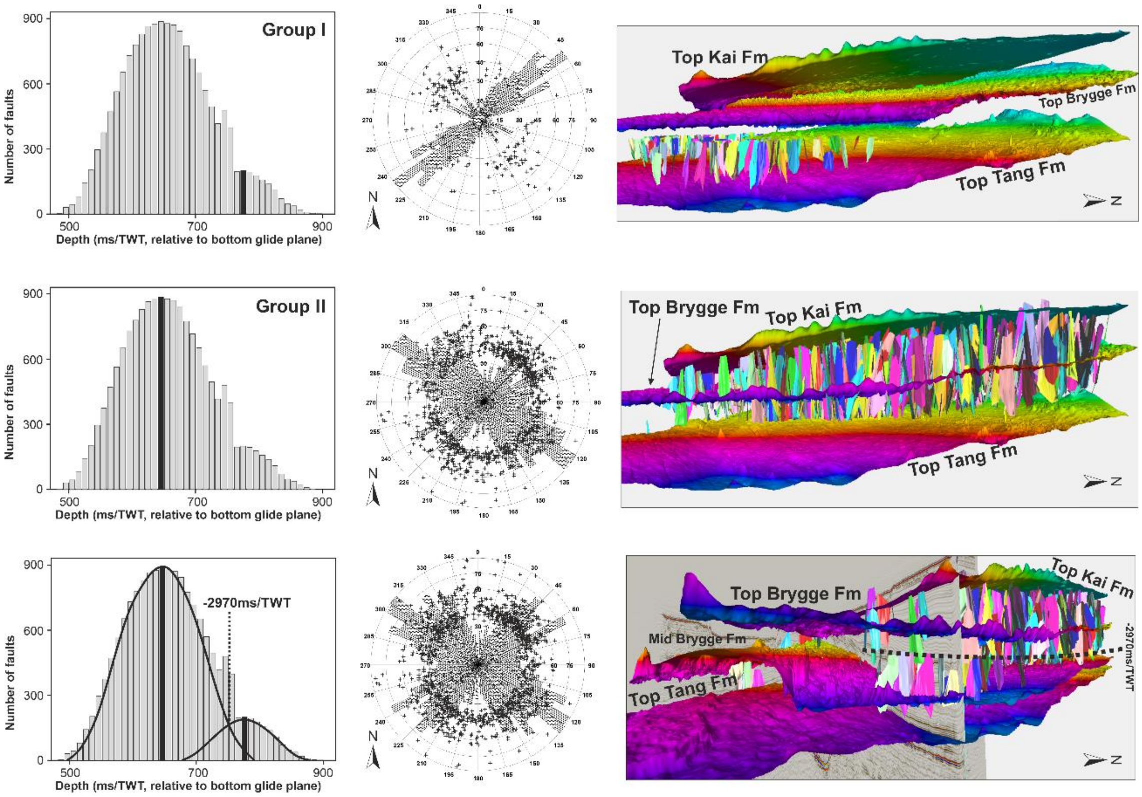

Figure 4.12. Structural data for the Group I and II polygonal faults interpreted in this thesis. The column to the left shows histograms of fault abundance with depth. The column in the middle shows the upper hemisphere stereonet diagram of faults marked in dark in the left hand-side column. The column to the right shows the 3D distribution maps of two groups of polygonal faults in relation to key seismic horizons.

4.6.2.3 Strike-slip faults

Even though the JMFC has been recognised as a weakness zone associated with deep-seated transfer faults in previous work (Surlyk et al., 1981; Torske and Prestvik, 1991), no evidence of strike-slip faults in post-breakup strata above JMFC has so far been observed on the mid-Norwegian margin. In the study area, strike-slip faults are recognised on the west flank of the SMA by their right-stepping en echelon geometries in map view (Fig. 4.4f), high dip angles (80° at minimum, F1 and F2 in Figs. 4.1c and 4.6), and variable throws (Fig. 4.9). Their upper tips are found in the Brygge Formation and stopped at the bottom of MTDs (Figs, 4.6 and 4.8). Furthermore, some segments show apparent normal displacement at their lower parts and apparent reverse displacements towards their upper tips (e.g. F1 in Fig. 4.8; F2 in Fig. 4.6). In map view strike-slip faults overlap with, and are sub-parallel to, the JMFC (Figs. 4.1b and 4.11a). They occur in areas where strata were further uplifted and eroded, and bounded the evacuation structure of Quaternary landslides (Figs. 4.6 and 4.7).

4.6.3 Fluid flow features

Fluid flow features comprise four main types in the study area. First, pipes and vents are observed on seismic profiles as eye-shaped vents, and vertical and narrow pipes link to magmatic sill intrusions in pre-breakup strata (Fig. 4.3). All vent structures are below the top Tang or top Tare Formations (H11 and H10, Figs. 4.1c, 4.3, 4.6 and 4.8), which were putatively formed before and during the continental breakup stages of the Northeast Atlantic. This distribution suggests a fluid migration process during the release of overpressure from heated organic carbon around sill intrusions (Aarnes et al., 2014; Berndt et al., 2000; Kjoberg et al., 2017; Planke et al., 2005; Svensen et al., 2004). The second type of fluid migration comprises positive high-amplitude anomalies (PHAAs) and (sub) circular depressions (pockmarks), both of which indicate relatively slow fluid seeps (Ho et al., 2012)(Fig. 4.13). It can be noticed that most of these sub-circular depressions are located where faults are linked (Fig. 4.13b). Those PHAAs and depressions are observed in the Kai Formation, and are especially obvious in the centre of the SMA.

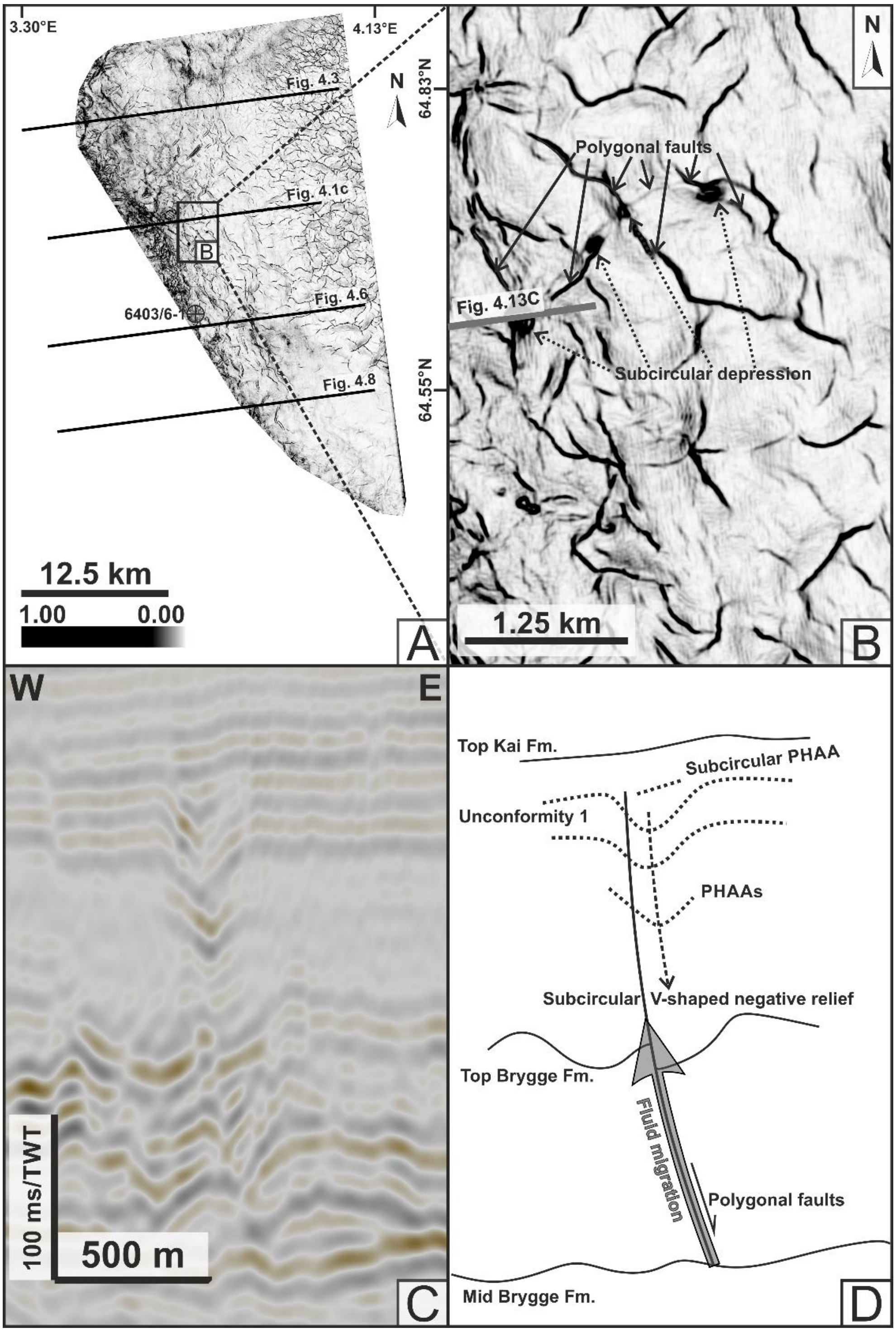

Figure 4.13. Examples of fluid migration taken from the interpreted seismic volume. Based on the variance map of Unconformity 1, several sub-circular depression can be interpreted, suggesting the occurrence of long-term fluid migration on the palaeo-seafloor in the form of pockmarks. Consequently, depressions along this pathway are shown in seismic data as several sub-circular, V-shaped negative features with positive high-amplitude anomalies (PHAAs).

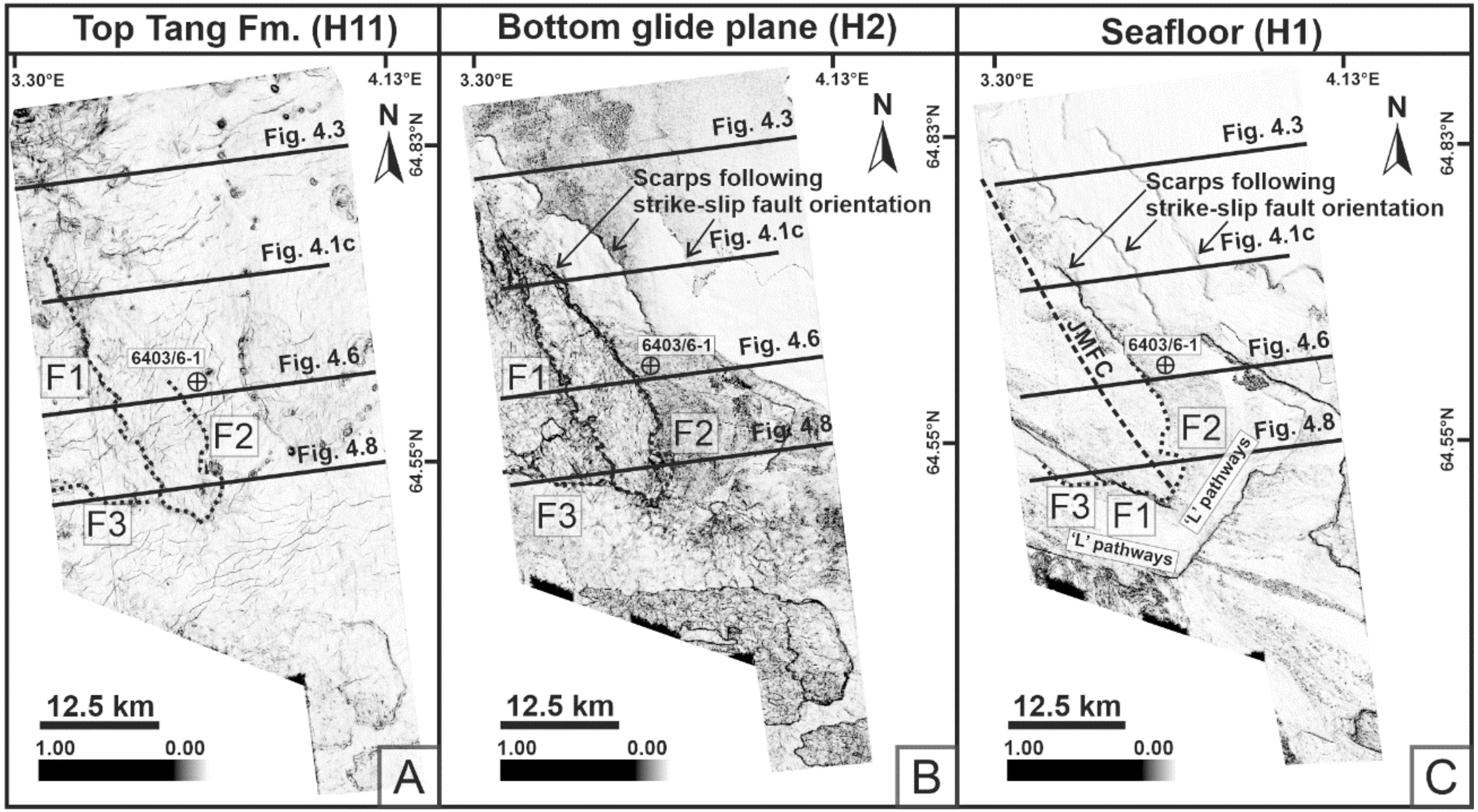

Figure 4.14. Three variance maps highlighting the relationship between faults and landslide scarps. Faults F1, F2, and F3 are recognised at the top of the Tang Formation as forming the headwall and lateral scarps of landslides. This latter character stresses the control of faults on the geometry of submarine landslides around the SMA.

The third type of fluid features comprises high-amplitude reflections ('bright spots') in otherwise transparent, homogeneous strata, a very common feature in the Upper Brygge Formation. This type is particularly observed in strata that are surrounding faults above vent structures (Figs. 4.1c, 4.3 and 4.6).

A fossilised Opal A/CT boundary (H8) is observed in the study area as a diagenetic front that was formed during burial. It records specific temperatures and pressure changes in fluid-rich environments (Berndt et al., 2004). Opal A/CT boundaries have been identified on many dome structures of the mid-Norwegian margin (Omosanya, 2018), including the SMA. The detailed process of development of Opal A/CT boundary is still unclear, but the influence of fluid in their formation is significant (Riis et al., 2005).

4.7. Discussion

4.7.1. Development of faults and its influence on submarine landslides around the South Modgunn Arch

The development of polygonal faults in this study has been addressed by seismic interpretation and faults analyses, which reveal a distinct difference between Group I and Group II faults, in both their distribution and nature (Fig. 4.12). Group I polygonal faults were formed around the SMA under a Southwest-Northeast compressional stress field since the middle Miocene. As suggested by the multiple unconformities in the Kai Formation, this tectonic and faulting process continued until the Quaternary. After a first stage of uplift, the SMA was affected by mid-ocean ridge push, with Northwest-Southeast compression contributing to the formation of Group II polygonal faults.

Group II faults show significant differences between faults at the centre of the SMA (Area I) and its flanks (Area II) (Figs. 4.5e, 4.5f, 4.9 and 4.10). The clear boundary between these two areas on the east flank of the SMA (Fig. 4.5d) excludes the possibility of all faults in Group II being formed at the same time by differential compaction. Thus, the main hypothesis proposed in this work to explain the formation of Group II faults considers the reactivation of polygonal faults in Area I. These polygonal faults were formed during the first stages of compression affecting the SMA and later reactivated during the formation of Group II polygonal faults. Such a hypothesis is supported by the larger throws of faults in Area I (Fig. 4.9), which can result from their longer activity and by their dominant Northwest-Southeast strike because resulting from prolonged extension in the hinge zone of the SMA.

The long-term activity of faults around the SMA is not only suggested by the polygonal faults, but also by the presence of radial and strike-slip faults on variance maps from the top Tang Formation (Figs. 4.8, 4.14a and 4.14b). As previously mentioned, regional compressional stresses were first oriented Northeast-Southwest in the middle Miocene, and then changed to a Northwest-Southeast direction after the deposition of the Kai Formation. Strike-slip faults reveal reverse displacements at their upper tips. Combining with their North-northwest strike (Fig. 4.4c), the reactivation of strike-slip faults can have been triggered by Northeast-Southwest compression during the middle Miocene as an antithetic shear (Group I, Fig. 4.12), or later Northwest-Southeast compression as a synthetic shear in a 'classical' Riedel shear model (Group II, Fig. 4.12).

Around the SMA, a close control of faults on slope instability is suggested by the observed spatial correlation between faults and landslide scarps. The local scarps of MTDs are shown in both seismic profiles and variance maps as a lateral boundary for multiple MTDs, i.e., marking the boundaries of discrete slope movements (Figs. 4.8, 4.14b and 4.14c). Because the seismic characters of individual scarps are obviously different from undisturbed strata, it is possible to recognise the former in structural and variance maps as sharp bathymetric features with high variance (Figs. 4.7, b, c, e and f). In the study area, the largest scarps occur over developed faults: F1, F2 and F3 (Fig. 4.14). As a result of multiple submarine slides, the scarps can be divided into several types, including scarps formed around strike-slip, radial and polygonal faults. In the specific case of strike-slip faults, they controlled the development of submarine landslides by forming the lateral scarps of MTDs (Figs. 4.6 and 4.7e) or the boundaries of individual remnant blocks (Fig. 4.1c).

The triggering mechanism behind the formation of these multiple (recurrent) landslides is still unclear. Based on the seismic interpretation in this thesis and the available data from Well 6403/6-1, important fluid migration is assumed and was likely enhanced by the broad folding of the SMA and by long-term activity of some of the mapped faults (Figs. 4.13 and 15). Data from well 6403/6-1 shows that the Neutron Porosity values, a proxy for the recognition of hydrogen (Ellis, 1990), shows maxima in Upper Brygge strata and in the Kai Formation, but is low above and below these same intervals (Fig. 4.2). As the Neutron Porosity detects the abundance of hydrogen, these maxima may be a result of water or gas hydrates, and any negative anomalies can be due to the presence of gas, which has a low hydrogen density.

The seismic data shows high-amplitude reflections towards the highly faulted Upper Brygge strata, further proving the existence of fluid in highly faulted strata. Furthermore, the PHAAs and depressions have suggested faults as conduits of fluid in study area. It has been suggested by previous work that the migration and accumulation of fluids could have weakened the seafloor sediments, contributing to slope instability (Nichols, 1995). This can partly explain why most evacuation structures are located on anticlines that were previously faulted (Lawrence and Cartwright, 2010).

4.7.2. Faults as markers of tectonic uplift and mass wasting

The seismic interpretation and fault analysis indicate that the development of faults, and their association with fluid migration and submarine landslides, can be divided into three distinct stages. In all three stages, faults acted as markers of the deposition of post-breakup strata, uplift of the SMA, and mass wasting, as summarised below (Fig. 4.15):

Stage I: After the intrusion of magma before and during the breakup of Northeast Atlantic, post-breakup strata (Brygge Formation) were deposited above intrusion-related vents and forced folds (Figs. 4.3 and 4.8). Consequently, due to the differential compaction above positive structures, radial faults started developing (Fig. 4.15a).

Stage II: From the mid Miocene, the Kai Formation was deposited synchronously with tectonic uplift of the SMA under a Northeast-Southwest compressional stress, as documented by the multiple stacked unconformities (H4-H6), erosion of Brygge Formation (H7), and the thickness changes observed in the Brygge and Kai Formations (Figs. 4.1c and 4.6). At the same time, Group I polygonal faults were developed in both the Brygge and Kai Formations. Their strike is predominantly Northeast-Southwest (40-65°) around the SMA. Few Northwest-Southeast (110-135°) faults may have been formed at this stage, and they were likely reactivated in a later stage. High-amplitude reflections, resulting from the accumulation of fluid around polygonal and radial faults in the Brygge Formation, indicate that these faults acted as fluid conduits during tectonic uplift. Based on the Riedel model (Jenkins, 1992), a Northeast-Southwest compression stress can lead to a North-northwest-striking antithetic shear zone, which correlates with the strike-slip faults observed in the study area.

Stage III: Since the tectonic uplift ceased on the SMA, the Naust Formation was deposited on top of this structure and regional stress fields changed to a Northwest-Southeast direction until the present day (Fig. 4.15c). This oriented compressional stress has controlled the development of Group II polygonal faults as shown by their predominant Northwest-Southeast (110-135°) strike, and reactivated the strike-slip faults by creating a North-northwest oriented synthetic shear zone. Faults in the Brygge and Tare Formation have also controlled the development of submarine landslides, comprising the boundary scarps of MTDs during their formation. Compared with the Naust Formation, the intensely faulted Upper Brygge Formation contain more fluid and have lower density. Consequently, the Upper Brygge strata were weaker and lighter, allowing the remobilization of younger sediment inside the evacuation structure.

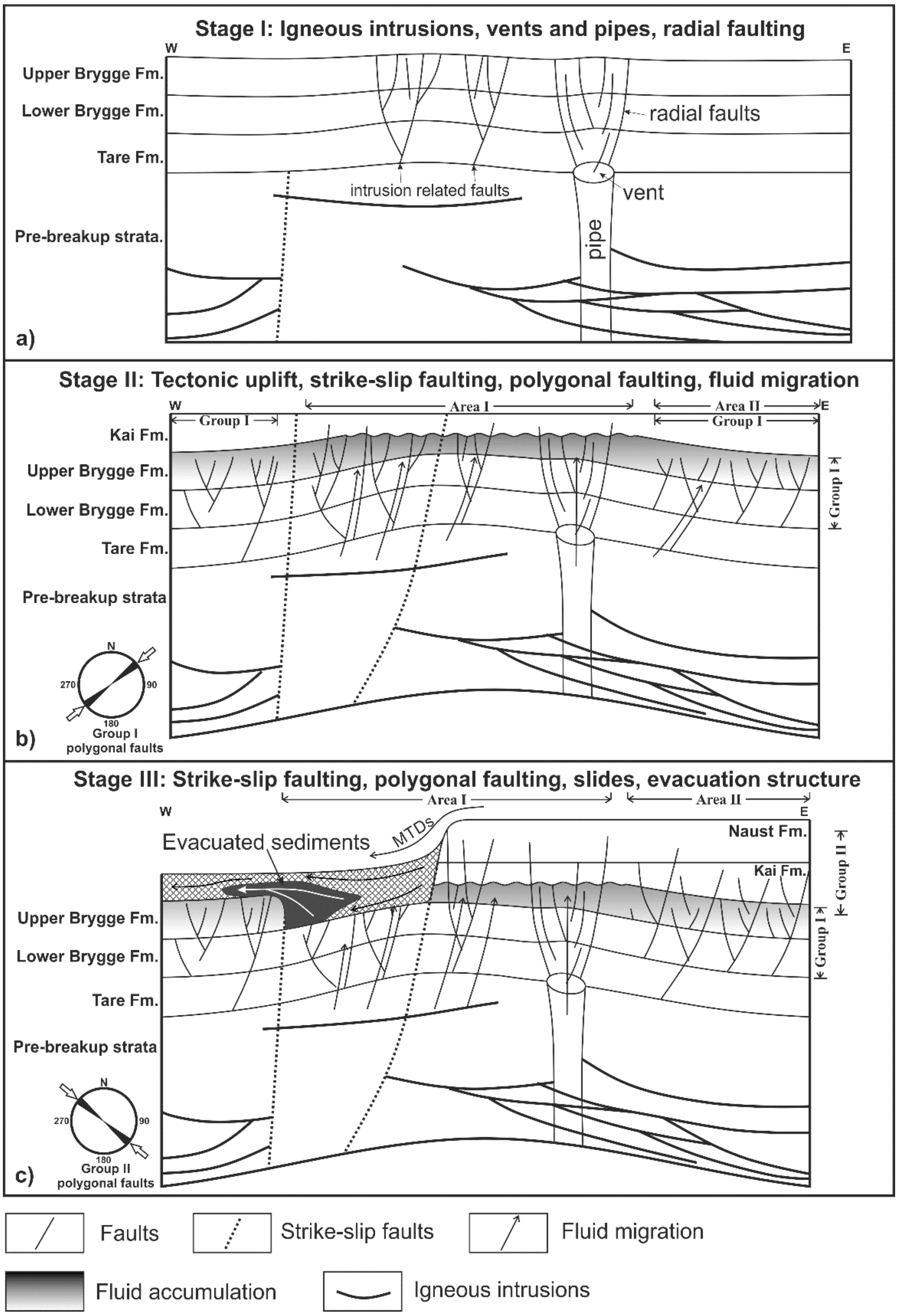

Figure 4.15. Diagram summarising the relationship between tectonic uplift, faulting, fluid migration and landslides around the SMA. Stage I: Intrusion of sills, formation of vents and radial faults before tectonic uplift. Stage II: NE-SW compressional stress and uplifting process of SMA. At the same time, the development of group I polygonal faults contributed to further fluid migration. Strike-slip faults were also reactivated at this stage. Stage III: Development of group II polygonal faults and submarine landslides. The polygonal faults in the centre are long-lived, contributing to further fluid migration and the generation of recurrent submarine landslides.

4.8 Chapter-Specific Conclusions

This work focused on understanding how the development of a Cenozoic compressional structure, the South Modgunn Arch, influenced the evolution of the northern sector of the Storegga Slide. The main results of this study can be summarised as follows.

a) The long-term activity of faults in study area is a result of the combination of two tectonic stages that include the tectonic uplift of SMA under Northeast-Southwest compressional stress during the middle Miocene, and later Northwest-Southeast compression due to mid-ocean ridge push.

b) During Stage I, Group I polygonal faults were generated around the SMA with a predominant Northeast-Southwest strike. Some faults were formed on top of the SMA (Area I) with a Northwest-Southeast strike.

c) Later, Group II polygonal faults were formed with a predominant Northwest-Southeast strike under the influence of mid-ocean ridge push (Stage II), which reactivated older faults in Area I. Faults in Area I were presumably active during both tectonic stages and contributed to fluid migration.

d) Important fluid migration and (local) accumulation in the study area is suggested by both well core tests and seismic interpretation. The existence and distribution of positive high-amplitude anomalies, depressions, high amplitude reflections and vents show a correlation between vents, faults and fluid migration. As a result, fluid was trapped in the Upper Brygge Formation. The lower density of Upper Brygge strata allowed the remobilisation of intensively faulted and weakened sediment inside an evacuation structure, making this structure a main region of enhanced slope instability.

e) The results in this work can be correlated with other parts of Northeast Atlantic and Southeast Asia where tectonic structures in oceanic crust extend to nearby continental margins, promoting local deformation, folding, uplift and seismicity.

CHAPTER FIVE

Styles of slope instability on a Quaternary sub-arctic continental margin: The northwestern flank of the Storegga Slide

5. Styles of slope instability on a Quaternary sub-arctic continental margin: The northwestern flank of the Storegga Slide

5.1 Abstract

Multiple regional submarine landslides have been observed around the Northeast Atlantic margin, However, the initiation processes and features of this slope instability since the onset of the northern hemisphere glaciations is still unclear. This study uses high-quality seismic and borehole data to investigate an area of the mid-Norwegian margin recording long-term instability. Results include the recognition of pre-Holocene landslides along the northwestern flank of Storegga Slide, a giant submarine landslide formed at ~ 8200 years b.p., suggesting that slope instability started in this area during the early Pleistocene. Locally, seismic and borehole data prove the presence of: i) three early Pleistocene slope failures, two of which occurred before a first regional-scale submarine slide , ii) a unit comprising mass-wasting deposits of high density, which reveals local compression and sediment creep, iii) an unstable upper slope revealing seafloor cracks. Importantly, fluid pipes increase in abundance to more than 100 below some of the oldest landslides in the study area, with the majority of pipes terminating below glide planes. The results of this study show that the lithologic (density) changes of sediment and periodic fluid migration are some of the primary factors promoting long-term instability in the Storegga Slide. This has led to multiple slope failures that vary in their style from local evacuation structures to chaotic mass-transport deposits. This work proves that older mass-wasting deposits still reveal the precondition and initiation factors that caused long-term instability on the Norwegian margin. Through the detailed interpretation of local slope failures, regional landslides and further instability can be expected in the future on the northwestern flank of the Storegga Slide.

5.2 Introduction

Submarine landslides, comprising one of the most important offshore geohazards, can trigger recurrent phases of seafloor deformation, sediment remobilisation and, in extreme cases, catastrophic tsunamis (Harbitz et al., 2006; Locat and Lee, 2002). Along the Northeast Atlantic sub-arctic continental margin, multiple submarine landslides have been recorded since Quaternary in the form of mass-transport deposits (MTDs) on seismic profiles, by deformation features on the sea floor, and tsunami episodes on shore (Elger, 2016; Pope et al., 2018). Offshore Norway, the Storegga Slide has evacuated around 3000 km^3 of strata since ~ 8200 years b.p., affecting an area of the continental slope with approximately 95,000 km^2 (Haflidason et al., 2005) (Fig. 5.1). Within the Storegga Slide per se, multiple pre-Holocene slides have been recognised and sampled, from Slide W occurring before 1.7 Ma, to the Tampen slide at 0.15 Ma. Such a time span suggests more than 1 Ma of instability on the Mid-Norwegian slope (Solheim et al., 2005).

At least three pre-Storegga mass-wasting intervals are recorded along the northwestern flank of the Storegga Slide, the oldest being Slide W and comprising remarkable evacuation structures, followed by Slides S and R in the form of discrete intervals with slide blocks (Riis et al., 2005; Solheim et al., 2005) (Figs. 5.2, 5.4 and 5.5). Although an early Quaternary slope failure has been recognised around the headwall scarp of the Storegga Slide (Lawrence and Cartwright, 2009), the initial phases of development of the northwestern part of this same slide are still not fully understood. For instance, recurrent slides and slumps have been identified along the northern scarp of the Storegga Slide and identified as post-Storegga instability (Haflidason et al., 2004). Recent work on the adjacent South Modgunn Arch (SMA) has led to the identification of multiple features of submarine landslides, and poses the question of how long instability has been occurring in this particular region (Song et al., 2020).

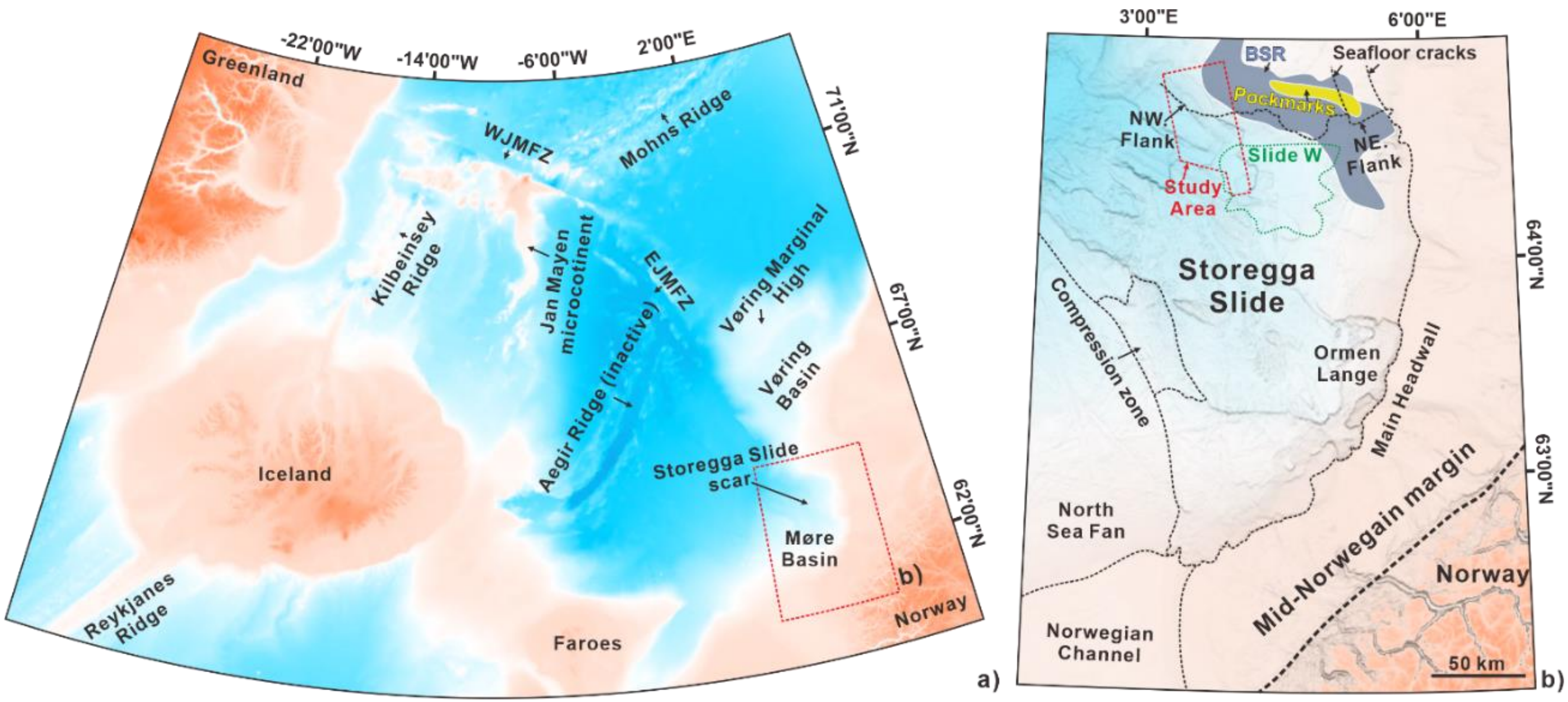

Figure 5.1. a) Map of the mid-Norwegian margin in the Northeast Atlantic. b) Location of the study area on the northwest flank of the Storegga Slide, mid-Norwegian margin, including the distribution of pockmarks fields, BSRs (Bunz et al., 2003), compression zones (Haflidason et al., 2004), Slide W (Solheim et al., 2005) and seafloor cracks (Mienert et al., 2010; Sönke et al., 2011). Maps are modified from GEBCO (2020).

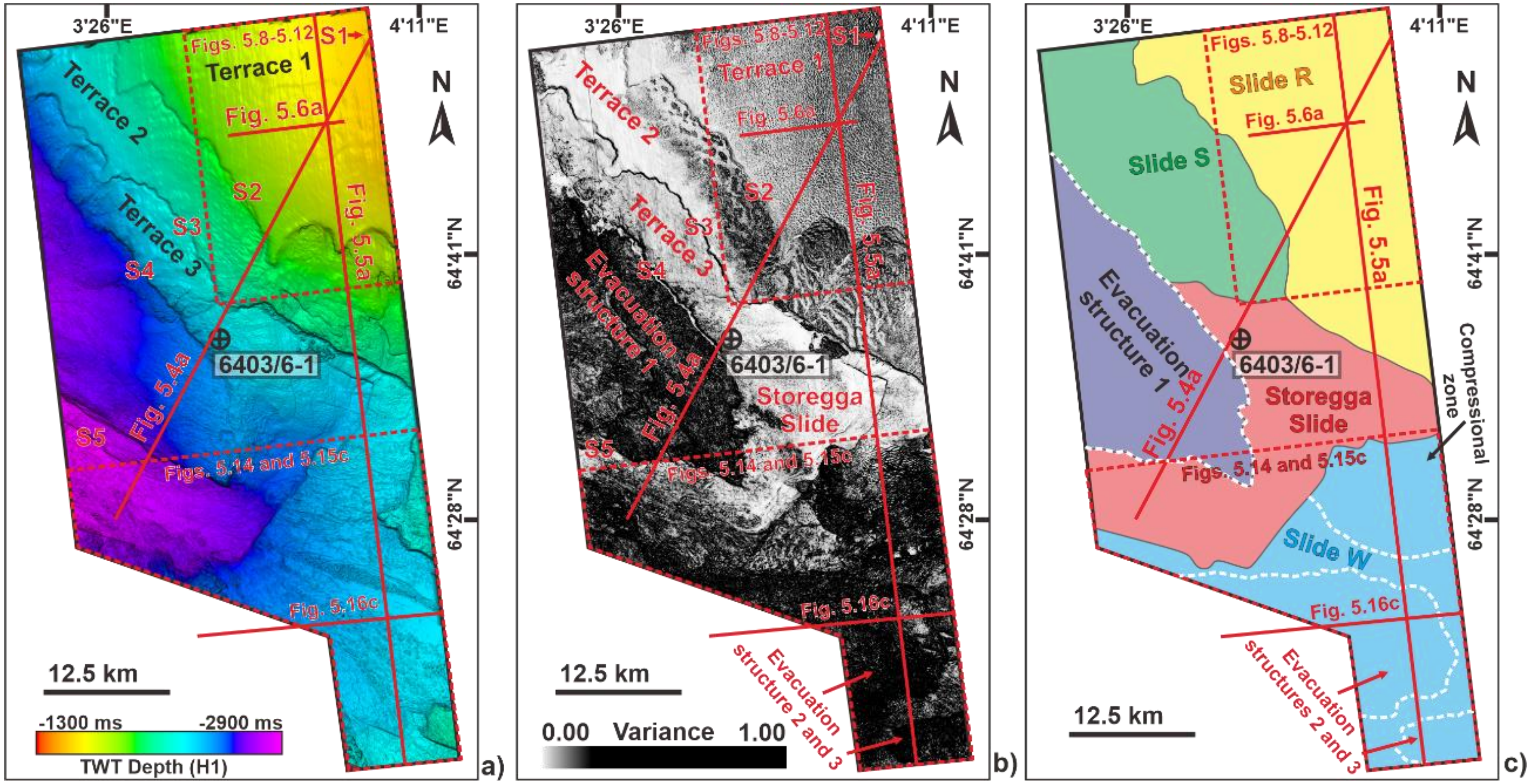

Figure 5.2. a) Relief map of the modern sea floor. Multiple slides are suggested by the presence of intersecting overlapping scarps. b) Variance map 50 ms above the bottom glide plane, showing main features of multiple submarine slides. c) Relationship of multiple Quaternary slides in the study area highlighting the presence of evacuation structures, Slide W, S, R and the Storegga Slide (Solheim et al., 2005).

This work investigates the sequence of slope instability events around the northern Storegga Slide based on 3D seismic data, focusing on its poorly studied northwestern flank near the SMA (Fig. 5.1b). Seismic attribute maps such as seismic amplitude, structural and variance slices reveal distinct features that were associated with palaeo-instability on the continental slope. In addition, density data from this same northwestern flank is used to investigate its role on the initiation of slope instability (Fig. 5.3). By focusing on the chronology of Quaternary submarine slides around the Storegga Slide, and resulting structures affecting the modern sea floor, this chapter addresses the following research questions:

a) What features occurred related to initial slope instability before the occurrence of the first regional-scale landslide in the Storegga Slide?

b) How could lithological variations, particularly those leading to density reversal, control the development of slope instability and corresponding deformation styles?

c) What potential slope deformation structures are recurrent and affect the modern sea floor?

In addition to a new interpretation on the development of evacuation structures, this study has also revealed two early slope-failure events and one potential zone posed for modern instability. Accordingly, both density reversal and fluid accumulation are presented as key factors of long-term instability in the study area.

5.3 Data and Approach

This research uses high resolution 3D seismic and well data from the northwestern flank of the Storegga Slide, on the mid-Norwegian margin (Fig. 5.1). The seismic data comprise acquired records of the reflection of seismic waves from the boundary where acoustic-impedance changes (Veeken, 2007). In this study, positive seismic reflectors suggest higher impedance values below, e.g. the sea floor with higher density and acoustic speed than water, whereas negative seismic reflectors indicate a decrease in acoustic impedance. The studied dataset covers several side- and headwall scarps of Quaternary submarine slides, including Slides W, S, R and the Storegga Slide proper (Bryn et al., 2003; Solheim et al., 2005) (Fig. 5.2). In addition to well 6403/6-1 in the study area, several exploration wells have also been drilled in around the studied region of the mid-Norwegian margin, providing detail lithostratigraphic and wireline information on sub-surface stratigraphic units (Dalland, 1988; Hjelstuen et al., 2005) (Fig. 5.3). In this study, the seismic data were interpreted on Schlumberger's Petrel®, and relevant seismic attribute maps were compiled using this same software. Local structures were investigated by compiling variance and seismic amplitude maps, together with the interpretation on vertical seismic sections (Figs. 5.4-5.16). In contrast to seismic amplitude, which reflects changes in acoustic impedance, variance maps reveal the contrast between adjacent seismic reflections, such as when a fault or unconformity is found (Sanderson, 1991).

The density of strata normally increases during diagenesis together with a with decrease in porosity (Terzaghi, 1925). However, on the mid-Norwegian margin, a density reversal is recognised in the form of high density glacial/marine deposits overlying low density marine oozes (Riis et al., 2005; Vogt, 1997). In order to analyse density reversals in sub-surface strata, the *submerged density* (ρ) is used in this study and defined as the difference between saturated rock density (ρ_{sat}) and water density (ρ_w) considering the Biot's ratio (α):

$$\rho = \rho_{sat} - \alpha\rho_w$$

Equation 5.1

Due to the fact that the contact between a fluid and a solid influences the effective stress, a stress coefficient - the Biot's ratio - is used to estimate the reduction in effective stress that results from the presence of pore fluid in the sediment. Thus, as defined in Equation 5.1, *submerged density* represents the net load that is carried by the rock skeleton, which is later the subject of strata consolidation and deformation. On the mid-Norwegian margin, the value of Biot's ratio has been tested by Lothe et al. (2004) and used in this study.

The Mohr-Coulomb failure criterion, which considers material failure to be a function of normal stress, shear strength and material cohesion of a volume of sediment, is considered in this study to influence slope instability. The shear strength of a volume of sediment, calculated via the failure envelope represented by Equation 5.2, is not only limited by the physical properties of this same sediment, but is also controlled by the variable stress conditions imposed by loading, pore pressure and the Biot's ratio (see Equations 5.1, 5.2 and 5.3) (Biot, 1955):

$$T = \sigma_n \tan \varphi + c$$

Equation 5.2

$$\sigma_n = \rho g h - \alpha P e$$

Equation 5.3

Here, T is the shear strength, σ_n represents the effective vertical stress (a correction will be needed for a dipping glide plane), φ is the angle of internal friction, c is the internal cohesion of rock and Pe is excess pore pressure. The parameter h represents the thickness of strata above the glide zone of a landslide. The effective normal stress (σ_n) and shear strength (T) will decrease when pore pressure increases.

5.4 Geological Setting

5.4.1 Tectonic evolution of the northwestern flank of the Storegga Slide

Located along the Jan Mayen Fracture Corridor, the study area has experienced multiple tectonic events since the syn-rift and continental breakup phases forming the NE Atlantic. Multiple structures were generated within what is a faulted, unstable post-rift sequence (Anell et al., 2009; Maystrenko et al., 2018). Close to the Paleocene-Eocene boundary, widespread magmatic intrusions affected Cretaceous-Paleocene strata before the final stage of continental breakup in the NE Atlantic, forming large hydrothermal vent complexes in the study area (Kjoberg et al., 2017). Remarkable eye-shaped vents are

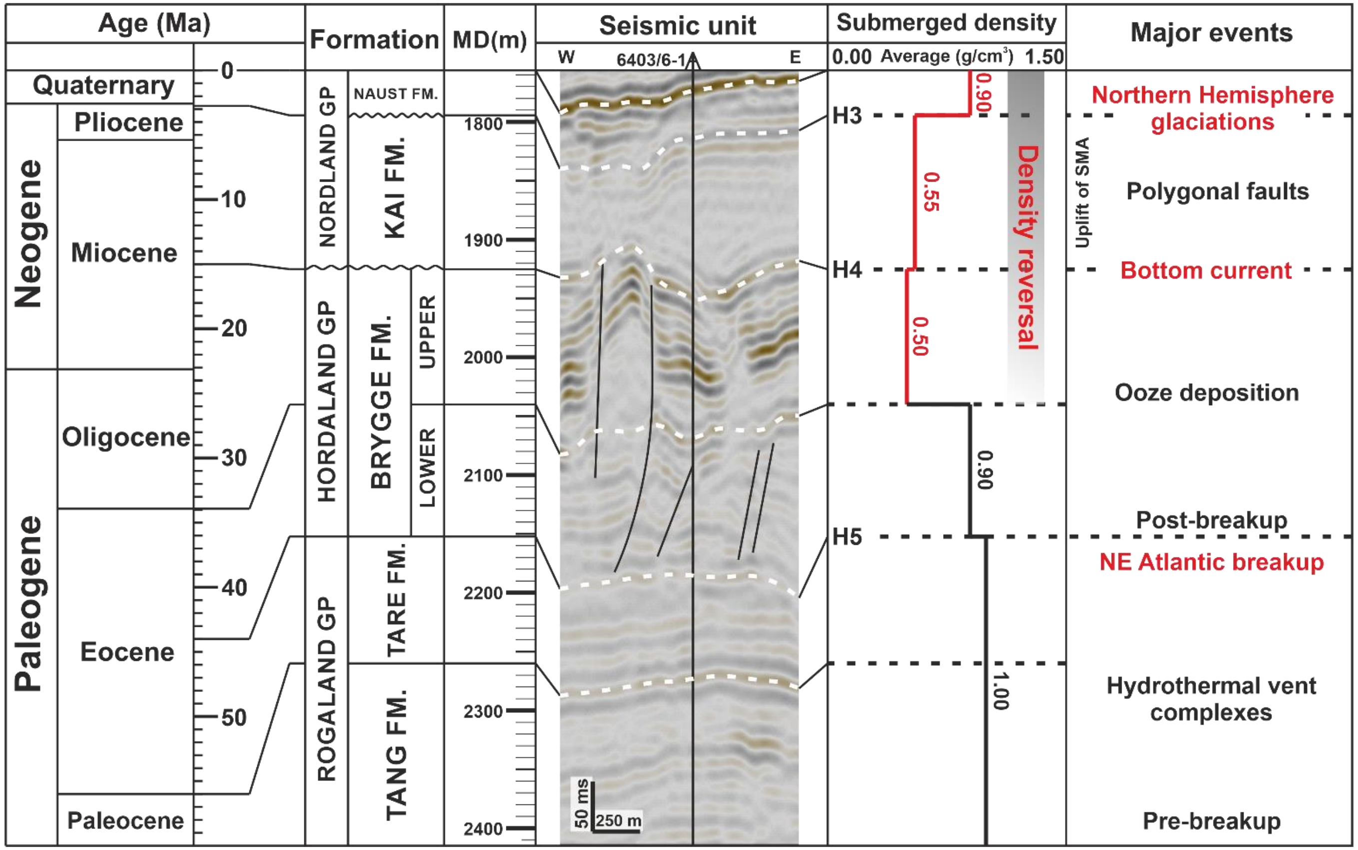

Figure 5.3. General correlation panel amongst seismic data and main seismic-stratigraphic units in the South Modgunn Arch. Interpreted key seismic horizons include Horizon 3 - Top Kai Formation, Horizon 4 - Top Brygge Formation; Horizon 5 - Top Tara Formation. Seismic units, local stratigraphy and undrained density are modified from Song et al. (2020). Submerged density values in its corresponding column are further calculated from Equation 5.1.

observed in the study area as local, positive-relief features forming, at the same time, groups of radial faults due to differential compaction (Omosanya et al., 2018; Roelofse et al., 2021). From the Middle Miocene to late Pliocene, episodic tectonic uplift of the South Modgunn Arch (SMA) has not only created a regional anticline, but also contributed to the generation of a first family of polygonal faults in ooze intervals, which were then overlaid by (and linked to) a second family of Quaternary polygonal faults (Song et al., 2020). Even though the majority of these polygonal faults is limited to pre-Quaternary marine oozes, some still propagated into the glacial-marine Naust Formation, the principal unit revealing long-term slope instability on the mid-Norwegian margin (Berndt et al., 2003; Forsberg and Locat, 2005).

5.4.2 Lithostratigraphy of post-rift strata

Following the tectonic and magmatic events associated with continental breakup in the NE Atlantic region, the depositional environment of the post-rift sequence records important changes. The Brygge Formation, the first unit deposited above a continental breakup sequence *sensu* Soares et al. (2012) (Tare Formation), was deposited from the Early Eocene to the Early Miocene (Eidvin et al., 2007). Significant volumes of biogenic oozes were accumulated together with intervals of sandstone, siltsone, limestone and marl (Dalland, 1988; Riis et al., 2005). On seismic data, the Brygge Formation can be divided into, at least, two seismic packages: the upper Brygge Formation with a relatively low *submerged density* of 0.5 g/cm^3, and the lower Brygge Formation recording a relatively higher *submerged density* of 0.9 g/cm^3 (Fig. 5.3). Due to the multiple tectonic events affecting the study area, the two intervals were highly deformed by radial faults formed above hydrothermal vents, and by two groups of polygonal faults, before the generation of a regional unconformity marking the uplift of the SMA (Song et al., 2020).

Together with the episodic uplift of the SMA, and the establishment of semi-permanent ocean currents, the fine-grained Kai Formation was deposited from the Middle Miocene to the Pliocene, in deep waters, above the Top Brygge unconformity (Chand et al., 2011; Eidvin et al., 2007). Similar to sediment below, the Kai Formation is dominated by calcareous and siliceous oozes with a *submerged density* of 0.55 g/cm^3 (Ireland et al., 2011; Neagu et al., 2010b) (Fig. 5.3). Some minor, localised unconformities in this formation mark the episodic uplift of the SMA (Song et al., 2020). Furthermore, a regional scale Opal A/CT transition was also formed in association with the formation of polygonal faults, following the collapse of porosity and shear strength during diagenetic processes (Neagu et al., 2010b).

The Naust Formation overlies the Kai Formation and was deposited after the onset of Quaternary glaciations in the Northern Hemisphere during the Early Pleistocene. On the Norwegian margin, the Naust Formation is characterised by alternating glacial and marine deposits (Chand et al., 2011; Forsberg and Locat, 2005). Its average *submerged density* reaches 0.9 g/cm^3 in study area, a value higher than that recorded in both the Kai and upper Brygge formations (Dalland, 1988; Song et al., 2020) (Fig. 5.3). Berg et al. (2005) subdivided the clay-rich Naust formation into five (5) well-dated packages (units), marking the progradation of sediment wedges during ice-sheet advance (Newton and Huuse, 2017; Rise et al., 2005). Multiple slope failure events followed the progradation of the latter sediment packages, varying in age from Slide W formed in the early Quaternary to the Storegga slide at 8200 years b.p. (Fig. 5.5c).

5.4.3 Sequence of Quaternary instability

In contrast to its main headwall, the northern flank of the Storegga Slide witnessed multiple Quaternary slope failures that are older than this later slide, including two instability events generating slide blocks and multiple evacuation structures (Lawrence and Cartwright, 2010; Riis et al., 2005; Solheim et al., 2005; Song et al., 2020). During Slide W, which is the oldest regional slide in the Storegga Slide, a series of evacuation structures was formed as a result of fluid migration and density reversal (Riis et al., 2005). Above these evacuation structures, an interval of marine ooze mounds are observed in the form of topographic highs above mass-transport deposits (Lawrence and Cartwright, 2010). Occurring at the base of the Naust Formation, previous research dated the initiation of slide blocks to Slide S (Fig. 5.4), correlating it with a series of glacial advances on the

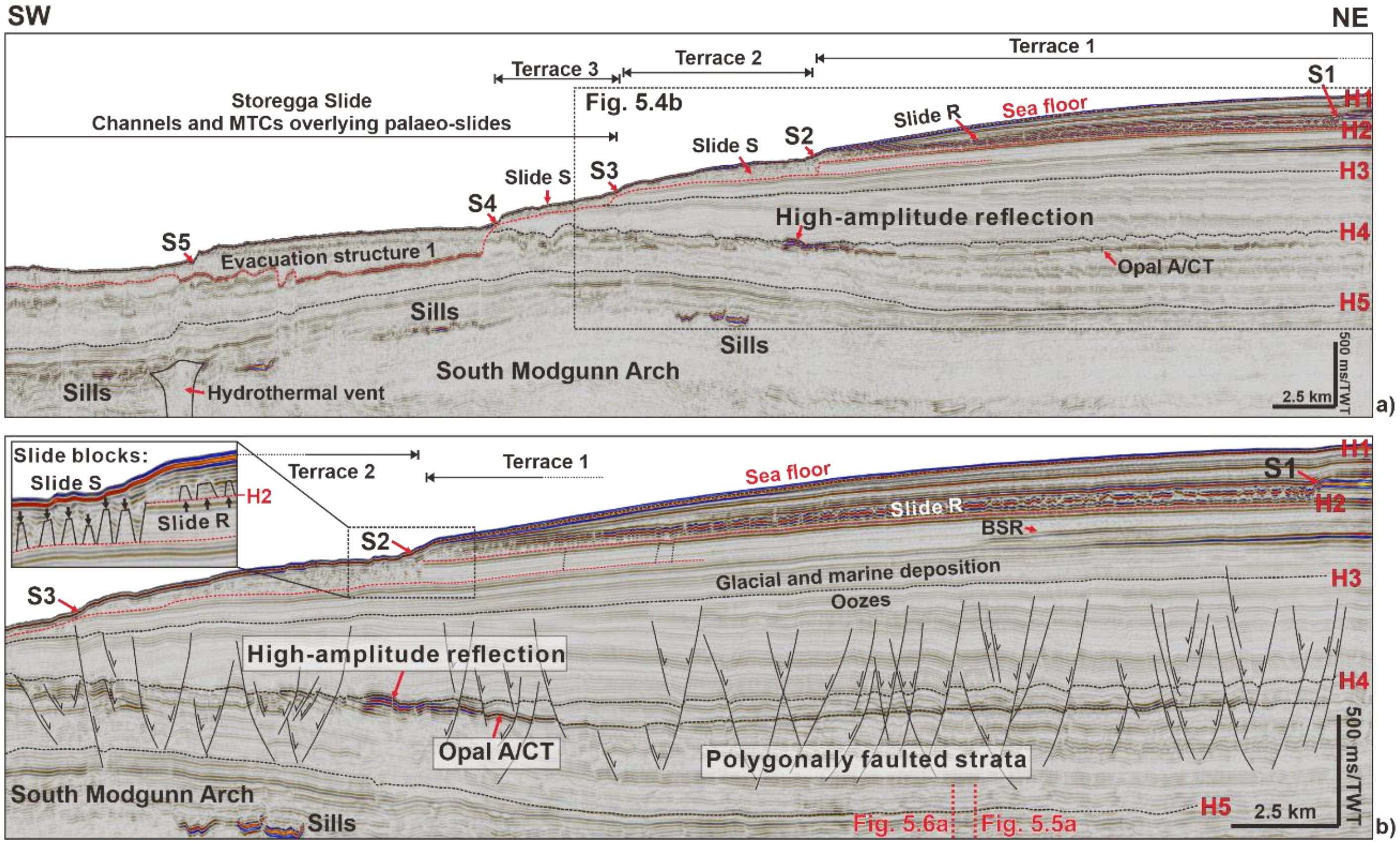

Figure 5.4. Seismic profiles of the study area highlighting the distribution of multiple slides above the South Modgunn Arch. Location of seismic profile shown in Figure 5.2. Horizon 1: sea floor; Horizon 2: bottom glide plane of multiple slides; Horizon 3: top of the Kai Formation; Horizon 4: top of Brygge Formation; Horizon 5: top of Tare Formation. The Opal A/CT transition does not follow the geometry of any refection, but is locally uplifted around the SMA.

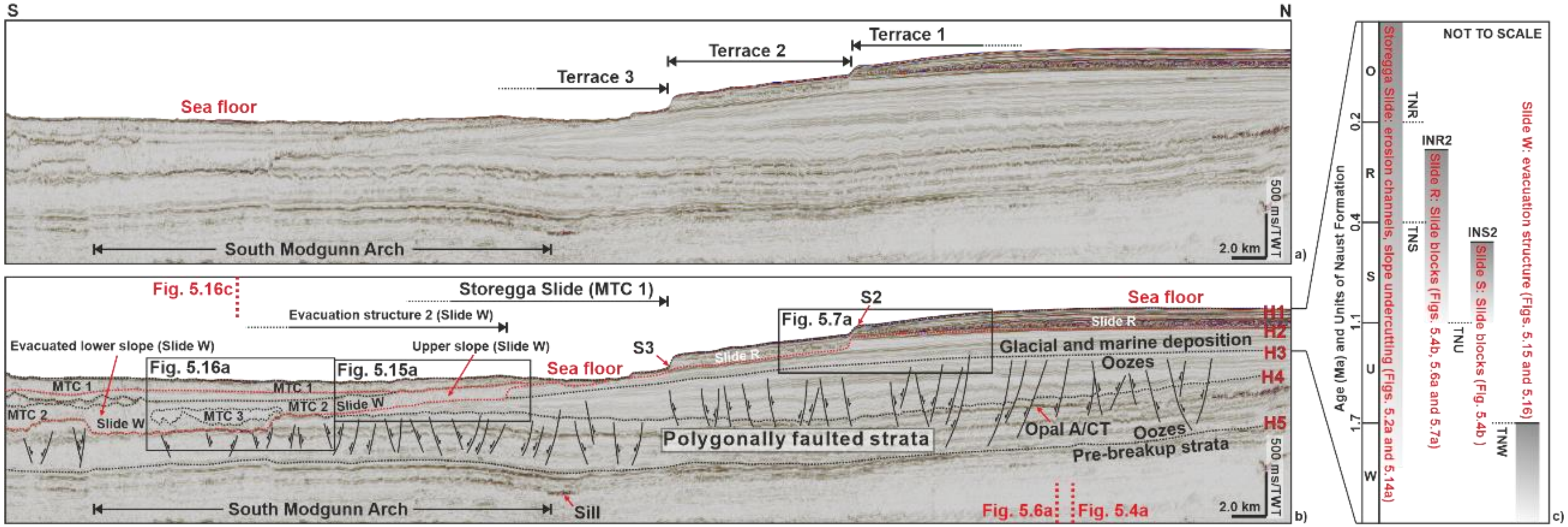

Figure 5.5. Detailed correlation between seismic profiles and known landslide deposits on the SMA. a) Uninterpreted and b) Interpreted north-south seismic profile across the study area. Location of seismic profile shown in Figure 5.2. c) Sequence of slope instability within the Naust Formation. The order and time of main subunits and instability events are based on Solheim et al. (2005). The detail of upslope and downslope MTCs is shown in Figs. 5.7, 5.15 and 5.16.

continental shelf (Bryn et al., 2003; Sejrup et al., 2000). Detailed seismic interpretation further suggests a link between the remobilisation of strata in Terrace 2 (Naust Formation) and the formation slide blocks in the Terrace 1, within the so-called Slide R (Bull et al., 2009b) (see slide blocks in Fig. 5.7b).

Since the larger Storegga Slide occurred, evidence for long-term instability has been recorded in the study area in the form of local slumping, multiple debris channels, locally deformed strata, and near-seafloor faults (Haflidason et al., 2005, 2004). A series of en echelon cracks and faults is observed on the sea floor north of the Storegga Slide headwall, striking nearly parallel to the shelf edge, at around 500 m water depth (Mienert et al., 2010) (Fig. 5.1b). Similar to features discovered along the U.S. Atlantic margin, these crown cracks relate to the release of shallow fluid due to post-glacial ocean warming and subsequent dissociation of gas hydrates (Hill et al., 2004). As a result of rapid sediment transport and deposition during inter-glacial periods, subsurface pipes and pockmarks were triggered by excess pore pressures in sediment before the formation of these same seafloor cracks and faults (Hustoft et al., 2009). In the study area, the combination of seafloor cracks, faults and pockmarks is frequently observed within glacial-marine intervals, further emphasising the instability induced by shallow excess pore pressure during the Quaternary (Figs. 5.4-5.13).

5.4.4 Fluid migration and accumulation

On the mid-Norwegian margin, the release of fluids associated with high excess pore pressure has been widely observed in the form of pockmarks and associated bottom-simulating reflectors (BSRs) and strong amplitude anomalies formed below a gas hydrate stability zone (GHSZ) (Berndt et al., 2004; Bünz et al., 2003). Both the warm-water inflows and glaciation-related eustatic sea level controlled the depth and extent of this GHSZ (Mienert et al., 2005). Based on benthic foraminifera, a rapid increase of bottom-water temperature has occurred since the end of Younger Dryas (Berstad et al., 2003). Due to their sensitivity to temperature increases, dissociated gas hydrates built up excess pore pressures around the headwall of the Storegga Slide (Sultan et al., 2004; Xu and Germanovich, 2006).

Similarly to other slope failures on high-latitude continental margins, interbedded glacial and marine deposits such as those in the Naust Formation contribute to a weakening of slope strata and the accumulation of excess pore pressures in glacial intervals, remobilising the more sensitive marine clays in a second stage (Leynaud et al., 2007). Together with rapid sediment deposition and loading, gas hydrate dissociation, tectonic tilting, and the dewatering of oozes in the Brygge and Kai formations have all contributed to the migration of fluid to the shallower Naust Formation via polygonal faults, further increasing excess pore pressure during the time of deposition of the Storegga Slide (Gay and Berndt, 2007; Hustoft et al., 2007). In the study area, fluid migration was recorded as: a) hydrothermal vent complexes as a result of focused fluid flow associated with magmatic sill intrusion during the breakup of NE Atlantic (Roelofse et al., 2021). b) pockmarks on the palaeo-seafloor and pipes at beneath as the conduit of fluid that migrated through polygonal faults (Song et al., 2020).

5.5 Evidence of Quaternary slope instability

5.5.1 Pre-Slide W instability and sediment creep

The Naust W unit (Berg et al., 2005), corresponding to the 'Naust N' or 'Naust 2' in other publications such as Rise et al., 2010 and Rydningen et al., 2016, was deposited from ~2.6 to 1.7 Ma above the ooze-rich Kai Formation. The upper boundary of the Naust W unit coincides with the top of Slide W, a high-amplitude positive reflection in the studied data set (Solheim et al., 2005) (Figs. 5.6 and 5.7). Recurrent slope instability deformed Slide W, which was also eroded by debris channels during the failure of the Storegga Slide (Fig. 5.15a). Upslope, two local landslides are further recognised and their positions suggest that slope instability was triggered before Slide W, so far recognised in the literature as the first failure event in the study area (Figs. 5.10 and 5.11). In order to illustrate the character of slope instability preceding Naust W, four seismic Horizons were mapped within this latter unit, between the top of Slide W and the top of the Kai Formation (Horizons B, C, D and E in Figs. 5.10-5.12).

On the variance map of Horizon E, the first negative seismic reflection above the Kai Formation, pockmarks are observed as high-variance features with a sub-circular geometry (Fig. 5.12). Their average diameter reaches 60 m, with local depressions or rises up to ~20 ms (about 17 m) in height (see Fig. 5.12c). Some of the observed pockmarks are isolated, while others are close to normal faults linking to polygonal faults in the Kai Formation (Figs. 5.12b-f). Moreover, seismic interpretation reveals more than 130 fluid pipes, which are observed as narrow areas of subdued amplitude and sharp up-bending or down-bending reflectors, at the level of Horizon E, the highest value in the entire Naust Formation (Fig. 5.13).

Consequently, the negative-polarity Horizon (D) was interpreted and mapped 50 ms above Horizon E (Fig. 5.11). Pockmarks are still observed in Horizon D but much less frequently and with no apparent changes in their size (Figs. 5.11d and 5.13). In the south, a mass-wasting deposit (Slide X) pre-dating Slide W is revealed in the form of detached blocks with high amplitude and associated chasms (blocks 1-3 in Figs. 5.7c and 5.11c). Formed between Horizons B and E, the thickness of this blocky landslide reaches 40 ms (about 28 m), and is 6 km wide (Figs. 5.7b, 5.7c and 5.11a). In contrast to Slides S and R, where blocks show a constant width, the blocks within this Slide X have widths varying from 50 to 500 metres. The strike of some of the blocks detached from the headwall is also variable, in places perpendicular to the strike of headwall, or showing local rotation by ~45^o (blocks 1-3 in Fig. 5.11c).

On the headwall of the Slide X, and behind several slide-related faults, three high-amplitude areas are observed as local positive features (Figs. 5.7d and 5.11b). These elliptical structures show major axes that are 1-3 km long, and minor axes that are 1 km-long (Fig. 5.11b). Beneath these positive-relief features, a normal fault is interpreted as a structure growing out of polygonal faults in the Kai Formation (Figs. 5.7b and 7d). Local amplitude highs are interpreted to represent gas pockets, or ‘flags’, mainly where polarity inversion is also observed along continuous seismic reflections (Fig. 5.7d).

Between Horizon D and the top of Naust W, a positive reflector Horizon (B) was also mapped (Fig. 5.10a). Groups of en-echelon and partly connected cracks are observed

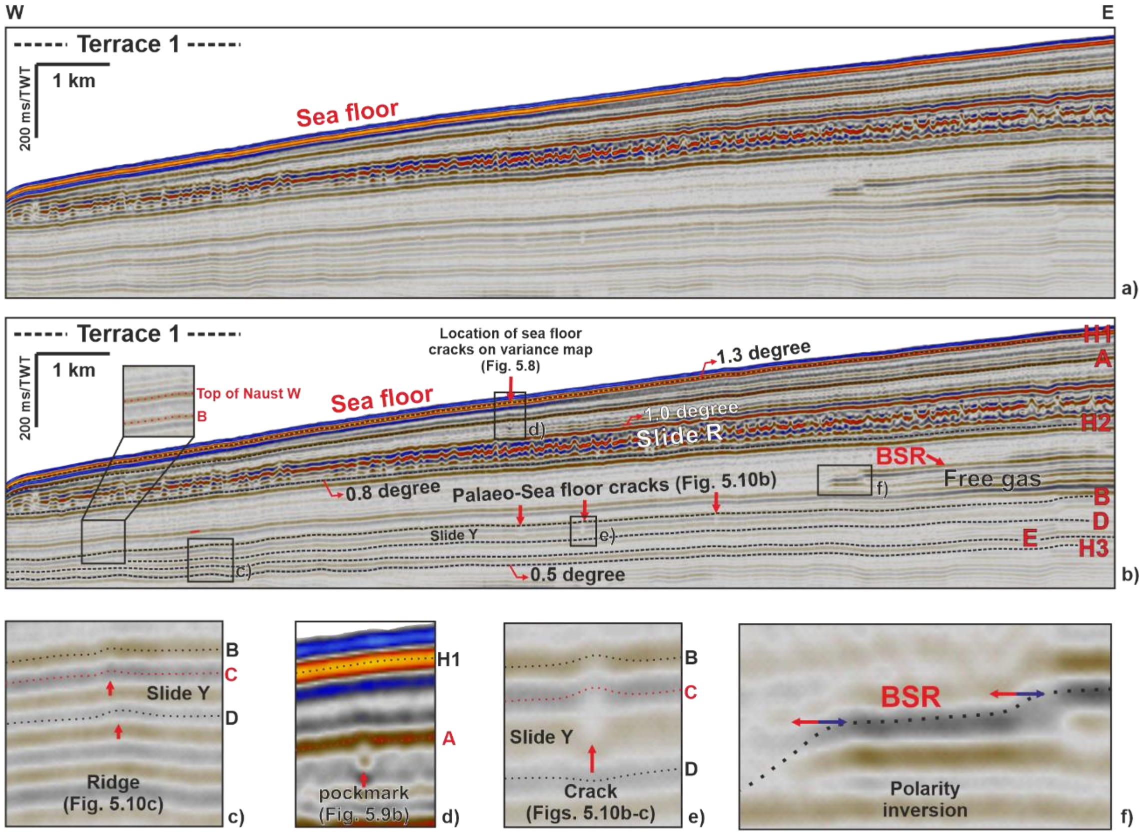

Figure 5.6. a) Uninterpreted and b) interpreted west-east seismic profile crossing Terrace 1. Location of seismic profile shown in Figure 5.2. c) One of the ridges observed on the lower continental slope (see Fig. 5.10c). d) Palaeo-pockmarks are observed beneath the modern sea floor. e) One of the en-echelon palaeo-sea floor cracks shown in Figure. 5.10b. f) Free gas accumulated beneath a BSR, leading to a lateral polarity reversal in amplitude. The average dip angle of Terrace 1 increased from 0.5 degrees on the Top of Kai Formation (Horizon 3) to 1.3 degrees on the modern sea floor (Horizon 1).

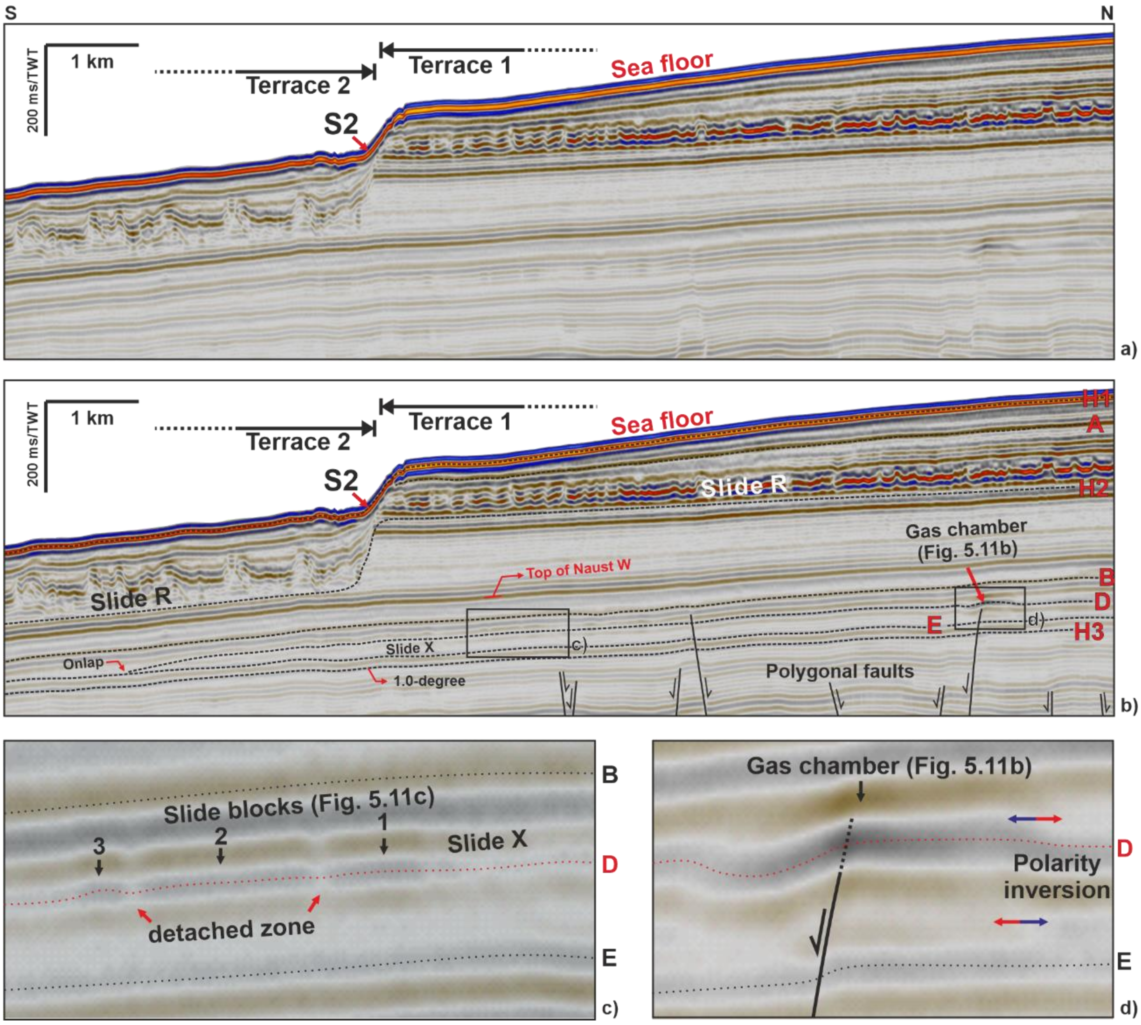

Figure 5.7. a) Uninterpreted and b) interpreted north-south seismic profile crossing Terraces 1 and 2. Location of seismic profile shown in Figure 5.5. c) Slide blocks of Slide X are detached on a steeper slope reaching 1.0 degrees. d) A reversal in seismic polarity is observed laterally close to the tip of a polygonal fault, and revealed as a gas chamber in Figure 5.11b.

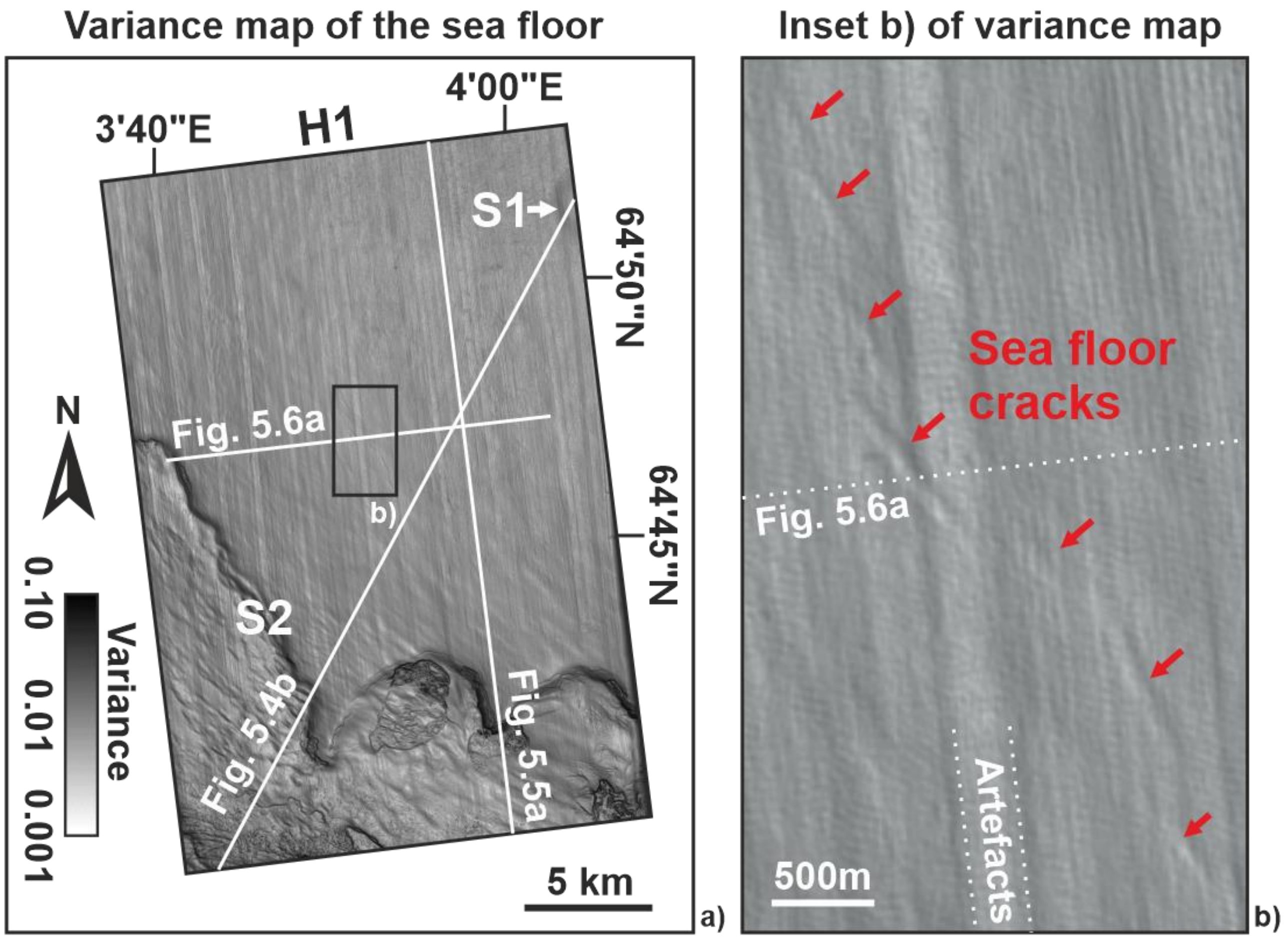

Figure 5.8. a) Variance map of the modern sea floor (Horizon1), and b) detail on the same variance map of sea floor cracks. These en-echelon cracks are only observed on the variance maps with a logarithmic scale and are not observed on seismic profiles (Fig. 5.6d).

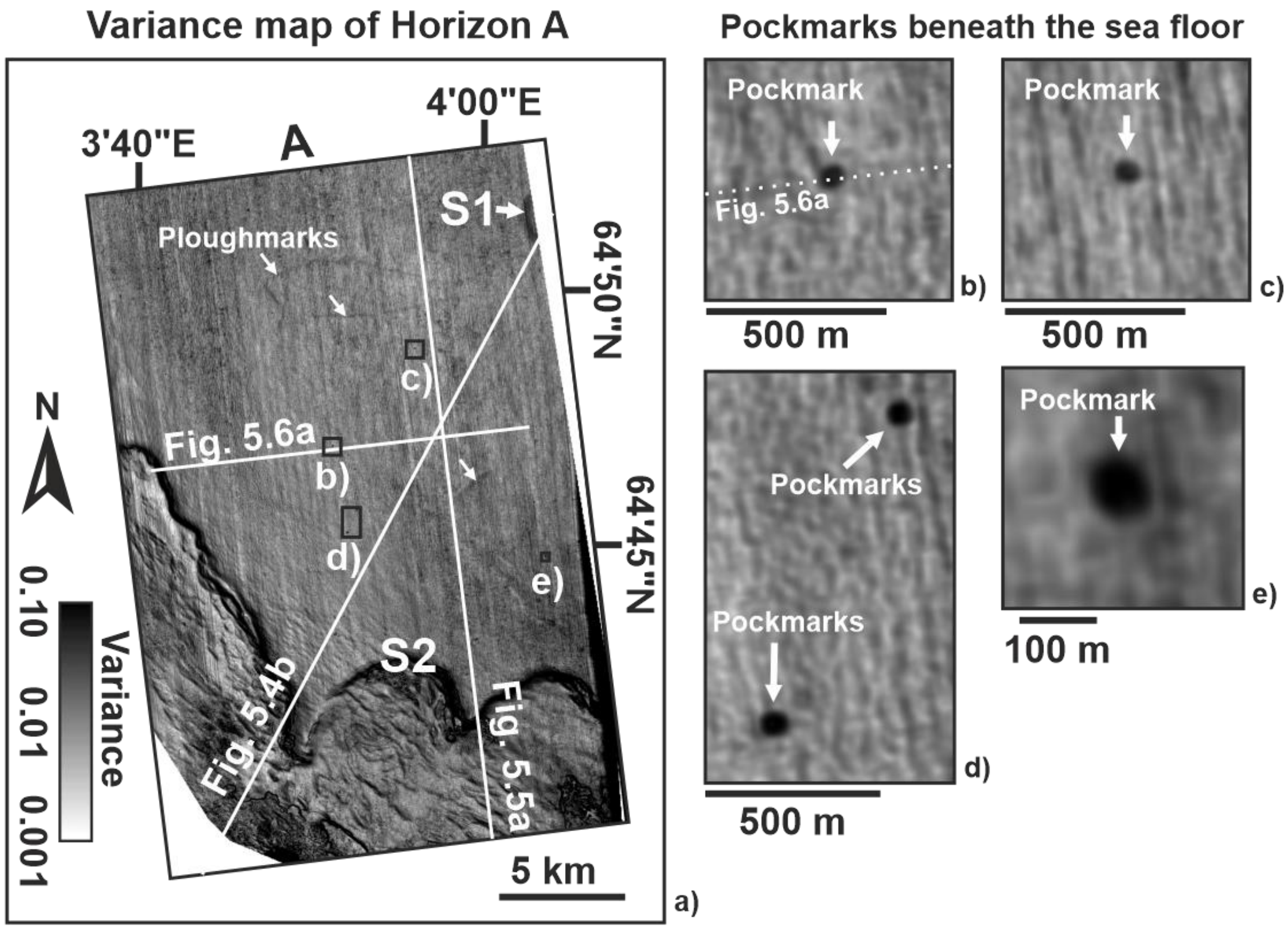

Figure 5.9. a) Variance map of a positive reflector (Horizon A) computed ~ 40 ms below the modern sea floor. b-e) Pockmarks on Horizon A are about 60 m wide. Ploughmarks are observed on this same horizon.

on seismic amplitude maps (see the green and red zones in Fig. 5.10b). These cracks are ~4 km long and 40 m wide, sizes that are similar to the seafloor cracks on the shelf edge of the mid-Norwegian and U.S. Atlantic margin (Hill et al., 2004; Mienert et al., 2010). The cracks have no apparent offset but are associated with pipe structure on seismic data (Fig. 5.6e). Downslope from these cracks, two local ridges show positive relief and a width of approximately 40 m; they follow the same strike of cracks upslope (Figs. 5.6c and 5.10c). Apart from the amplitude anomalies and the pipe structure on the upper part of the slope (and local relief on the lower slope), no further slide-related features are observed between Horizon D and the top of Naust W.

5.5.2. Sediment evacuation structures

Close to the centre of the Storegga Slide, multiple debris channels associated with slope instability are revealed as local erosion features (Haflidason et al., 2005) (Fig. 5.14a). In parallel, several evacuation structures are observed below the debris channels in form of local craters with chaotic seismic reflections (Riis et al., 2005) (Figs. 5.4a and 5.16). Similar to Evacuation Structure 1 on the lower slope (Song et al., 2020), Evacuation Structure 2 consists of a central crater and a relatively high step formed in its downslope section (Figs. 5.14b and 5.16c). A group of NE-SW-trending blocks is revealed on a variance map 50 ms above their bottom glide plane (Fig. 5.15d). Seismic profiles further image a group of thrust faults between discrete slide blocks, indicating local compression on the northern flank of Evacuation Structure 2 (Figs. 5.15a-b). Though the top of this zone of compression was eroded by channels during the main period of instability associated with the Storegga Slide, suggested by the overlying erosional surface (Figs. 5.14 and 5.15a), a gentle bottom glide plane is observed as negative seismic reflection within the Kai Formation – in all effects, a 1^{o} glide plane formed between Horizons 3 and 4 (Fig. 5.15a). Close to its northern boundary, where the thrust faults are clearer, a headwall scarp is identified as the last thrust fault separating compressed blocks from undeformed strata (Fig. 5.15b).

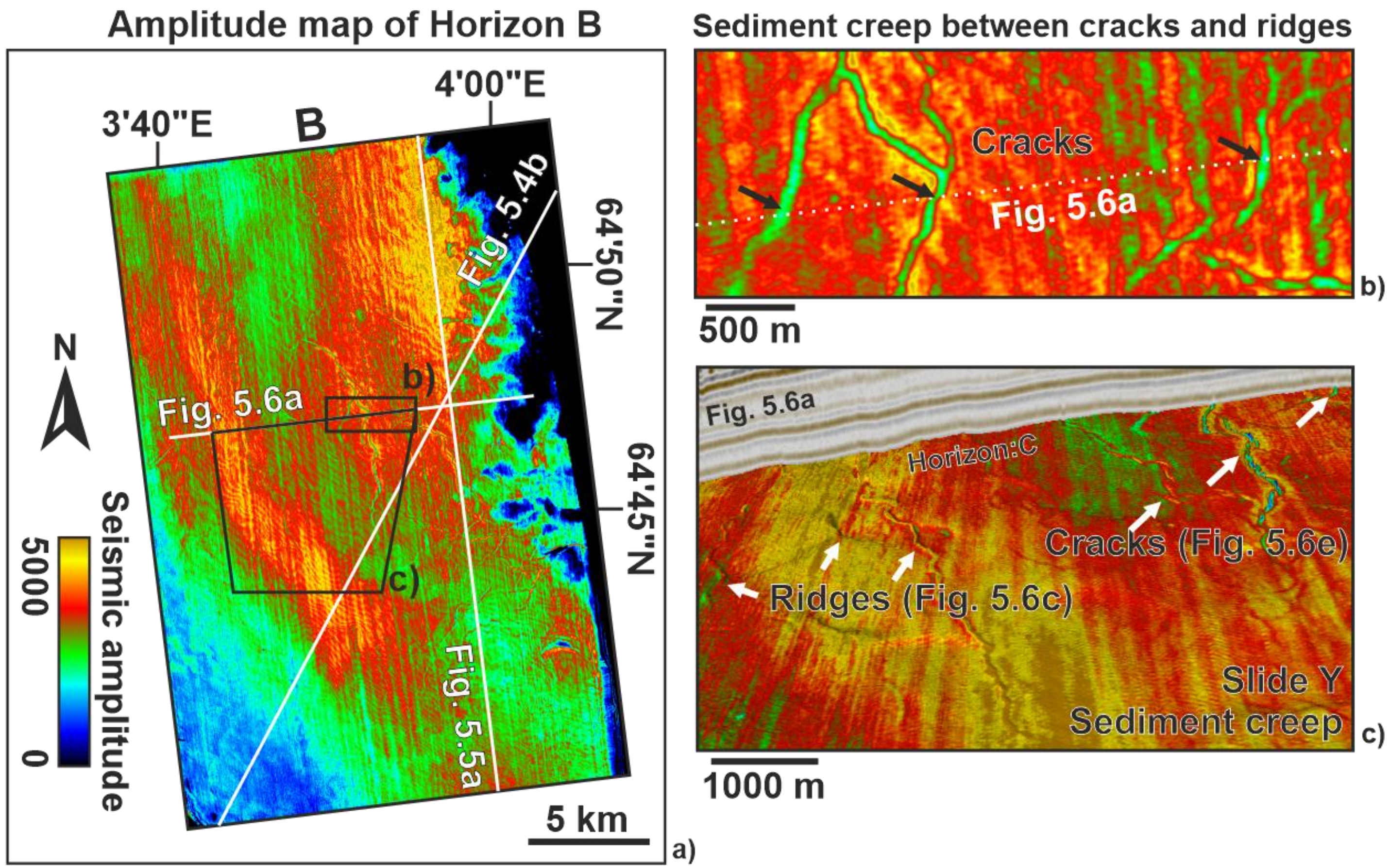

Figure 5.10. a) Amplitude maps of Horizon B, a positive seismic reflector immediately below the top Naust W. b) En-echelon and connected palaeo-seafloor cracks are shown as local low-amplitude features. c) On the lower slope, several ridges are observed as topographic highs at the level of Horizon C.

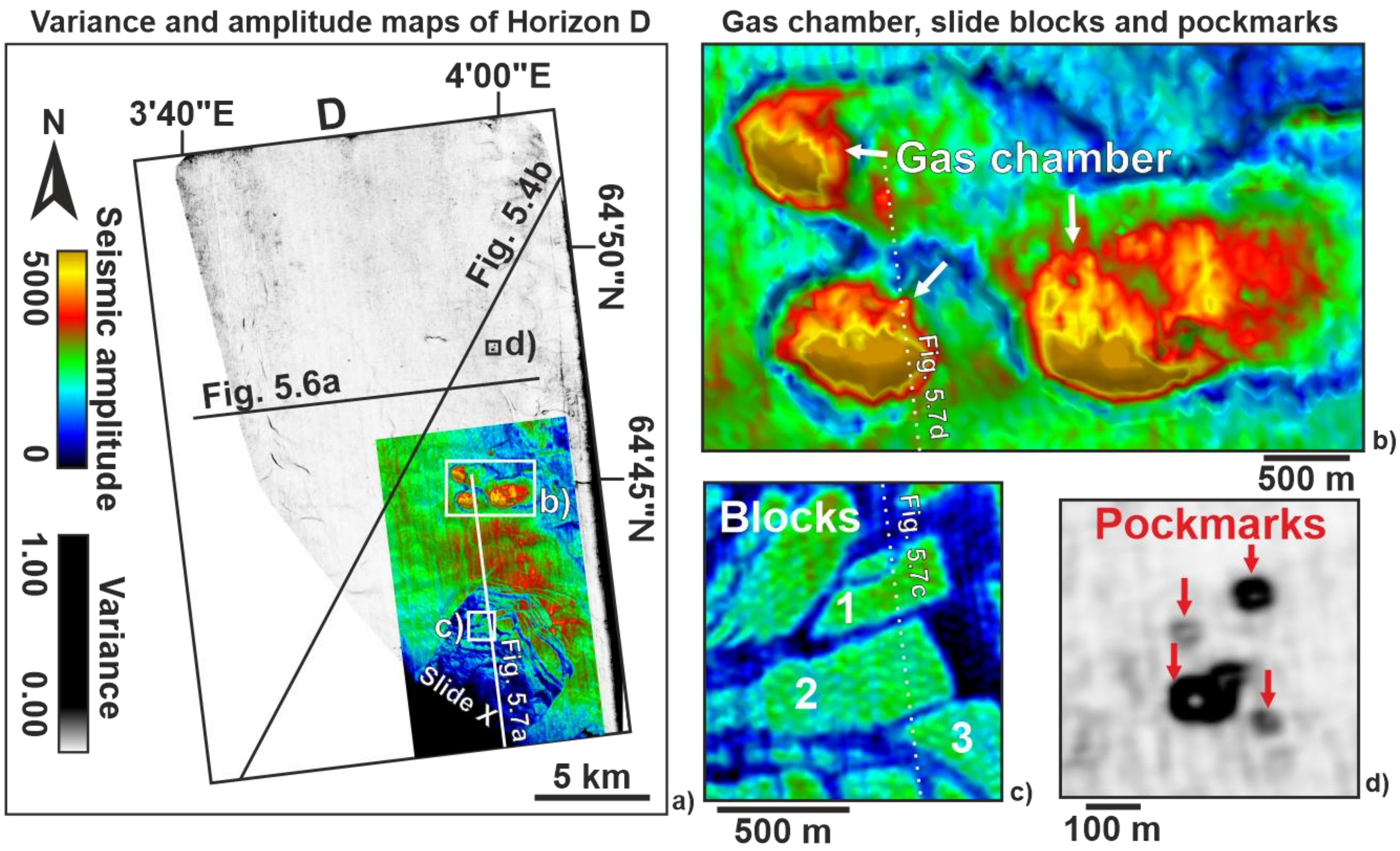

Figure 5.11. a) Variance map overlain by the amplitude map of Horizon D, a negative reflector beneath Horizon B. b) Gas 'flags', and c) slide blocks shown as local high-amplitude features d) Few pockmarks are observed at the level of Horizon D.

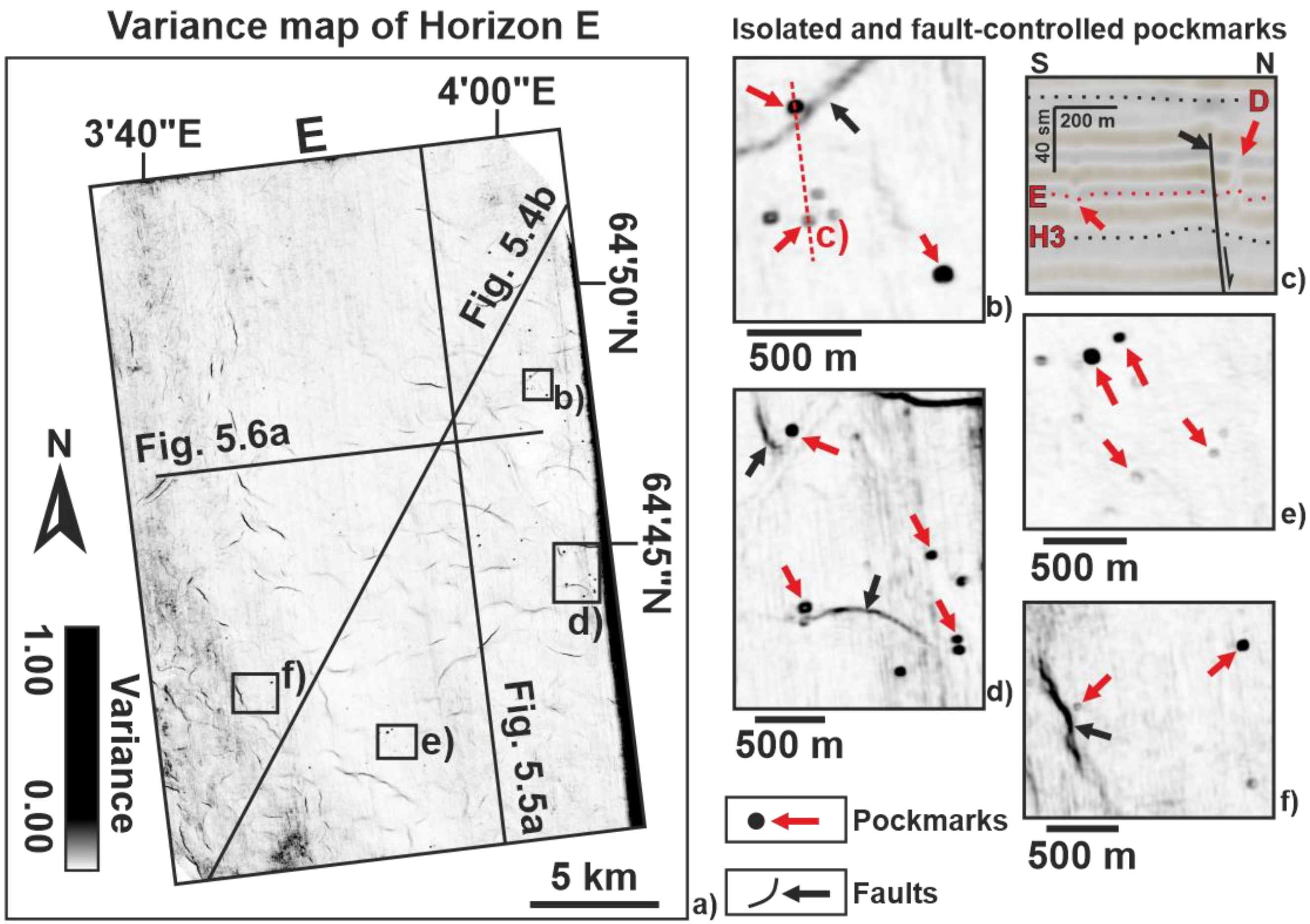

Figure 5.12: a) Variance map of Horizon E, a negative seismic reflector above Top Kai (Horizon 3). b-f) Regional pockmarks are observed close to faults and also as relatively isolated features.

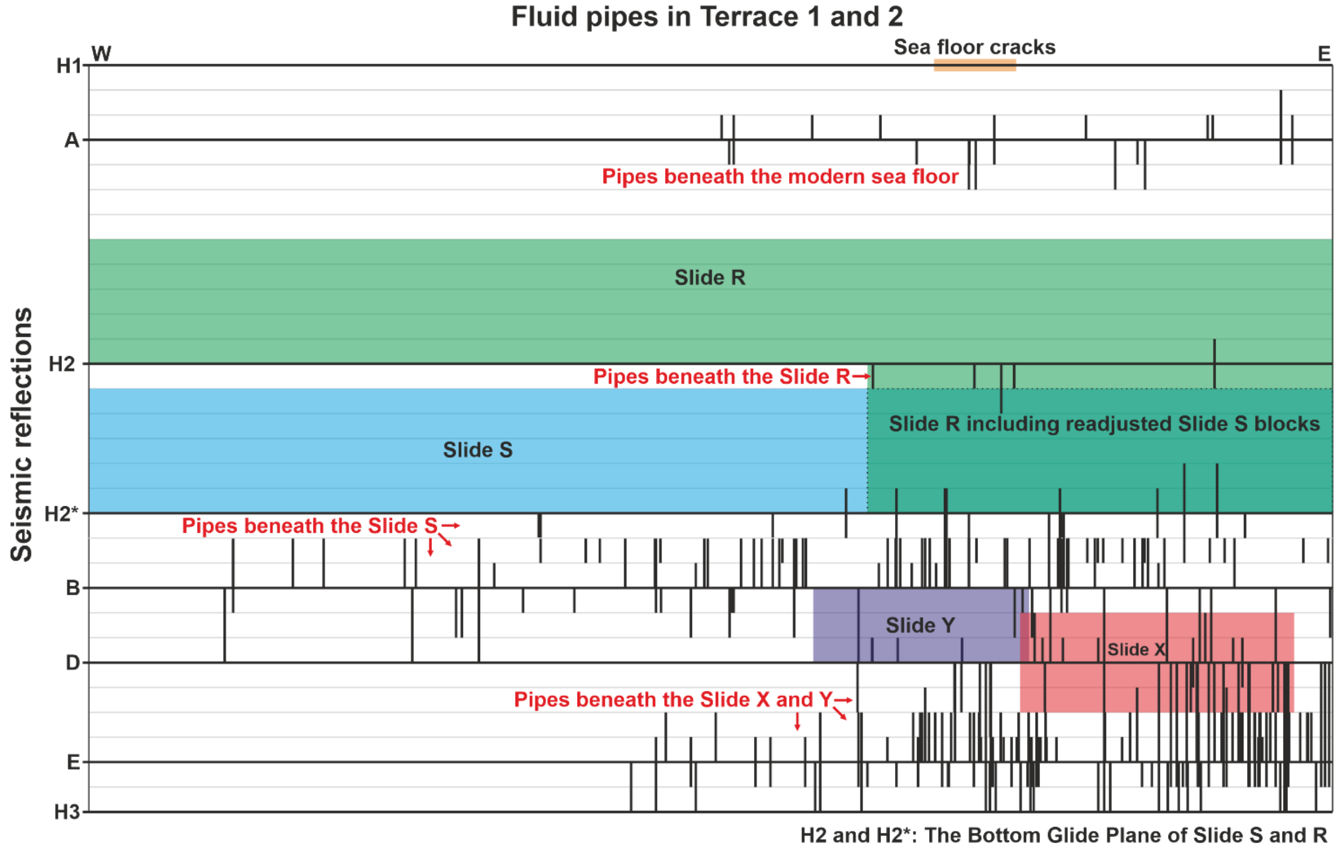

Figure 5.13. Distribution of pipes in terraces 1 and 2. Vertical black lines represent the range of pipes, relative to key reflections, including the sea floor (Horizon 1), a reflector below this latter (Horizon A), the bottom glide plane beneath regional slides (Horizon 2 and 2*), reflectors recording early instability (Horizons B, D and E) and the Top Kai (Horizon 3). The abundance of pipes has declined before both regional slides (Slide R and S) and local instability (Slide X, Y and seafloor cracks).

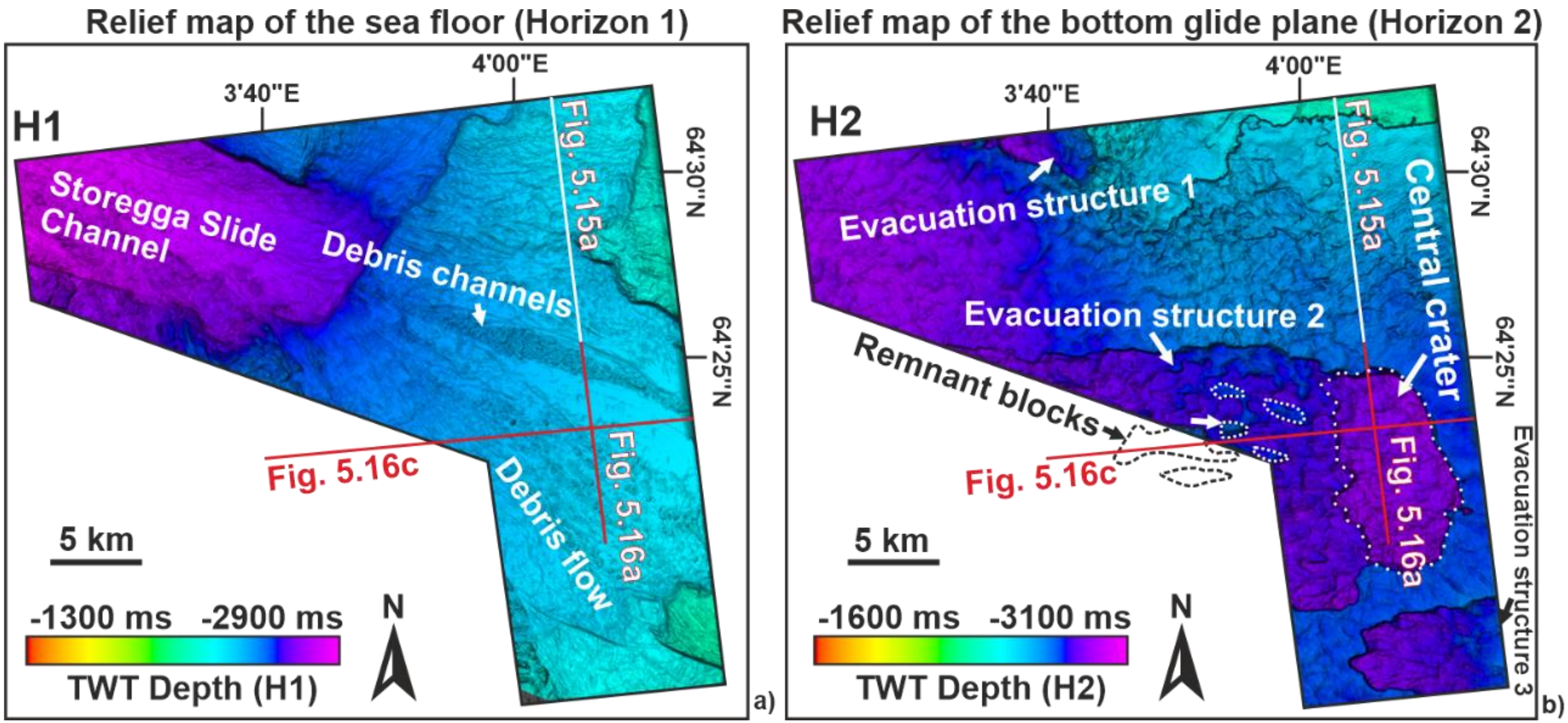

Figure 5.14. a) Storegga Slide showing evidence of multiple debris channels and flows on the modern sea floor (Horizon 1). b) Two-way structural map of the bottom glide plane in Horizon 2. The evacuation structures in b) are marked as local depressions, inside which a central crater is revealed in the area of lowest relief. Remnant blocks are highlighted by the dashed lines.

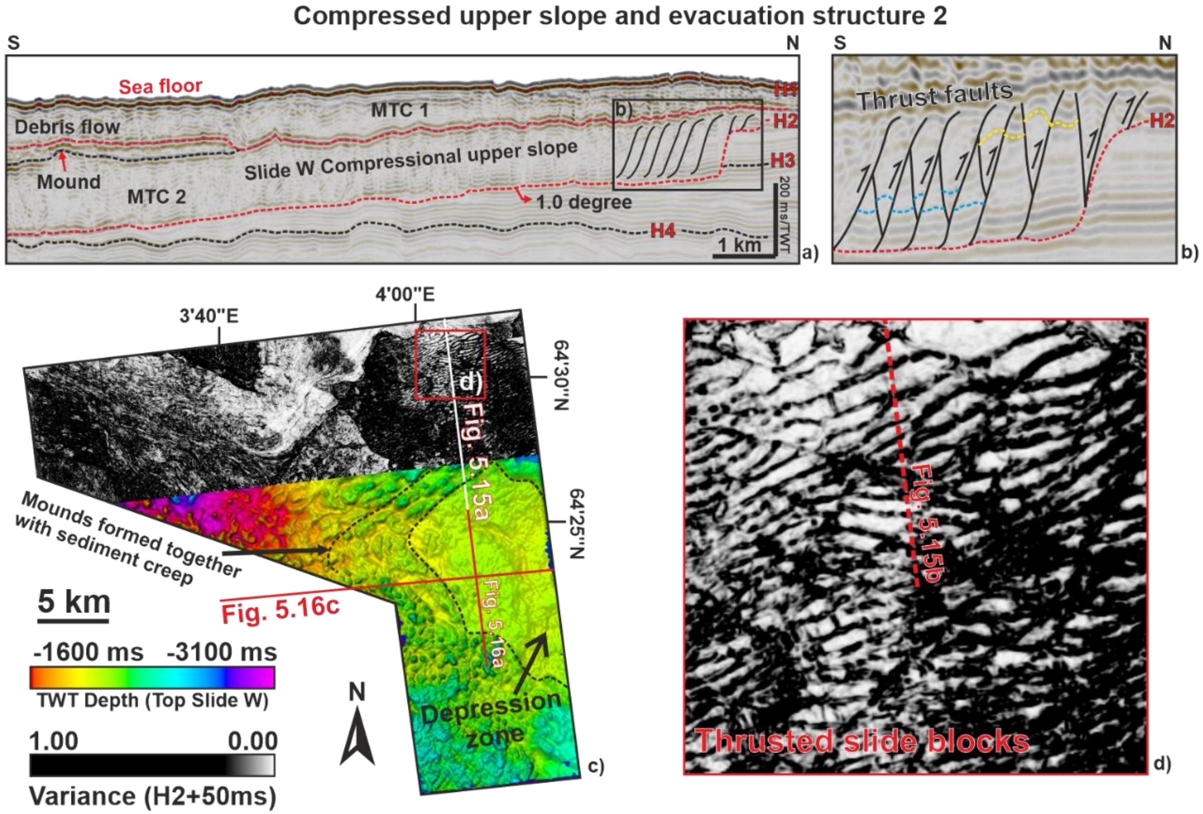

Figure 5.15. a-b) Seismic profiles across the slope (on its northern side) and above evacuation structure 2. Here, a compressed upper slope with mound and thrust faults is observed. c) Variance map of a time slice 50 ms above the glide plane (Horizon 2), covered by the relief of top Slide-W. The westward creep mounds on top Slide-W contain curved lineations. d) The compressional upper slope contains northeast-southwest blocks to the north of the depression zone, where both the top and the glide plane of Slide W show local topographic lows (see depression zone in Fig.5.15c and central crater in Fig. 5.14b).

Upslope from Evacuation Structure 2 (Fig. 5.14b), a depression herein called 'central crater' is bounded by a 100 ms (about 70 m) high scarp to the west and 200 ms high (about 140 m) scarps to the north, east and south. These scarps separate the central crater from the less faulted upper Brygge Formation (Figs. 5.16a and 5.16c). A higher terrace in Evacuation Structure 2 is observed beyond the west flank of the central crater, and comprises remnant blocks inside (Figs. 5.14b and 5.16c). Based on the internal seismic character of strata filling Evacuation Structure 2, there are at least two distinct mass-transport deposits inside this latter: a) MTC 2 fills the bulk of the Evacuation Structure, while MTC 3 occurs as a transparent package within MTC 2 (Fig. 5.16). Away from the central crater, there is no clear boundary between the upper and lower parts of MTC 2 (see the region without MTC 3 in Figs. 5.16a and 5.16c). Between the upper and lower MTC 2, MTC 3 is identified as a unit with near-transparent reflections with an irregular lower boundary (Figs. 5.16b and 5.16d). This same boundary overlies semi-coherent blocks in the lower MTC 2 (Figs. 5.16a-b). The 200 m thick MTC 3 comprises multiple zones based on its varying thickness (Fig. 5.16). Upslope on the east side of central crater, MTC 3 overlies its glide plane but a deformed unit occurs in between (Figs. 5.16c-d). This deformed unit is assumed to be a liquefied part interval in the upper Brygge Formation, while the distribution of MTC 3 is limited to the interior of the central crater (see the lateral boundary of MTC 3 in Figs. 5.15c, 5.16a and 5.16c).

Downslope from the central crater, a terrace is observed in Evacuation Structure 2 (Fig. 5.14b); the top of MTC 2 in this terrace has a blocky geometry (Figs. 5.15c and 5.16c). Although no apparent dip is observed along the bottom glide plane of MTD 2 on this terrace (Fig. 5.16c), a group of westward curved lineations is nevertheless noticed in Fig. 5.15c. There is also a positive seismic reflector beneath the bottom glide place that represents a unit of 'floating mounds' on the surface of Slide W (Fig. 5.16c), corresponding to the mounds above craters in Slide W (Riis et al., 2005). The strikes of these >1000 m wide and >100 m thick mounds vary from NE-SW to the north to NW-SE to the south, presenting curved lineations in between (Figs. 5.15c and 5.16c).

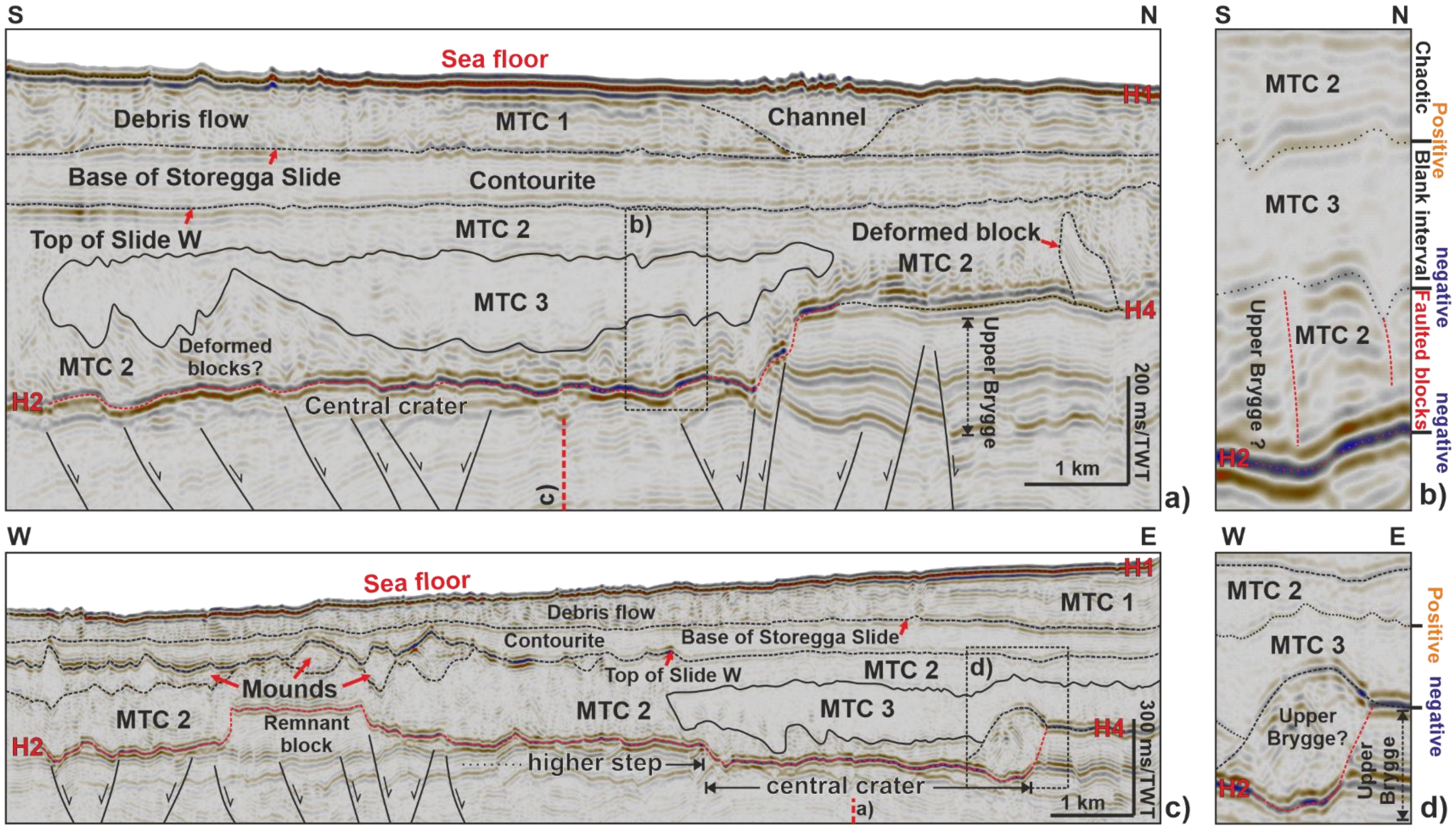

Figure 5.16. Seismic profiles across evacuation structure 2. a-b) Two MTCs are observed within this evacuation structure. The upper MTC 2 has chaotic internal reflections, whereas the lower MTC 2 contains deformed blocks. The MTC 3 in the middle covers the deformed blocks in MTC 2. c) A unit of mounds is observed on top of MTC 2. d) A deformed unit is covered right beneath MTC 3. The distribution of MTC 3 is limited to the centre of the crater in a) and c).

5.5.3 Slope instability features on the modern sea floor

On Terrace 1, where Slide R correlates with one single slope instability event, the variance maps of the sea floor and seismic reflector below reveal fault families over fluid-related pockmarks (Figs. 5.8 and 5.9). At the level of Horizon A, a positive reflector ~ 40 ms below the sea floor, several pockmarks are observed as high-variance features with circular shapes (Fig. 5.9). Similarly to the pockmarks below the Slide X and Y, their average width is about 60 m and their height is about 20 ms (Fig. 5.6d). Along with the iceberg ploughmarks observed on the mid-Norwegian margin shelf (Montelli et al., 2018), at least three ploughmarks are observed in study area on this Horizon (A) with west-east orientation (Fig. 5.9a), representing a deglaciation event that occurred at the same time. No other fractures are observed in this interval, but pockmarks occur along the Horizon A (Fig. 5.9), suggesting fluid escape features at this level are isolated and ceased their activity before the deposition of strata just below the modern sea floor (Fig. 5.13).

On the modern sea floor, en-echelon cracks are observed on the variance map as northwest-striking fractures, about 800m long and 80 m wide (Fig. 5.8b). Considering the logarithmic value of variance plotted here (see values in the colour bar in Fig. 5.8a), sea floor cracks with small variance contrast are not apparent on the interpreted seismic volume due to the resolution limits of the available dataset.

5.6 Distribution of recurrent pipes and multiple slides

Along with the recognition of multiple slope failures, including regional slides and local instability on the terraces 1 and 2 (Figs. 5.6, 5.7, 5.8, 5.10 and 5.11), recurrent pipes have been identified in Figs. 5.9 and 5.12. The spatial and temporal distribution of these pipes and slope failures across terraces 1 and 2 is shown by the bar plots in Figure. 5.13, where the relative range of pipes are marked by horizontal and vertical bold black lines separately. Following the methodology presented in Alves (2012) and Roelofse et al. (2020), and considering the resolution of seismic data in the Naust Formation, each seismic reflector represents a vertical distance of about 8 m.

A group of pipes is observed below the seafloor cracks (Figs. 5.6d, 5.8 and 5.9). The number of pipes through this Horizon A is about 15, then disappearing on the modern sea floor (Fig. 5.13). Their distribution is limited on the east side of Terrace 1 and 2, accompanying the seafloor cracks. Due to the progradation of sediment from the upper slope to the east, the number of reflectors between the relatively steep modern sea floor and the gentler Horizon A decreases from about 4 in the east upper slope to 1 in the west (Fig. 5.6a). Thus, an average number of reflectors is given as 2 between Horizon 1 and A in Fig. 5.13.

Two units with slide blocks were identified in Terrace 1 and 2, comprising Slides S and R (Solheim et al., 2005). A series of readjusted blocks were formed with Slide S before being reactivated by Slide R; the distribution of these two units of slide blocks is presented in Fig. 5.13 as green, blue and overlapping areas. Below the east part of Slide R, where the Slide S blocks were readjusted, five (5) pipes are observed along its glide plane (see the pipes along the Horizon 2 beneath Slide R in Fig. 5.13). About 15 pipes were found right below the glide plane of Slide S, focusing on its eastern part below the readjusted blocks (see the Horizon 2* beneath Slide S in Fig. 5.13). Within the strata below Slide S, the abundance of pipes increases markedly to about 100, near Horizon B. The majority of these pipes terminate in seismic reflections below the glide plane of Slide S, rather than penetrating the latter.

A similar decrease in the number of pipes is also observed in the case of Slides X and Y. Along Horizon D, i.e. the glide plane of the creeping Slide Y (Figs. 5.6c and 5.6e), Slide X and pockmarks are revealed on amplitude and variance maps (Fig. 5.11). The number of pipes affecting Horizon D is about 30, mainly focusing fluid to the east where Slides X and Y are located (Fig. 5.13). Below this horizon, the abundance of pipes sharply increases to about 130 along Horizon E, where pockmarks are also visible (Figs. 5.12 and 5.13). In addition to its focused distribution to the east, the number of fluid pipes decreases about 70 along the bottom of Slide X, representing a similar reduction in the number of pipes to what is recorded at the glide planes of Slides S and R.

5.7 Discussion

5.7.1 Evidence for slope instability preceding Slide W (~1.7 Ma)

Pipes and pockmarks have been widely observed on the shelf edge of the Norwegian margin, such as in the Nyegga, Troll, Morvin and Haltenpipe field (Hovland et al., 2010; Hustoft et al., 2009; Karstens et al., 2018). In the study area, multiple intervals with pipes and pockmarks are found within the glacially controlled Naust Formation (Fig. 5.13). Inside the Naust W unit, the oldest interval in the Naust Formation above polygonally faulted oozes, fluid flow is revealed in the form of abundant pockmarks at the level of Horizon E, and include both isolated pockmarks and other pockmarks close to faults (Fig. 5.12). Associated fluid pipes are mainly observed around 40 ms (about 28 m) above the Kai Formation, suggesting that a marked fluid escape event was triggered after the initial deposition of the Naust W unit (Fig. 5.13). Supported by the rapid disappearance of pockmarks in overlying MTCs, these putatively short-term fluid-flow pipes ceased to exist after slope failure was initiated above them (Fig. 5.13).

One possible source of excess pore pressure capable of generating hydraulic fractures and associated fluid pipes, is fluid accumulated beneath impermeable layers (Cartwright and Santamarina, 2015). Charges in the gas hydrate stability zone (GHSZ) can lead to the dissociation of gas hydrate and subsequent fluid migration to the sea floor (Crémière et al., 2016). However, these changes in the GHSZ are unlikely to be the reason for the generation of fluid pipes below Slide W, as the BSR is located well within the Naust Formation and around 300 m below the modern sea floor (Bünz et al., 2003), much deeper than the pipe identified in this study at few reflections below the Slide X and Y (Fig. 5.13). Considering that pipes and pockmarks were also observed around top of the Kai Formation, dehydration processes acting on ooze intervals and corresponding fluid migration should have occurred before Quaternary (Song et al., 2020). In addition, as the Opal A/CT transition zone imaged in the study area does not follow the modern sea floor and was locally uplifted around the SMA (Fig. 5.4), this diagenetic front was likely formed during Miocene-Pliocene tectonic compression and became inactive since that time, leaving behind a fossilised Opal A/CT transition zone (Davies and Cartwright, 2002;

Neagu et al., 2010). Even though biogenic methane from oozes could still migrate through polygonal faults and pipes (Chand et al., 2011), fluid originated from this Opal A/CT transition zone is not plausible as the main source of short-term fluid escape recorded in this study (Figs. 5.9 and 5.12).

Rapid deposition and compaction during inter-glacial periods enhanced the lithological and permeability anisotropies recorded in the study area, and thus the subsurface accumulation of fluid (Leynaud et al., 2007). On the upper part of the Storegga Slide, groups of palaeo-pipes have been identified as resulting from overpressure accumulated during maximum glaciation periods within thick debris deposits (Plaza-Faverola et al., 2011). During the last (Weichselian) inter-glacial stage, extremely high sediment loading – resulting from fast sediment progradation onto the mid-Norwegian margin - increased pore fluid pressure in the Nyegga area, leading to extensive fluid venting before the onset of the Storegga Slide (Hustoft et al., 2009). Moreover, the coexistence of ploughmarks and pockmarks along Horizon A suggests enhanced fluid flow during inter-glacial periods (Fig. 5.9). In the Gulf of Mexico, pore pressure data have shown that hydrostatic stresses near the sea floor (<200 mbsf) can rise 70% within quickly deposited impermeable layers (Flemings et al., 2008). Considering this values of stress are high enough to generate hydraulic fractures (Newton and Huuse, 2017; Rozhko et al., 2007), the fluid overflow beneath the Slide X and Y is interpreted as resulting from the rapid compaction of sediment within glacial-marine strata and corresponding build-up of excess pore pressure in near-seafloor strata.

The excess pore pressure beneath an impermeable layer can also weaken its strength, decrease the effective stress of sediment within it, and further contribute to slope instability (Leynaud et al., 2004, 2009). Above pipes and pockmarks in Horizons D and E (Figs. 5.11 and 5.12), two small-scale slides X and Y are identified in the seismic amplitude maps in Figs. 5.10 and 5.11. The oldest instability event is Slide X and contains abundant slide blocks (Fig. 5.11c). Compared to other areas, where the average of the slope is ~ 0.5^{o}, the continuous glide plane beneath MTD X reaches a value close to 1.0^{o}, comprising the steepest area of the slope in its upper part (Fig. 5.7b). Moreover, the onlap of this interval on strata below suggests there was no lateral support on the toe area before the onset of this same mass-transport deposits (Fig. 5.7b). For a submarine landslide to occur above a gentle glide plane that is <1.0^{o}, reduced support at the toe is thought to be the key conditions to its onset, promoting increases in shear stress along the glide plane (Micallef et al., 2007a). Similar to other Quaternary slides around the headwall of the Storegga Slide, the decreased effective vertical stress resulting from excess pore pressures built in particular intervals further enhanced slope instability by reducing the shear strength of sediment (see Equations 5.2 and 5.3). Consequently, the slope instability preconditioning Slide X was likely accelerated by the build-up of excess pore pressures, oversteepening of the continental slope, and the loss of lateral (and toe) support (see the slide blocks in Figs. 5.17c-d), conditions that were similar to those recorded by younger landslides such as the Naust S, R and O.

Other evidence for slope instability in the Naust W unit is recorded in the form of Slide Y (Horizon B) where cracks with less than 40 m displacement and compressional ridges show similar strikes (Figs. 5.6c, 5.6e and 5.10c). As cracks and chasms are located on the upper continental slope, while the compressional ridges are relatively lower on the slope, this Slide Y likely resulted from local sediment creep (Li et al., 2016). Contrasting with giant zones of sediment creep, in which progressive extensional and compressional structures are recorded in seismic data as a succession of deformed and faulted strata (Li et al., 2016; Saint-Ange et al., 2014), the inconspicuous offsets observed along faults and the limited height of compressional ridges observed within in the Naust W suggests short-term creep movements in the study area (Figs. 5.6c, 5.6e and 5.10c). In summary, the deformation styles of strata on the upper slope, together with their slope-parallel strikes, reveal that gravitational processes were a driving force for slope instability, but other processes must have triggered near-seafloor and short-term instability on a gentle slope with ~0.5^{o} in gradient, such as accumulated fluid through pipes and pockmarks below (see the pipes below the glide planes of Slide R, S, Y and X in Fig. 5.13).

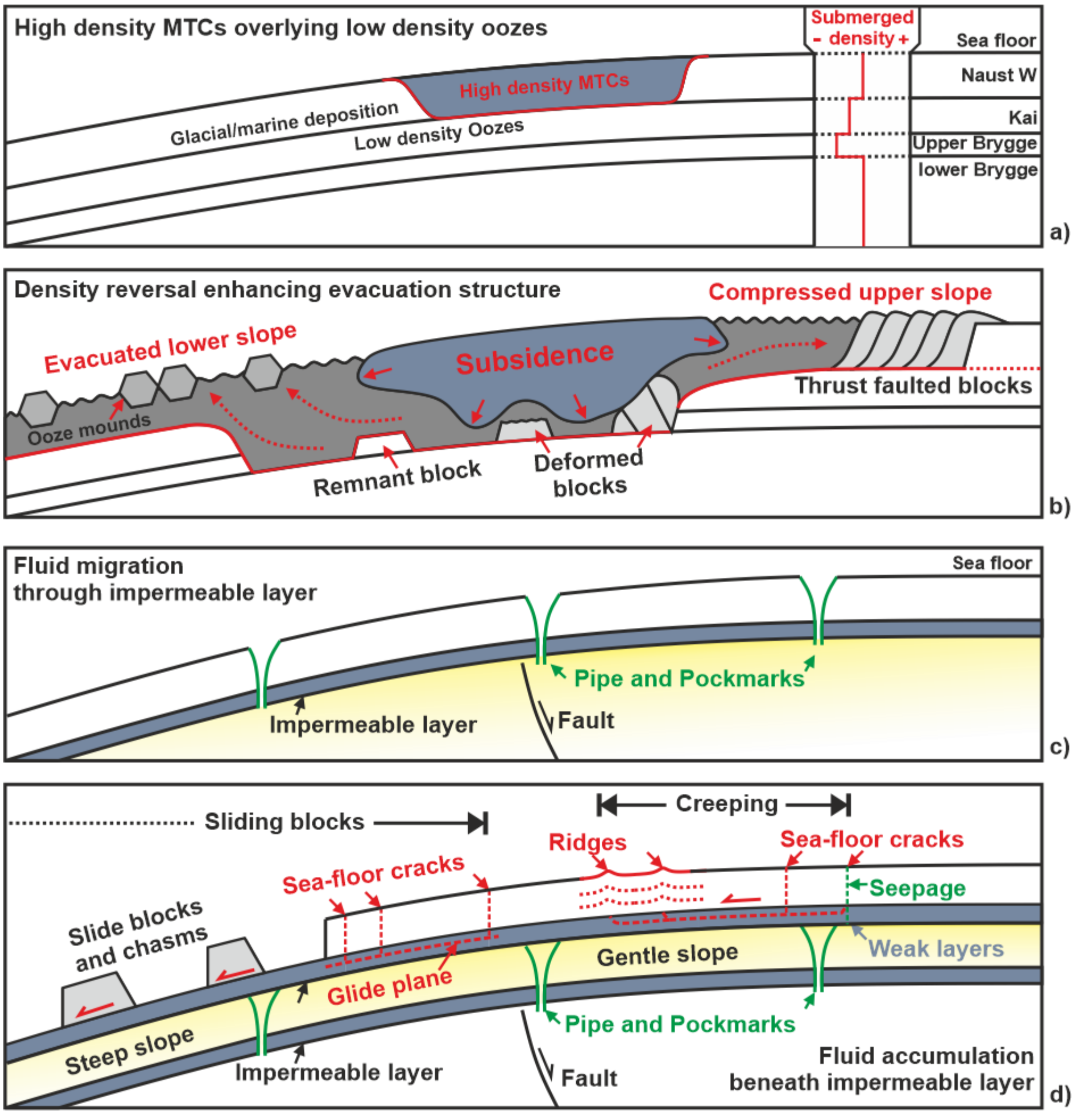

Figure 5.17. a-b) Diagram showing how density reversal generated a local evacuation structure in the study area. After a unit of high density MTCs was deposited above the low density oozes in a), strata were crushed to generate deformed and remnant blocks during the burial of this high density unit. On the confined upper slope, evacuated oozes compressed strata to form thrust faulted blocks. On the lower slope, deformed and evacuated low density oozes floated on MTCs, thus forming mounds on the palaeo-seafloor. c-d) Diagram showing the sequence of instability after a fluid escape event. Above a regional pockmark field, which records a short-term shallow fluid escape in c), the overlying interval can still accumulate fluid below (yellow interval). Build-up of excess pore pressure increases slope instability, leading to the generation of slide blocks on the slopes where lateral support is not sufficient, and causing shallow creep on a gentle slope with subsurface cracks and ridges. The propagation of the basal glide plane can further fracture the sea floor, creating seafloor cracks. These shallow seafloor cracks can evolve into fluid conduits in due time.

5.7.2 Seismic-scale features indicating slope instability on the modern sea floor

In the study area, scarp S3 limits groups of debris channels and glide planes (Fig. 5.2a). Even though near-seafloor slumps and faults between scarps S3 and S2 have been dated as occurring after the Storegga Slide above readjusted blocks of Slide R, Terrace 1 formed between scarp S2 and S1 is thought to comprise a stable part of the upper slope without any deformation features on the modern sea floor (Haflidason et al., 2005). The variance map in Fig. 5.8b shows a group of sea floor cracks on Terrace 1 without further faulting and with a fluid pipe below (Figs. 5.6b and 5.6d). Downslope, scarp S2 relates to reduced lateral support by local undercutting. In contrast to the seafloor cracks observed on shelf edge (Nyegga area), where local extension occurred as a consequence of Storegga Slide (Reiche et al., 2011), scarp S2 was originally formed during Slide S and later reactivated by Slide R, suggesting reduced lateral support is not the only reason for its formation.

Since a buried pockmark field is observed below Terrace 1, a short-term fluid escape event may have occurred before the sea floor was deformed, or fractured (Figs. 5.8, 5.9 and 5.13). Indicated by the iceberg ploughmarks on the same horizon, a deglaciation event was accompanying this short-term excess pore pressure (Fig. 5.9a). Compared with 0.5^{o} glide plane beneath the Slide Y, the gradient of the modern sea floor approaches 1.3^{o}, a similar value to the glide plane of Slide X (Figs. 5.6b and 5.7b). Such a slope gradient could further promote slope instability by inducing local changes in shear stress.

Importantly, such a slope configuration has been observed offshore northern Norway, where sea floor cracks are located on the upper slope of slide scars, sharing a same glide plane (Laberg et al., 2013). The absence of fluid-flow features (pipes or pockmarks), close to these seafloor cracks indicates that the build-up of excess pore pressure below was not yet increased so that the sediment is liquefied of locally fractured. However, if excess pore pressure continues to increase, the modern sea floor can be the locus of future slope failure (decreased shear strength by excess pore pressure in

Equations 5.2 and 5.3), such as those associated with the area of sediment creep (Slide Y) and slide blocks (Slide X) observed in Figs. 5.10 and 5.11.

5.7.3 Density reversal as a control on the development of evacuation structures

Multiple evacuation structures are observed along the bottom of Slide W in the form of local topography lows (Lawrence and Cartwright, 2010) (Fig. 5.14b). In parallel, units of coherent mounds are frequently observed above the infilling MTCs on the lower (downslope) areas of craters (Riis et al., 2005). These mounds comprise deformed ooze deposits floating on MTCs due to their lower density, representing processes occurring during the last phases of slope instability (Riis et al., 2005). Previous research has suggested the development of evacuation structures either initiated local instability after its eruption by periodic fluid flow, or was liquefied by accumulated fluid and covered by impermeable Naust Formation, contributing to a final eruption under a sliding load during Slide W (Lawrence and Cartwright, 2010). However, the existence of longitudinal remnant blocks inside crater in the study area (Fig. 5.14b), revealing the direction of slope movement, has questioned their development between the main slide event and the eruption of oozes. Contrasting with the destabilization of MTCs by the eruption of gas-saturated and low-density underlying strata, the observation of a coherent unit within MTCs and related surrounding deformation suggests a different interaction between slide and evacuation structure (Fig. 5.16).

Together with their E-W strikes, the overlapping of shortened and thrusted blocks suggests extrusion of sediment from the south and confinement to the north (Lawrence and Cartwright, 2009) (see the variance map in Fig. 5.15d and thrust faults in Fig. 5.15b). On the modern sea floor, local compression is also observed in the form of sub-parallel ridges along the southern flank of the Storegga Slide resulting from lateral compression during major slope instability episodes (Haflidason et al., 2004) (Fig. 5.1b). In this study, a local depression zone indicates the source of compression and shortening on the slope (see the relief of top of Slide W, the depression zone in Fig. 5.15c). The local creep of mounds also indicates a compression imposed from the east (see zone of sediment creep in Fig. 5.15c). However, in contrast to the southern flank of Storegga Slide where the compression zone was accompanied by run-outs of more than 400 km, the creep-related mounds on top of Slide W suggest only a limited distance of transport of a few kilometres (see the curved lineations in Fig. 5.15c). The coexistence of ridges and deformed blocks on the lower parts of the slope suggest they were formed simultaneously as the last phase of Slide W (Figs. 5.15 and 5.16).

Considering that the geometry of MTC 3 follows that of a depression below, its formation should be closely related to the observed evacuation structures (Figs. 5.15c, 5.16a and 5.16c). The top and bottom of MTC 3 are respectively positive and negative reflections when interpreted in seismic data; this character indicates MTC 3 has a higher acoustic impedance than the surrounding strata (Figs. 5.16b and 5.16d). Moreover, the formation of MTC 3 correlates with Slide W, a slope failure that removed strata from Naust W. Based on the documented density reversal of shallow sediment (Fig. 5.3), and the distribution of MTC 3 (Fig. 5.16), it is proposed that Evacuation Structure 2 in Fig. 5.14b should have firstly been covered by MTC 3, and this high-density interval (Naust W related MTC 3) sank into low-density oozes (MTC 2), which were then mixed and deformed by the overlying MTC 3 (Figs. 5.17a-b). On the upper slope, local compression has led to the formation of thrust faults between blocks that strike perpendicularly to the source of deformation (Figs. 5.15b and 5.17b). On the lower slope, this high-density unit could not only deform the lower strata to deform blocks and deform MTCs (the lower and upper MTC-2 in Figs. 5.16b and 5.16d), but also evacuate them downslope as a mixture of mass-wasted strata and creeping mounds (Figs. 5.16c and 5.17b).

Compared with the Kai Formation between Horizons 3 and 4, the upper Brygge Formation below has the lowest density of all post-rift strata (Fig. 5.3). Above the infilling MTCs as a mixture of ooze and glaciogenic derived sediments, the mounds were identified as a highly deformed but coherent unit detached from upper Brygge Formation (Riis et al., 2005). Considering that the MTC 2 contains chaotic and blocky strata, the interpreted data suggest that the lower MTC 2 is also a unit of deformed oozes (part of the upper Brygge Formation), which has stopped withdrawing (or evacuating) due to the weight of MTC 3 (Fig. 5.16b, 5.16d and 5.17b). In contrast, the deformed upper Brygge

Formation just downslope from MTC 3 contains remnant blocks that are parallel to the direction of compression described above (Fig. 5.14b).

5.8 Chapter-Specific Conclusions

As one of the largest areas of unstable sedimentary strata, the Holocene Storegga Slide complex records multiple slope failure events since the deposition of glacial-marine Naust Formation in the last 2.6 Ma. However, the initiation and current situation of this instability have not been presented in detail for the northwestern flank of the Storegga Slide. In this study, the interpretation of high-resolution seismic data from this latter area recognised two slope failure events occurring before the first regional-scale slide on the mid-Norwegian margin. Seafloor cracks also indicate a current unstable upper slope, where further failure could occur with additional instability. Main conclusions are as follows:

a) Two types of slope failure, shallow sliding blocks (Slide X) and creep (Slide Y), comprise the oldest instability events in the study area. Fluid accumulation within glacial-marine deposits should be a primary factor of this early instability phenomenon. Slope oversteepening and lack of lateral support (i.e. undercutting) could further precondition these slope failures, forming slide blocks on the steeper slopes and promoting sediment creep on the gentler upper slope.

b) Density reversal is a significant trigger of instability around the study area, especially above liquefied low-density marine oozes. The corresponding subsidence of high-density intervals into oozes can not only deform sediments below, but also compress surrounding strata into thrust faulted blocks and deformed coherent intervals, which float on adjacent MTCs forming ooze mounds.

c) A group of seafloor cracks and faults above regional pockmarks suggest an early stage of slope failure on the upper continental slope. Similar with the slides X and Y, these seafloor cracks should be preconditioned by fluid accumulated below and by the reduced lateral support of the slope during the distinct landslide events that compose the larger Storegga Slide.

d) Compared to regional slope failure events such as the Storegga Slide and Slide W on the mid-Norwegian margin, local instability is rare in the study area at present. However, older mass-wasting deposits still reveal the precondition and initiation factors causing long-term instability around the South Modgunn Arch. Through the detailed interpretation of local slope failures, regional slides and further instability can be expected on the northwestern flank of the Storegga Slide in the future.

CHAPTER SIX

Critical features and mechanisms marking long-term instability on continental slopes: Evidence from the northern flank of the Storegga Slide, Norway

6. Critical features and mechanisms marking long-term instability on continental slopes: Evidence from the northern flank of the Storegga Slide, Norway

6.1 Abstract

The Storegga Slide is one of the largest submarine landslides recorded on Earth since the last glacial maximum. Focusing on the poorly studied northern scarp of the Storegga Slide, this study uses high-quality three-dimensional (3D) seismic data and several seismic attributes, including root-mean square amplitude, structural relief, and variance maps, to investigate how weak layers, pre-existing scarps, and mass-transport complexes (MTCs) controlled long-term instability. During its retrogressive sliding process, instability along new slide scarps contributed to recurrent slope failure after the main Storegga Slide event at 7000-8200 years b.p., generating new MTCs and erosional features. By combining 3D seismic data with numerical models, the research shows that: a) deformed strata and overlying submarine channels characterise sediment creep in older MTCs, b) slide blocks can be partly remobilised after their main translation phase, leading to further faulting and sliding, c) a combination of weak layers, scarps, slope undercutting and pre-existing MTCs is key to generating new areas of slope instability. As a corollary, this work demonstrates that MTC-prone sequences are favourably predisposed to becoming areas of continental slopes with recurrent, long-term instability.

6.2 Introduction

The mid-Norwegian margin has been unstable for the last million years, comprising a number of submarine landslides such as the Storegga Slide with an age of 7000-8200 years b.p., and the relatively older Tampen Slide, R-Slide, Møre Slide and S-Slide (Bryn et al., 2003; Solheim et al., 2005). The S-Slide (500 ka) appears to have been followed by recurrent instability episodes sourced from different parts of the mid-

Norwegian continental slope (Bryn et al., 2005). Stratigraphic information indicate these recurrent landslides were chiefly triggered by climatic cycles that caused the progradation and retreat of ice sheets, associated changes in sediment supply, and gas hydrate dissociation (Berg et al., 2005; Bryn et al., 2003; Mienert et al., 2005). Hence, detailed geochronological and bathymetric data have highlighted the significance of long-term slope instability offshore of Norway (Haflidason et al., 2005, 2004).

The study area, located on the poorly studied northern flank of the Storegga Slide (between 64°11'N to 64°56'N and 3°14'E to 4°16'E; Fig. 6.1a and 6.1b), records at least two main landsliding events; the main Storegga Slide at 7000-8000 years b.p., and the Slide R dated as 300 ka old (Bryn et al., 2003; Bryn et al., 2005). Recent seismic data from the northern flank of Storegga Slide indicate that many landslide scarps coincide with pre-existing faults propagating from buried slope strata (Song et al., 2020). However, the northern flank of the Storegga Slide remains poorly documented, and evidence for recurrent mass-wasting at different scales of observation is still scarce in this part of the mid-Norwegian margin. More so, the study area is dominated by a middle Miocene antiform (south Modgunn Arch) deforming Quaternary deposits in which multiple submarine landslides have occurred (Fig. 6.1c). Although these two main sliding events can be identified above the south Modgunn Arch, instability continued as a frequent phenomenon along the Storegga Slide sidewalls between 6 to 2 ka (Barrett et al., 2021; Haflidason et al., 2005).

Multiple conceptual and numerical models have been proposed in the last few decades to explain slope instability (Bryn et al., 2005; Fell et al., 2007). Theoretical models describe the onset of slope instability by considering pre-conditioning factors such as the presence of weak layers, fluid migration, excess overburden loading, high pore pressures, etc. (Bromhead, 2013; L'Heureux et al., 2013; Quinn et al., 2011). In parallel, numeric models have allowed the detailed analysis of the parameters controlling the onset and subsequent development of submarine landslides (Breard et al., 2019). In order to investigate the mechanisms, source areas and nature behind this long-term slope instability, 3D seismic and borehole data are interpreted here and used to complete a Computational Fluid Dynamics approach (CFD) to characterise near-seafloor strata. The focus of this chapter is on understanding the role of weak layers and pre-existing fractures, such as faults and slide scarps, as capable of concentrating local deformation. The scenarios modelled in this work are important as they consider different predisposing factors in slope instability such as physical properties of strata, pre-existing fractures, weak layers, and slope undercutting. The results of this work can, therefore, be applied to submarine landslides across the world. In summary, this chapter addresses the following research questions:

a) What near-seafloor depositional features are indicators of long-term slope instability on continental margins?

b) How can pre-existing fractures, such as slide blocks and scarps, be used as evidence for multiple, successive events of slope instability?

c) To what extent do certain near-seafloor structures preferentially concentrate local deformation to precondition recurrent mass wasting?

6.3 Geological Setting

6.3.1 Evolution of the South Modgunn Arch, mid-Norwegian margin

The study area is located on the northern flank of the Storegga slide, mid-Norwegian margin, between 62°N and 70°N, and separates the Vøring and Møre basins (Fig. 6.1a). Slope instability around the Storegga Slide results from multiple factors, including the presence of multiple weak layers, fault activity, the build-up of pore pressures in slope sediment, increases in the shear stress imposed on near-seafloor strata, sediment loading, and earthquakes (Barrett et al., 2021; Leynaud et al., 2009; Masson et al., 2006). The base of the Storegga Slide comprises multiple weak layers dipping gently oceanwards (Haflidason et al., 2004; L’Heureux et al., 2013). The low shear strength of these weak layers results from the presence of pelagic oozes and marine deposits with low permeability, which hinder fluid migration and locally increase pore pressures (Lawrence and Cartwright, 2009; Urlaub et al., 2018). Rapid deposition of sediment during interglacial periods and the concomitant accumulation of contourite units further

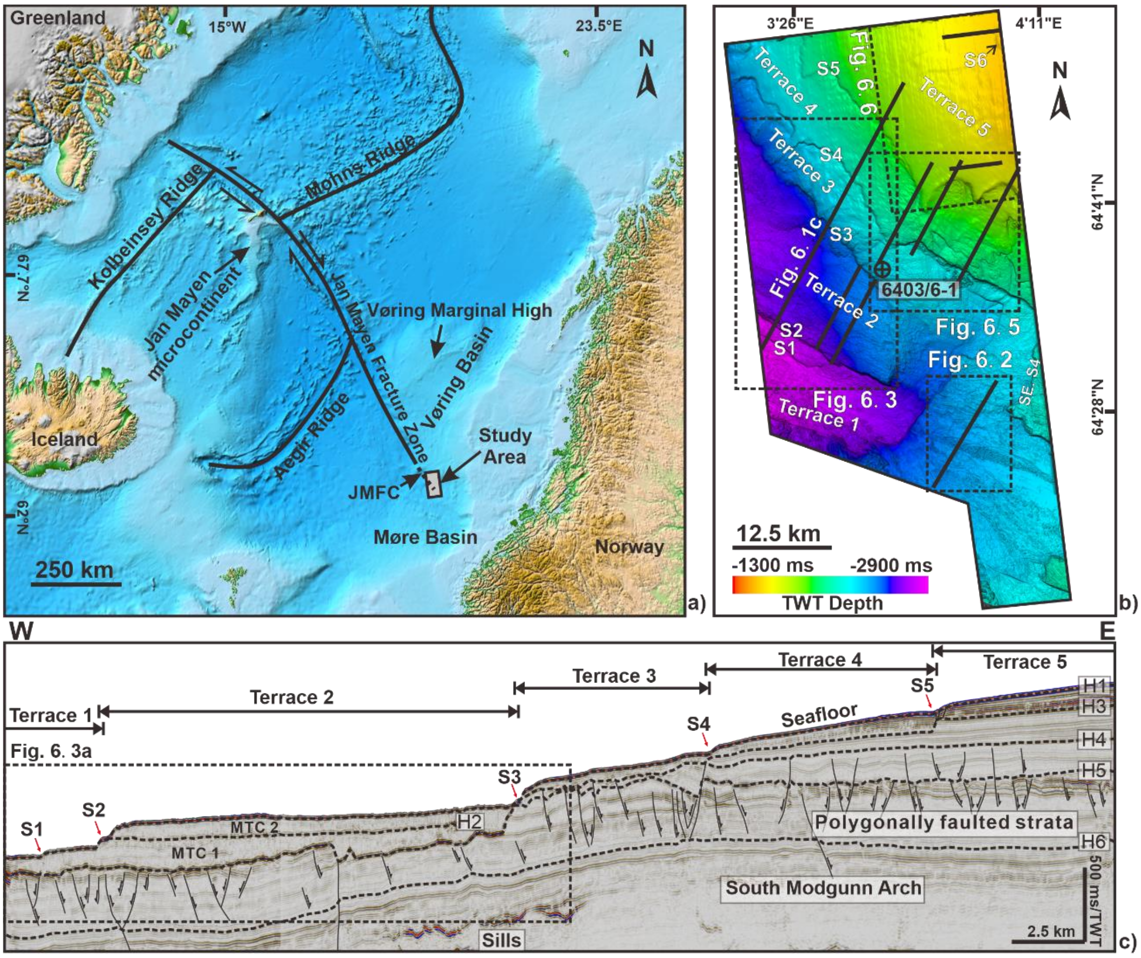

Figure 6.1. Location and structure of study area. a) Bathymetric and topographic map modified from ETOPO1, NOAA National Geophysical Data Center, showing the location of the study area on the mid-Norwegian margin between the Vøring and the Møre basins. b) Detailed two-way time (TWT) structure map of the sea floor. Highlighted by the black lines and rectangles are the four areas and five seismic profiles discussed in this thesis. c) Seismic profile crossing all the terraces in the study area. Location is shown in Fig. 6.1b. H1: sea floor; H2: inner glide plane between MTCs; H3: bottom glide plane of MTC 1; H4: top of the Kai Formation; H5: top of the Brygge Formation; H6: top of the Tare Formation, forming the ‘basement’ unit inside of which no slope instability features are observed in seismic data.

contributed to increasing overburden and pore pressures around the modern Storegga Slide, promoting slope instability in multiple areas (Bryn et al., 2005; Laberg and Camerlenghi, 2008; Pope et al., 2018).

The morphology of the Storegga Slide has been related to the landslides initiating on the middle to lower slope regions before retrogressing in an upslope direction (Baeten et al., 2013; Bryn et al., 2003; Haflidason et al., 2005, 2004; Kvalstad et al., 2005a). In parallel, slide blocks were formed after the release of lateral support (undercutting) on the continental slope (Kvalstad et al., 2005a; Micallef et al., 2009). Landslide deposits and slide blocks are observed above multiple and single glide zones, representing variable mechanisms of slope instability (Barrett et al., 2021).

6.3.2 Lithostratigraphy

Based on data from exploration well 6403/6-1, the lithostratigraphy of the study area can be divided into a breakup sequence forming the sub-Storegga 'basement' strata (i.e. below horizon H6, Fig. 6.1c), that has not been deformed by slope instability processes, and post-breakup units above. The recurrent landslides investigated in this work occur in post-breakup strata between horizons H1 and H6, including the Brygge, Kai and Naust formations (strata above H6 in Fig. 6.1c). Post-breakup strata are unstable and were partly remobilised by submarine landslides (Figs. 6.1c, 6.3a-6.3c, 6.5a-6.5c). The Kai and Brygge formations (respectively between horizons H4-5 and H5-6; Fig. 6.1c), Late Eocene to Late Pliocene in age and deposited above the breakup sequence, are composed of marine claystone with intervals of sandstone, siltstone, limestone, and marl. Biogenic ooze, with relatively high porosity and water content when compared with clay or sand, predominates in these units (Lawrence and Cartwright, 2010). The undrained density of the Brygge Formation reaches 1400 kg/m^3 in well 6403/6-1. Lowered shear strengths of oozes, and corresponding slope instability, have been recognised by Pittenger et al. (1989) based on Ocean Drilling Program measurements on cores, and in regional seismic data (Davies and Clark, 2006; Pittenger et al., 1989).

The upper Pliocene to Holocene Naust Formation comprises the youngest sediments in the study area and glaciomarine deposits influenced by short sea-level fluctuations (Berg et al., 2005). Along the mid-Norwegian margin, multiple submarine landslides occur within the Naust Formation (Solheim et al., 2005). At least two slope instability events have occurred around the south Modgunn Arch; the MTCs 1 and 2 in Figs. 6.1c, 6.2a, and 6.3a-6.3c. Previous research has indicated that MTCs in the study area were sourced from the upper continental slope, where the Naust Formation was remobilised *en masse* (Haflidason et al., 2005, 2004). Hence, the physical properties of MTCs used in the modelling are based on well-log data from the Naust Formation, which reveals an average density of 1850 kg/m^3 (Song et al., 2020). In parallel, the *Biot's ratio* (α) of shallow sediment on the mid-Norwegain margin varies between 0.95 and 1.00 (Lothe et al., 2004). Together with an ocean water density between 1000 and 1060 kg/m^3 (Pawlowicz, 2013), an average *submerged density* of the Naust Formation at 900 kg/m^3 is therefore calculated by Equation 6.3 and used in the numerical modelling.

6.4 Data and methods

6.4.1 Seismic interpretation

This work uses time- and depth-migrated 3-D seismic data from the mid-Norwegian margin, together with information from one exploration well (6403/6-1; Fig. 6.1b). The seismic data cover 263 km^2 of the northern flank of the Storegga Slide, over the south Modgunn Arch (Figs. 6.1a and 6.1b). The central part of this arch was drilled at well 6403/6-1, which provided lithostratigraphic and wireline information such as formation tops, depth and bulk density. Dates for seismic stratigraphic units are therefore based on seismic-well ties and published information for the Norwegian margin (Berg et al., 2005; Bryn et al., 2005a; Forsberg and Locat, 2005; Kjoberg et al., 2017).

Seismic interpretation used Schlumberger Petrel® and included local structural and stratigraphic analyses to extract 3-D subsurface data and relevant seismic attributes. In order to visualise the multiple MTCs and structures, RMS amplitude, two-way time (TWT) structure and variance maps were computed for key geological features and seismic horizons. TWT structure maps are based on the mapping of the sea floor (horizon H1) and an internal glide plane (horizon H2 and H3) (Figs. 6.1-6.6). Slide scarps, faults,

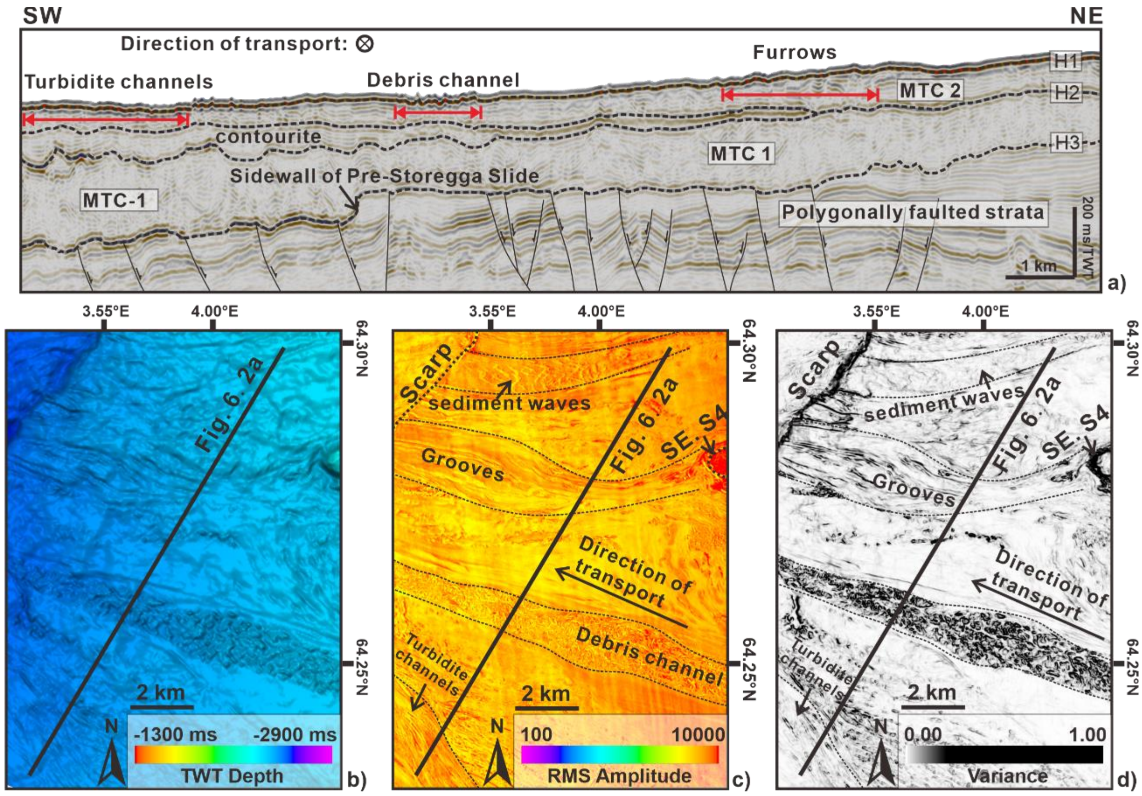

Figure 6.2. Example of submarine channels in the study area. a) Seismic profile showing typical turbidite and debris channels on the upper continental slope. Location is shown in Figs. 6.1b and 6.2b-6.2d. MTC 1 was formed before the main stage of collapse of the Storegga slide, probably in association with the ‘R slide’ (Bryn et al., 2003; 2005). b) TWT structure map of the sea floor (H1). The grooves and sediment waves inside turbidite channels help distinguish them from debris channels, which present a rugged internal character. Location of this TWT structure map is shown in Fig. 6.1b. c) RMS amplitude map of the sea floor (H1). The chaotic aspect of strata inside debris channels contrasts with that of turbidite channels, which are smoother and show lineations within them. d) Variance map of the sea floor (H1). The chaotic and high variance of debris channels are indicative of their presence on the sea floor.

slumped strata, and submarine channels are features with high variance and high RMS amplitude (Figs. 6.2c, 6.2d, 6.3e and 6.3f) whereas small-scale MTCs comprise high-relief, low-variance features (Figs. 6.3d, 6.3f, 6.5d and 6.5e). Based on the geometry of channels, furrows and blocks, sinuosity, size and orientation data were gathered and plotted in Fig. 6.7.

6.4.2 Numerical Modelling

As one of the major offshore geohazards, submarine landslides often comprise a failed volume of strata affected by internal softening and liquefaction before evolving into debris and turbidity flows during their downslope movement (Boukpeti et al., 2012). Considering that the study area is located near recurrent submarine landslides and multiple scarps (Bryn et al., 2003) (Figs. 6.1 and 6.2), ANSYS Fluent® is used in this work as the CFD modelling tool for the numerical simulation of the initial sliding processes occurring on the continental slope after it was undercut. The clay-rich Naust formation, including failed intervals and associated weak strata, or layers, are modelled as non-Newtonian fluids. In the CFD models, strata (non-newton fluid) are modelled as an Eulerian material using a finite-volume technique. All boundaries between walls and fluid are defined as no-slip boundaries. In addition, momentum and mass transfer processes are modelled by solving the Navier-Stokes equations and additional transport equations. In ANSYS Fluent®, different instability scenarios are set as 2D planar models with laminar flow. This work considers four main scenarios – Scenarios 1 to 4 – to explain slope instability features in the study area.

The reduction of shear strength (τ_y) during initial sliding and run-out is modelled as a function of accumulated plastic shear strain (ξ). According to De Blasio et al. (2005), Dutta et al. (2018) and Einav and Randolph (2005), this strain-softening process is expressed by Equation 6.1 below:

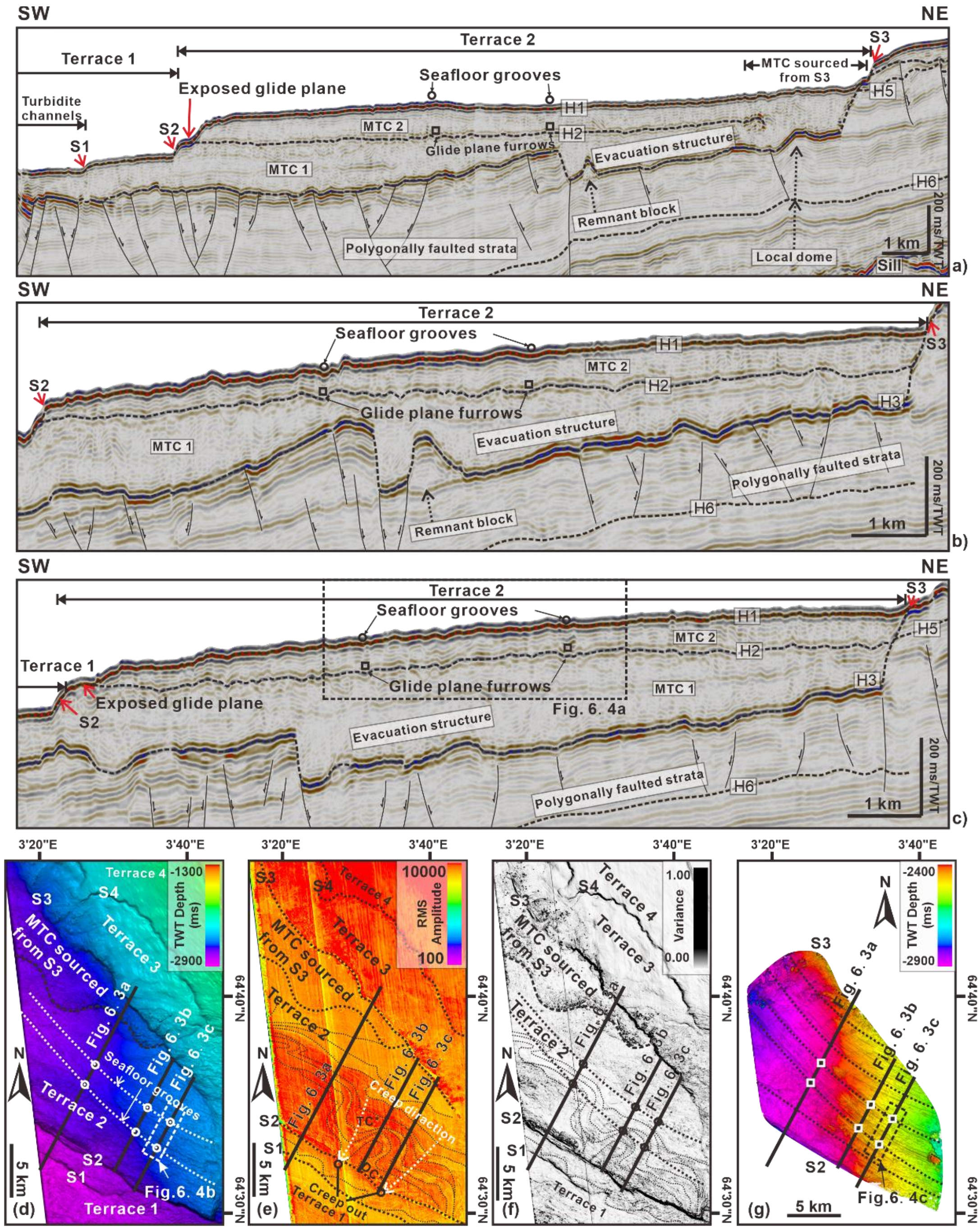

Figure 6.3. a-c) Seismic profile crossing Terrace 2. The location of furrows on the glide plane of MTC 2 and seafloor grooves are marked by circles and rectangles in the seismic line. Their location is shown in Fig. 6.3d. d) TWT structure map of the sea floor (H1). A group of northwest-southeast grooves is identified on the sea floor and marked by a white dashed line. e) RMS amplitude map of the sea floor (H1). Deformed submarine channels are distinguished by their amplitude. Sinuosity is higher here because of internal creeping of MTC 2, which occurred after scarp S2 was formed. f) Variance map of the sea floor (H1). Both channels and curved submarine lineations are shown by high variance values. g) TWT structure map of the inner glide plane (H2) between MTCs 1 and 2.

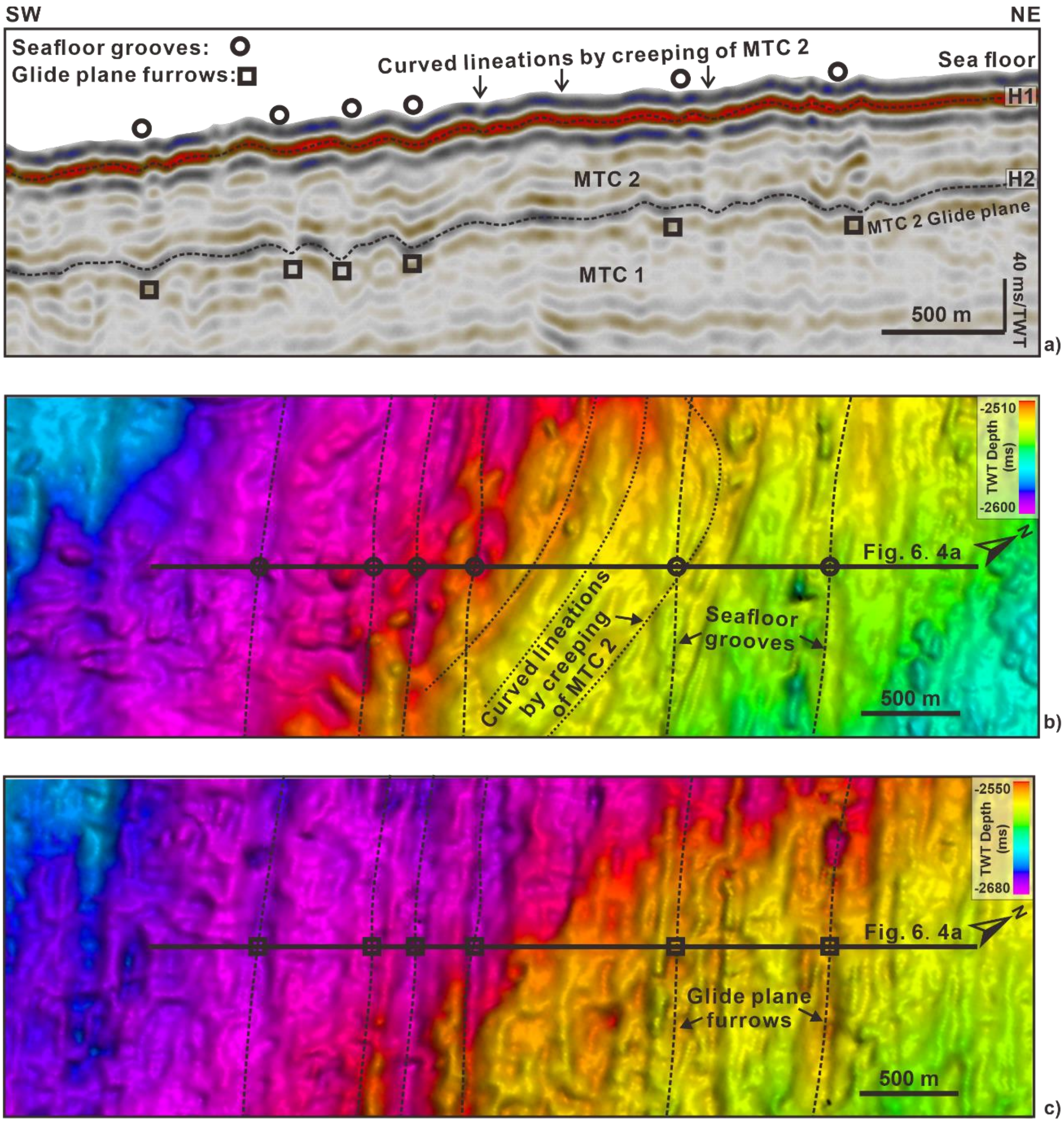

Figure 6.4. Figure showing a comparison between grooves, observed on the sea floor, and furrows, which are developed on the glide planes of MTCs. a) Enlarged seismic profile taken from Fig. 6.3c. The sea floor grooves are marked by black circles, and the glide plane furrows are highlighted by the black rectangle. b) and c) Relief maps of the sea floor (horizon H1) and the glide plane of MTC 2 (horizon H2). The distribution of grooves and furrows are represented as local depression on the sea floor and glide plane. The same location and geometry between these two groups of lineaments suggests differential compaction has occurred since MTC 2 was deposited.

$$\tau_y = \begin{cases} \left[\frac{1}{S_t} + \left(1 - \frac{1}{S_t}\right) * e^{-3\xi/\xi_{95}}\right] * S_{up}\,; & \boldsymbol{if}\ \xi \leq \xi_{95} \\ \left[S_{u95} - \frac{\left(S_{u95} - \tau_{y(ld)}\right)(\xi - \xi_{95})}{\xi_{ld} - \xi_{95}}\right]\,; & \boldsymbol{if}\ \xi_{95} < \xi \leq \xi_{ld} \\ \tau_{y(ld)}\,; & \boldsymbol{if}\ \xi > \xi_{ld} \end{cases}$$

Equation 6.1

where τ_y = Mobilised shear strength;

S_t = Sensitivity. The ratio of intact undrained shear strength to remolded undrained shear strength;

ξ = Accumulated plastic shear strain;

ξ_{95} = Value of accumulated shear strain where 95% of soil strength is reduced;

S_{up} = Peak undrained shear strength of soil;

S_{u95} = Undrained shear strength of soil at ξ_{95};

$\tau_{y(ld)}$ = Large-strain shear strength with shear wetting

ξ_{ld} = Shear wetting parameter

During the strain-softening process, decreases in the shear strength of a failed mass are represented by the *strength ratio* (τ_y/S_{up}). However, ANSYS Fluent® does not provide an option to define accumulated plastic shear strain (ξ), a parameter further controlling the shear strength of the failed material (τ_y in Equation 6.1). To set an initial shear strength that increases with depth, and track the strain accumulated during downslope sliding, modelling approach in this chapter included the additional transport equations proposed by Dutta and Hawlader (2019):

$$\frac{\partial}{\partial \mathrm{t}}(\rho\phi) + div(\rho\phi\boldsymbol{u}) = div(\Gamma gard\phi) + S_\phi$$

Equation 6.2

where ρ is the density of the flowing material, assumed as the *submerged density* of strata in this study, $\boldsymbol{u}$ is the velocity vector, and Γ is the diffusion coefficient, which has been set as zero as the diffusivity of strain is neglected in this study. In Equation 6.2, S_{ϕ} is a source term representing the increase of strain in each time step. Accordingly, the variable ϕ is equal to the accumulated strain (ξ) that will be imported to Equation 6.1 to update the mobilised shear strength (τ_y).

The parameter *Submerged density* (ρ_e) follows Equation 6.3 below:

$$\rho_e = \rho_{sat} - \alpha\rho_w$$

Equation 6.3

where

ρ_{sat} = density of water-saturated rock

ρ_w = density of water

α = Biot's ratio

The shear behaviour of multiphase Eulerian materials is defined using the dynamic viscosity (μ_d). Except for the air (which as a default setting on the modelling package), failed strata are modelled in ANSYS Fluent® as a visco-plastic non-newton fluid in which μ_d is defined as $S_u/\dot{\gamma}$, with $\dot{\gamma}$ being the strain rate; and S_u representing the shear strength (τ_y) of the failed material that is calculated from Equation 6.1 (Dutta et al., 2018). To ensure the numerical stability during very small deformation events, the minimum value of $\dot{\gamma}$ in this study is set as 0.0001. Further discussion on this modeling approach adopted in this work is available in (Debnath, 2018; Dutta et al., 2018; Dutta and Hawlader, 2019).

6.5 Diagnostic features marking long-term slope instability

6.5.1 Local physiography

Located on the northern flank of the Storegga Slide, the study area was sub-divided into five terraces delimited by multiple scarps (Terrace 1 to 5, and scarps S1 to S6 in Fig. 6.1b). Relief in these terraces varies from the L-shaped Terrace 1 to a smooth sea floor in Terrace 5, further upslope (Fig. 6.1c). Multiple MTCs are observed inside these terraces. MTC 1, which is exposed on the sea floor in Terrace 1, but covered by MTC 2 in Terrace 2, reveals multiple furrows on its upper surface (Fig. 6.3g). Similarly the top boundary of MTC 2, which coincides with the sea floor in Terrace 2, comprises multiple seafloor grooves and submarine channels (Figs. 6.3d-6.3f). There is also evidence for local slides derived from ocean-dipping slide scarps (MTCs sourced from scarps in Figs. 6.3d-6.3f, 6.5d and 6.5e).

Two intervals, containing the Unit 1 and 2 slide blocks separately, are identified beneath the smooth sea floor of Terraces 4 and 5 (Figs. 6.5 and 6.6). Slide blocks in Unit 1 are located in Terrace 4 and draped by a contourite interval. Here, local folds and fractures are developed above these slide blocks (Figs. 6.5a, 6.5d and 6.5e). Several secondary slides are also recognised above these folds, accompanying local scarps and channels (see scarps S4.1 to S4.4 in Figs. 6.5c and 6.5e). In Terrace 5, slide blocks within Unit 2 are faulted and covered by undeformed strata (Figs. 6.6c and 6.6d). Based on the scale and orientation of these blocks, Unit 2 can be roughly divided into northern and southern parts (Fig. 6.6b). Additionally, several glide planes are recognised underneath the MTCs and associated slide blocks (Figs. 6.5a-6.5c). These basal glide planes, or zones (Alves, 2015b) formed at different levels and their relative depths and correlate with changes in the geometry of the overlying slide blocks (Figs. 6.5b and 6.5c).

6.5.2 Slumping of older, pre-existing MTCs

On the northern flank of the Storegga Slide, a predominant NW-direction of sediment transport is revealed by grooves on the sea floor (Haflidason et al., 2004). Submarine channels are also aligned in this direction and form linear erosional features

(Figs. 6.2b-6.2d). Their sinuosity is about 1.02, showing they are barely curved features (Fig. 6.7a). Here are distinguished two types of submarine channel - debris and turbidite channels - based on their internal character. The multiple grooves and sediment waves observed inside these turbidite channels distinguish them from the debris channels, which contain chaotic debris with high variance coefficient (Figs. 6.2b-6.2d). The seismic profile in Fig. 6.2a shows two MTCs beneath such grooves, with relative chaotic seismic reflections inside (e.g. MTCs 1 and 2 in Figs. 6.1c, 6.2a, 6.3a-6.3c, and 4a).

Debris channels in Terrace 2 show a complex geometry and are bounded by slide scarps to the north and south (S2 and S3 in Figs. 6.3a-6.3c). In this area, a group of relatively straight grooves are NW-striking (see the straight dash line ‘Seafloor grooves’ on Terrace 2 in Figs. 6.3d, 6.3f and 6.4b). At the same time, a group of curved features overlap those straight grooves, likely comprising deformed slope strata, including fragments of older debrites likely deposited by debris channels (see the sinuous line in Figs. 6.3e, 6.3f and 6.4b). The structural map of horizon H2, imaging the glide plane between MTC 1 and MTC 2, also shows a group of straight furrows with a sinuosity approaching 1.01 (Fig. 6.7a). Compared to the straight channels and grooves shown in Figs. 6.2c, 6.2d, 6.3d and 6.3f, curved strata – including evidence for older submarine channels - show an average sinuosity of 1.18 (Figs. 6.3e, 6.3f and 6.7a). This suggests the older submarine channels were deformed after the gravity flows that generated them.

Slope undercutting in Terrace 1 indicates that scarp S2 separating Terrace 1 from Terrace 2 was formed after the deposition of MTC 2, deforming any previous grooves and channels crossing this latter MTC. Geochronological dating from sediment cores have revealed that the main landslide deposits resulting from the undercutting of Terrace 1 belong to a younger instability event originated on the northern flank of the Storegga Slide (Haflidason et al., 2005). The changing depth and inner structure of MTCs around scarp S1 suggest the occurrence of multiple landsliding and erosional events after Terrace 1 was undercut. The collapse of strata around scarp S3, and its corresponding MTC, are shown in Terrace 2 by their higher relief and variance coefficients (Fig. 6.3d). There are no linear features inside this MTC.

6.5.3 Slide blocks

Submarine spreading around the headwall of the Storegga Slide is recorded as an interval with slide blocks (Kvalstad et al., 2005a). This gravity-driven sliding process was triggered by a loss of lateral support on the continental slope (undercutting), overloading, and build-up of pore pressure (Baeten et al., 2013; Bradley et al., 2019). Above a glide plane, the tops of the less deformed slide blocks are oriented perpendicular to their direction of movement (Micallef et al., 2016). In the study area, at least two intervals with slide blocks (Units 1 and 2) are associated with Slide R and draped by a contourite interval (Figs. 6.5a - 6.5c). Beneath the sea floor in Terrace 4 (above Unit 1), the interior of the slide blocks is increasingly chaotic downslope from scarp S5 (Figs. 6.5a - 6.5c). These blocks were detached above multiple weak layers (their glide planes follow different weak layers on both sides of ‘cross points’ in Figs. 6.5b and 6.5c) and become smaller in a downslope direction (blocks 6-1 in Fig. 6.5b), having been further disrupted to form debrites (Figs. 6.5a and 6.5b). Above the deeper glide plane (horizon H3), most blocks shown on the variance time slices are arcuate (blocks 6-1, included in Fig. 6.5b, in Fig. 6.5f). These blocks are spaced 1000-2000 m apart and up to 80 ms high (Figs. 6.5a-6.5c). The length (L) of the blocks varies from 800 m to 3600 m, and their width (W) ranges from 200 m to 600 m (Fig. 6.7b).

Due to differential compaction, the strata above the blocks developed folds that generate seafloor relief (local folds in Fig. 6.5d). Some of these positive features also accompany areas with high variance, particularly where faults propagate to the sea floor from the tops and flanks of the slide blocks (faults on folds as high variance on the sea floor in Figs. 6.5a and 6.5e). Several small-scale slides are sourced from scarp S5 (Figs. 6.5b, 6.5d and 6.5e). Beneath an exposed glide plane, there is a group of faults linking this glide plane to slide blocks underneath (faults between headwall area of local slide and blocks’ ridges in Fig. 6.5b). Multiple failure events are also revealed by MTCs sourced from scarp S4, where overlapping channels of high relief and variance occur above Terrace 3 (Figs. 6.5b-6.5e). The source of these turbidite flows can be tracked to secondary scarps in Terrace 4 (S4.1 to S4.4 in Figs. 6.5c and 6.5e), which are located above the downslope side of features with positive relief formed by differential compaction above slide blocks (Blocks 1 to 4 in Fig. 6.5c).

6.5.4 Gravitationally-spread slide blocks

Slide blocks in Unit 2 reveal variable geometries (Fig. 6.6). Contrasting with the large blocks and chasms in Terrace 4 (Unit 1), the slide blocks in Terrace 5 (Unit 2) are relatively small (see the blocks on both sides of S5 in Fig. 6.5f). These blocks are closely attached and up to 80 ms tall (Unit 2 slide blocks in Fig. 6.5a and 6.5b). The length (L) of blocks varies from 800 m to 3600 m, and their width (W) ranges from 200 m to 600 m (Fig. 6.7b). To the north, close to their source at scarp S6 (Fig. 6.6b), the dominant strike of slide blocks approaches a N-S direction, whereas chasms show secondary NW-SE and NE-SW directions (Figs. 6.6c and 6.7d). To the south, disrupted blocks reveal polygonal chasms striking to the NW along scarp S5 (Figs. 6.6d and 6.7c). Blocks to the north show greater length-width ratios without an obvious change in width (Fig. 6.7c).

6.6 Numerical modelling

The existence of slope undercutting has been revealed by the multiple scarps interpreted in seismic data (Figs. 6.1b and 6.1c). In parallel, the gentle glide plane at horizon H3 matches the level of stratified beds on the intact upper slope (Fig. 6.1c), suggesting the presence of weak layers at the broader, regional scale, on the mid-Norwegian margin (L'Heureux et al., 2012). Geochronology and physical property data show these weak layers correlate with the presence of marine clays deposited during interglacial stages, with high clay content and lower shear strengths, where clay content increase from 30-40% in glacial deposits to 50-60% in marine clay, while shear strength decreased by around least 20% (Bryn et al., 2003; L'Heureux et al., 2013). The blocky detached intervals above represent stiffer glacial deposits with relatively lower clay content (Berg et al., 2005; Solheim et al., 2005). Considering that weak layers offshore Norway have varying thicknesses, varying from centimetres to meters (Kvalstad et al., 2005b; L'Heureux et al., 2012), a single negative seismic reflector is within the seismic resolution limits of the Naust Formation (Roelofse et al., 2021). Thus, in the models completed in this thesis, weak layers are considered as 8-m thick marine clays (Fig. 6.8c). In parallel, each failed interval (Units 1 and 2; Figs. 6.5a and 6.5b) is about 70-m thick.

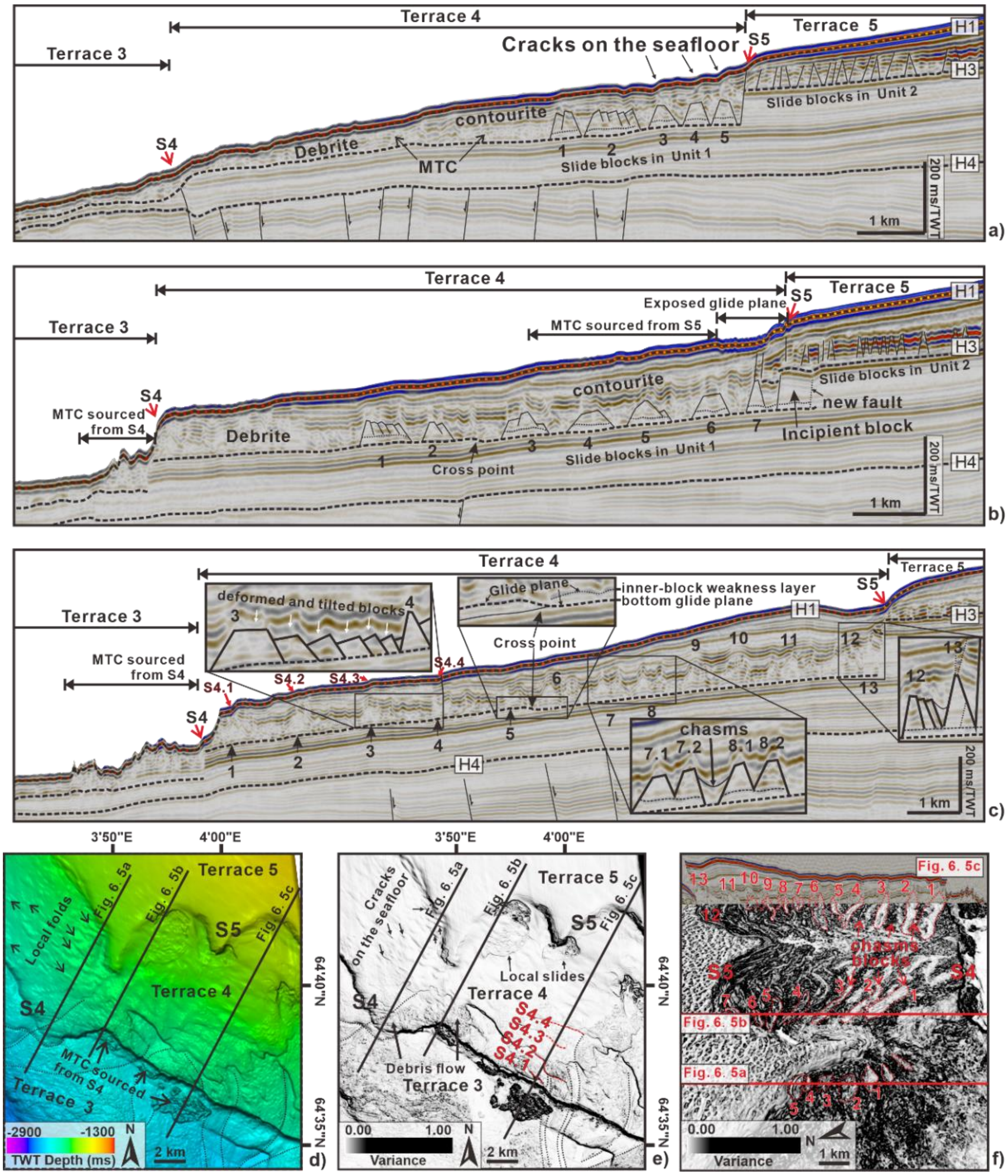

Figure 6.5. a-c) Selected seismic profiles across Terrace 4. Slide blocks in Unit 1 are draped by a thin interval of contourites, and differential compaction in these same contourite deposits generated small-scale folds above blocks. Due to a loss in lateral support (undercutting) on the continental slope when the Storegga Slide occurred (7,000-8,000 years b.p.), slope failure was resumed along scarps and folds generating local MTCs, secondary scarps (S4.1- S4.4) and faults. d-e) TWT structure and variance maps of the sea floor (H1). The location of these maps is shown in Fig. 6.1b. Local folds above slide blocks are observed as local seafloor highs (see Fig. 6.5d). Faults on folds are high-variance features in Fig. 6.5e. f) 3D view of a variance slide extracted 50 ms above the bottom glide plane of the slide blocks (horizon H3). The locations of profiles a-c are shown by the red lines in Fig. 6.5f. Slide blocks in Units 1 and 2 are separated by scarp S5.

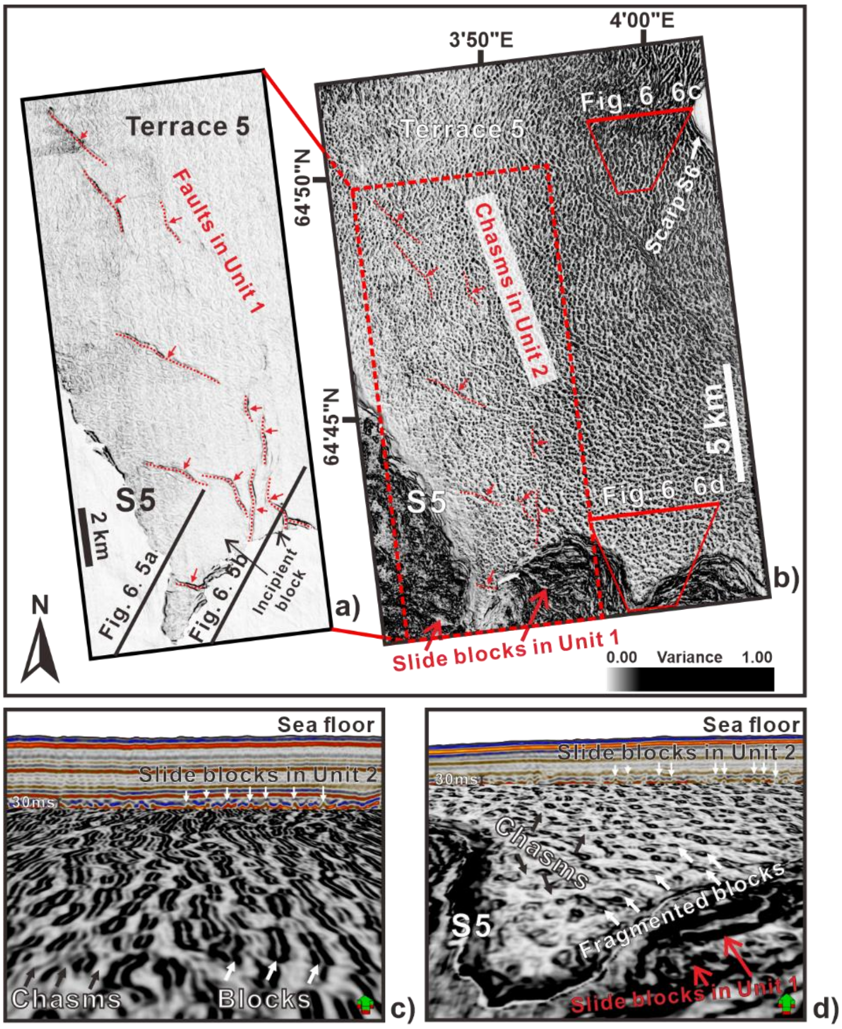

Figure 6.6. a) Variance maps of the bottom glide plane (horizon H3) of slide blocks in Unit 2. b) Variance map of 50 ms time-slice above H3 (H3-50ms). Faults in Unit 1 (Fig. 6.5b) are located along the glide plane (H3) and inside the slide blocks in Unit 2 (H3-50ms), forming chasms in between discrete blocks. c-d) Comparison between blocks near the headwall and sidewall of Unit 2. The locations of the two areas are marked in Fig. 6.6b. Close to the headwall (S6) in the Fig. 6.6c, longitudinal blocks are shown as narrow low variance features. Slide blocks nearer the sidewall (S5) of Unit 2 have smaller sizes and irregular shapes in Fig. 6.6d.

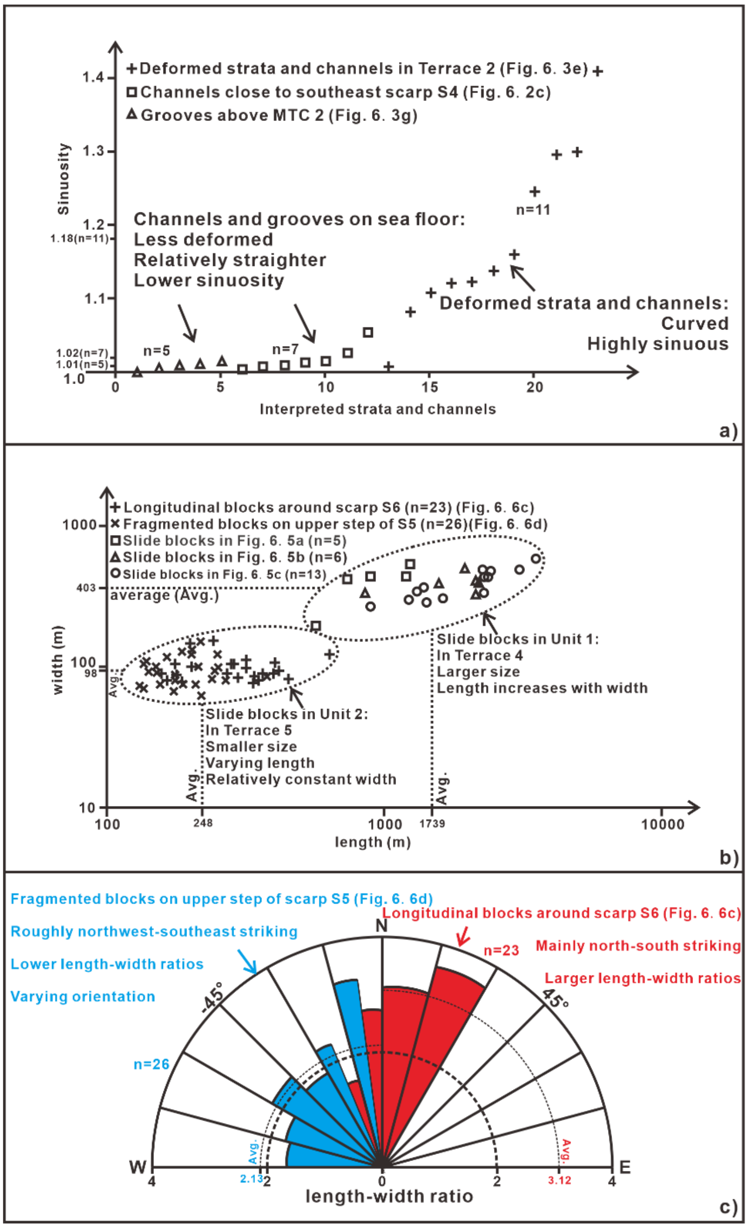

Figure 6.7. Higher sinuosity and length-width ratio resulting from the deformation of MTCs. a) Sinuosity of deformed strata and submarine channels. The initial channels, slope strata and accompanying grooves show very low sinuosity. However, submarine channels in Terrace 2 are markedly sinuous because of sediment creep occurring after the continental slope was undercut. b) Geometrical data for slide blocks in Units 1 and 2. Blocks in Unit 1 are larger in Terrace 4, where they are on average 1739 m long and 403 m wide with a positive correlation. Slide blocks in Unit 2 are, in Terrace 5, 248 m long and 98 m wide on average, showing no clear correlation. c) Geometry and orientation of slide blocks in Unit 2. Longitudinal blocks around the headwall have a larger length-width ratio (3.12) and strike roughly in a north-south orientation. The highly fragmented blocks around scarp S5 have a relatively low length-width ratio (2.13) and were rotated in a northwest-southeast direction, along the strike of the scarp.

Based on published sediment core data, the initial strength of glacial deposits was set as 25 kPa at the sea floor to increase with depth by a value of 2.4 kPa/m (Gauer et al., 2005). The soft marine clays interbedded with the glacial deposits are considered to have an homogeneous strength of 5 kPa (L'Heureux et al., 2012). The sensitivity of glacial deposits and marine clay was set at 3 and 7, respectively (L'Heureux et al., 2012, 2013). A range of ξ_{95} between 10-50 was tested on soft clays (Einav and Randolph, 2005) Smaller values of ξ_{95} = 2.0 and ξ_{ld} = 10.0, also included in the simulations, have been used in the past in the successful modelling of slide blocks (Debnath, 2018). Due to the fact that the shear strength of fully softened clay can barely be recovered from its residual value after the initial slope failure, and the MTDs are apparently fully deformed before its deposition (Mesri and Huvaj-Sarihan, 2012; Mesri and Shahien, 2003), the physical properties of MTDs in this study were set to a value similar to marine clay with only residual strength.

To illustrate the evolution of slope instability and the development of initial sliding after slope undercutting, four modelling scenarios are considered in this study. They represent different types of failed strata: 1) pre-existing MTDs on the continental slope, 2) glacial deposits, 3) slope-propagating glide planes along a weak layer, and 4) multiple intervals with weak layers (Fig. 6.8). All scenarios were modelled on gently (1^{o}), right-dipping slope with a no-slip boundaries on their left side and below. The dip angle of undercutting boundary on lower slope was set at an angle of 30^{o} relative to the continental slope (Fig. 6.8).

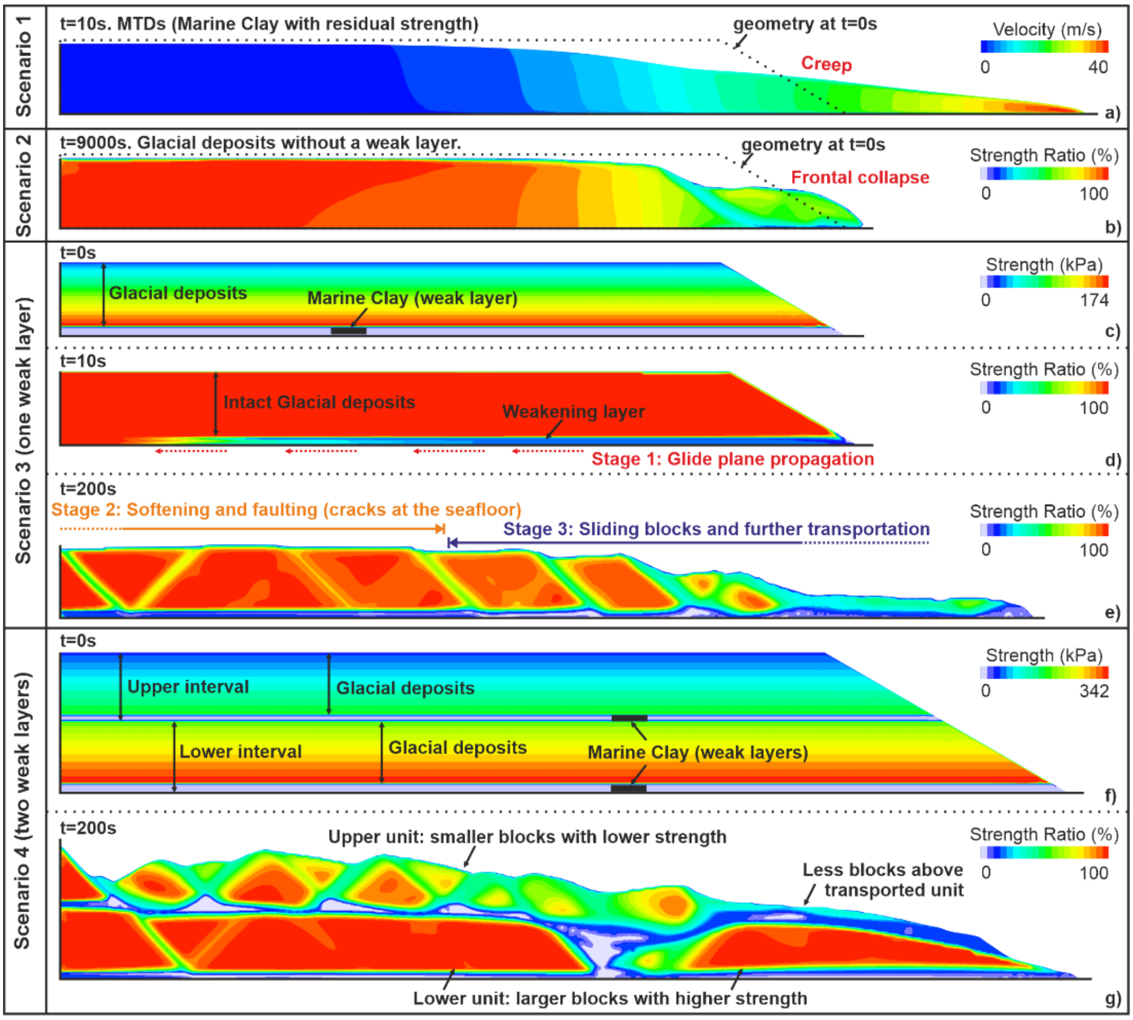

Figure 6.8 (see caption on next page)

Figure 6.8. Computational fluid dynamics (CFD) models completed in this work. All models are set on a gentle (1o), right dipping slope with no-slip boundaries at the bottom and left. a) Scenario 1: The undercut slope is composed of MTDs with a homogeneous, but weak, constant residual strength that resembles marine clay. The dashed line represents the initial geometry of the slope. The elongation of the slope strata after movement is initiated suggests sediment creep predominates when pre-existing MTDs are undercut. b) Scenario 2: The slope is composed of glacial deposits without a weak bottom layer. The initial geometry is similar to Scenario 1. Frontal collapse is observed in a much longer period (t=9000 s) and restricted to the frontal part of the undercut slope. c-e) Scenario 3: Following the initial geometry of Scenarios 1 and 2, slope strata consist of 62-m thick glacial deposits with a 8-m thick marine clay at the bottom. In d), t=10s, the scenario reflects glide plane propagation (stage 1) due to a fast weakening of the basal layer. Later in e), at t= 200s, slope failure develops in two distinct stages stage 2 and 3, which reflect the development of softening and faulting of slope strata (stage 2) without apparent sliding, to fully detached coherent units and translated slope strata (stage 3). f-g) Scenario 4: Two intervals similar to Scenario 3 (c) are vertically stacked in (f) considering an increase in the initial strength of glacial deposits with depth. Due to the presence of an intermediate weak layer separating the stacked intervals, two distinct units of slide blocks are developed with different strength and geometries.

6.6.1 Scenario 1- Sediment creep in pre-existing, older MTDs

Together with geochronological data, which proves slope undercutting along Terrace 1 occurred after the main Storegga event (Haflidason et al., 2005), chaotic seismic reflections below Terrace 2 show that MTC 2 had already been deposited in the study area before slope undercutting occurred along Scarp 2 (Fig. 6.3). As the initial thickness of this interval (MTC 2 in Fig. 6.3) was changed by further slope instability processes, a 70-m thick MTD was modelled in Scenario 1 replicating the thickness of failed material in Scenarios 2 and 3 (Fig. 6.8a). Revealing a constant low shear strength, the residual strength of marine clay, sediment creep is observed in Scenario 1 at t=10s and could be expected to continue in time (Fig. 6.8a). Except for its frontal elongation, no particular structure is observed within this fully softened and deformed interval (Fig. 6.8a).

6.6.2 Scenario 2- Frontal collapse of glacial deposits

To illustrate the sensitivity of the continental slope to the physical properties of its strata, and thus highlight the effect of weak layers in controlling slope stability processes, Scenario 2 considered an interval comprising glacial deposits with the same initial geometry to Scenarios 1 and 3 (Fig. 6.8b). Compared to the relatively soft MTDs modelled in Scenario 1, the harder glacial deposits record increasing strength with depth and reveal limited slope failure in the toe area at t=9000s, a much longer period than considered in Scenario 1 (Figs. 6.8a and 6.8b). In addition, the frontally collapsed part of the MTD was separated from relatively intact slope strata by a softened zone recording the lowest strength ratio (see light blue area in Fig. 6.8b). Similar slope instability is also observed and identified as a style of slope failure circles limited to the toe region of MTDs, and associated with local slope failure within homogeneous material (Steward et al., 2011; Taylor, 1937).

6.6.3 Scenario 3- Upslope propagation of slope instability after undercutting

Both the seismic data in this study (Fig. 6.5) and the published research (Kvalstad et al., 2005b; L'Heureux et al., 2012, 2013) suggest the presence of soft marine clay in between harder glacial deposits. Considering that the interval comprising slide blocks in Units 1 and 2 are ~70-m thick and occur at the same level of intact upper slope strata in Fig. 6.5, and that seismic resolution is ~ 8 m in the Naust Formation, Scenario 3 considered the deformation of a 62-m thick glacial interval over a 8-m thick marine clay (Fig. 6.8c).

At t=10 s, a glide plane propagates along weak layer (marine clay) towards the upper slope (Fig. 6.8d). At this stage (1), even though the strength of the weak layer is reduced to its residual strength after the continental slope is undercut, no further deformation is observed in the harder glacial deposits above (Fig. 6.8d). However, together with the softening of the basal weak layer, slope instability is shown to propagate to upper slope. At t=200s, a group of faults develops on the upper slope by concentrating softening in parts of the glacial deposits, above, thus forming cracks on the sea floor and fractures below (Stage 2 in Fig. 6.8e). A further softening of strata in the lower slope occurs as a third stage, when the unit above the marine clays is fully detached and evolves into a series of slide blocks (Stage 3 in Fig. 6.8e).

6.6.4 Scenario 4 – Vertically stacked intervals with weak layers

Considering there are two units of slide blocks observed in Terraces 4 and 5 (Figs. 6.5, 6.6 and 6.7b), Scenario 4 considers the two intervals modelled in Scenario 3 to be vertically stacked (Fig. 6.8f). The initial strength of glacial deposits once more increases with depth by 2.4 kPa/m. After t=200s, two units with slide blocks are observed due to a decrease in strength along softened zone (in this case, faults) formed between coherent triangular and trapezoidal blocks (Fig. 6.8g). Compared to the lower unit, the upper one has a lower strength at the start of the model (t=0s in Fig. 6.8f), and is deformed into a series of smaller blocks (Fig. 6.8g). Upslope, the upper unit with slide blocks is relatively well preserved and overlies the lower unit still without apparent downslope movement (Fig. 6.8g). On the lower slope, a fully detached lower unit with slide blocks corresponds to a third stage of instability - further strain-softening occurs both inside and above the lower unit, while the upper unit loses its strength and internal coherence (Fig. 6.8g).

6.7 Discussion

6.7.1 Slumped strata and deformed submarine channels as indicators of recurrent slope instability

In the study area, post-Storegga instability is documented in the form of deformed strata, deformed debrites and channel-fill strata. Sediment creep of an older, pre-existing MTC is recognised in this work by the detailed interpretations (and geomorphological analyses) of seafloor grooves and submarine channels (Figs. 6.3 and 6.4). There are at least two MTCs in Terrace 2, the lowest of which is named MTC 1 in this paper. MTC 1 was first generated before the Storegga Slide, and eroded the continental slope - including parts Storegga Slide per se later in its development - due to recurrent, long-term instability (Figs. 6.1c and 6.2a). MTC 2 accumulated above MTC 1 and is now exposed on the sea floor as part of the Storegga Slide. It reveals furrows and grooves on both its glide plane (horizon H2) and top surface (horizon H1) (Figs. 6.4b and 6.4c). A group of NW-striking furrows is observed on the TWT structure map of its basal glide plane (see dash line in Figs. 6.3g and 6.4c). In parallel, a distinct group of NW-striking grooves are identified on TWT structure and variance maps of the sea floor (Figs. 6.3d, 6.3f and 6.4b). These two groups of lineations share not only orientation and size, but also the same location and geometry (Figs. 6.4a-6.4c), suggesting that differential compaction within MTC 2 affects younger strata insomuch as the structure along its glide plane are observed on the modern sea floor.

Deformed strata with high sinuosity, including older debrites, are identified in Terrace 2 on the RMS amplitude and variance maps of the sea floor (Figs. 6.3e and 6.3f). These are sinuous (1.18 in Fig. 6.7a) and comprise alternating debrites and turbidites, suggesting they originally developed in association with NW-flowing gravity currents, similarly to the debrites and turbidites identified on the upper continental slope (Figs. 6.2b-6.2d). Close to scarp S2, MTDs sourced from this latter interfinger with high-sinuosity deformed strata, indicating that all are associated with the deformation of MTC 2 (see area between scarps S1 and S2 in Figs. 6.3d-6.3f). Hence, it is suggested that sinuous, deformed strata on the sea floor result from the creeping of MTC 2 after the continental slope was undercut along the Terrace 1. Based on the presence of grooves on the sea floor, the sediment creeping process affecting MTC 2 should have occurred due to reduced lateral support along S2 after its initial deposition. In addition, the formation of an L-shaped slide scar in Terrace 1 can be associated with a later phase of recurrent instability of the Storegga Slide, matching the chronostratigraphic data available for the study area, and justifying the presence of deformed MTCs in the study area - themselves effective indicators of recurrent slope instability.

The recognition of sediment creeping in the study area is further supported by the CFD models in this thesis (Scenarios 1 and 2 in Figs. 6.8a and 6.8b). Free scarps generated on the lower slope reflect reduced lateral support via slope undercutting along Terrace 1. These scenarios are recorded in the initial step of the CFD model (t=0s in Fig. 6.8a). The elongation of MTDs in Scenario 1 (Fig. 6.8a) represents the downslope creep of MTC 2 in Terrace 2 (Figs. 6.3 and 6.4), a character that differs from the classical slope failure circles (frontal collapse) identified in the toe area of landslides (Taylor, 1937) in relatively intact and stiffer slopes, as modelled in the Scenario 2 (Fig. 6.8b).

6.7.2 Slide blocks as markers of distinct slope instability processes

Two intervals with slide blocks (Units 1 and 2) are recognised in Terraces 4 and 5 (Figs. 6.5a, 6.5b and 6.6b). Both intervals are bounded by discrete basal glide zones and overlying contourite and glacial-marine depositions (Figs. 6.5a – 6.5c). The development of slide blocks has been related in previous work on the Storegga Slide to reduced lateral support and subsequent internal fracturing of near-seafloor strata (Gauer et al., 2005; Kvalstad et al., 2005a). In this study, the overlapping of two intervals with slide blocks, and the marked difference between these two intervals, suggest a more complicated failure mechanism than previously assumed for the Storegga Slide. Slide blocks in Unit 1 occur in the southern part of Terrace 4 (Figs. 6.1b and 6.5d). Above these blocks, seismic-attribute maps of the sea floor reveal local folds and multiple secondary scarps (S4.1 – S4.4 in Figs. 6.5c and 6.5e). Since the MTCs from scarp S4 overlap some of the submarine channels in Terrace 3, the formation of secondary scarps S4.1 - 4.4 should have occurred no earlier than the Storegga Slide and was followed by the collapse of scarp S4 (Fig. 6.5d). High-variance values above seafloor folds (Fig. 6.5e), together with faults propagating vertically from the slide blocks' tops (Fig. 6.5a), reveal enhanced instability of the sea floor above blocky intervals.

Despite the slope-collapse features observed along scarp S4, no obvious secondary deformation is observed in the slide blocks composing Unit 1, suggesting the slope remained relatively stable after the last phase of Storegga Slide collapse. However, fractures and secondary scarps above slide blocks point out to the existence, at present, of an unstable sea floor in the study area (S4.1-S4.4, cracks on folds and slides from scarp S5; Figs. 6.5a, 6.5b and 6.5e). Based on this working hypothesis, the reduction in lateral support on the continental slope resulting from the collapse of the Storegga Slide contributed to a slight downslope readjustment of slide blocks, and corresponding deformation above them, generating small-scale cracks and local slides on the sea floor (cracks in Figs. 6.5a and 6.5e, and scarps S4.1 – S4.4 in Figs. 6.5c and 6.5e). Together with the limited movement of slide blocks, this instability migrated upslope towards the pre-existing slide scarp S5, above which both faults and local mass-wasting features are observed (faults linking slide blocks to the exposed glide plane in Figs. 6.5b and 6.5e). As the basal glide zones of many of these slide blocks coincide with distinct seismic reflector at the same level, at different depths, the extent of these weak layers beneath slide blocks is another essential precondition factor for the genesis, and continuation in time, of slope instability.

Long-term instability in Unit 1 slide blocks, including their readjustment and fracturing (cracks and scarps) on the modern sea floor, therefore results from of further softening and faulting (Stage 2 in Scenario 3, Fig. 6.8e) triggered by recurrent slope undercutting. During the first sliding event (Unit 1 in Terrace 4, Fig. 6.5), multiple fractures were developed between and inside blocks (see deformed and incipient blocks in Figs. 6.5a-c). Once the residual strength of these fractures, and of the glide plane, is re-instated in the overlying strata, a further reduction of lateral support (slope undercutting) within the same interval can re-initiate the sliding process by the propagation of the glide plane along weak residual-strength layers (Stage 1). Accordingly, softening, faulting and readjustment of blocks above (Stage 2) can occur at any time, originating an unstable sea floor with cracks and scarps (Figs. 6.5e and 6.8e).

Slide blocks in Unit 2 are relatively small (Figs. 6.6 and 6.7b). Inside Unit 2, significant geometric differences are also observed. Longitudinal blocks and chasms close to scarp S6 (Figs. 6.6b and 6.6c), show a dominant north-south orientation that is perpendicular to the local slope gradient (Figs. 6.6c and 6.7c). In contrast, slide blocks close to scarp S5 roughly strike to the NW (Figs. 6.6d and 6.7c), have a relatively constant width of about 98 m, and reveal a common basal glide plane (Fig. 6.7b). However, their length-width ratio decreases from 3.12 in the north to 2.13 in the south (Fig. 6.7c). Slide blocks in Unit 2 are interpreted to be stable since they were formed as no fractures are observed in the strata overlying the blocks (Figs. 6.6c and 6.6d). Previous research suggested that the strike of slide blocks should be parallel to the local slope and perpendicular to their direction of downslope transport (Baeten et al., 2013; Kvalstad et al., 2005a). This is true for the blocks around scarp S6 (Fig. 6.6c), but their strikes show multiple orientations close to scarp S5 (Fig. 6.6d). Thus, it is suggested that the occurrence of rotated, disrupted blocks close to scarp S5 is associated with secondary deformation, which further broke the slide blocks and re-oriented them to their present-day geometry.

The movement of slide blocks in Unit 2 was previously proposed to relate to the remobilization of slide blocks in Unit 1 close to scarp S5 (Bull et al., 2009b). Seismic data reveal a group of faults located within the same interval where slide blocks are observed in Unit 1, but on the northern side of scarp S5 (see incipient block and relative faults in Figs. 6.5b and 6.6a). These faults in Unit 1 propagate into Unit 2 as longitudinal chasms (see the red dashed line in Figs. 6.6a and 6.6b). Thus, slide blocks in Unit 1, which contributed to a reduction in the lateral support on scarp S5, should have been reactivated during or after the slide blocks in Unit 2 were generated and moved downslope. During this reactivation, new faults ('new fault' in Figs. 6.5b and 'faults in unit 1' in Fig. 6.6a) were formed behind scarp S5 before the formation of new detached slide blocks (e.g., incipient block in Figs. 6.5b and 6.6a). Hence, the disrupted slide blocks in Unit 2 - showing low length-width ratios and varying orientations - became markers of scarp retreat, and corresponding changes in local stress field, near scarp S5 (Fig. 6.6d).

The faults and chasms in Units 1 and 2 delayed the formation of slide blocks in lower unit (1) to no earlier than the deposition of upper unit (2), correlating with Scenario 4, in which two intervals with weak layers are undercut simultaneously (Figs. 6.8f and 6.8g). In this case, after the propagation of the glide plane to the upper slope along fully softened weak layers, the width of slide blocks in the lower unit is larger than in the upper unit, replicating the seismic interpretation in this thesis (Figs. 6.7b and 6.8g). Moreover, in Scenario 4 at t=200s, the lower unit is still in stage 2 on the upper slope, whereas the upper unit has already evolved into stage 3 with a dramatically decrease in strength occurring together with downslope movement (Fig 6.8g). This hysteretic development of instability within the lower unit results from the existence of a harder lower unit separated from an upper unit by a weak layer, and justifies the apparent correlation between fault and chasms in the lower and upper units during their softening and sliding (Figs. 6.6a, 6.6b and 6.8g). Therefore, after the weakening of this intermediate weak layer, it is proposed that the two units (lower and upper) were separated into two isolated sliding regions that were not linked, or interacting, in any way or form. Consequently, the lower interval with higher strength resulted in the generation of large blocks, while the softer, lower strength interval above generated relatively smaller slide blocks (Figs. 6.7b and 6.8g).

6.7.3 Weak layers, pre-existing fractures and MTCs as features promoting long-term instability

Through the mapping of deformed strata, submarine channels and slide blocks in near-seafloor strata, three intervals with evidence for secondary deformation are identified. In these intervals, a combination of MTCs, accompanying weak layers (glide planes) and pre-existing fractures is recorded. Slope instability is further promoted by reduced lateral support on the continental slope, triggering local sediment creep in near-seafloor MTCs, and secondary deformation in slide blocks. To evaluate the mechanisms responsible for this instability, and associated triggers, four CFD models have been carried out and discussed with seismic interpretation.

A critical factor of long-term instability is the built-up of a permanent weak frame. As clay content prevents the recovery of shear strength from residual values after slope instability ensues, the sliding of the clay-rich Naust Formation could be paused and preserved, rather than stopped and reset. In other words, once slope undercutting occurs or other unstable conditions are satisfied, the sliding of strata on continental slopes can be resumed at any time, such as recorded with the lateral creep of MTC 2 after the slope was undercut along S2, or when of the readjustment of slide blocks in Unit 1 after the Storegga Slide. Thus, weak layers, pre-existing fractures and MTCs become the key factors controlling long-term slope instability. Even though the study area is currently in a relatively stable situation after the Storegga Slide, considering the multiple slide occurred historically, and the long-term instability observed in this study, further sliding could be expected in around the Modgunn Arch and on the broader mid-Norwegian margin.

6.8 Chapter-Specific Conclusions

This study identifies key features marking long-term instability around the northern flank of the Storegga slide, Central Norwegian Sea. The combination of slope undercutting, pre-existing MTCs and fractures, and multiple weak layers on the continental slope preconditioned the study area to long-term instability. The main results of this work can be summarised as follows:

a) Turbidite and debris channels observed on the sea floor record long-term slope instability by increasing their sinuosity, thus revealing sediment creep inside older MTCs.

b) Together with local slope failure above pre-existing fractures, the local readjustment of slide blocks is an evidence for long-term slope instability. CFD models show that readjustments contribute to the fracturing of overlying strata to the sea floor, as also revealed by the cracks, faults, and slumps above buried slide blocks.

c) In such a setting, the loss of lateral support from slope undercutting has the potential to propagate deformation along weak layers, and destabilise fractures and slide blocks. As presented in the CFD models, after slope undercutting the upslope-propagating weakening process along weak layers preconditions further softening, faulting and sliding behaviour within relatively stiffer and intact slope strata.

d) The built-up of a permanent weak frame is a key factor preconditioning the long-term instability, including weak layers, pre-existing fractures and MTCs. After the initial sliding process ceases, and once a certain condition is satisfied (such as a further slope undercutting), slope instability can be resumed.

As a corollary, this chapter shows that the combination of pre-existing MTCs, fractures and weak layers is likely to be a significant precondition for long-term slope instability on many continental slopes with similar characteristics. Together with lateral undercutting as a trigger, a regional unstable continental margin could evolve into a self-sustaining area of recurrent slope instability, prolonged in time through millennia or even several millions of years, as is the case of the study area at the northern flank of the Storegga Slide.

CHAPTER SEVEN

Summary of Findings and Discussion of Results

7. Summary of Findings and Discussion

7.1 Preamble

The results chapters in this thesis are focused on understanding the development of long-term instability and their relationship with extensional faults on the mid-Norwegian margin. The main findings of Chapters 4, 5 and 6 are summarised and presented in this chapter. As major fluid conduits, extensional faults contributed to the fluid migration and accumulation in sub-surface strata. With fast deposition during glacial cycles, induced excess pore pressures evolved into a critical precondition of long-term slope instability via the abrupt decrease in the strength of weak layers.

7.2 Summary of scientific results

7.2.1 Chapter 4: Large-scale tectonic movements affecting the South Modgunn Arch

The first data chapter of this thesis focuses on the tectonic events that occurred adjacently to the South Modgunn Arch since the breakup of the Northeast Atlantic Ocean (Fig. 7.1). Several key seismic horizons were interpreted in Chapter 4, including the top of the breakup sequence (Tare Formation) and stratigraphic boundaries in post-rift strata of the Brygge, Kai and Naust formations (Figs. 7.3). Seismic profiles reveal important hydrothermal venting within the breakup sequence. In the post-rift sequence, local unconformities in parts of the Brygge and Kai formations document successive phases of tectonic uplift in the South Modgunn Arch that preceded the deposition of the glacial-marine Naust Formation (unconformities below H3 in Fig. 4.1c).

The automatic fault extraction and ant tracking options in Schlumberger Petrel® were used to map the tectonic structures deforming the South Modgunn Arch. The same Petrel algorithms were useful to plot the 3D distribution of faults observed in the interpreted 3D seismic volume. Based on their distribution, geometry and periods of activity, the faults in the study area were classified in three main types: strike-slip, radial and polygonal faults (Fig. 4.2). Associated with tectonic movements along the Jan Mayen Fracture Corridor, strike-slip faults were first generated as deep-seated transfer faults between different segments of a rifted margin before continental breakup. For the first time, this work documents how active were these same strike-slip faults during the post-rift phase, when they formed steep structures with variable throws. Due to subsequent slope instability, the upper tips of these strike-slip faults were eroded and two main strike-slip faults are observed beneath the bottom glide plane of submarine landslides. Radial faults were identified above sill intrusions, which formed hydrothermal vents and forced folds (Fig. 7.4). Differential compaction was the main process forming radial faults, and the activity of these latter is limited to post-rift strata. They ceased in the Kai Formation (Upper Miocene to Upper Pliocene) where throws values as measured in seismic data markedly decrease to zero (Fig. 4.2).

Polygonal faults are observed all along the mid-Norwegian margin in association with localised fluid flow conduits (Berndt et al., 2003). In Chapter 4, fluid migration is identified in the form of fluid chimneys, pipes and pockmarks occurring together with high-amplitude anomalies (i.e. ‘flags’, flat and bright spots) (Fig. 7.7). Based on the results of automatic fault extraction and ant tracking models, two groups of polygonal faults were identified around the South Modgunn Arch based on their differing depths and strikes (Fig. 7.4). The lowermost family of polygonal faults strikes to the Northeast, while the uppermost fault family shows a Northwest strike (Fig. 4.12). The lowermost family follows the strike of the South Modgunn Arch and, therefore, was likely formed during the uplift of this latter structure, followed by generation of a polygonal fault family striking perpendicularly to the Jan Mayen Fracture Corridor. This is the first time tectonic activity on the South Modgunn Arch is related to the Jan Mayen Fracture Corridor, suggesting that strike-slip fault zones on continental margins have a significant impact on slope instability.

7.2.2 Chapter 5: Relative timing of submarine slope instability

After characterising the tectonic events affecting the South Modgunn Arch, and the long-term instability processes documented in this region, the relative timing of submarine landslides was addressed in Chapter 5. As a term of reference, the Naust Formation was deposited in the late Pliocene, accompanying multiple glaciation episodes in the Northern hemisphere (Chand et al., 2011; Forsberg and Locat, 2005). The first regional-scale submarine slide on the Storegga Slide has been identified as Slide W, which occurred within the Naust W unit (Solheim et al., 2005). Chapter 2 documents at least two slope failures occurring prior to Slide W. The lower slide was named as Slide X and, underneath this latter, a regional pockmark field was observed to interact with polygonal faults growing from the Kai Formation. Adjacently to the Slide X, which is about 40 m thick, few slide blocks are shown as high-amplitude features (Fig. 5.11). Above these slide blocks, a localised creeping slide (Slide Y) is suggested by the presence of several cracks and ridges on the upper and lower slope, independently (Fig. 5.10). On the modern sea floor, cracks are also evident by their variable variance values. A second pockmark field was noticed below these cracks, but other evidence of fluid flow is absent on the modern sea floor.

The presence of pipes and pockmarks beneath Slide X, and the evidence for seafloor cracks in differing parts of the study area (and at contrasting depths) suggests that multiple processes are able to increase, and trigger, slope instability around the South Modgunn Arch. Considering that pipes and pockmarks comprise efficient fluid conduits (Cartwright et al., 2015), excess pore pressure must have been able to build up, locally, before some of the interpreted slope failures occurred. However, only a few pockmarks were observed in the same interval where seafloor cracks and Slide X are observed, indicating that excess pore pressure may have not built up to a critical value in such conditions, or was dissipated when seafloor cracks were formed. It is therefore suggested that palaeo-pockmarks comprise the fluid conduits that induced fluid migration upwards, but hydraulic fracturing may have followed (and, thus, dissipated) any build-up of pore pressure in the sediment. In addition to the heterogeneous permeability of glacial-marine strata, trapped fluid was able to increase the excess pore pressure and slope instability occurred in these same areas (pockmark below sea floor cracks Fig. 7.10).

Similarly to the evacuation structures observed around several other anticlines in the Storegga Slide, there are three evacuation structures around the South Modgunn Arch that formed local topographic lows - one of which is located above a relative gentle slope as part of Slide W (Fig. 7.2c, 7.2d, 7.4, 7.5 and 7.6). In addition, local compressional features were identified in the form of thrusted slide blocks in the north of the study area.

Even though mounds floating on MTCs were frequently observed in the downslope side of these evacuation structures, there is evidence of slow sediment creep in these same mounds via the appearance of curved lineations on seismic attribute maps. Inside the MTCs filling the evacuation structure, there is an interval with a transparent seismic character, named MTC 3 in this study. Considering the density reversal recorded from the Naust Formation to the Brygge Formation, it is proposed that this evacuation structure was formed due to the sinking of the high-density MTC 3 into the lower-density Kai and Brygge formations (Fig. 5.17). This phenomenon not only deformed the upper part of the slope under a compressional regime, but also evacuated oozes below MTC 3 in the direction of the lower continental slope.

7.2.3 Chapter 6: Diagnostic features of long-term instability on continental margins

Chapter 6 focused on characterising the geological features that are diagnostic of long-term instability on continental margins. Seismic attributes such as RMS amplitude, two-way time (TWT) structure and variance maps were used to understand the styles of slope instability on the South Modgunn Arch. Considering that most glide planes of MTDs coincide with negative seismic reflections in the study area, and are correlated with soft marine oozes, the existence of weak layers is presumed in this chapter to be a key predisposing factor for slope instability. Hence, in this chapter slope tendency was calculated along the mapped bottom glide planes under a given stress field, and finite element analyses were developed to quantify downslope strata displacement and plastic strain above these same glide planes. Different frictional coefficients, representing the variable strength of weak layers, were used in the models. By modelling the displacement and strain of the interpreted MTDs, it was proposed that weak layers can propagate the glide plane upslope, contributing to increasing the area of continental slopes remobilised by an instability event. Proof of this process is the secondary deformation and rotation of slide blocks documented in the more recent MTDs, and the fracturing of the modern sea floor above these same blocks (Figs. 7.9 and 7.10).

Features associated with long-lived slope instability are varied in the study area, the first of which comprise pervasive lineations on the sea floor. In this thesis were documented several lineations on the sea floor and in glide planes, such as turbidite channels, debris channels and grooves, formed during slope instability processes (Fig. 6.4). In particular areas where lineations cross-cut each other, sediment creep is evoked as a key process – a characteristic better recorded by deformed debris channels that kept deforming and whose sinuosity increased as a result.

Slide blocks are a second type of feature associated with long-term instability around the Storegga Slide (Figs. 6.5 and 6.6). On the upper part of the continental slope are observed two intervals with slide blocks that are correlated with Slide R and S. These two intervals show variations in block length (long axis) and their strikes relative to the headwall scarp where they first originated (Fig. 6.7).

7.3 Main preconditioning factors of long-term slope instability

7.3.1 Preface

The factors induce slope failures are multiple, from glacial cycles, pore overpressure, weak layers and oversteepening as long-term preconditions to earthquakes, volcanic and human activity as short-term triggers (Laberg et al., 2003; Leynaud et al., 2009; Sultan et al., 2004a; Urlaub and Hjelstuen, 2020). Northern Hemisphere glaciation, as one critical pre-condition, has contributed many submarine landslides on continental margins around North Atlantic, such as Norwegian margin, Southwest Barents Sea and the northern part of U.S. Atlantic margin (Fig. 7.1a) (Huhn et al., 2019; Nielsen et al., 2005; Pope et al., 2018). At the same time, different preconditions have been proposed to dominant these instabilities in different regions.

Along the U.S. Atlantic margin, where numerous canyons and gullies are characterised by their erosional relief (Brothers et al., 2013; Mitchell, 2004; Vachtman et al., 2013), tens of Quaternary landslides are recognised to derived from canyons or the continental slope (Chaytor et al., 2007; Twichell et al., 2009). Compared to canyon-derived landslides, those on the continental slope mostly originate on the upper rise or lower continental slope and present a large area (and removed volumes) of strata via subsequent retrogressive failures (Twichell et al., 2009). The largest landslide on this margin, identified along the southern New England margin, was induced by earthquakes during glacial rebound (Chaytor et al., 2007). At the same time, weak layers, rapid deposition and pore overpressure are suggested to precondition other regional slides on the U.S. Atlantic margin (ten Brink et al., 2009).

Series of regional submarine slides are also documented in the form of MTCs and associated scars on the west Barents Sea margin, from its north section (up to around 1,000,000 km^2) to its south section (around 100,000 km^2) (Hjelstuen et al., 2007; Llopart et al., 2015; Rebesco et al., 2012; Safronova et al., 2017). Along the southwest Barents Sea margin the Bjørnøya Fan Slide Complex, consisting of three buried mega-slides, has been documented as one of the biggest slope failures on the Northeast Atlantic margin (Hjelstuen et al., 2007). In addition to earthquakes as short-term triggers, low eustatic sea level and rapid sedimentation rates during the Northern Hemisphere Glaciations, occurring on soft Miocene-Oligocene strata, are suggested to precondition this slope to instability (Hjelstuen et al., 2007; Knies et al., 2009). On the northwest Barents Sea margin, regional and thick meltwater plumites have been proposed to act as weak layers with enhanced pore overpressures, and were able to precondition the latter megaslides (Llopart et al., 2015).

Along the Norwegian margin, several large submarine landslides have been related to the Scandinavian Ice Sheet such as the Andøya Slide, Trænadjupet Slide and Nyk Slide on the north-Norwegian margin, and the Storegga Slide on the mid-Norwegian margin (Bryn et al., 2003; Laberg et al., 2002, 2000; Lindberg et al., 2004; Solheim et al., 2005) (Fig. 7.1b) . Comprising one of the most unstable continental slopes on Earth, the Storegga area (complex) experienced multiple regional submarine slides during the Quaternary (Fig. 7.1). In addition to the Storegga Slide proper (~8200 years b.p.), at least three regional slope failures have been observed around the southern flank of the Storegga Slide - the Tampen slide, Møre slide and Slide S - which occurred in last million years (Bryn et al., 2003).

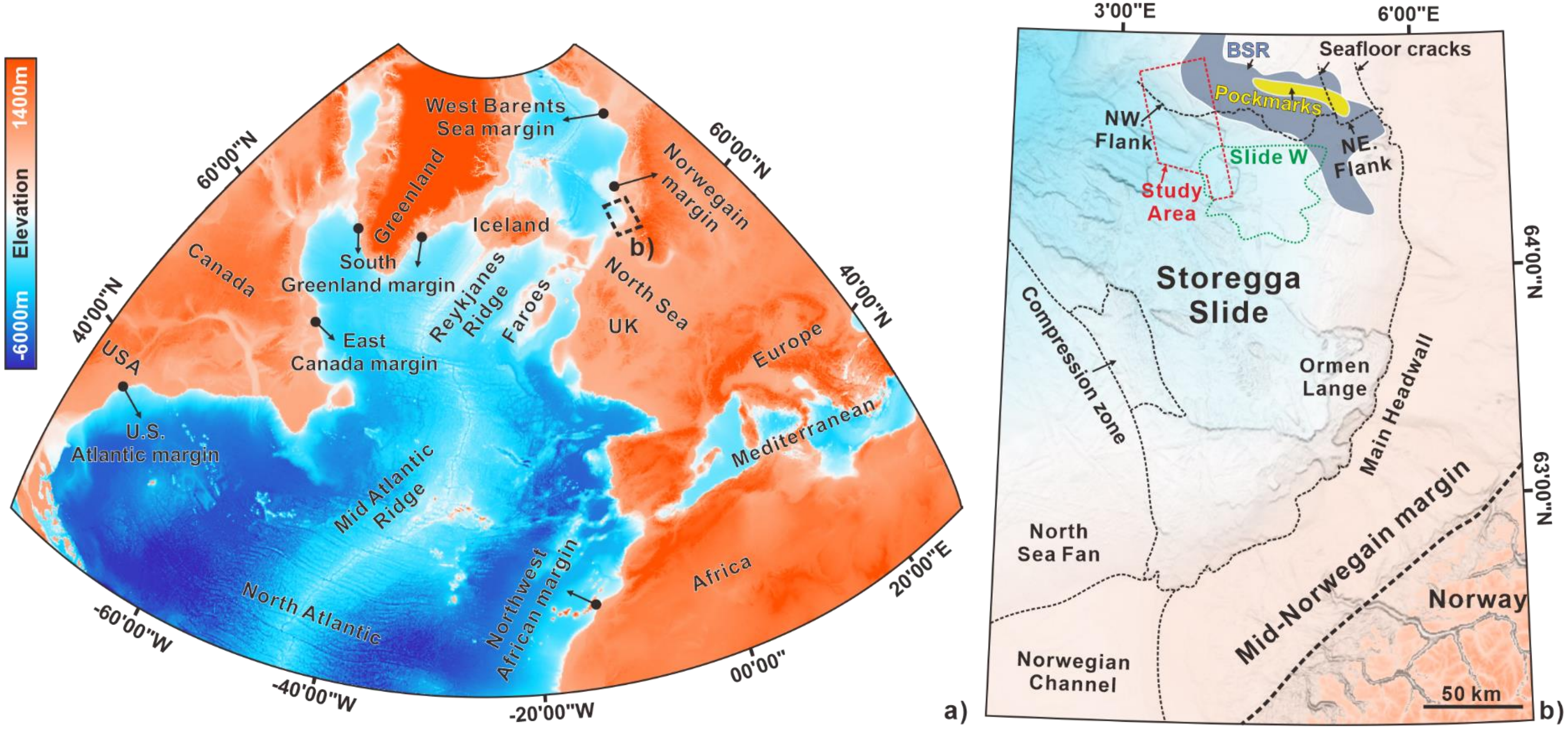

Figure 7.1. a) Location of the continental margins in the context of North Atlantic Ocean, Modified from GEBCO (2020). b) Map showing the location of the study area, pockmarks fields (yellow zone), BSR (grey zone), compression zone, Slide W, seafloor cracks and slide blocks (red dots) on the mid-Norwegian margin. NW Flank - northwest flank of the Storegga Slide, NE Flank - northeast flank of the Storegga Slide.

Along the northern flank of the Storegga Slide, Slide W, S and R have been considered as spanning 1.7 Ma to 0.2 Ma (Solheim et al., 2005) (Fig. 7.2). This long-term instability and recurrent regional submarine landslides have marked the mid-Norwegian margin as one of the most unstable area on earth and led to amount of research on its preconditioning factors. However, due to the erosion by multiple slide events and limited data from moderately to poorly failed regions, the preconditioning factors for this long-term instability are still not clear. Combining high-resolution seismic and borehole data, this study reveals two Pre-Slide W slope failures (Slide X and Y) and one group of seafloor cracks below the features recognised by Solheim et al. (2005), further extending the timespan of this long-term instability to the whole of the Quaternary (Fig. 7.3).

In the study area, slope failures reveal different diagnostic features, including evacuation structures (Figs. 7.4-7.6), slide blocks (Figs. 7.7 and 7.8), local slump and erosional channels (Chapter 6). These features suggest that varying preconditioning factors favour slope instability such as excess pore pressure, reduced lateral support on the slope and density reversal in slope strata (Chapters 5 and 6). Seismic interpretation also reveal multiple fault systems beneath the studied Quaternary landslides, from intrusion-related radial faults in Eocene strata to Pliocene-Quaternary polygonal faults (Chapter 4). Overlapping fault systems contributed to the formation of fluid conduits as recorded in seismic data by the high-amplitude anomalies and pockmarks that occur around these faults (Chapters 4 and 5). Accompanying the heterogeneous permeability in glacial-marine deposits, migrated fluid accumulated inside the Naust Formation, thus preconditioning the generation of multiple submarine slides (Chapter 5).

The excess pore pressure resulting from sub-surface fluid migration is a critical preconditioning factor for instability in weak layers, decreasing their shear strength, leading to the bed-parallel propagation of glide planes, and promoting the onset of local instability in multiple parts of the continental slope (Chapter 5). The oversteepening of the continental slope via tectonic uplift is also an effective way to increase instability by increasing the shear stress imposed on specific beds. Overall, the main long-term preconditioning factors considered in this study include tectonic uplift, the presence of multiple fault systems and local fluid migration.

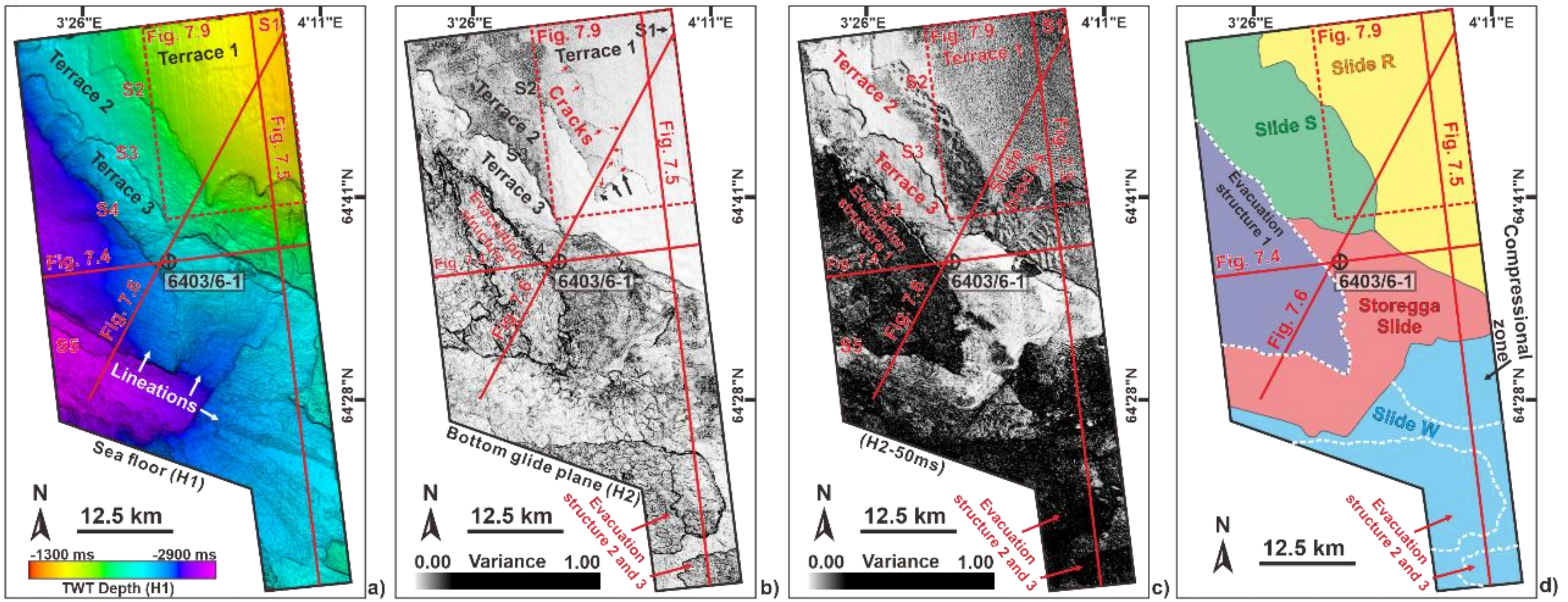

Figure 7.2: a) Relief map of the sea floor (Horizon H1) in the study area. b) Variance map of the bottom glide plane (Horizon 2). c) Variance map extracted 50ms (about 30 m) above the glide plane. d) Relative location of multiple Quaternary slides in the study area, on the northwest flank of the Storegga Slide, based on their interaction above the bottom glide plane. The Storegga Slide is observed on the modern sea floor as debris flow and erosional channels in a). Evacuation structures are shown by variance maps b) and c).

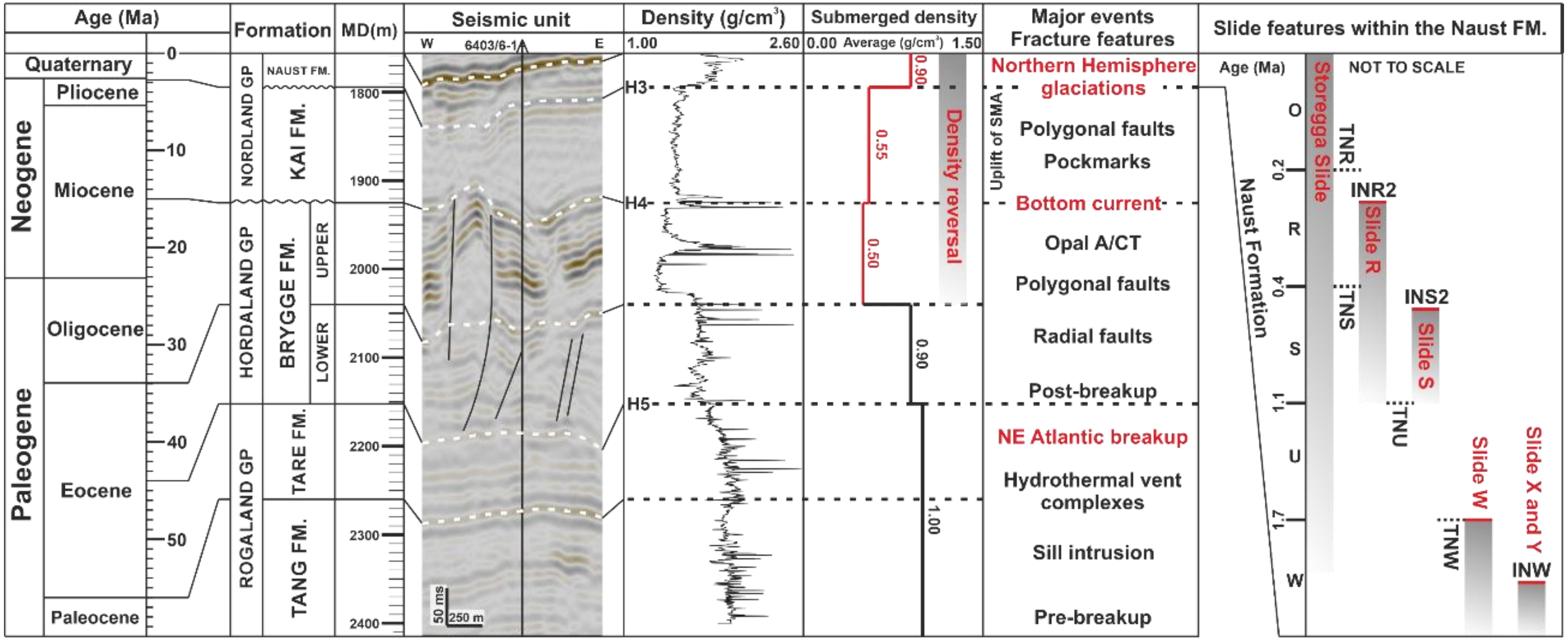

Figure 7.3. General correlation panel amongst seismic data and main seismic-stratigraphic units in the South Modgunn Arch. Key seismic horizons interpreted include H3 - Top of the Kai Formation, H4 - Top of the Brygge Formation; H5 - Top of the Tara Formation. Submerged density values in their corresponding column are calculated from Equation 7.3.

7.3.2 Tectonic uplift generating positive relief and associated fault systems

A series of submarine slides occur along the mid-Norwegian margin, from the Vigrid Slide on the Vøring Plateau to the Tampen Slide above the North Sea Fan (Rise et al., 2010). In addition, several Cenozoic domes in the Norwegian Sea, such as the Naglfar Dome in the Vøring Basin and the Isak Dome in the Møre Basin (Doré et al., 2008a), also reveal multiple phases of slope instability on their flanks. The history of Quaternary instability above such domes has not been fully documented in spite of the multiple evacuation structures documented on their tops (Riis et al., 2005; Rise et al., 2006).

In contrast to relief-controlled slope instability, such as instability recorded near the shelf-break and on volcano islands, the domal structures formed on the gentle mid-Norwegian margin during the Cenozoic were overlain by fine-grained marine oozes and glacial-marine deposits after tectonic uplift ceased (Gómez and Vergés, 2005), suggesting that local slope oversteepening of such domes did not directly increase slope angle to promote slope instability. After comparing the South Modgunn Arch with the Helland-Hansen Arch (HHA) on the upper continental slope, at least two other phenomena were putatively able to locally increase slope instability above these anticlines: differential compaction and local uplift induced by growing faults.

Considering that the oceanward flank of the South Modgunn Arch was deformed (and partially removed) during Quaternary slope instability, deposits around the less-eroded HHA better record post-uplift deformation within the Naust Formation, the host of most of the Quaternary MTDs considered in this thesis. In contrast to the Modgunn Arch, which was initiated in the Miocene, the HAA to the east of this latter arch was formed from the Oligocene to the Miocene (Lundin and Doré, 2002). A period of decreasing amplitude in the HAA was followed by a final period of relative slope stability in the last million years (Gómez and Vergés, 2005). In this arch, tectonic folding contributed to less than half of its present-day amplitude; differential compaction and the

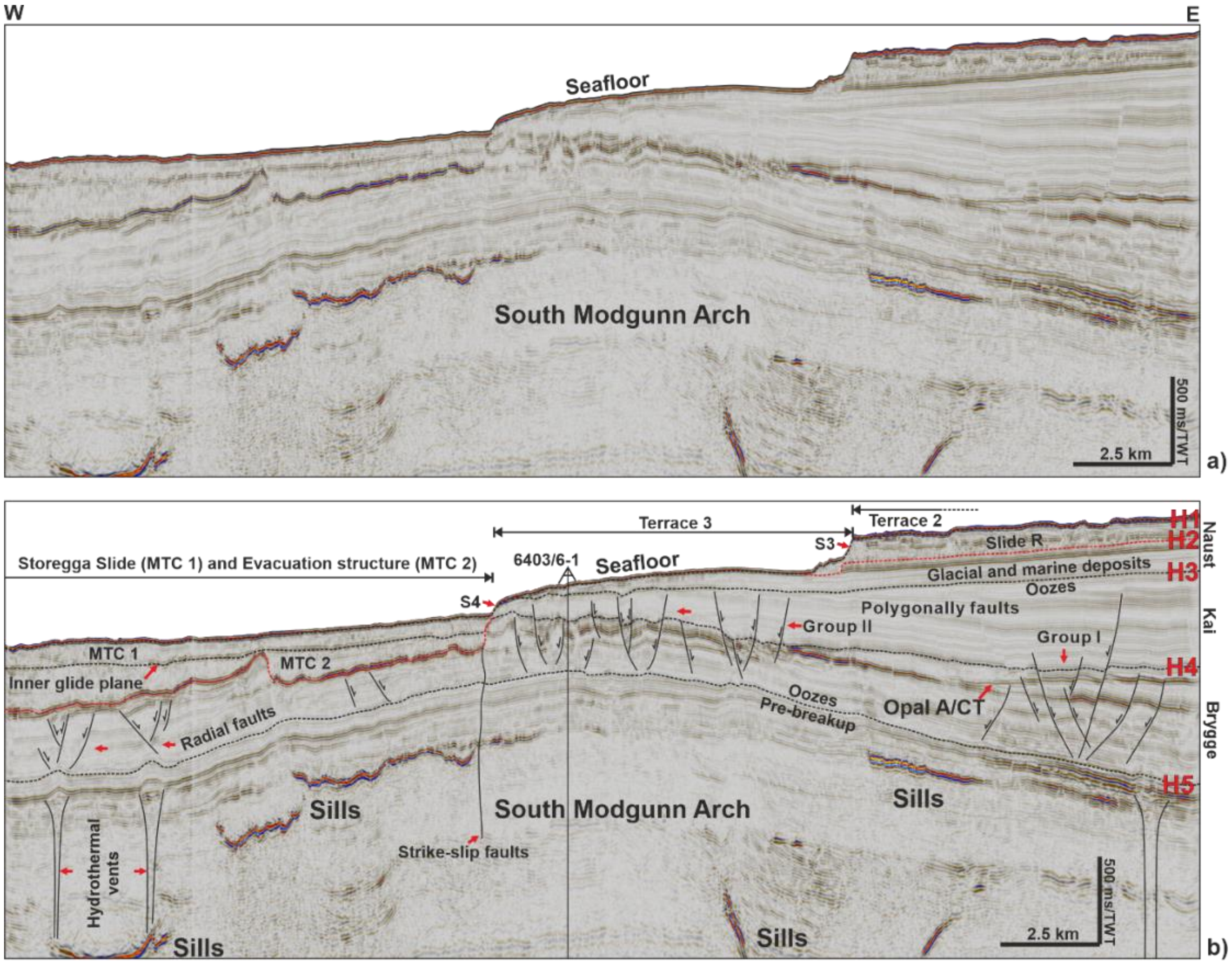
W
E
Seafloor
South Modgunn Arch
500 ms/TWT
2.5 km
a)
Terrace 3
Terrace 2
S3
Slide R
H1
H2
H3
H4
H5
Naust
Kai
Brygge
Storegga Slide (MTC 1) and Evacuation structure (MTC 2)
6403/6-1
Seafloor
Glacial and marine deposits
Oozes
S4
Polygonally faults
Group II
Group I
MTC 1
MTC 2
Inner glide plane
Radial faults
Oozes
Pre-breakup
Opal A/CT
Sills
South Modgunn Arch
Sills
Strike-slip faults
Hydrothermal vents
Sills
Sills
500 ms/TWT
2.5 km
b)

Figure 7.4 (previous page). a) Uninterpreted and b) interpreted east-west seismic profile across the study area. Location is shown in Figure 7.2. Magma intrusions that formed before and during the breakup of the Northeast Atlantic are marked as sills. Related hydrothermal vents are observed above the intrusions. In the post breakup sequence, polygonal faults and Opal A/CT transition are mainly limited to oozes. An evacuation structure is interpreted as a local crater on the west flank of South Modgunn Arch. Multiple submarine slides are interpreted as chaotic or blocky seismic reflectors above discrete glide planes. H1 - modern sea floor, H2 - bottom glide plane, H3 - Top of the Kai Formation, H4 - Top of the Brygge Formation, H5 - Top of the Tare Formation.

progradation of a sedimentary wedge onto the margin lead to the increase in amplitude of the HAA after tectonic uplift ceased (Gómez and Vergés, 2005; Kjeldstad et al., 2003).

In the case of the South Modgunn Arch, though its western flank was removed by recent landslides, the decreasing thickness of glacial-marine deposits over its east flank suggests the deposition of a sedimentary wedge similar to that accumulated on the HAA. Though very gentle (~ 0.5º), the top of the Kai formation on this east flank still dips towards the ocean, westwards, indicating that differential compaction was not sufficient enough to reverse its dip direction, or slope gradient (Fig. 7.10). Radial faults above hydrothermal vents also suggest that differential compaction did not occur after the Pliocene over the South Modgunn Arch (Chapter 4). The fossilised opal A/CT boundary, and the top Kai horizon that limits the majority of polygonal faults in the study area, reflect a relative tectonic stable period after tectonic uplift ceased (Chapter 5) (Neagu et al., 2010b). Thus, along with the polygonally faulted, oceanward dipping top Kai horizon (Horizon 3), it is proposed that the inherent positive relief from South Modgunn Arch could have only partly increased the dip angle of its eroded west flank during the Quaternary. In contrast to the HAA, the fault families crossing the post-Oligocene (break-up) interval are a key preconditioning factor of slope instability in the study area.

There are at least three types of faults around the South Modgunn Arch: radial faults, strike-slip faults and polygonal faults. Radial faults were formed due to the differential compaction of sediment during diagenesis. Their development was limited to pre-Quaternary strata, and mainly occur in the Tare and Brygge formations (Fig. 7.4). Along with a decrease in the throw of radial faults in the Kai Formation, differential

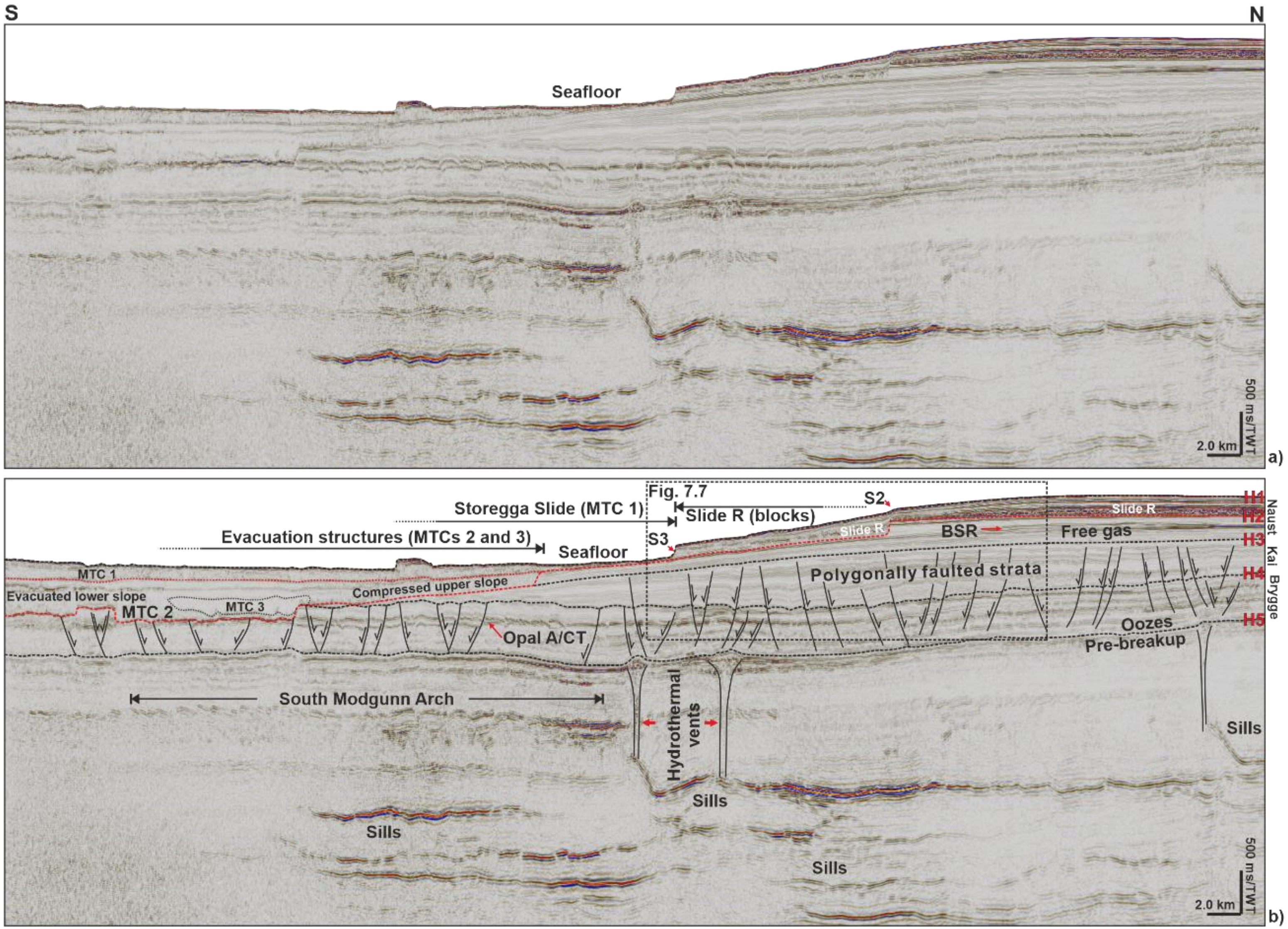
S
N
Seafloor
500 ms/TWT
2.0 km
a)
Fig. 7.7
S2
Storegga Slide (MTC 1)
Slide R (blocks)
Slide R
Slide R
BSR
Free gas
H1
H2
H3
H4
H5
Naust
Kai
Brygge
Evacuation structures (MTCs 2 and 3)
S3
Seafloor
MTC 1
Evacuated lower slope
MTC 2
MTC 3
Compressed upper slope
Polygonally faulted strata
Opal A/CT
Oozes
Pre-breakup
South Modgunn Arch
Hydrothermal vents
Sills
Sills
Sills
Sills
500 ms/TWT
2.0 km
b)

Figure 7.5 (previous page). a) Uninterpreted and b) interpreted north-south seismic profile across the study area. Location is shown in Figure 7.2. Magma intrusions and related hydrothermal vents are observed beneath the bottom to post-breakup sequence (Horizon 5). Polygonal faults and Opal A/CT transition are mainly limited to ooze deposits. An evacuation structure is interpreted as a local crater on the southern side of South Modgunn Arch, with an evacuated lower slope and compressed upper slope. Free gas is noticed below the BSR. H1 - modern sea floor, H2 - bottom glide plane, H3 - Top of the Kai Formation, H4 - Top of the Brygge Formation, H5 - Top of the Tare Formation.

compaction processes terminated in the study area before the north hemisphere (Quaternary) glaciations.

As effective fluid conduits, polygonal faults are identified within marine oozes of the Brygge and Kai formations, which extend throughout the mid-Norwegian margin (Chand et al., 2011). Together with a series of pipes that originated from polygonal faults, continued growth and activity of polygonal faulting since Miocene are suggested in this work (Chapter 5) (see also Berndt et al., 2003). Though the initiation of polygonal faults is still not clear, one possible hypothesis is that they were caused by fluid expulsion during Opal A to Opal CT conversion, which occurred together with an increase in sediment loading imposed by glaciogenic debris. They both contributed to confined stress conditions, which are essential to generate polygonal faults (Chand et al., 2011). Even though the strike of polygonal faults generally shows no specific orientation on a large scale of analysis, the specific dip direction polygonal faults show in the study area suggests the existence of an oriented stress field such as that imposed by gravitational loading, shear and stratigraphic heterogeneities (Turrini et al., 2017; Wrona et al., 2017b) (Fig. 5.12 in Chapter 5).

Around the South Modgunn Arch there are two groups of overlapping polygonal faults. The first group formed during a phase of compression and uplift regime affecting the South Modgunn Arch (Fig. 7.4). Above, the second group of polygonal faults shows a NW-SE strike perpendicular to the mid-Norwegian margin (Chapter 4). If one compares the northwest flank of the Storegga Slide with the west flank of the HHA, it is

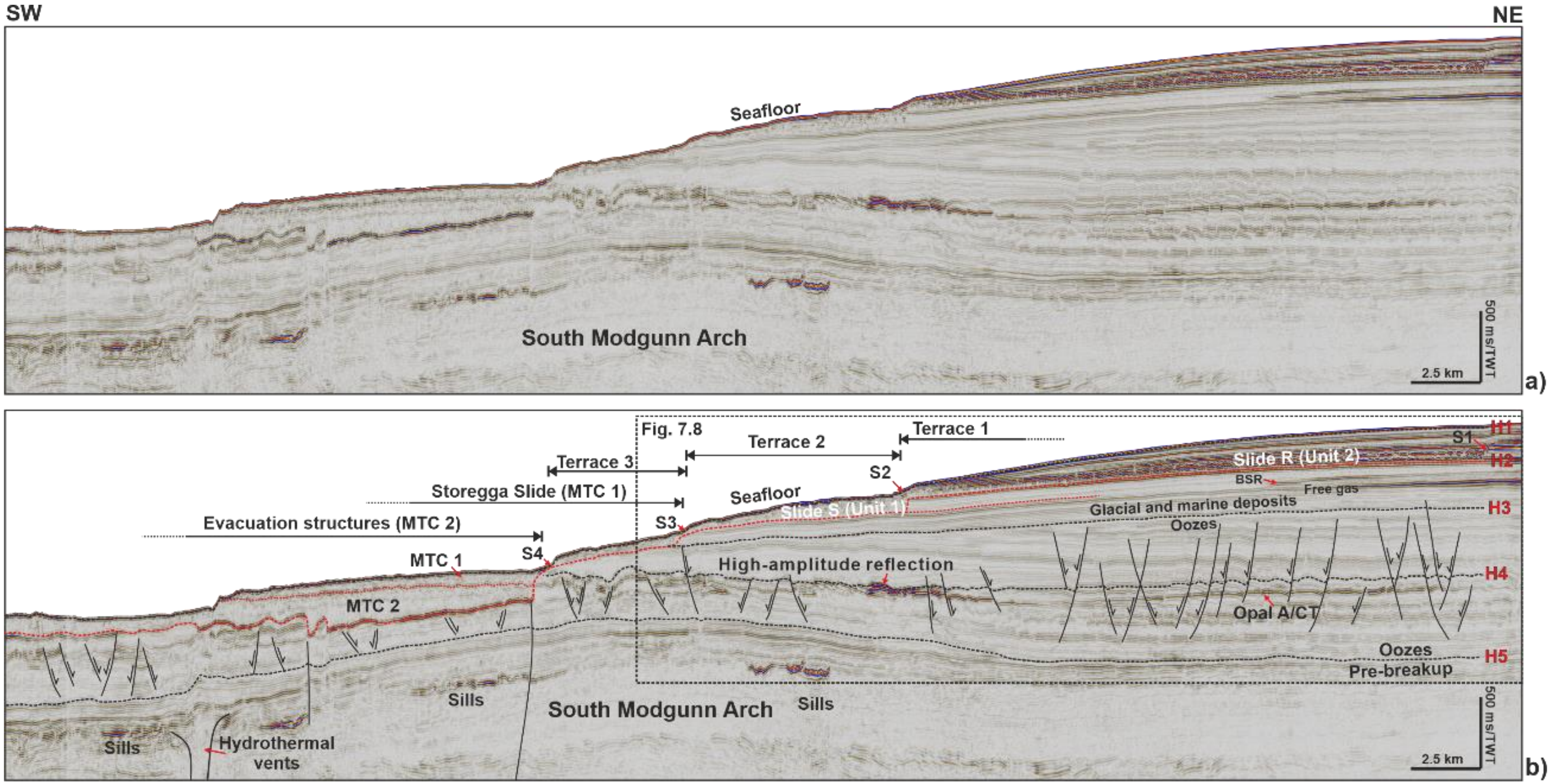

Figure 7.6. a) Uninterpreted and b) interpreted northeast-southwest seismic profile across the study area. Location is shown in Figure 7.2. Multiple glide planes are shown as red dashed lines. H1 - modern sea floor, H2 - bottom glide plane, H3- Top of the Kai Formation, H4 - Top of the Brygge Formation, H5 - Top of the Tare Formation.

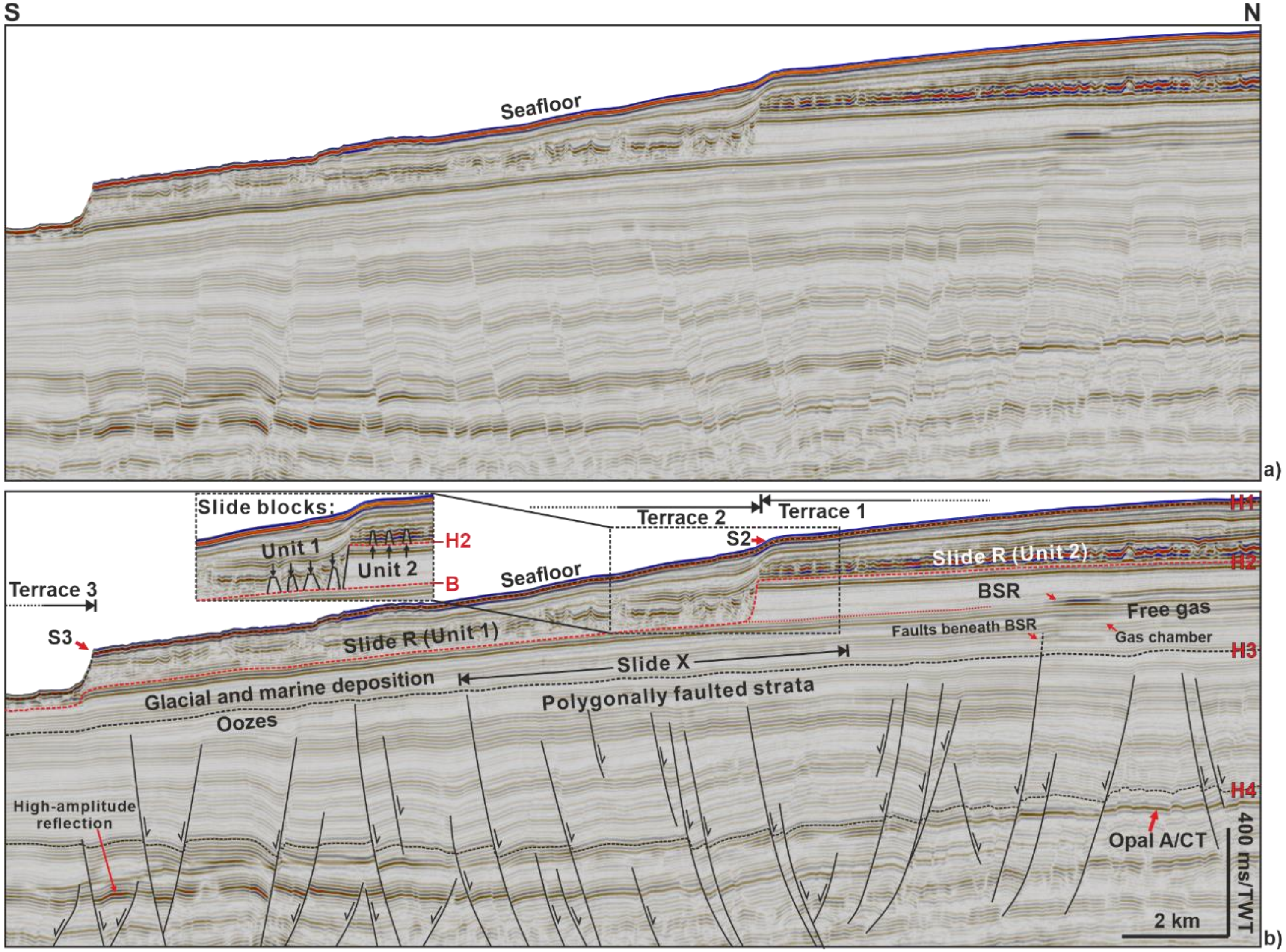
S
N
Seafloor
a)
Slide blocks:
Unit 1
Unit 2
H2
B
Terrace 2
Terrace 1
S2
H1
Slide R (Unit 2)
Terrace 3
Seafloor
BSR
Free gas
Gas chamber
Faults beneath BSR
S3
Slide R (Unit 1)
Slide X
H3
Glacial and marine deposition
Oozes
Polygonally faulted strata
H4
High-amplitude
reflection
Opal A/CT
400 ms/TWT
2 km
b)

Figure 7.7 (previous page). a) Uninterpreted and b) interpreted north-south seismic profile from Figure 7.5. Above the polygonally faulted oozes (Brygge and Kai formations), long-term instability is indicated by the presence of multiple submarine slides, including the Slide X and the Slide R, containing intervals with slide blocks. A gas chamber is observed below the BSR and next to a broad polygonal fault system.

clear that a distinct, earlier stage of polygonal faulting coincided with the uplift of the South Modgunn Arch. This early faulting event was accompanied by intensive fluid migration, as suggested by the fossilised Opal A/CT transition zone at depth, and the fluid pipes imaged in pre-Quaternary strata (Chapter 4 and 5). A similar phenomenon is also observed on the northeastern flank of the Storegga Slide, where two events of polygonal faulting were separated by the rapid emplacement of debris flows in the late Pleistocene, enhancing fluid flow and the generation of pockmarks on the sea floor (Gay and Berndt, 2007). Considering that only a few polygonal faults have grown into the Naust Formation, and the presence of fluid pipes in the same area as indicated above, long-term fluid migration could be an essential factor accompanying tectonic uplift on the South Modgunn Arch and on other continental margins across the world.

7.3.3 Fluid migration and accumulation

Evidence of fluid migration and accumulation are widely observed on continental margins, and such fluids are further considered as a critical preconditioning factor for slope failure. Along the northern margin of the Pearl River Mouth Basin, South China Sea, gas accumulated below the sea floor is recognised in the form of enhanced seismic reflections beneath MTCs within a porous basal glide zone (Sun et al., 2017). Underlying giant MTCs in the southern Scotia Sea, series of pipes sourced from magmatic sills were also observed below a glide plane of an MTD, suggesting important fluid migration and seepage before the slope failure ensued (Somoza et al., 2018). On the mid-Norwegian margin, together with the fluid pipes imaged on seismic data, both the regional fossilised opal A/CT transition and the base of

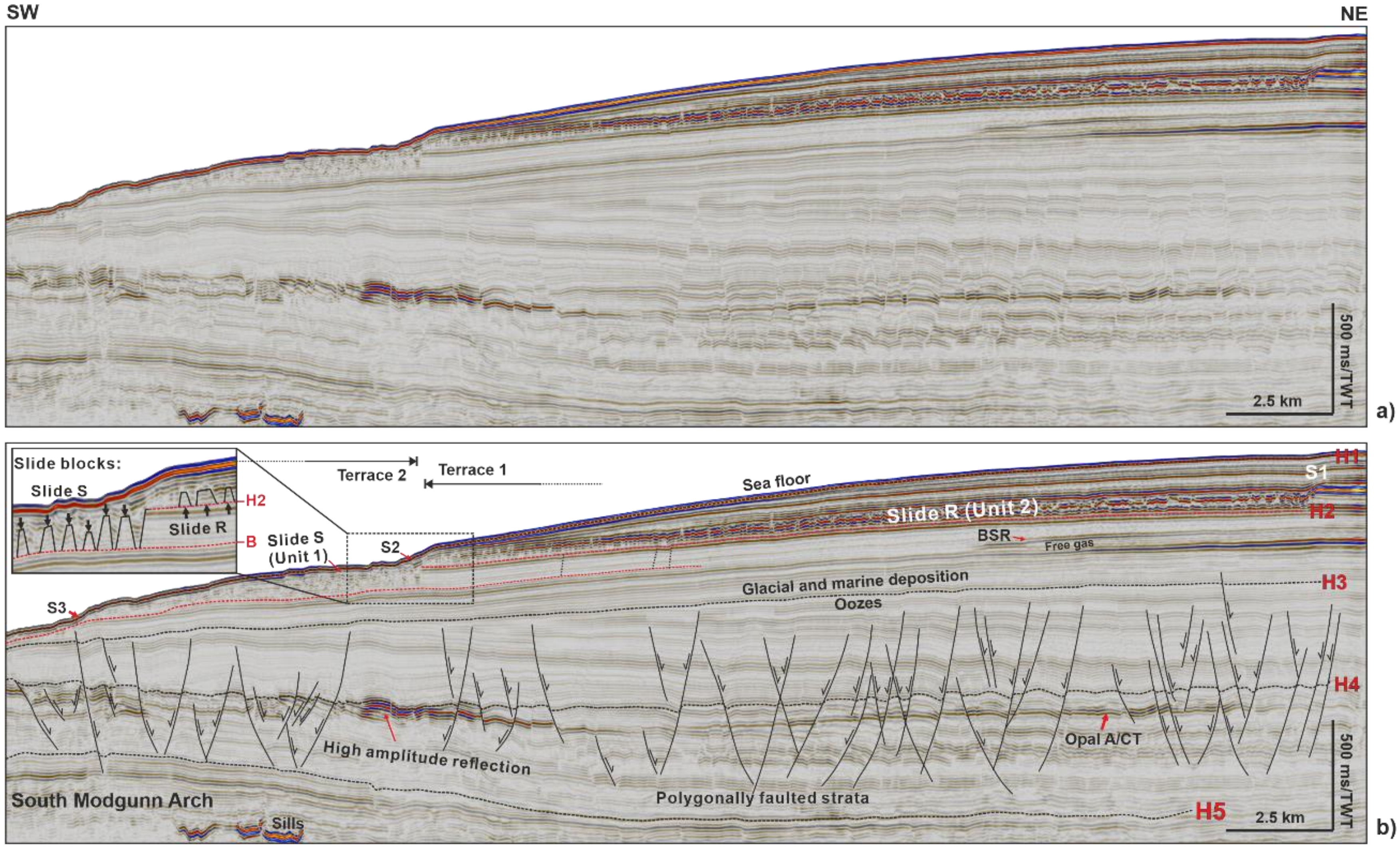

SW
NE
500 ms/TWT
2.5 km
a)
Slide blocks:
Slide S
Slide R
H2
B
Terrace 2
Terrace 1
Sea floor
Slide S (Unit 1)
S2
Slide R (Unit 2)
H1
S1
H2
BSR
Free gas
Glacial and marine deposition
Oozes
H3
S3
H4
High amplitude reflection
Opal A/CT
South Modgunn Arch
Sills
Polygonally faulted strata
H5
500 ms/TWT
2.5 km
b)

Figure 7.8 (previous page). a) Uninterpreted and b) interpreted northeast-southwest seismic profile from Figure 7.6. Both the Slide R and Slide S contain slide blocks. It is suggested that blocks in the Slide S were reactivated and readjusted during the movement of Slide R, generating a series of fractures within Slide S and R that are sub-parallel to scarp S2 (Chapter 6).

the gas hydrate stability zone relate to the expulsion and accumulation of fluid (Bünz et al., 2003; Neagu et al., 2010b). Ongoing fluid seepage is observed in shallow sediment cores and seismic data (Hustoft et al., 2007; Ivanov et al., 2007). Excess pore pressure, as a result of fluid accumulation, is thought to be an efficient process to increase slope instability by reducing vertical effective stress and frictional resistance (Kvalstad et al., 2005b). Along the headwall of Storegga Slide, a series of piezometer measurements have identified excess pore pressures beneath slide blocks, named as *spreading structures* by Strout and Tjelta (2005). In parallel, the transferred pore pressure were also modelled and presumed to reduce the stability of the distal parts of the Storegga Slide to precondition slope failure (Bryn et al., 2005a). Even though the study area is located on the northwestern flank of the Storegga Slide, in a relatively proximal part of the margin, the multiple slide blocks and pockmarks imaged in Chapter 5 have highlighted the importance of excess pore pressures, further indicating the existence of long-term fluid migration and accumulation. Thus, to better understand long-term slope instability, it is essential to characterise sub-surface fluid migration system and the corresponding build-up of excess pore pressures.

The earliest formation of fluid flow features in the study area is related to the intrusion of magmatic sills during continental breakup of NE Atlantic, at the time when the Tara Formation was deposited (Peron-Pinvidic and Osmundsen, 2018). At this time, massive hydrothermal vents and conduits were sourced from the tops and tips of sill intrusions, resulting in the formation of long-term fluid conduits that were later reutilised (Roelofse et al., 2021). In the Brygge and Kai formations, i.e. above the breakup-related Tare Formation, a suite of radial faults developed right above these hydrothermal vents by differential compaction (Omosanya et al., 2018).

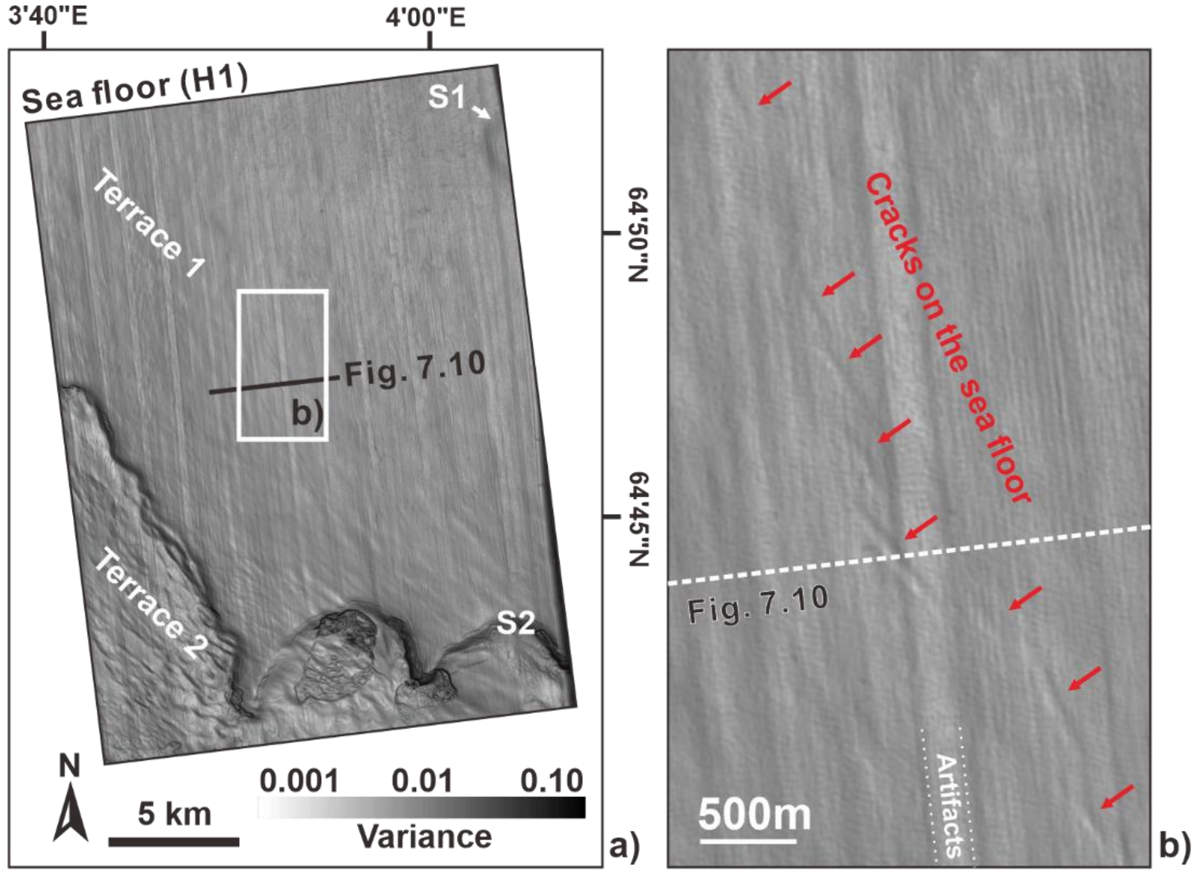

Figure 7.9. a) Variance map of the modern sea floor (Horizon 1), and b) detailed view of seafloor cracks on the same variance map. These en-echelon cracks are only observed on the variance maps when a logarithmic scale is applied, and are not observed on seismic profiles (Fig. 7.5d).

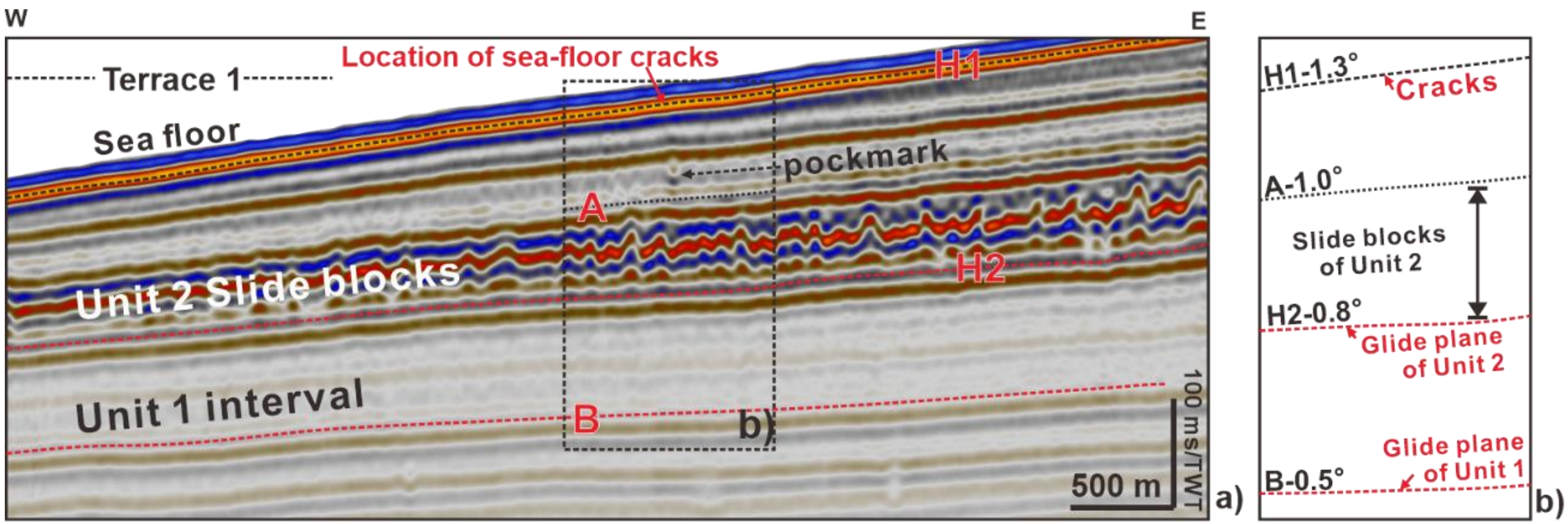

Figure 7.10. a) A west-east seismic profile crossing seafloor cracks. Its location is shown in Figure 7.9. b) Dip angle of several key seismic horizons, including the modern sea floor, the top of Slide R (Horizon A above slide blocks in Unit 2), and multiple glide planes (Horizons 2 and B).

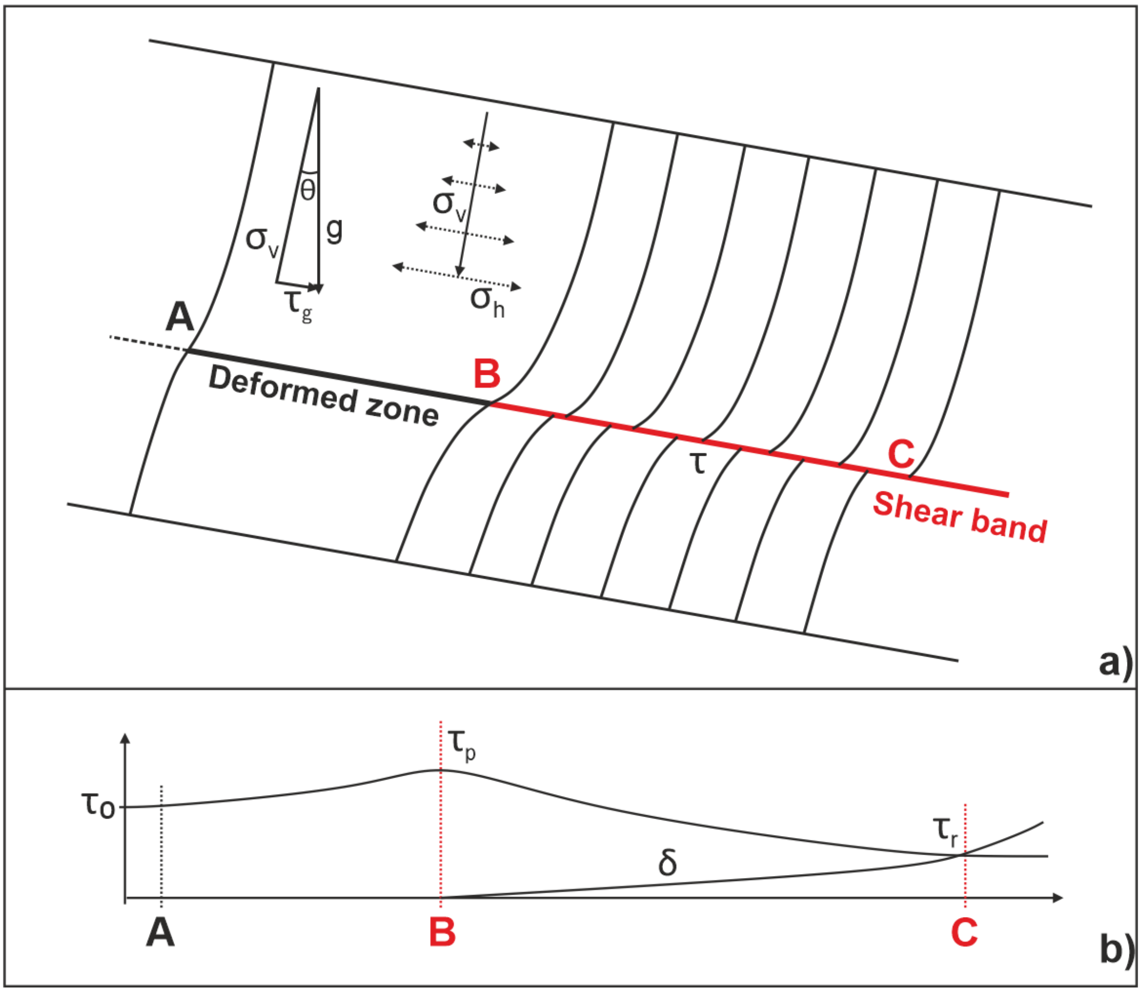

Figure 7.11. Shear stress, horizontal stress and displacement along a shear band, as an example of a basal shear zone of a landslide. Zone B-C represents the shear band where the strata have been fractured and the yield strength has been passed. Along this B-C shear band, the shear resistance decreases from its top value to residual value. On the upper slope, the zone A-B represents a deformed area where shear resistance increases from initial strength to its highest value. Along the whole shear zone A-C, the released energy is driven by the shear stress and horizontal stress, whereas the shear resistance could absorb this energy by shear strain and displacement. Figure modified from Quinn et al. (2011).

Parameters	**Value**
Dip angle of slope (θ)	0-2 [degree]
Thickness of strata above weak layer (h)	20-200 [m]
Young's modulus of strata (E')	15 [Mpa]
Poisson ratio (v)	0.4
Initial friction angle before fracture(φ)	25 [degree]
Residual friction angle after fracture(φ)	15 [degree]
Internal cohesion along weak layers(c)	4 [Kpa]
Gravitational acceleration (g)	9.8 [m/s^2]
Nominal displacement ($\bar{\delta}$)	0.5 [m]
Submerged density (ρ)	800 [kg/m^3]
Biot's ratio (α)	0.95
Width of fracture (w)	20 [m]

Table 7.1: Parameters used in the calculation of the critical excess pore pressure ratio (Pcr)

In the study area, the activity of these radial faults ceased in the early Miocene synchronously with the initial deposition of the Kai Formation (Song et al., 2020). Fluid migration through these hydrothermal vents and radial faults is observed in the Brygge Formation as local high-amplitude reflections occurring above magmatic sills, vents and radial faults (Fig. 7.6). Similar fluid-related ‘flags’ are also recorded in the Vøring Basin, where hydrothermal vent complexes acted as high-permeability zones promoting long-term lasting seep since their formations until the present day (Svensen et al., 2003).

Together with the faults described above, polygonal fault systems have been recognised as competent fluid conduits in sedimentary basins all over the world. Offshore New Zealand, polygonal faults above buried conical features became main conduits for palaeo-fluid sourced from groundwater flux, as evidenced by the palaeo-pockmarks generated beneath the modern sea floor (Hoffmann et al., 2019; Waghorn et al., 2018). In the Lower Congo Basin, accumulated thermogenic fluid migrated from palaeo-channels (reservoirs) to hydrate stability zones via polygonal faults, before reaching the sea floor via pipes and pockmarks (Gay et al., 2006). On the mid-Norwegian margin, polygonal faults were preferentially formed within the ooze-rich Brygge and Kai formations and have been identified as fluid conduits since their initial formation in the Miocene (Berndt et al., 2003). In the Nyegga area, located around the Northeastern flank of the Storegga Slide, a complex of shallow chimneys and pockmarks formed above gas hydrates and polygonal faults suggests long-term fluid migration generated active seeps on the modern sea floor (Hustoft et al., 2007; Mazzini et al., 2006).

A first key result in this thesis is the observation that fluid chimneys and gas chambers are located near the upper tips of polygonal faults, a character further demonstrating that long-term fluid migration occurs through polygonal faults (Chapter 4). Together with the interaction between two groups of polygonal faults and other types of faults, a well-developed fluid conduit system above the South Modgunn Arch would have contributed to the build-up of excess pore pressures within the Naust Formation, promoting slope instability (Fig. 7.7).

The phenomena leading to the diagenesis and dehydration of marine oozes constitute another source of fluids on continental margins (Urlaub et al., 2018). During the diagenesis of siliceous oozes, high porosity Opal-A is transformed into denser crystalline Opal-CT before experiencing further dehydration to quartz, a process leading to the expulsion of pore fluids (Isaacs, 1981; Kastner, 1981). This process is controlled by temperature and time and can be enhanced by tectonic events and rapid deposition, until the sub-surface strata where it occurs is fossilised as a *diagenetic front* (Wrona et al., 2017a). Along the NE Atlantic margin, fossilised Opal A/CT transformation is generally recognised in the form of bottom-simulating reflectors (BSR), though locally irregular, with a similar polarity to the sea floor – a seismic character that contrasts with BSRs formed at the gas hydrate stability zone (Davies and Cartwright, 2002). On the mid-Norwegian margin, Opal A/CT transition zones have been dated between the Late Miocene and Early Pliocene, and identified over deformed regional structures such as anticlines and synclines (Neagu et al., 2010b). In the study area, this same Opal A/CT shift was accompanied by tectonic uplift on the South Modgunn Arch from Late Miocene to the Pliocene (Chapter 5).

The second key result in this work is that ooze-related (diagenetic) fluid expulsion occurred before the deposition of the glacial-marine Naust Formation, which hosts most of the Quaternary mass-transport deposits studied in the study area (Chapter 5). Hence, considering that polygonal faults are interpreted to have formed concomitantly to the Opal A/CT diagenesis, fluid released during both events increased Quaternary slope instability due to the provision of long-term fluid conduits via the polygonal faults, rather than through the triggering of short-term fluid expulsion as suggested in Davies et al. (2009).

7.4 From local slope undercutting to regional instability: A physical analysis of gravitational spreading

Gravitational spreading structures, also known as subaqueous lateral spreading, have been recognised over the Modgunn Arch near landslide headwalls, responding to local slope undercutting to form a series of 'stretched' slide blocks with well-defined chasms (Figs. 7.7 and 7.10). Due to their widespread distribution and remarkable geometry, multiple mechanical models have been proposed to explain such a gravitational spreading phenomenon, focusing on simulating the effect of glide-plane propagation, the role of lateral support losses (or undercutting), sediment loading, and pore-pressure build-up as triggers of gravitational spreading in specific parts of the Norwegian margin (Alves, 2015a; Bradley et al., 2019; Kvalstad et al., 2005a; Micallef et al., 2007b).

In this sub-chapter, seismic reflection data from the northern flank of Storegga Slide are combined with well and experimental data to determine the precondition factors leading to the upslope propagation of glide planes along weak layers. This sub-chapter corroborates that: **a)** after local slope undercutting, the strength of discrete weak layers is the primary factor controlling the propagation of the glide plane in an upslope direction; **b)** beneath a gentle slope with a relatively small sediment load, excess pore pressure favours the growth of glide planes; **c)** locally, excess pore pressures can be reduced via hydraulic fractures rather than leading to glide-plane propagation. This chapter not only reveals an extended unstable upper slope around the Storegga Slide, by recognising new fractures on the modern sea floor, but also provides new insights into the propagation of glide planes due to slope undercutting.

7.4.1 Physics of slope instability and its geological setting

Slope instability is usually triggered by one or multiple factors such as rapid deposition, earthquakes and dissolution of gas hydrate (Talling et al., 2014). On the toe area of submarine slides, where retrogressive slope failure is commonly initiated, short-term triggers include excess pore pressure induced by downslope fluid flow, sediment loading on the upper part of the continental slope, and earthquakes initiating local slumps and debris flows (Masson et al., 2010; Piper et al., 1999). After slope undercutting removes support from the toe areas of continental slopes, shear strain is concentrated on specific layers, reducing their strength and leading to the propagation of failure upslope (Bryn et al., 2005a). Along the upper headwall of the Storegga Slide, the last recorded phase of slope failure is observed as regional slide blocks formed above a very gentle glide plane with about 1^{o} in gradient (Haflidason et al., 2005; Micallef et al., 2007a). In this thesis, instability features vary from local slumps along slide scarps, to regional slide blocks and multiple erosional features that record long-term instability (Chapter 6).

Slide blocks formed above well-defined glide planes are observed below multiple mass-transport complexes (Chapter 5). They are similar to other blocks documented near the headwalls of submarine landslides in northern Svalbard, northern Gulf of Mexico, Northwest Australia, and on the Norwegian margin (Micallef et al., 2007b; Sawyer et al., 2009; Vanneste et al., 2006; Wu et al., 2021). The development of these gravitational spreading structures evolved, in the areas mentioned above, following a retrogressive failure mode with coherent slide blocks progressively forming above a gently sloping weak layer, generating a deformed sea floor with a series of parallel ridges and chasms (Alves, 2015a; Gauer et al., 2005). The initiation and propagation of its glide plane in weak layers has been widely discussed (Alves, 2015a; Bradley et al., 2019; Kvalstad et al., 2005a).

Increases in pore pressure, and the subsequent decrease in the strength of discrete layers, are believed as primary factors initiating and maintaining regional slope failure (L'heureux, 2012; Sultan et al., 2004a). Along the Norwegian margin, low-permeability weak layers typically occur within clay-rich Naust Formation, accompanied with charged fluid and corresponding excess pore pressure from oozes below (Bryn et al., 2003; Sultan et al., 2004a; Trincardi et al., 2004). Rapid deposition and compaction of sediment on the continental margin during the Holocene deglaciations enhanced permeability anisotropies in slope sediment, leading once more to local excess pore pressures beneath less permeable layers (Leynaud et al., 2009, 2007). Together with regional glacioisostatic rebound and associated seismic events as ultimate triggers, retrogressive slope failure occurred above the strain-softening weak layers, generating slide blocks with slight rotations and minor displacements (Bryn et al., 2003; Bull et al., 2009b; Micallef et al., 2007b).

To clarify the precondition to glide-plane propagation along weak layers, excess pore pressures, the strength of discrete layers, the presence of local structures, sediment loading and slope steepening, are considered in this section. Aiming at discussing the role of weak layers and slope undercutting in the triggering of submarine landslides, this section focus on the following aspects:

a) How can the strength of weak layers control the propagation of glide planes?

b) Why is the excess pore pressure a significant precondition favouring the propagation (and generation) of fractures in weak layers?

7.4.2 Weak layers and excess pore pressure

In contrast to the headwall and the northeast flank of the Storegga Slide, gravitational spreading structures in the study area - including weak layers, glide plane and slide blocks - are observed beneath the modern sea floor (see multiple glide planes and units with slide blocks in Figs. 7.7 and 7.8). Beneath these structures, multiple glide planes following weak layers are imaged as high-amplitude negative reflections with an opposite polarity to the sea floor (Fig. 7.10). Previous research has suggested the existence of multiple glide planes beneath the Unit 2 slide blocks (marked as the negative-polarity horizon H2 in Fig. 7.10). Sea-floor cracks (Fig. 7.9), also observed above propagated glide planes, point to potential weak layers beneath the modern sea floor.

In the Naust Formation, excess pore pressures are recorded beneath the gas hydrate stability zone and regional subsurface pockmarks (Chapter 5). BSRs in this unit are interpreted as negative reflections cross-cutting the slope strata (Haacke et al., 2007) (Figs. 7.7 and 7.8). Below these BSRs, an interval with high-amplitude reflector indicates the accumulation of free gas (Bünz and Mienert, 2004) (Figs. 7.7 and 7.8).

Multiple regional pockmarks are also observed beneath the modern sea floor and early Quaternary slides X and Y (Chapter 5). This thesis considered that the most likely reason for this excess pore pressure is fast deposition of slope strata accompanying the fast expulsion of fluid accumulated in glacial-marine sediment (Leynaud et al., 2007). For instance, in the Gulf of Mexico, hydrostatic stresses near the sea floor (<200 mbsf) can rise 70% within quickly deposited impermeable layers (Flemings et al., 2008). This seems to fit well with data from the northeastern flank of the Storegga Slide, where extensive fluid venting is explained by increased pore pressure during the fast progradation of sediment onto the mid-Norwegian margin, before the onset of the Storegga Slide (Hustoft et al., 2009).

7.4.3 Strength of weak layers as the primary trigger of slope instability

For brittle rocks, the relationship between normal stress, shear strength and material cohesion can be described by the Mohr-Coulomb failure criterion:

$$T = \sigma_n \tan\varphi + c$$

Equation 7.1

$$\tau_g = (\rho_{sat} g h - \alpha Pp) \sin\theta$$

Equation 7.2

where

T = shear strength

σ_n = effective normal stress, could be reduced by pore overpressure

φ = the angle of internal friction

c = the internal cohesion of rock.

τ_g = gravitationally induced shear stress on glide plane with dip angle θ

Pp = pore pressure, including the hydrostatic pressure and pore overpressure

h = thickness of strata above glide plane

θ = dip angle of slope

ρ_{sat} = saturated rock density,

Thus, when shear strength (T) is equal to shear stress (τ_g), tanφ represents a critical frictional coefficient along the fracture plane (blue line in Fig. 7.13).

Submerged density (ρ) is also used in this study, defined by the difference between saturated rock density (ρ_{sat}) and water density (ρ_w), considering the Biot's ratio (α):

$$\rho = \rho_{sat} - \alpha\rho_w$$

Equation 7.3

Even though the Coulomb-Mohr failure criterion is widely used to calculate the shear strength (T) of rocks and sediment in laboratory experiments (Equation 7.1), the critical frictional coefficient ($\tan\varphi$) resisting the gravitationally induced shear stress on 1° glide planes (τ_g in Equation 7.2) is only in the order of 0.01-0.02 (Fig. 7.12), a value much lower than the cohesive strength of clay-rich sediment (Ikari and Kopf, 2011). A presumed reason for such low values of friction is that the stress concentrated on shear zones (basal shear zones) dramatically decreases the strength of these recently-formed basal shear zones, maintaining (and promoting) the propagation of the glide plane of landslides within a positive feedback process (Quinn et al., 2011).

Considering the balance of energy during fracturing and faulting, the J-integral of crack mechanics is used in this sub-section as the principal fracture-propagation criterion (Equation 7.4) (Palmer and Rice;, 1973). The minimum value of the initial glide plane (l in Equation 7.4) is assumed to be the size of end region (ω) (Equation 7.6), where the shear strength decreases from τ_p to τ_r (Puzrin et al., 2017; Quinn et al., 2011). During the propagation of glide plane, the released geopotential energy is comprised of both weight component (τ_g) and horizontal stress as part of body force (σ_h) (Fig. 7.11). On opposite, this energy could be absorbed by shear stress (τ_r) and displacement (δ) during sliding process (Fig. 7.11). The criterion for the propagation of glide planes is based on the J-integral, which is an energy balance type of the Griffith theory and independent form path (Palmer 1973). Its dimensionless form is expressed:

$$((\tau_g - \tau_r)l/h + p^0)/(\tau_p - \tau_r) = \sqrt{}((2E'/(\tau_p - \tau_r)) * (\bar{\delta}/h))$$

Equation 7.4

where

l = critical (minimum) length to initiate the propagation of glide plane

E' = Young's modulus of deformed strata

$\bar{\delta}$ = a nominal displacement, defined by

$$\bar{\delta} = \int (\tau - \tau_r)d\delta/(\tau_p - \tau_r)$$

Equation 7.5

τ_p and τ_r = peak and residual shear strengths

p^0 = a normal lateral pressure, averaged over the height h

In this study, to simulate the critical situation after slope undercutting, a minor critical length (l) is assumed as an estimated size for the toe region (ω) (Palmer 1973; Quinn, 2011), where the shear strength decreases from τ_p to τ_r:

$$\omega \approx 125\bar{\delta}$$

Equation 7.6

Correspondingly, the critical frictional coefficient ($\tan\varphi$) for the propagation of glide plane under a varying overloading (h) is plotted in Fig. 7.12 as orange line. Under a specific strength of weak layer ($\varphi = 25°$), a potential EPP from Equation 7.4 to precondition the growth of glide plane is further expressed as critical excess pore pressure (Pe) ratio ($Pcr1$) (green line in Fig. 7.12) by:

$$Pcr = Pe/(\rho g h)$$

Equation 7.7

Due to a localised EPP can also contribute to hydraulic fractures, along which fluid upward migrate and leave seepage and pipe structure, the corresponding critical excess pore pressure (Pe) for an extension-tensile fracture is calculated from Griffith's theory (Rozhko 2007) as:

$$Pe = (k_b(\sigma_v - \sigma_h) + k_\tau + k_\sigma(\sigma_v + \sigma_h))/k_f$$

Equation 7.8

where

$k_f = 2(\beta_\tau + \beta_\sigma)$

$k_\tau = 2\sigma_T$

$k_\sigma = 1$

$k_b = 1$

$\beta_\tau = \alpha(1 - 2v)/4(1 - v)\ln(4h/w)$

$\beta_\sigma = 1 - \alpha(1 - 2v)(1 - 1/2\ln(4h/w))/2(1 - v)$

$\sigma_T = \tau - \sigma''_m$

$\tau = C\cos\varphi + \sigma''_m \sin\varphi$

$\sigma''_m = \dfrac{\sigma_v + \sigma_h}{2} - p_f$

σ_v = effective vertical stress

$\sigma_h = \sigma_v * v/(1 - v)$ = effective horizontal stress

p_f = fluid pressure

v = Poisson ratio

w = width of fracture

Correspondingly, the critical excess pore pressure ratio ($Pcr2$) for hydraulic fractures is a result from Equations 7.7 and 7.8, and plotted in Fig. 7.12 as a red line.

The maximum length (lm) of the failure surface during its propagation could be simply calculated as follows (Quinn 2011):

$$lm = \rho g h^2 / 6(\rho g h \sin\theta - \tau_r)$$

Equation 7.9

As plotted propagation criterion (Fig. 7.12), the critical frictional coefficient is about 0.2-0.3 beneath thin weak layers, decreasing with sediment loading. As the clay-rich Naust Formation is assumed to have a 25° frictional angle before failure (0.47 frictional coefficient) (Micallef et al., 2007a), a sediment loading of about 100 m is required to start the propagation of fractures without any other trigger, as represented by the intersection point between the orange line and horizontal dash line in Fig. 7.11. Under these conditions (range 3 in Fig. 7.12), the released geopotential energy, driven by weight component (τ_g) and horizontal stress (σ_h), is equal or larger than the strain energy absorbed by shear stress (τ_r) and displacement (δ) during sliding process, contributing to a phenomenon that maintains the propagation of the basal glide plane as a single fracture (Fig. 7.11). This means, in mathematical terms, that Equation 7.4 is satisfied until the breakup of strata occurs over the basal glide plane (lm in Equation 7.9), an event leading to the formation of a new headwall with reduced support (Mode 3 in Fig. 7.12).

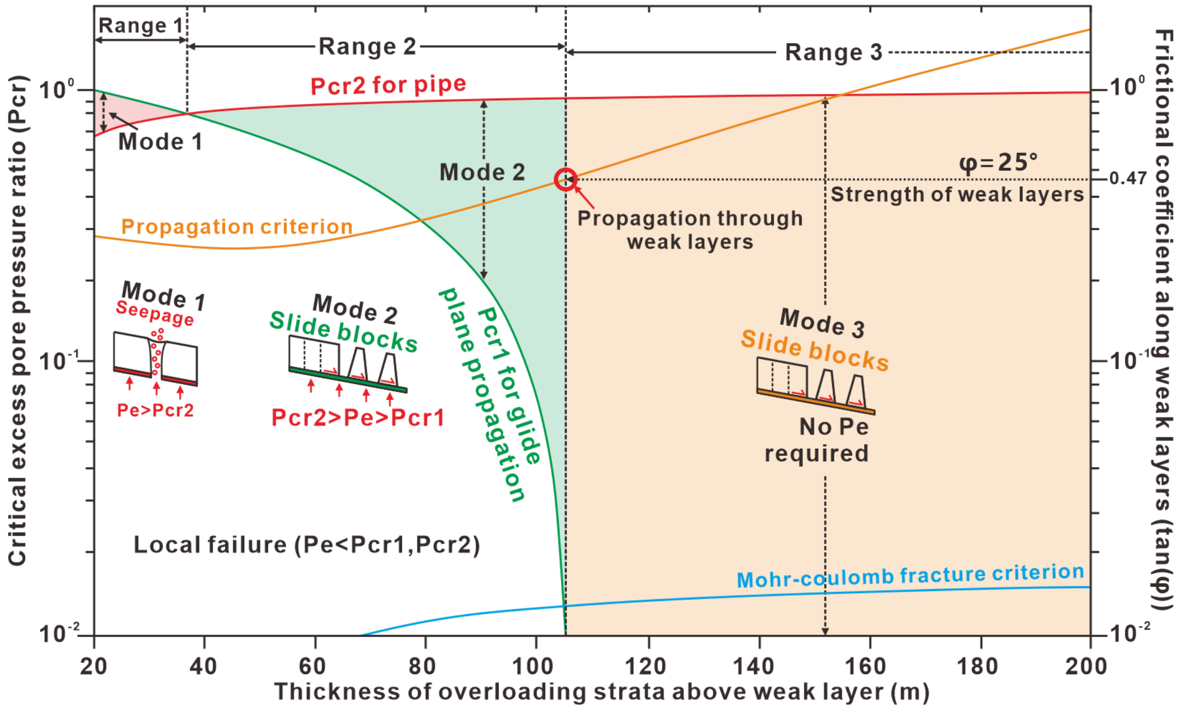

Figure 7.12. Comparison between fracture criteria and required excess pore pressure (EPP) necessary to precondition glide plane propagation. By considering the energy balance during the propagation of glide planes (J-integral in Equation 7.4), a greater strength than that assumed by the Mohr-coulomb fracture criterion (Equation 7.1) is needed to resist the propagation of a glide plane (orange line is higher then blue line). When the strength of a weak layer is reduced (as modelled assuming a 25 degree initial frictional angle in this model), sediment loading can maintain the propagation of glide plane after slope undercutting occurs (range 3) without EPP (orange area, Mode 3); Under reduced sediment loading (range 2), the existence of critical excess pore pressure ratio (Pcr) can further contribute to slope failure. Once the EPP is higher than Pcr1, the glide plane can maintain its propagation (green area, Mode 2) until the EPP is not sufficient or larger than Pcr2 (red area, Mode 1) separately. Range 1-3 represent the range of sediment loading, and Mode 1-3 are the corresponding failure modes.

Event	Interval	Everage Overload (m)	Dip angle (degree)	Failure mode	Required Pcr
Slide S	B - H2	50	0.45	2 - Sufficient EPP	0.68
Slide R (Unit 1)	B - A	100	0.45	2 - Sufficient EPP	0.10
Slide R (Unit 2)	H2- A	55	0.8	2 - Sufficient EPP	0.62
Pockmarks within Naust FM.		25	0.5-1.0	1 – Fluid seepage	0.72
Slide X and Y		40	0.5-1.0	2 - Sufficient EPP	0.78
Ormen Lange area*		135*	0.9*	3 – Sufficient overload	0.00
Slide blocks around main headwall*		45-95*	0.9*	2 - Sufficient EPP	0.2-0.6

*(Aaron et al., 2007)

Table 7.2: Parameters and results of critical excess pore pressure ratio (Pcr) calculations.

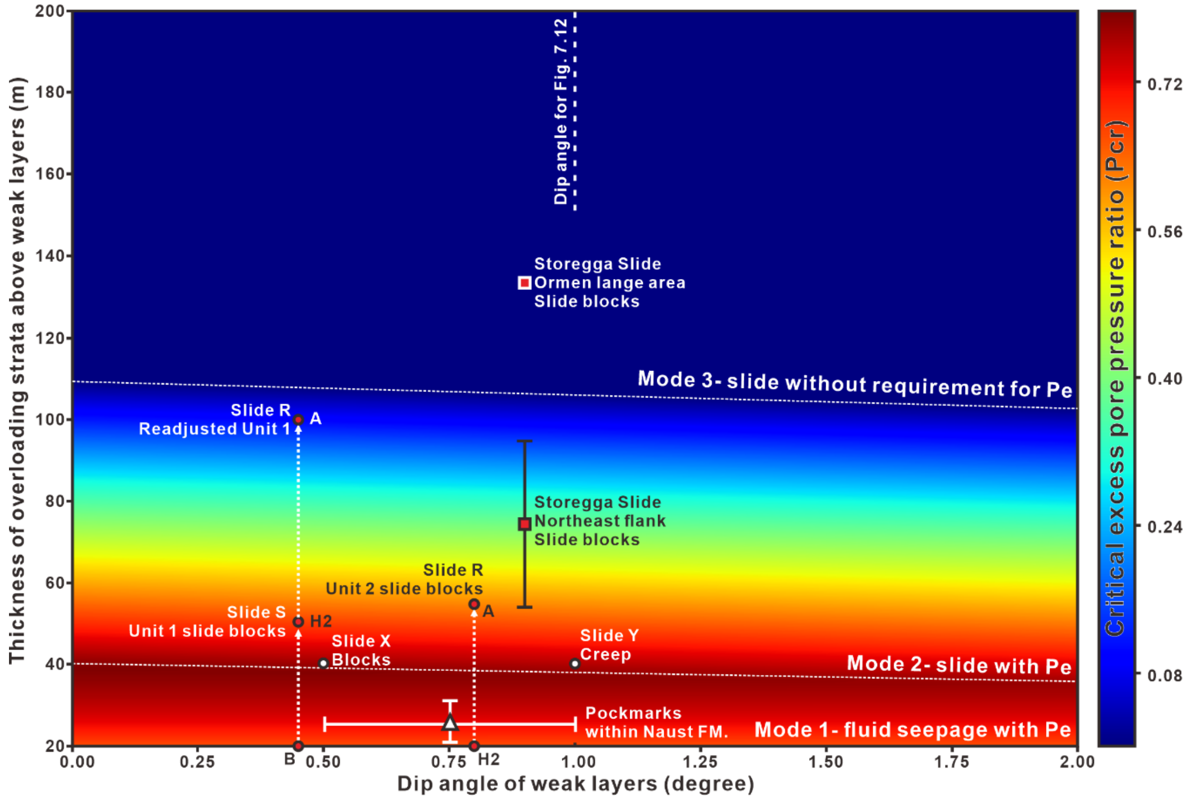

Figure 7.13. Critical excess pore pressure ratio (Pcr) as a function of dip angle and sediment loading. The graph shows the Pcr (colour coded) under different failure modes. Mode 1: excess pore pressure (EPP) is released by the formation of leakage conduits before precondition the propagation of the glide plane. Mode 2: EPP is required to precondition the propagation of the glide plane along weak layers after the continental slope is undercut. Mode 3: No EPP is required during the propagation of the glide plane. The red and white dots represent different circumstances in which slope failure and pockmarks where formed in the study area in this thesis, and around the Storegga Slide (Table 7.2).

7.4.4 Excess pore pressure favouring the growth of glide planes

The occurrence of gravitational spreading structures is not limited to thick strata; it is also observed along the edges of the Storegga Slide in intervals thinner than 100 m (Kvalstad et al., 2005b; Micallef et al., 2007a), leading to the postulate that excess pore pressures occur in these regions (Leynaud et al., 2007). Based on Equation 7.4, when sediment loading is lower than a critical value (left boundary of range 3 in Fig. 7.12), a certain value of excess pore pressure, increasing with decreasing sediment loading (green line in Fig. 7.12), can maintain the growth of a glide plane after slope undercutting occurs (Mode 2 in range 2, Fig. 7.12). Its value is expressed as $Pcr1$, representing the ratio to sediment loading stress (Equation 7.7).

The equations above are helpful to rate the relative importance of discrete triggering factors of slope instability but, nonetheless, the increase of excess pore pressure is not unlimited on a given continental slope. In the study area, fluid pockmarks and pipe structures indicate that the release of fluid on the (palaeo-) sea floor occurs above a certain threshold value of pore pressure (Fig. 5.13 in Chapter 5). Beneath BSRs, where gas hydrates begin to dissolve in the available pore space, free gas is accumulated to build up excess pore pressure (Paull et al., 2008). When excess pore pressure reaches a value large enough to fracture the adjacent strata, pipe structures can form from BSRs expelling fluid to the sea floor, or feeding it to high permeability layers (Elger et al., 2018; Rozhko et al., 2007). A critical value excess pore pressure can be estimated using Equation 7.8 and expressed as $Pcr2$ (see red line in Fig. 7.12). Thus, excess pore pressures high enough to trigger gravity spreading structures are limited between $Pcr1$ and $Pcr2$ in the range 2 (see area between green and red lines in Fig. 7.12). A distinct condition is given in Fig. 7.12 as range 1, where the value of $Pcr2$ is lower than $Pcr1$ – this suggests that the build-up of excess pore pressure is hindered (i.e. fluid is released) before a high enough pore-pressure value leads to the propagation of a glide plane (Mode 1 in Fig. 7.12).

Seismic data from the mid-Norwegian margin and laboratory experiments with gas hydrates have suggested that the occurrence of a gas-hydrate stability zone (GHSZ) and related BSR is limited to a specific depth range, which is dependent on temperature and pressure (Mienert et al., 2005). Due to the positive correlation observed between sediment loading and excess pore pressure required to fracture the GHSZ (Equation 7.8), the critical excess pore pressure forming pipes sourced from gas hydrates should be sufficient to fracture all overlying strata, rather than stopping inside the low-permeable Naust Formation, as observed by the distribution of pockmarks around the Storegga Slide (Cartwright and Santamarina, 2015; Colin, 2020).

A third key result in this thesis is that, in the Naust Formation, the different permeability values recorded amongst marine and glacial deposits not only favour the release of gas from BSRs, but also contribute to the long-term accumulation of fluid and build-up of excess pore pressure in strata, as suggested by the irregular BSR and several fluid pipes observed at distinct intervals (Figs. 7.7 and 7.10). Consequently, due to the fact that excess pore pressure forming fluid pipes is larger than that required to propagate the MTCs glide-planes when draped by enough sediment ($Pcr2 > Pcr1$ in range 2 and 3, Fig. 7.12) it is reasonable to assume that. during the multiple submarine slides in the Storegga Slide, excess pore pressure within the Naust Formation was large enough to favour the propagation of glide plane, suggest an estimated Pcr value of around 0.2–0.3 at the time of occurrence of the Storegga Slide (Kvalstad et al., 2005b).

7.4.5 Development of long-term instability over the Modgunn Arch

In contrast to the main headwall and northern flank of the Storegga Slide, where gravitational spreading structures occur in the form of slide blocks (Kvalstad et al., 2005a; Micallef et al., 2007b), palaeo-seafloor fractures (cracks) occur above the slide blocks of Slide R (Chapter 5). In parallel, multiple glide planes and fluid pipes are observed beneath these slide blocks, suggesting the long-term build-up of excess pore pressure and subsequent slope instability (Chapter 5). Due to variations in slope gradient and sediment loading above weak layers (Fig. 7.10), the precondition of these slide blocks and pipes are estimated and plotted in Table 7.2 and Fig. 7.13, where range 1-3 and mode 1-3 represent the three different unstable circumstances and failure modes separately (Figs. 7.12 and 7.13).

Based on the results of Chapter 6, Unit 1 was unstable and hosted Slide S before being partly reactivated by Slide R (Fig. 7.2). During the initiation of Slide S within Unit 1 (Fig. 7.8), sediment was about 50 m above its basal glide plane (see height of Slide S blocks in Fig. 7.8). This corresponds to Mode 2 in Fig. 7.12, where sufficient excess pore pressure is a key preconditioning factor for the propagation of a glide plane to occur (see point 'H2, Slide S above B' in Fig. 7.13). After Slide S was initiated, at least 55 m strata was deposited above horizon H2 until Slide R occurred in Unit 2 (A - H2 in Fig. 7.10, point 'A, Slide R above H2' in Fig. 7.13). Sediment accumulated above the glide plane of Unit 1 (Horizon B) reached at a value of about 100 m (point 'A, Slide R above B' in Fig. 7.13). Hence during Slide R, once the excess pore pressure was sufficient to precondition the sliding blocks in Unit 2 (the point 'A' above H2 in Fig. 7.13), it would have been large enough to reactivate the slide blocks in Unit 1 (the point 'A' above B in Fig. 7.13), as these latter blocks would have required relatively small values of pore pressure to be remobilised (the critical EPP on point A above H2 is higher than the point above B in Fig. 7.13). This simultaneous gliding along multiple weak layers is recorded by interactions between Unit 2 slide blocks and Unit 1 in seismic data (Chapter 6).

During the Storegga Slide, slope undercutting was limited by scarp S3 (Fig. 7.2). Without a deeply-cut upper continental slope, a limited readjustment of Unit 1 slide blocks is suggested in this work based on the presence of seafloor cracks and local slumps along scarp S2 (Chapters 5 and 6). On the upper continental slope (Terrace 1), seafloor cracks are observed without further fracturing below (Figs. 7.9 and 7.10), suggesting limited near-seafloor sliding and deformation (Chapter 5). Therefore, a fourth key result in this thesis is that instability around the Storegga Slide is not only limited by the scarps where local slope failure was initiated, but also extends to the gentler upper slope in the form of seafloor cracks generated by the propagation of glide planes (Figs. 7.9 and 7.10). Since the current depth of those potential weak layers (between Horizon A and 1) belong to range 1-2 (less than 100 m in Fig. 7.12), further gravitational instability could be initiated by local slope undercutting with or without excess pore pressure, i.e. depending solely on slope gradient and sediment loading (Fig. 7.13).

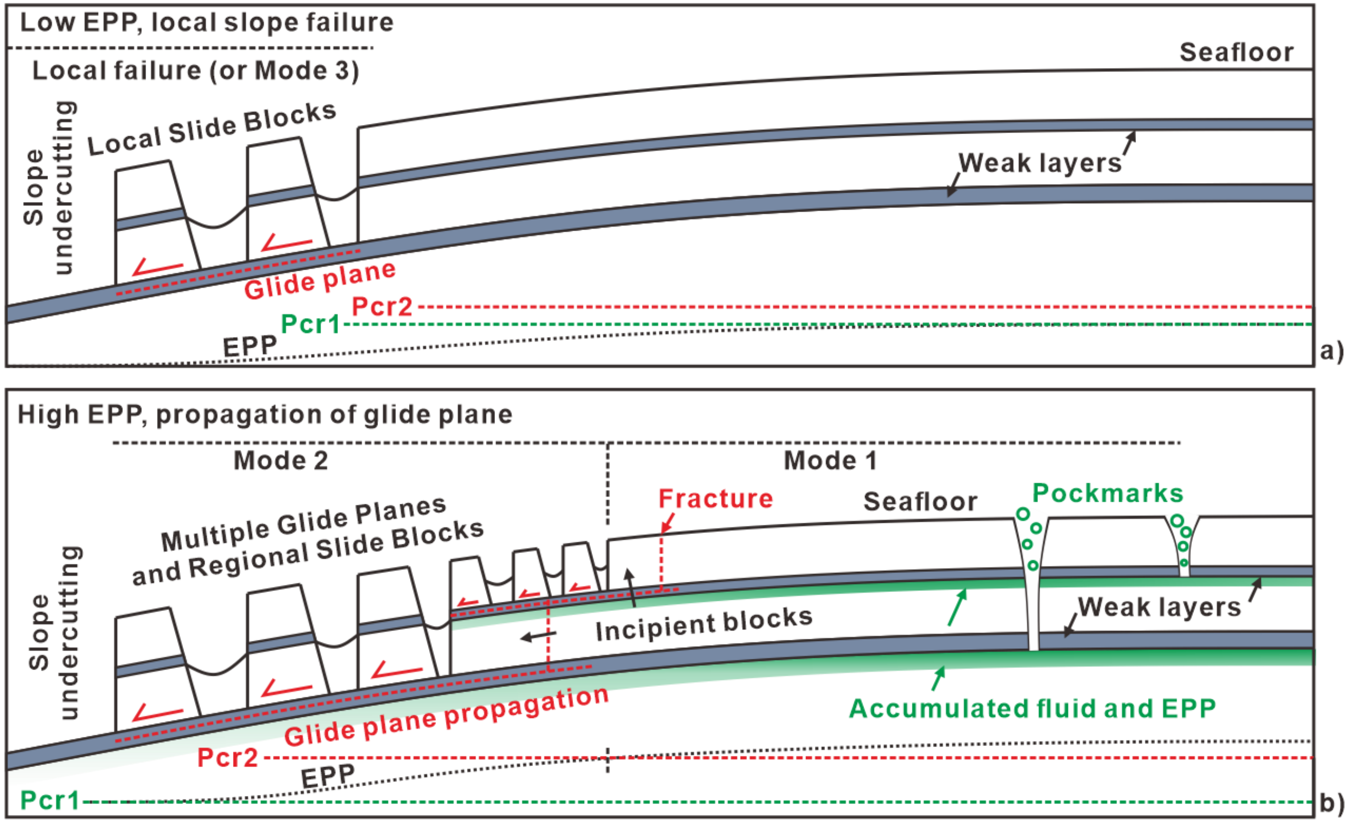

Figure 7.14. Schematic development of an area of slope instability, from local slope undercutting to submarine lateral spreading. a) Without sufficient excess pore pressure (EPP < Pcr 1), undercutting of the continental slope increases instability around its scarp, creating local slope failure around the undercut area (shown by Mode 3 above , in which sediment loading is enough to trigger instability). b) With sufficient excess pore pressure (EPP > Pcr 1), the glide plane further propagates along weak layers (Mode 2), until pore pressure is not enough to support this propagation, with excess fluid pressure being released by pipes and pockmarks (Mode 1).

7.4.6 From local slope undercutting to regional gravitational spreading

The balance between released geopotential energy, comprised of weight component and horizontal (body) stress, and absorbed fracture energy, such as shear stress during strain and displacement, is considered as the critical situation for glide plane propagation by the J- integral (Equation 7.4). After local slope undercutting, a headwall with reduced support is exposed as a scarp on the sea floor (such as S3 in Fig. 7.7). Above weak layers terminating against these same scarps, the released geopotential energy is no less than the absorbed strain energy during lateral sliding (Equation 7.4), and the glide plane will propagate beyond the scarp until the final break-up (separation) of an overlying slab (Equation 7.9). Sediment loading along steep slopes and weak layers with low strength (represented by the higher thickness of overloading and lower frictional coefficient (tan φ) value in Fig. 7.12) can efficiently maintain glide plane propagation by controlling the value of released and absorbed energy during the strain and further slide of overlying strata (the red circle in Fig. 7.12 presents a situation in which this balance is achieved without EPP). In contrast, along a gentle slope with thinner deposits accumulated above weak layers, a putative glide plane cannot maintain its propagation (the range 1 and 2 area in Figs. 7.12 and 7.13).

Without sufficient excess pore pressure and sediment loading ($Pcr < Pcr1$), local slope undercutting can only cause local slope failure in a region adjacent to where the undercut slope will occur, rather than propagating this instability upslope (Fig. 7.14a). Hence, a fifth key result in this work is that when excess pore pressure is large enough ($Pcr > Pcr1$ in Fig. 7.12), the effective normal stress is dramatically lowered along a glide plane, and geopotential energy may be enough to trigger the upslope propagation of a glide plane, specifically along the weakest layers (Mode 2 in Figs. 7.12, 7.13 and 7.14b). Sediment loading controls the excess pore pressure required to cause hydraulic fracture, limiting the formation of pipes and pockmarks (see pipe on the upper slope in Fig. 7.14b). When excess pore pressure beneath a low permeable layer is extremely high ($Pcr > Pcr2$), tensile fractures can vertically propagate to the sea floor and form high-pressure conduits for fluid (see Mode 1 and the area above the red line in Fig. 7.12). Such a process could occur not only within range 1 in Fig. 7.12, where excess pore pressure can be released before preconditioning the propagation of a glide plane ($Pcr1 > Pcr2$ in

Fig. 7.12, Mode 1 in Fig. 7.14b), but also in ranges 2 and 3 where glide plane propagation is yet to be triggered by slope undercutting ($Pcr2 > Pcr1$ in Fig. 7.12),

7.5 Limitations of this research

This thesis considered the development of long-term instability on a sub-Artic continental margin near northwest flank of the Storegga Slide, mid-Norwegian margin (Fig. 7.1). High resolution three-dimensional seismic data were used, along with the ant-tracking, slip-tendency technology, allowing for reconstructing and analysing the tectonic events affecting the study area, and map related structures and landslides. The development of polygonal faults could be studied at the meter scale, yet the resolution of seismic data is still a hindering factor in this research, as revealed by the decreased abundance of faults in the Naust Formation. Similar limitation is also shown in the identification of pipes in the Naust Formation. The width of pipes could be on only a few meters as shown in the published literature, but the distance between seismic profiles in the 3D seismic volume is beyond that value, suggesting a loss of data.

Apart from the inherent maximum resolution of seismic data, the lack of sediment core from the well 6403/6-1 has also limited a more detailed analysis of local parameters such as sediment shear strength, which is crucial in the development of slope instability. Well 6403/01 is located on the crest of the South Modgunn Arch, as the purpose of this well was to find petroleum and potential trap in this structure. However, only a few meters of MTCs were drilled above the eroded Kai Formation. The lack of borehole information in both Naust and Kai formations has limited the modelling of slope instability undertaken in this thesis. In addition, due to the lack of pore pressure data, the postulate explaining the formation of subsurface pipes and the propagation of glide planes could not be further 'ground truthed'.

Shortcomings in numerical simulation also limit a more complete knowledge of slope instability as a process. Even though the CFD approach followed in this thesis can model the development of slope failure by decreasing the viscosity and shear strength of the failed mass considering it as fluid, it neglects the presence of cohesive sediment on the continental slope that may be only slumped or even not deformed, i.e. it simply assumes that all material is potentially unstable and focuses on the relative order (and degree) of deformation in failed strata. Furthermore, the criteria for glide plane propagation used in the models can only suggest instability of a particular are on the slope under specific circumstances, rather than assuming 4D variations in the physical properties and structure with the continuous development of instability process. Thus, a series of physical models would be crucial to complement this research and understand the effect of excess pore pressure along specific weak layers.

7.6 Further work

Seismic data acquired from the northwest flank of Storegga Slide are used in the thesis. Access to more data will be crucial to verifying our model and hypothesis. Slope instability on the mid-Norwegian margin was initiated by the Northern hemisphere glaciations in early Quaternary, and recorded as multiple slope failure events within the Naust and lower formations. Along the south flank of the Storegga Slide there are at least two extra slides not documented in this thesis, the Tampen Slide and More Slide, both of which are related to the development (and failure) of weak layers on the continental slope. On the northeast flank of the Storegga Slide, both regional pipes and obvious sea floor cracks are observed, as well as the headwall of Slide W, S and R. By comparing the features of these pre-Storegga slides and with the interpretation from this study, the influence of polygonal faults, fluid migration and weak layers to slope instability could be batter analysed. Moreover, this study proposed several models about the importance of weak layers and excess pore pressure. With additional data along the mid-Norwegian margin, these models could be further improved and ‘ground truthed’.

Slope instability along continental margins is a common phenomenon all over the world. Their expression varies from slides and slumps to debris flows and turbidity currents. This thesis has focused on the built-up of instability, including the precondition factors for slope failure and ensuing deformation. Highlighted in this work were the importance of weak layers and the propagation of glide planes. However, the abnormal strain of weak layers as a consequence of glide plane propagation, has yet to be clearly observed, partly because this pre-slide structure could be a transient process that is very hard to record in-situ. Thus, to verify the models in this thesis, additional numerical modelling and core tests should be carried out in the future. In parallel, even though excess pore pressures have been documented along many a continental slope, a specific validation between this pressure and development of slope failure is still lacking in the literature. A possible solution to this is extensive surveying along continental slopes such as that of the mid-Norwegian margin, monitoring seafloor deformation - including slides and cracks.

As concluded in Chapters 5 and 6, the modern Storegga Slide in still a potential failure zone, especially its northern flank where sea floor cracks are observed. If there is an additional survey focusing on understanding future areas predisposed to slope instability, a detailed investigation of these shallow structures could be achieved by high-resolution seismic data complemented with sediment cores and geotechnical testing.

CHAPTER EIGHT

Conclusions of this Thesis

8. Conclusions

This thesis provides a very detailed analysis of the development of extensional faults and long-term slope instability on the northwestern flank of Storegga Slide, mid-Norwegian margin. Below is a summary of the main conclusions from this extensive work:

8.1 Conclusion of Chapter 4

- The long term activity of faults in the study area is a result of the combination of tectonic uplift on a continental margin anticline (South Modgunn Arch) during the Middle Miocene, and ridge push from a mid ocean ridge afterward.
- Important fluid migration and (local) accumulation, which can weaken seafloor strata, is suggested by both borehole data and seismic interpretation.
- Multiple submarine slides could have scarps vertically overlapped and inherited from older episodes of faulting.

8.2 Conclusion of Chapter 5

- Two types of slope failure, shallow sliding blocks (Slide X) and creep (Slide Y), comprise the oldest instability events in the study area, with fluid accumulation in glacial-marine deposits being shown as primary factors in their triggering.
- Density reversal is a significant trigger of instability, especially above liquefied low-density marine oozes.
- A group of cracks on the modern sea floor above regional pockmarks suggests an early stage of slope failure on the upper continental slope.

- Local instability is rare at present but can be expected if local conditions promote higher pore pressures and slope angles.

8.3 Conclusion of Chapter 6

- Turbidite and debris channels observed on the sea floor record long-term slope instability by increasing their sinuosity, thus revealing sediment creep inside older MTCs.
- Together with local slope failure above pre-existing fractures, the local readjustment of slide blocks is evidence for long-term slope instability. CFD models show that readjustments contribute to the fracturing of overlying strata to the sea floor, as also revealed by the cracks, faults, and slumps above buried slide blocks.
- The loss of lateral support from slope undercutting has the potential to propagate deformation along weak layers, and destabilise fractures and slide blocks. As presented in the CFD models, after slope undercutting the upslope-propagating weakening process along weak layers preconditions the further softening, faulting and sliding in relatively stiff and intact slope strata.
- The built-up of a permanent weak frame is a key factor preconditioning the long-term instability, including weak layers, pre-existing fractures and MTCs. After the initial sliding process ceases, and once a certain condition is satisfied (such as a further slope undercutting), slope instability can be resumed.

References

References

Aarnes, I., Planke, S., Trulsvik, M., Svensen, H., 2014. Contact metamorphism and thermogenic gas generation in the Vøring and Møre basins, offshore Norway, during the Paleocene–Eocene thermal maximum. J. Geol. Soc. London. 172, 588–598. https://doi.org/10.1144/jgs2014-098

Alendal, G., Berntsen, J., Engum, E., Furnes, G.K., Kleiven, G., Eide, L.I., 2005a. Influence from "Ocean Weather" on near seabed currents and events at Ormen Lange. Mar. Pet. Geol. 22, 21–31. https://doi.org/10.1016/j.marpetgeo.2004.10.011

Alendal, G., Berntsen, J., Engum, E., Furnes, G.K., Kleiven, G., Eide, L.I., 2005b. Influence from 'Ocean Weather' on near seabed currents and events at Ormen Lange. Mar. Pet. Geol. 22, 21–31. https://doi.org/10.1016/J.MARPETGEO.2004.10.011

Alves, T., Fetter, M., Busby, C., Gontijo, R., Cunha, T.A., Mattos, N.H., 2020. A tectono-stratigraphic review of continental breakup on intraplate continental margins and its impact on resultant hydrocarbon systems. Mar. Pet. Geol. 117, 104341. https://doi.org/10.1016/j.marpetgeo.2020.104341

Alves, T.M., 2015a. Submarine slide blocks and associated soft-sediment deformation in deep-water basins: A review. Mar. Pet. Geol. 67, 262–285. https://doi.org/10.1016/j.marpetgeo.2015.05.010

Alves, T.M., 2015b. Submarine slide blocks and associated soft-sediment deformation in deep-water basins: A review. Mar. Pet. Geol. 67, 262–285. https://doi.org/10.1016/j.marpetgeo.2015.05.010

Alves, T.M., 2012. Scale-relationships and geometry of normal faults reactivated during gravitational gliding of Albian rafts (Espírito Santo Basin, SE Brazil). Earth Planet. Sci. Lett. 331–332, 80–96. https://doi.org/10.1016/j.epsl.2012.03.014

Alves, T.M., Omosanya, K., Gowling, P., 2015. Volume rendering of enigmatic high-amplitude anomalies in southeast Brazil: A workflow to distinguish lithologic features from fluid accumulations. Interpretation 3, A1–A14.

https://doi.org/10.1190/INT-2014-0106.1

Anell, I., Thybo, H., Artemieva, I.M., 2009. Cenozoic uplift and subsidence in the North Atlantic region: Geological evidence revisited. Tectonophysics 474, 78–105. https://doi.org/10.1016/j.tecto.2009.04.006

Bacon, M., Simm, R., Redshaw, T., 2007. Structural interpretation. 3D Seism. Interpret. United Kingdom Univ. Press. Cambridge 57–101.

Baeten, N.J., Laberg, J.S., Forwick, M., Vorren, T.O., Vanneste, M., Forsberg, C.F., Kvalstad, T.J., Ivanov, M., 2013. Morphology and origin of smaller-scale mass movements on the continental slope off northern Norway. Geomorphology 187, 122–134. https://doi.org/10.1016/j.geomorph.2013.01.008

Barrett, R.S., Bellwald, B., Talling, P.J., Micallef, A., Gross, F., Berndt, C., Planke, S., Myklebust, R., Krastel, S., 2021. Does Retrogression Always Account for the Large Volume of Submarine Megaslides? Evidence to the Contrary From the Tampen Slide, Offshore Norway. J. Geophys. Res. Solid Earth 126. https://doi.org/10.1029/2020JB020655

Bartoli, G., Sarnthein, M., Weinelt, M., Erlenkeuser, H., Garbe-Schönberg, D., Lea, D.W., 2005. Final closure of Panama and the onset of northern hemisphere glaciation. Earth Planet. Sci. Lett. 237, 33–44. https://doi.org/10.1016/j.epsl.2005.06.020

Berg, K., Solheim, A., Bryn, P., 2005. The Pleistocene to recent geological development of the Ormen Lange area. Mar. Pet. Geol. 22, 45–56. https://doi.org/10.1016/j.marpetgeo.2004.10.009

Berndt, C., 2005. Focused fluid flow in passive continental margins. Philos. Trans. R. Soc. A Math. Phys. Eng. Sci. 363, 2855–2871. https://doi.org/10.1098/rsta.2005.1666

Berndt, C., Bünz, S., Clayton, T., Mienert, J., Saunders, M., 2004. Seismic character of bottom simulating reflectors: Examples from the mid-Norwegian margin. Mar. Pet. Geol. 21, 723–733. https://doi.org/10.1016/j.marpetgeo.2004.02.003

Berndt, C., Bünz, S., Mienert, J., 2003. Polygonal fault systems on the mid-Norwegian margin: A long-term source for fluid flow. Geol. Soc. Spec. Publ. 216, 283–290. https://doi.org/10.1144/GSL.SP.2003.216.01.18

Berndt, C., P, S.O., Planke, S., Eldholm, O., Mjelde, R., 2000. High velocity breakup related sills in the Vøring Basin off Norway. J. Geophys. Res. Solid Earth 105(B12), 28443–28454.

Berndt, C., Planke, S., Alvestad, E., Tsikalas, F., Rasmussen, T., 2001. Seismic volcanostratigraphy of the Norwegian Margin: Constraints on tectonomagmatic break-up processes. J. Geol. Soc. London. 158, 413–426. https://doi.org/10.1144/jgs.158.3.413

Berstad, I.M., Sejrup, H.P., Klitgaard-Kristensen, D., Haflidason, H., 2003. Variability in temperature and geometry of the Norwegian Current over the past 600 yr; stable isotope and grain size evidence from the Norwegian margin. J. Quat. Sci. 18, 591–602. https://doi.org/10.1002/jqs.790

Biot, M.A., 1955. Theory of elasticity and consolidation for a porous anisotropic solid. J. Appl. Phys. 26, 182–185. https://doi.org/10.1063/1.1721956

Boukpeti, N., White, D.J., Randolph, M.F., Low, H.E., 2012. Strength of fine-grained soils at the solid-fluid transition. Geotechnique 62, 213–226. https://doi.org/10.1680/geot.9.P.069

Bradley, K., Mallick, R., Andikagumi, H., Hubbard, J., Meilianda, E., Switzer, A., Du, N., Brocard, G., Alfian, D., Benazir, B., Feng, G., Yun, S.H., Majewski, J., Wei, S., Hill, E.M., 2019. Earthquake-triggered 2018 Palu Valley landslides enabled by wet rice cultivation. Nat. Geosci. 12, 935–939. https://doi.org/10.1038/s41561-019-0444-1

Breard, E.C.P., Dufek, J., Roche, O., 2019. Continuum Modeling of Pressure-Balanced and Fluidized Granular Flows in 2-D: Comparison With Glass Bead Experiments and Implications for Concentrated Pyroclastic Density Currents. J. Geophys. Res. Solid Earth 124, 5557–5583. https://doi.org/10.1029/2018JB016874

Brekke, H., 2000. The tectonic evolution of the Norwegian Sea continental margin, with emphasis on the Voring and More basins. Geol. Soc. London 167, 327–378.

Bromhead, E.N., 2013. Reflections on the residual strength of clay soils, with special reference to bedding-controlled landslides. Q. J. Eng. Geol. Hydrogeol. 46, 132–156. https://doi.org/10.1144/qjegh2012-078

Brothers, D.S., ten Brink, U.S., Andrews, B.D., Chaytor, J.D., 2013. Geomorphic characterization of the U.S. Atlantic continental margin. Mar. Geol. 338, 46–63. https://doi.org/10.1016/j.margeo.2012.12.008

Bryn, P., Berg, K., Forsberg, C.F., Solheim, A., Kvalstad, T.J., 2005a. Explaining the Storegga Slide. Mar. Pet. Geol. 22, 11–19. https://doi.org/10.1016/j.marpetgeo.2004.12.003

Bryn, P., Berg, K., Stoker, M.S., Haflidason, H., Solheim, A., 2005b. Contourites and their relevance for mass wasting along the Mid-Norwegian Margin. Mar. Pet. Geol. 22, 85–96. https://doi.org/10.1016/j.marpetgeo.2004.10.012

Bryn, P., Solheim, A., Berg, K., Lien, R., Forsberg, C.F., Haflidason, H., Ottesen, D., Rise, L., 2003. The Storegga Slide Complex; Repeated Large Scale Sliding in Response to Climatic Cyclicity. pp. 215–222. https://doi.org/10.1007/978-94-010-0093-2_24

Bull, S., Cartwright, J., Huuse, M., 2009a. A review of kinematic indicators from mass-transport complexes using 3D seismic data. Mar. Pet. Geol. 26, 1132–1151. https://doi.org/10.1016/j.marpetgeo.2008.09.011

Bull, S., Cartwright, J., Huuse, M., 2009b. A subsurface evacuation model for submarine slope failure. Basin Res. 21, 433–443. https://doi.org/10.1111/j.1365-2117.2008.00390.x

Bünz, S., Mienert, J., 2004. Acoustic imaging of gas hydrate and free gas at the Storegga slide. J. Geophys. Res. Solid Earth 109, 1–15. https://doi.org/10.1029/2003JB002863

Bünz, S., Mienert, J., Berndt, C., 2003. Geological controls on the Storegga gas-hydrate system of the mid-Norwegian continental margin. Earth Planet. Sci. Lett. 209, 291–307. https://doi.org/10.1016/S0012-821X(03)00097-9

Cartwright, J., 2011. Diagenetically induced shear failure of fine-grained sediments and the development of polygonal fault systems. Mar. Pet. Geol. 28, 1593–1610. https://doi.org/10.1016/j.marpetgeo.2011.06.004

Cartwright, J., James, D., Bolton, A., 2003. The genesis of polygonal fault systems: A review. Geol. Soc. Spec. Publ. 216, 223–234. https://doi.org/10.1144/GSL.SP.2003.216.01.15

Cartwright, J., Santamarina, C., 2015. Seismic characteristics of fluid escape pipes in sedimentary basins: Implications for pipe genesis. Mar. Pet. Geol. 65, 126–140. https://doi.org/10.1016/j.marpetgeo.2015.03.023

Cartwright, J.A., Trudgill, B.D., Mansfield, C.S., 1995. Fault growth by segment linkage: an explanation for scatter in maximum displacement and trace length data from the Canyonlands Grabens of SE Utah. J. Struct. Geol. 17, 1319–1326. https://doi.org/10.1016/0191-8141(95)00033-A

Chand, S., Rise, L., Knies, J., Haflidason, H., Hjelstuen, B.O., Bøe, R., 2011. Stratigraphic development of the south Vøring margin (Mid-Norway) since early Cenozoic time and its influence on subsurface fluid flow. Mar. Pet. Geol. 28, 1350–1363. https://doi.org/10.1016/j.marpetgeo.2011.01.005

Chaytor, J.D., Twichell, D.C., Brink, U.S. Ten, Buczkowski, B.J., Andrews, B.D., 2007. Revisiting Submarine Mass Movements Along The U.S. Atlantic Continental Margin: Implications For Tsunami Hazards, in: Submarine Mass Movements and Their Consequences. Springer Netherlands, Dordrecht, pp. 395–403. https://doi.org/10.1007/978-1-4020-6512-5_41

Chopra, S., Castagna, J., Portniaguine, O., 2006. Seismic resolution and thin-bed reflectivity inversion. CSEG Rec. 31, 19–25. https://doi.org/doi:10.1190/1.2369941

Clausen, J.A., Gabrielsen, R.H., Reksnes, P.A., Nysæther, E., 1999. Development of intraformational (Oligocene-Miocene) faults in the northern North Sea: Influence of remote stresses and doming of Fennoscandia. J. Struct. Geol. 21, 1457–1475.

https://doi.org/10.1016/S0191-8141(99)00083-8

Crémière, A., Lepland, A., Chand, S., Sahy, D., Condon, D.J., Noble, S.R., Martma, T., Thorsnes, T., Sauer, S., Brunstad, H., 2016. Timescales of methane seepage on the Norwegian margin following collapse of the Scandinavian Ice Sheet. Nat. Commun. 7, 1–10. https://doi.org/10.1038/ncomms11509

Cukur, D., Kim, S.-P.P., Kong, G.-S.S., Bahk, J.-J.J., Horozal, S., Um, I.-K.K., Lee, G.-S.S., Chang, T.-S.S., Ha, H.-J.J., Völker, D., Kim, J.-K.K., 2016a. Geophysical evidence and inferred triggering factors of submarine landslides on the western continental margin of the Ulleung Basin, East Sea. Geo-Marine Lett. 36, 425–444. https://doi.org/10.1007/s00367-016-0463-5

Cukur, D., Kim, S.P., Kong, G.S., Bahk, J.J., Horozal, S., Um, I.K., Lee, G.S., Chang, T.S., Ha, H.J., Völker, D., Kim, J.K., 2016b. Geophysical evidence and inferred triggering factors of submarine landslides on the western continental margin of the Ulleung Basin, East Sea. Geo-Marine Lett. 36, 425–444. https://doi.org/10.1007/s00367-016-0463-5

Dalland, A., 1988. A lithostratigraphic scheme for the Mesozoic and Cenozoic succesion offshore Norway north of 62° N. Norw. Pet. Dir. Bull.

Dalland, A., Worsley, D., Ofstad, K., Norway. Oljedirektoratet., 1988. A lithostratigraphic scheme for the Mesozoic and Cenozoic and succession offshore mid- and northern Norway. Oljedirektoratet, Stavanger.

Dan, G., Sultan, N., Savoye, B., 2007. The 1979 Nice harbour catastrophe revisited: Trigger mechanism inferred from geotechnical measurements and numerical modelling. Mar. Geol. 245, 40–64. https://doi.org/10.1016/j.margeo.2007.06.011

Davies, R.J., Cartwright, J., 2002. A fossilized Opal A to Opal C/T transformation on the northeast Atlantic margin: Support for a significantly elevated palaeogeothermal gradient during the Neogene? Basin Res. 14, 467–486. https://doi.org/10.1046/j.1365-2117.2002.00184.x

Davies, R.J., Clark, I.R., 2006. Submarine slope failure primed and triggered by silica and its diagenesis. Basin Res. 18, 339–350. https://doi.org/10.1111/j.1365-

2117.2006.00297.x

Davies, R.J., Ireland, M.T., Cartwright, J.A., 2009. Differential compaction due to the irregular topology of a diagenetic reaction boundary: A new mechanism for the formation of polygonal faults. Basin Res. 21, 354–359. https://doi.org/10.1111/j.1365-2117.2008.00389.x

Davies, R.J., Stewart, S.A., Cartwright, J.A., Lappin, M., Johnston, R., Fraser, S.I., Brown, A.R., 2004. 3D Seismic Technology: Are We Realising Its Full Potential? Geol. Soc. Mem. 29, 1–10. https://doi.org/10.1144/GSL.MEM.2004.029.01.01

Day, S., Llanes, P., Silver, E., Hoffmann, G., Ward, S., Driscoll, N., 2015. Submarine landslide deposits of the historical lateral collapse of Ritter Island, Papua New Guinea. Mar. Pet. Geol. 67, 419–438. https://doi.org/10.1016/j.marpetgeo.2015.05.017

De Blasio, F.V., Elverhøi, A., Issler, D., Harbitz, C.B., Bryn, P., Lien, R., 2005. On the dynamics of subaqueous clay rich gravity mass flows - The giant Storegga slide, Norway. Mar. Pet. Geol. 22, 179–186. https://doi.org/10.1016/j.marpetgeo.2004.10.014

Debnath, B., 2018. Modelling of downslope displacement of failed soil blocks originating from submarine landslides. Memorial University of Newfoundland.

Debnath, B., Hawlader, B., 2017. Performance of Computational Fluid Dynamics and Finite Element Methods for Modeling Downslope Displacement of Failed Soil from Submarine Landslides. Geoh.

Dewhurst, D.N., Cartwright, J.A., Lonergan, L., 1999. The development of polygonal fault systems by syneresis of colloidal sediments. Mar. Pet. Geol. 16, 793–810. https://doi.org/10.1016/S0264-8172(99)00035-5

Doré, A.G., 1991. The structural foundation and evolution of Mesozoic seaways between Europe and the Arctic. Palaeogeogr. Palaeoclimatol. Palaeoecol. 87, 441–492. https://doi.org/10.1016/0031-0182(91)90144-G

Doré, A.G., Lundin, E.R., Kusznir, N.J., Pascal, C., 2008a. Potential mechanisms for the genesis of Cenozoic domal structures on the NE Atlantic margin: Pros, cons and some new ideas. Geol. Soc. Spec. Publ. 306, 1–26. https://doi.org/10.1144/SP306.1

Doré, A.G., Lundin, E.R., Kusznir, N.J., Pascal, C., 2008b. Potential mechanisms for the genesis of Cenozoic domal structures on the NE Atlantic margin: pros, cons and some new ideas. Geol. Soc. London, Spec. Publ. 306, 1–26. https://doi.org/10.1144/sp306.1

Døssing, A., Japsen, P., Watts, A.B., Nielsen, T., Jokat, W., Thybo, H., Dahl-Jensen, T., 2016. Miocene uplift of the NE Greenland margin linked to plate tectonics: Seismic evidence from the Greenland Fracture Zone, NE Atlantic. Tectonics 35, 257–282. https://doi.org/10.1002/2015TC004079

Dura, T., Horton, B.P., Cisternas, M., Ely, L.L., Hong, I., Nelson, A.R., Wesson, R.L., Pilarczyk, J.E., Parnell, A.C., Nikitina, D., 2017. Subduction zone slip variability during the last millennium, south-central Chile. Quat. Sci. Rev. 175, 112–137. https://doi.org/10.1016/j.quascirev.2017.08.023

Dutta, S., Hawlader, B., 2019. Pipeline–soil–water interaction modelling for submarine landslide impact on suspended offshore pipelines. Geotechnique 69, 29–41. https://doi.org/10.1680/jgeot.17.P.084

Dutta, S., Hawlader, B., Phillips, R., 2018. Numerical modelling of a steel catenary riser section in the touchdown zone under cyclic loading. Ocean Eng. 164, 168–180. https://doi.org/10.1016/j.oceaneng.2018.06.040

Edward L. King; Hans Petter Sejrup; Haflidi Haflidason; Anders Elverhøi; Inge Aarseth, 1996. The submarine fan situated in the northeastern. Mar. Geol. 130, 293–315.

Eidvin, T., Bugge, T., Smelror, M., 2007. The Molo Formation, deposited by coastal progradation on the inner Mid-Norwegian continental shelf, coeval with the Kai Formation to the west and the Utsira Formation in the North Sea. Nor. J. Geol. Geol. Foren. 87.

Einav, I., Randolph, M.F., 2005. Combining upper bound and strain path methods for evaluating penetration resistance. Int. J. Numer. Methods Eng. 63, 1991–2016. https://doi.org/10.1002/nme.1350

Elger, J., 2016. Studies of submarine slope failures in the North Atlantic: Causes, timing and consequences. Christian-Albrechts-Universität.

Elger, J., Berndt, C., Rüpke, L., Krastel, S., Gross, F., Geissler, W.H., 2018. Submarine slope failures due to pipe structure formation. Nat. Commun. 9, 1–6. https://doi.org/10.1038/s41467-018-03176-1

Ellis, D. V., 1990. Some insights on neutron measurements. IEEE Trans. Nucl. Sci. 37, 959–965. https://doi.org/10.1109/23.106743

Faleide, J.I., Bjørlykke, K., Gabrielsen, R.H., 2015. Geology of the Norwegian Continental Shelf, in: Petroleum Geoscience. Springer Berlin Heidelberg, Berlin, Heidelberg, Heidelberg, pp. 603–637. https://doi.org/10.1007/978-3-642-34132-8_25

Faleide, J.I., Bjørlykke, K., Gabrielsen, R.H., 2010. Geology of the Norwegian Continental Shelf, in: Petroleum Geoscience. Springer Berlin Heidelberg, Berlin, Heidelberg, pp. 467–499. https://doi.org/10.1007/978-3-642-02332-3_22

Faleide, J.I., Tsikalas, F., Breivik, A.J., Mjelde, R., Ritzmann, O., Engen, Ø., Wilson, J., Eldholm, O., 2008. Structure and evolution of the continental margin off Norway and the Barents Sea. Episodes 31, 82–91. https://doi.org/10.18814/epiiugs/2008/v31i1/012

Faleide, J.I., Vagnes, E., Gudlaugsson, S.T., 1993. Late Mesozoic-Cenozoic evolution of the southwestern Barents Sea, in: Petroleum Geology Conference Proceedings. Geological Society of London, pp. 933–950. https://doi.org/10.1144/0040933

Fell, R., Glastonbury, J., Hunter, G., 2007. Rapid landslides: The importance of understanding mechanisms and rupture surface mechanics. Q. J. Eng. Geol. Hydrogeol. 40, 9–27. https://doi.org/10.1144/1470-9236/06-030

Flemings, P.B., Long, H., Dugan, B., Germaine, J., John, C.M., Behrmann, J.H., Sawyer, D., 2008. Erratum to “Pore pressure penetrometers document high overpressure near the seafloor where multiple submarine landslides have occurred on the continental slope, offshore Louisiana, Gulf of Mexico" [Earth and Planetary Science Letters 269/3-4 (2008) 309-32. Earth Planet. Sci. Lett. 274, 269–283. https://doi.org/10.1016/j.epsl.2008.06.027

Forsberg, C.F., Locat, J., 2005. Mineralogical and microstructural development of the sediments on the Mid-Norwegian margin. Mar. Pet. Geol. 22, 109–122. https://doi.org/10.1016/j.marpetgeo.2004.12.002

Gaina, C., Gernigon, L., Ball, P., 2009. Palaeocene–Recent plate boundaries in the NE Atlantic and the formation of the Jan Mayen microcontinent. J. Geol. Soc. London. 166, 601–616. https://doi.org/10.1144/0016-76492008-112

Gauer, P., Kvalstad, T.J., Forsberg, C.F., Bryn, P., Berg, K., 2005. The last phase of the Storegga Slide: Simulation of retrogressive slide dynamics and comparison with slide-scar morphology. Mar. Pet. Geol. 22, 171–178. https://doi.org/10.1016/j.marpetgeo.2004.10.004

Gay, A., Berndt, C., 2007. Cessation/reactivation of polygonal faulting and effects on fluid flow in the Vøring Basin, Norwegian Margin. J. Geol. Soc. London. 164, 129–141. https://doi.org/10.1144/0016-76492005-178

Gay, A., Lopez, M., Cochonat, P., Séranne, M., Levaché, D., Sermondadaz, G., 2006. Isolated seafloor pockmarks linked to BSRs, fluid chimneys, polygonal faults and stacked Oligocene-Miocene turbiditic palaeochannels in the Lower Congo Basin. Mar. Geol. 226, 25–40. https://doi.org/10.1016/j.margeo.2005.09.018

Gay, A., Lopez, M., Cochonat, P., Sermondadaz, G., 2004. Polygonal faults-furrows system related to early stages of compaction - upper Miocene to recent sediments of the Lower Congo Basin. Basin Res. 16, 101–116. https://doi.org/10.1111/j.1365-2117.2003.00224.x

Gee, M.J.R., Gawthorpe, R.L., Friedmann, S.J., 2006. Triggering and evolution of a giant submarine landslide, offshore Angola, revealed by 3D seismic stratigraphy and geomorphology. J. Sediment. Res. 76, 9–19. https://doi.org/10.2110/jsr.2006.02

Gernigon, L., Lucazeau, F., Brigaud, F., Ringenbach, J.-C., Planke, S., Le Gall, B., 2006a. A moderate melting model for the Vøring margin (Norway) based on structural observations and a thermo-kinematical modelling: Implication for the meaning of the lower crustal bodies. Tectonophysics 412, 255–278. https://doi.org/10.1016/J.TECTO.2005.10.038

Gernigon, L., Lucazeau, F., Brigaud, F., Ringenbach, J.-C.C., Planke, S., Le Gall, B., 2006b. A moderate melting model for the Vøring margin (Norway) based on structural observations and a thermo-kinematical modelling: Implication for the meaning of the lower crustal bodies. Tectonophysics 412, 255–278. https://doi.org/10.1016/j.tecto.2005.10.038

Gernigon, L., Ringenbach, J.C., Planke, S., Le Gall, B., Jonquet-Kolstø, H., 2003. Extension, crustal structure and magmatism at the outer Vøring Basin, Norwegian margin. J. Geol. Soc. London. 160, 197–208. https://doi.org/10.1144/0016-764902-055

Gluyas, J.G., Swarbrick, R.E., 2021. Petroleum geoscience. John Wiley & Sons.

Goldsby, D.L., Tullis, T.E., 2002. Low frictional strength of quartz rocks at subseismic slip rates. Geophys. Res. Lett. 29, 25-1-25–4. https://doi.org/10.1029/2002gl015240

Gómez, M., Vergés, J., 2005. Quantifying the contribution of tectonics vs. differential compaction in the development of domes along the Mid-Norwegian Atlantic margin. Basin Res. 17, 289–310. https://doi.org/10.1111/j.1365-2117.2005.00264.x

Goulty, N.R., Swarbrick, R.E., 2005. Development of polygonal fault systems: A test of hypotheses. J. Geol. Soc. London. 162, 587–590. https://doi.org/10.1144/0016-764905-004

Graham Jenkins, D., 1992. Predicting extinctions of some extant planktic foraminifera. Mar. Micropaleontol. 19, 239–243. https://doi.org/10.1016/0377-8398(92)90030-N

Haacke, R.R., Westbrook, G.K., Hyndman, R.D., 2007. Gas hydrate, fluid flow and free gas: Formation of the bottom-simulating reflector. Earth Planet. Sci. Lett. 261, 407–420. https://doi.org/10.1016/j.epsl.2007.07.008

Haflidason, H., Lien, R., Sejrup, H.P., Forsberg, C.F., Bryn, P., 2005. The dating and morphometry of the Storegga Slide. Mar. Pet. Geol. 22, 123–136. https://doi.org/10.1016/j.marpetgeo.2004.10.008

Haflidason, H., Sejrup, H.P., Nygård, A., Mienert, J., Bryn, P., Lien, R., Forsberg, C.F., Berg, K., Masson, D., 2004. The Storegga Slide: Architecture, geometry and slide development. Mar. Geol. 213, 201–234. https://doi.org/10.1016/j.margeo.2004.10.007

Hamilton, E.L., 1979. VP/V8And Poisson's Ratios In Marine Sediments And Rocks. J. Acoust. Soc. Am. 66, 1093–1101. https://doi.org/10.1121/1.383344

Hansen, D.M., Cartwright, J., 2006. The three-dimensional geometry and growth of forced folds above saucer-shaped igneous sills. J. Struct. Geol. 28, 1520–1535. https://doi.org/10.1016/j.jsg.2006.04.004

Harbitz, C.B., Løvholt, F., Pedersen, G., Masson, D.G., 2006. Mechanisms of tsunami generation by submarine landslides: A short review. Nor. Geol. Tidsskr. 86, 255–264.

He, Y., Zhong, G., Wang, L., Kuang, Z., 2014. Characteristics and occurrence of submarine canyon-associated landslides in the middle of the northern continental slope, South China Sea. Mar. Pet. Geol. 57, 546–560. https://doi.org/10.1016/j.marpetgeo.2014.07.003

Hemphill-Haley, E., 1996. Diatoms as an aid in identifying late-holocene tsunami deposits. Holocene 6, 439–448. https://doi.org/10.1177/095968369600600406

Henrich, R., Baumann, K.H., 1994. Evolution of the Norwegian Current and the Scandinavian Ice Sheets during the past 2.6 m.y.: evidence from ODP Leg 104 biogenic carbonate and terrigenous records. Palaeogeogr. Palaeoclimatol. Palaeoecol. 108, 75–94. https://doi.org/10.1016/0031-0182(94)90023-X

Henrich, R., Kassens, H., Vogelsang, E., Thiede, J., 1989. Sedimentary facies of glacial-interglacial cycles in the Norwegian Sea during the last 350 ka. Mar. Geol. 86, 283–319. https://doi.org/10.1016/0025-3227(89)90090-X

Herdendorf, C.E., 1990. Distribution of the world's large lakes, in: Large Lakes. Springer, pp. 3–38.

Hill, J.C., Driscoll, N.W., Weissel, J.K., Goff, J.A., 2004. Large-scale elongated gas blowouts along the U.S. Atlantic margin. J. Geophys. Res. Solid Earth 109, 1–14. https://doi.org/10.1029/2004JB002969

Hjelstuen, B.O., Eldholm, O., Faleide, J.I., 2007. Recurrent Pleistocene mega-failures on the SW Barents Sea margin. Earth Planet. Sci. Lett. 258, 605–618. https://doi.org/10.1016/j.epsl.2007.04.025

Hjelstuen, B.O., Eldholm, O., Skogseid, J., 1999. Cenozoic evolution of the northern Vøring margin. Bull. Geol. Soc. Am. 111, 1792–1807. https://doi.org/10.1130/0016-7606(1999)111<1792:ceotnv>2.3.co;2

Hjelstuen, B.O., Sejrup, H.P., Haflidason, H., Nygård, A., Ceramicola, S., Bryn, P., 2005. Late Cenozoic glacial history and evolution of the Storegga Slide area and adjacent slide flank regions, Norwegian continental margin. Mar. Pet. Geol. 22, 57–69. https://doi.org/10.1016/j.marpetgeo.2004.10.002

Ho, J.J.L., Gorman, A.R., Crutchley, G.J., 2019. Seismic evidence for repeated vertical fl uid fl ow through polygonally faulted strata in the Canterbury Basin , New Zealand 109, 317–329. https://doi.org/10.1016/j.marpetgeo.2019.06.025

Ho, S., Cartwright, J.A., Imbert, P., 2012. Vertical evolution of fluid venting structures in relation to gas flux, in the Neogene-Quaternary of the Lower Congo Basin, Offshore Angola. Mar. Geol. 332–334, 40–55. https://doi.org/10.1016/j.margeo.2012.08.011

Hoffmann, J.J.L., Gorman, A.R., Crutchley, G.J., 2019. Seismic evidence for repeated vertical fluid flow through polygonally faulted strata in the Canterbury Basin, New Zealand. Mar. Pet. Geol. 109, 317–329. https://doi.org/10.1016/j.marpetgeo.2019.06.025

Hornbach, M.J., Manga, M., Genecov, M., Valdez, R., Miller, P., Saffer, D., Adelstein, E., Lafuerza, S., Adachi, T., Breitkreuz, C., Jutzeler, M., Le Friant, A., Ishizuka, O., Morgan, S., Slagle, A., Talling, P.J., Fraass, A., Watt, S.F.L., Stroncik, N.A., Aljahdali, M., Boudon, G., Fujinawa, A., Hatfield, R., Kataoka, K., Maeno, F., Martinez-Colon, M., McCanta, M., Palmer, M., Stinton, A., Subramanyam, K.S.V., Tamura, Y., Villemant, B., Wall-Palmer, D., Wang, F., 2015. Permeability and pressure measurements in Lesser Antilles submarine slides: Evidence for pressure-driven slow-slip failure. J. Geophys. Res. Solid Earth 120, 7986–8011. https://doi.org/10.1002/2015JB012061

Hovland, M., Heggland, R., De Vries, M.H., Tjelta, T.I., 2010. Unit-pockmarks and their potential significance for predicting fluid flow. Mar. Pet. Geol. 27, 1190–1199. https://doi.org/10.1016/j.marpetgeo.2010.02.005

Hsu, S.K., Kuo, J., Lo, C.L., Tsai, C.H., Doo, W. Bin, Ku, C.Y., Sibuet, J.C., 2008. Turbidity currents, submarine landslides and the 2006 Pingtung earthquake off SW Taiwan. Terr. Atmos. Ocean. Sci. 19, 767–772. https://doi.org/10.3319/TAO.2008.19.6.767(PT)

Huhn, K., Arroyo, M., Cattaneo, A., Clare, M.A., Gràcia, E., Harbitz, C.B., Krastel, S., Kopf, A., Løvholt, F., Rovere, M., Strasser, M., Talling, P.J., Urgeles, R., 2019. Modern Submarine Landslide Complexes 181–200. https://doi.org/10.1002/9781119500513.ch12

Hunt, J.E., Tappin, D.R., Watt, S.F.L., Susilohadi, S., Novellino, A., Ebmeier, S.K., Cassidy, M., Engwell, S.L., Grilli, S.T., Hanif, M., Priyanto, W.S., Clare, M.A., Abdurrachman, M., Udrekh, U., 2021. Submarine landslide megablocks show half of Anak Krakatau island failed on December 22nd, 2018. Nat. Commun. 12. https://doi.org/10.1038/s41467-021-22610-5

Hustoft, S., Dugan, B., Mienert, J., 2009. Effects of rapid sedimentation on developing the Nyegga pockmark field: Constraints from hydrological modeling and 3-D seismic data, offshore mid-Norway. Geochemistry, Geophys. Geosystems 10. https://doi.org/10.1029/2009GC002409

Hustoft, S., Mienert, J., Bünz, S., Nouzé, H., 2007. High-resolution 3D-seismic data indicate focussed fluid migration pathways above polygonal fault systems of the mid-Norwegian margin. Mar. Geol. 245, 89–106.

https://doi.org/10.1016/j.margeo.2007.07.004

Huuse, M., 2002. Cenozoic uplift and denudation of southern Norway: Insights from the North Sea Basin. Geol. Soc. Spec. Publ. 196, 209–233. https://doi.org/10.1144/GSL.SP.2002.196.01.13

Ikari, M.J., Kopf, A.J., 2011. Cohesive strength of clay-rich sediment. Geophys. Res. Lett. 38, 1–5. https://doi.org/10.1029/2011GL047918

Ireland, M.T., Davies, R.J., Goulty, N.R., Carruthers, D., 2011. Structure of a silica diagenetic transformation zone: The Gjallar Ridge, offshore Norway. Sedimentology 58, 424–441. https://doi.org/10.1111/j.1365-3091.2010.01170.x

Isaacs, C.M., 1981. Porosity reduction during diagenesis of the Monterey Formation, Santa Barbara coastal area, California.

Ivanov, M., Westbrook, G.K., Blinova, V., Kozlova, E., Mazzini, A., Nouzé, H., Minshull, T.A., 2007. First sampling of gas hydrate from the Vøring plateau. Eos (Washington. DC). 88, 1–4. https://doi.org/10.1029/2007EO190001

Japsen, P., Green, P.F., Nielsen, L.H., Rasmussen, E.S., Bidstrup, T., 2007a. Mesozoic-Cenozoic exhumation events in the eastern North Sea Basin: A multi-disciplinary study based on palaeothermal, palaeoburial, stratigraphic and seismic data. Basin Res. 19, 451–490. https://doi.org/10.1111/j.1365-2117.2007.00329.x

Japsen, P., Green, P.F., Nielsen, L.H., Rasmussen, E.S., Bidstrup, T., 2007b. Mesozoic–Cenozoic exhumation events in the eastern North Sea Basin: a multi-disciplinary study based on palaeothermal, palaeoburial, stratigraphic and seismic data. Basin Res. 19, 451–490. https://doi.org/10.1111/j.1365-2117.2007.00329.x

Jongepier, K., Rui, J.C., Grue, K., 1996. Triassic to Early Cretaceous stratigraphic and structural development of the northeastern Møre Basin margin, off Mid-Norway. Nor. Geol. Tidsskr. 76, 199–214.

Karstens, J., Haflidason, H., Becker, L.W.M., Berndt, C., Rüpke, L., Planke, S., Liebetrau, V., Schmidt, M., Mienert, J., 2018. Glacigenic sedimentation pulses triggered post-glacial gas hydrate dissociation. Nat. Commun. 9, 1–11.

https://doi.org/10.1038/s41467-018-03043-z

Kastner, M., 1981. Authigenic silicates in deep-sea sediments: formation and diagenesis. sea 7, 915–980.

Kawamura, K., Laberg, J.S., Kanamatsu, T., 2014. Potential tsunamigenic submarine landslides in active margins. Mar. Geol. 356, 44–49. https://doi.org/10.1016/j.margeo.2014.03.007

Kawamura, K., Sasaki, T., Kanamatsu, T., Sakaguchi, A., Ogawa, Y., 2012. Large submarine landslides in the Japan Trench: A new scenario for additional tsunami generation. Geophys. Res. Lett. 39, 3–7. https://doi.org/10.1029/2011GL050661

Kearey, P., Brooks, M., Hill, I., 2002. An introduction to geophysical exploration. John Wiley & Sons.

Kim, G.B., Cheng, W., Sunny, R.C., Horrillo, J.J., McFall, B.C., Mohammed, F., Fritz, H.M., Beget, J., Kowalik, Z., 2020. Three Dimensional Landslide Generated Tsunamis: Numerical and Physical Model Comparisons. Landslides 17, 1145–1161. https://doi.org/10.1007/s10346-019-01308-2

Kimbell, G.S., Stewart, M.A., Gradmann, S., Shannon, P.M., Funck, T., Haase, C., Stoker, M.S., Hopper, J.R., 2017. Controls on the location of compressional deformation on the NW European margin. Geol. Soc. Spec. Publ. 447, 249–277. https://doi.org/10.1144/SP447.3

King, J.J., Cartwright, J.A., 2020. Ultra-slow throw rates of polygonal fault systems. Geology 48, 473–477. https://doi.org/10.1130/G47221.1

Kjeldstad, A., Skogseid, J., Langtangen, H.P., Bjørlykke, K., Høeg, K., 2003. Differential loading by prograding sedimentary wedges on continental margins: An arch-forming mechanism. J. Geophys. Res. Solid Earth 108, 1–21. https://doi.org/10.1029/2001jb001145

Kjoberg, S., Schmiedel, T., Planke, S., Svensen, H.H., Millett, J.M., Jerram, D.A., Galland, O., Lecomte, I., Schofield, N., Haug, Ø.T., Helsem, A., 2017. 3D structure and formation of hydrothermal vent complexes at the Paleocene-Eocene transition, the Møre Basin, mid-Norwegian margin. Interpretation 5, SK65–SK81. https://doi.org/10.1190/INT-2016-0159.1

Knaust, D., 2009. Characterisation of a Campanian deep-sea fan system in the Norwegian Sea by means of ichnofabrics. Mar. Pet. Geol. 26, 1199–1211. https://doi.org/10.1016/j.marpetgeo.2008.09.009

Knies, J., Matthiessen, J., Vogt, C., Laberg, J.S., Hjelstuen, B.O., Smelror, M., Larsen, E., Andreassen, K., Eidvin, T., Vorren, T.O., 2009. The Plio-Pleistocene glaciation of the Barents Sea-Svalbard region: a new model based on revised chronostratigraphy. Quat. Sci. Rev. 28, 812–829. https://doi.org/10.1016/j.quascirev.2008.12.002

Kohli, A.H., Zoback, M.D., 2013. Frictional properties of shale reservoir rocks. J. Geophys. Res. Solid Earth 118, 5109–5125. https://doi.org/10.1002/jgrb.50346

Koptev, A., Cloetingh, S., Burov, E., François, T., Gerya, T., 2017. Long-distance impact of Iceland plume on Norway’s rifted margin. Sci. Rep. 7, 1–11. https://doi.org/10.1038/s41598-017-07523-y

Koson, S., Chenrai, P., Choowong, M., 2014. Seismic Attributes and Their Applications in Seismic Geomorphology. Bull. Earth Sci. Thail. 6, 1–9.

Krokmyrdal, Suchada Yaiying, 2017. Sedimentary environment and seismic anomalies of the upper Brygge and Kai formations on the northern part of the Mid-Norwegian Continental Shelf.

Krokmyrdal, Suchada Y., 2017. Sedimentary environment and seismic anomalies of the upper Brygge and Kai formations on the northern part of the Mid-Norwegian Continental Shelf.

Kvalstad, T.J., Andresen, L., Forsberg, C.F., Berg, K., Bryn, P., Wangen, M., 2005a. The Storegga slide: Evaluation of triggering sources and slide mechanics. Mar. Pet. Geol. 22, 245–256. https://doi.org/10.1016/j.marpetgeo.2004.10.019

Kvalstad, T.J., Nadim, F., Kaynia, A.M., Mokkelbost, K.H., Bryn, P., 2005b. Soil conditions and slope stability in the Ormen Lange area. Mar. Pet. Geol. 22, 299–

310. https://doi.org/10.1016/j.marpetgeo.2004.10.021

L'Heureux, J.-S., Longva, O., Steiner, A., Hansen, L., Vardy, M.E., Vanneste, M., Haflidason, H., Brendryen, J., Kvalstad, T.J., Forsberg, C.F., Chand, S., Kopf, A., 2012. Identification of Weak Layers and Their Role for the Stability of Slopes at Finneidfjord, Northern Norway, in: Submarine Mass Movements and Their Consequences. Springer Netherlands, Dordrecht, pp. 321–330. https://doi.org/10.1007/978-94-007-2162-3_29

L'heureux, J.S., 2012. A study of the retrogressive behaviour and mobility of Norwegian quick clay landslides. Landslides Eng. Slopes Prot. Soc. through Improv. Underst. - Proc. 11th Int. 2nd North Am. Symp. Landslides Eng. Slopes, 2012 981–987.

L'Heureux, J.S., Vanneste, M., Rise, L., Brendryen, J., Forsberg, C.F., Nadim, F., Longva, O., Chand, S., Kvalstad, T.J., Haflidason, H., 2013. Stability, mobility and failure mechanism for landslides at the upper continental slope off Vesterålen, Norway. Mar. Geol. 346, 192–207. https://doi.org/10.1016/j.margeo.2013.09.009

Laberg, J., Vorren, T.O., Mienert, J., Bryn, P., Lien, R., 2002. The Trænadjupet Slide: A large slope failure affecting the continental margin of Norway 4,000 years ago. Geo-Marine Lett. 22, 19–24. https://doi.org/10.1007/s00367-002-0092-z

Laberg, J.S., Baeten, N.J., Lågstad, P., Forwick, M., Vorren, T.O., 2013. Formation of a large submarine crack during the final stage of retrogressive mass wasting on the continental slope offshore northern Norway. Mar. Geol. 346, 73–78. https://doi.org/10.1016/j.margeo.2013.08.008

Laberg, J.S., Camerlenghi, A., 2008. Chapter 25 The Significance of Contourites for Submarine Slope Stability. Dev. Sedimentol. 60, 537–556. https://doi.org/10.1016/S0070-4571(08)10025-5

Laberg, J.S., Strasser, M., Alves, T.M., Gao, S., Kawamura, K., Kopf, A., Moore, G.F., 2017. Internal deformation of a muddy gravity flow and its interaction with the seafloor (site C0018 of IODP Expedition 333, Nankai Trough, SE Japan). Landslides 14, 849–860. https://doi.org/10.1007/s10346-016-0766-7

Laberg, J.S., Vorren, T.O., Dowdeswell, J.A., Kenyon, N.H., Taylor, J., 2000. The Andoya Slide and the Andoya Canyon, north-eastern Norwegian-Greenland Sea. Mar. Geol. 162, 259–275. https://doi.org/10.1016/S0025-3227(99)00087-0

Laberg, J.S., Vorren, T.O., Mienert, J., Haflidason, H., Bryn, P., Lien, R., 2003. Preconditions Leading to the Holocene Trænadjupet Slide Offshore Norway, in: Review Literature And Arts Of The Americas. pp. 247–254. https://doi.org/10.1007/978-94-010-0093-2_28

Lawrence, G.W.M., Cartwright, J.A., 2010. The stratigraphic and geographic distribution of giant craters and remobilised sediment mounds on the mid Norway margin, and their relation to long term fluid flow. Mar. Pet. Geol. 27, 733–747. https://doi.org/10.1016/j.marpetgeo.2009.10.012

Lawrence, G.W.M., Cartwright, J.A., 2009. The initiation of sliding on the mid Norway margin in the Møre Basin. Mar. Geol. 259, 21–35. https://doi.org/10.1016/j.margeo.2008.12.006

Leslie, S.C., Mann, P., 2016. Giant submarine landslides on the Colombian margin and tsunami risk in the Caribbean Sea. Earth Planet. Sci. Lett. 449, 382–394. https://doi.org/10.1016/j.epsl.2016.05.040

Leynaud, D., Mienert, J., Nadim, F., 2004. Slope stability assessment of the Helland Hansen area offshore the mid-Norwegian margin. Mar. Geol. 213, 457–480. https://doi.org/10.1016/j.margeo.2004.10.019

Leynaud, D., Mienert, J., Vanneste, M., 2009. Submarine mass movements on glaciated and non-glaciated European continental margins: A review of triggering mechanisms and preconditions to failure. Mar. Pet. Geol. 26, 618–632. https://doi.org/10.1016/j.marpetgeo.2008.02.008

Leynaud, D., Sultan, N., Mienert, J., 2007. The role of sedimentation rate and permeability in the slope stability of the formerly glaciated Norwegian continental margin: The Storegga slide model. Landslides 4, 297–309. https://doi.org/10.1007/s10346-007-0086-z

Li, W., Alves, T.M., Wu, S., Rebesco, M., Zhao, F., Mi, L., Ma, B., 2016. A giant, submarine creep zone as a precursor of large-scale slope instability offshore the Dongsha Islands (South China Sea). Earth Planet. Sci. Lett. 451, 272–284. https://doi.org/10.1016/j.epsl.2016.07.007

Li, W., Alves, T.M., Wu, S., Völker, D., Zhao, F., Mi, L., Kopf, A., 2015. Recurrent slope failure and submarine channel incision as key factors controlling reservoir potential in the South China Sea (Qiongdongnan Basin, South Hainan Island). Mar. Pet. Geol. 64, 17–30. https://doi.org/10.1016/j.marpetgeo.2015.02.043

Lien, T., 2005. From rifting to drifting: Effects on the development of deep-water hydrocarbon reservoirs in a passive margin setting, Norwegian Sea. Nor. Geol. Tidsskr. 85, 319–332.

Ligtenberg, J.H., 2005. Detection of Fluid migration pathways in seismic data: Implications for fault seal analysis. Basin Res. 17, 141–153. https://doi.org/10.1111/j.1365-2117.2005.00258.x

Lindberg, B., Laberg, J.S., Vorren, T.O., 2004. The Nyk Slide-morphology, progression, and age of a partly buried submarine slide offshore northern Norway. Mar. Geol. 213, 277–289. https://doi.org/10.1016/j.margeo.2004.10.010

Llopart, J., Urgeles, R., Camerlenghi, A., Lucchi, R.G., Rebesco, M., De Mol, B., 2015. Late Quaternary development of the Storfjorden and Kveithola Trough Mouth Fans, northwestern Barents Sea. Quat. Sci. Rev. 129, 68–84. https://doi.org/10.1016/j.quascirev.2015.10.002

Locat, J., Lee, H.J., 2002. Submarine landslides: Advances and challenges. Can. Geotech. J. 39, 193–212. https://doi.org/10.1139/t01-089

Locat, J., Leroueil, S., Locat, A., Lee, H., 2016. Weak layers: Their definition and classification from a geotechnical perspective, in: Submarine Mass Movements and Their Consequences, 6th International Symposium. Springer, pp. 3–12. https://doi.org/10.1007/978-3-319-00972-8_1

Løseth, H., Henriksen, S., 2005. A middle to late miocene compression phase along the Norwegian passive margin, in: Petroleum Geology Conference Proceedings. pp. 845–859. https://doi.org/10.1144/0060845

Lothe, A.E., Borge, H., Gabrielsen, R.H., 2004. Modelling of hydraulic leakage by pressure and stress simulations and implications for Biot's constant: An example from the Halten Terrace, offshore Mid-Norway. Pet. Geosci. 10, 199–213. https://doi.org/10.1144/1354-079303-579

Løvholt, F., Schulten, I., Mosher, D., Harbitz, C., Krastel, S., 2019. Modelling the 1929 grand banks slump and landslide tsunami. Geol. Soc. Spec. Publ. 477, 315–331. https://doi.org/10.1144/SP477.28

Lowrie, W., Fichtner, A., 2020. Fundamentals of geophysics. Cambridge university press.

Lundin, E., Doré, A.G., 2002. Mid-Cenozoic post-breakup deformation in the "passive" margins bordering the Norwegian-Greenland Sea. Mar. Pet. Geol. 19, 79–93. https://doi.org/10.1016/S0264-8172(01)00046-0

Lundin, E.R., Doré, A.G., 2011. Hyperextension, serpentinization, and weakening: A new paradigm for rifted margin compressional deformation. Geology 39, 347–350. https://doi.org/10.1130/G31499.1

Macías, J., Vázquez, J.T., Fernández-Salas, L.M., González-Vida, J.M., Bárcenas, P., Castro, M.J., Díaz-del-Río, V., Alonso, B., 2015. The Al-Borani submarine landslide and associated tsunami. A modelling approach. Mar. Geol. 361, 79–95. https://doi.org/10.1016/j.margeo.2014.12.006

Marrett, R., Allmendinger, R.W., 1992. Amount of extension on "small'' faults: an example from the Viking graben." Geology 20, 47–50. https://doi.org/10.1130/0091-7613(1992)020<0047:AOEOSF>2.3.CO;2

Masson, D.G., Harbitz, C.B., Wynn, R.B., Pedersen, G., Løvholt, F., 2006. Submarine landslides: Processes, triggers and hazard prediction. Philos. Trans. R. Soc. A Math. Phys. Eng. Sci. 364, 2009–2039. https://doi.org/10.1098/rsta.2006.1810

Masson, D.G., Wynn, R.B., Talling, P.J., 2010. Large landslides on passive continental margins: Processes, hypotheses and outstanding questions. Submar. Mass Movements Their Consequences - 4th Int. Symp. 28, 153–165. https://doi.org/10.1007/978-90-481-3071-9_13

Mattos, N.H., Alves, T.M., Omosanya, K.O., 2016. Crestal fault geometries reveal late halokinesis and collapse of the Samson Dome, Northern Norway: Implications for petroleum systems in the Barents Sea. Tectonophysics 690, 76–96. https://doi.org/10.1016/j.tecto.2016.04.043

Maystrenko, Y., Scheck-Wenderoth, M., 2009. Density contrasts in the upper mantle and lower crust across the continent-ocean transition: Constraints from 3-D gravity modelling at the Norwegian margin. Geophys. J. Int. 179, 536–548. https://doi.org/10.1111/j.1365-246X.2009.04273.x

Maystrenko, Y.P., Gernigon, L., Nasuti, A., Olesen, O., 2018. Deep structure of the Mid-Norwegian continental margin (the Vøring and Møre basins) according to 3-D density and magnetic modelling. Geophys. J. Int. 212, 1696–1721. https://doi.org/10.1093/gji/ggx491

Mazzini, A., Svensen, H., Hovland, M., Planke, S., 2006. Comparison and implications from strikingly different authigenic carbonates in a Nyegga complex pockmark, G11, Norwegian Sea. Mar. Geol. 231, 89–102. https://doi.org/10.1016/j.margeo.2006.05.012

Mesri, G., Huvaj-Sarihan, N., 2012. Residual Shear Strength Measured by Laboratory Tests and Mobilized in Landslides. J. Geotech. Geoenvironmental Eng. 138, 585–593. https://doi.org/10.1061/(asce)gt.1943-5606.0000624

Mesri, G., Shahien, M., 2003. Residual Shear Strength Mobilized in First-Time Slope Failures. J. Geotech. Geoenvironmental Eng. 129, 12–31. https://doi.org/10.1061/(asce)1090-0241(2003)129:1(12)

Micallef, A., Masson, D.G., Berndt, C., Stow, D.A.V., 2016. Submarine spreading in the Storegga Slide, Norwegian Sea. Geol. Soc. Mem. 46, 411–412. https://doi.org/10.1144/M46.88

Micallef, A., Masson, D.G., Berndt, C., Stow, D.A.V., 2009. Development and mass movement processes of the north-eastern Storegga Slide. Quat. Sci. Rev. 28, 433–448. https://doi.org/10.1016/j.quascirev.2008.09.026

Micallef, A., Masson, D.G., Berndt, C., Stow, D.A.V., 2007a. Morphology and mechanics of submarine spreading: A case study from the Storegga Slide. J. Geophys. Res. Earth Surf. 112, 1–21. https://doi.org/10.1029/2006JF000739

Micallef, A., Masson, D.G., Berndt, C., Stow, D.A.V., 2007b. Submarine spreading: Dynamics and development, in: Submarine Mass Movements and Their Consequences, 3rd International Symposium. Springer Netherlands, Dordrecht, pp. 119–127. https://doi.org/10.1007/978-1-4020-6512-5_13

Mienert, J., Vanneste, M., Bünz, S., Andreassen, K., Haflidason, H., Sejrup, H.P., 2005. Ocean warming and gas hydrate stability on the mid-Norwegian margin at the Storegga Slide. Mar. Pet. Geol. 22, 233–244. https://doi.org/10.1016/j.marpetgeo.2004.10.018

Mienert, J., Vanneste, M., Haflidason, H., Bünz, S., 2010. Norwegian margin outer shelf cracking: A consequence of climate-induced gas hydrate dissociation? Int. J. Earth Sci. 99, 207–225. https://doi.org/10.1007/s00531-010-0536-z

Miramontes, E., Garziglia, S., Sultan, N., Jouet, G., Cattaneo, A., 2018. Morphological control of slope instability in contourites: a geotechnical approach. Landslides 15, 1085–1095. https://doi.org/10.1007/s10346-018-0956-6

Mitchell, N.C., 2004. Form of submarine erosion from confluences in Atlantic USA continental slope Canyons. Am. J. Sci. 304, 590–611. https://doi.org/10.2475/ajs.304.7.590

Mohn, G., Manatschal, G., Beltrando, M., Masini, E., Kusznir, N., 2012. Necking of continental crust in magma-poor rifted margins: Evidence from the fossil Alpine Tethys margins. Tectonics 31, 1–28. https://doi.org/10.1029/2011TC002961

Møller Hansen, D., 2006. The morphology of intrusion-related vent structures and their implications for constraining the timing of intrusive events along the NE Atlantic margin. J. Geol. Soc. London. 163, 789–800. https://doi.org/10.1144/0016-76492004-167

Montelli, A., Dowdeswell, J.A., Ottesen, D., Johansen, S.E., 2018. 3D seismic evidence of buried iceberg ploughmarks from the mid-Norwegian continental margin reveals largely persistent North Atlantic Current through the Quaternary. Mar. Geol. 399, 66–83. https://doi.org/10.1016/j.margeo.2017.11.016

Neagu, R.C., Cartwright, J., Davies, R., 2010a. Measurement of diagenetic compaction strain from quantitative analysis of fault plane dip. J. Struct. Geol. 32, 641–655. https://doi.org/10.1016/j.jsg.2010.03.010

Neagu, R.C., Cartwright, J., Davies, R., Jensen, L., 2010b. Fossilisation of a silica diagenesis reaction front on the mid-Norwegian margin. Mar. Pet. Geol. 27, 2141–2155. https://doi.org/10.1016/j.marpetgeo.2010.09.003

Newton, A.M.W., Huuse, M., 2017. Late Cenozoic environmental changes along the Norwegian margin. Mar. Geol. 393, 216–244. https://doi.org/10.1016/j.margeo.2017.05.004

Ngeri, A.P., Tamunobereton-ari, I., Amakiri, A.R.C., 2015. Ant-Tracker Attributes: An Effective Approach To Enhancing Faultidentification And Interpretation. J. VLSI Signal Process. 5, 67–73. https://doi.org/10.9790/4200-05626773

Nichols, R.J., 1995. The liquification and remobilization of sandy sediments. Geol. Soc. Spec. Publ. 94, 63–76. https://doi.org/10.1144/GSL.SP.1995.094.01.06

Nielsen, T., De Santis, L., Dahlgren, K.I.T., Kuijpers, A., Laberg, J.S., Nygård, A., Praeg, D., Stoker, M.S., 2005. A comparison of the NW European glaciated margin with other glaciated margins. Mar. Pet. Geol. 22, 1149–1183. https://doi.org/10.1016/j.marpetgeo.2004.12.007

Nielsen, T.K., Larsen, H.C., Hopper, J.R., 2002. Contrasting rifted margin styles south of Greenland: Implications for mantle plume dynamics. Earth Planet. Sci. Lett. 200, 271–286. https://doi.org/10.1016/S0012-821X(02)00616-7

Nirrengarten, M., Gernigon, L., Manatschal, G., 2014. Lower crustal bodies in the Møre volcanic rifted margin: Geophysical determination and geological implications. Tectonophysics 636, 143–157. https://doi.org/10.1016/j.tecto.2014.08.004

Omosanya, K.O., 2018. Episodic fluid flow as a trigger for Miocene-Pliocene slope instability on the Utgard High, Norwegian Sea. Basin Res. 30, 942–964. https://doi.org/10.1111/bre.12288

Omosanya, K.O., Eruteya, O.E., Siregar, E.S.A., Zieba, K.J., Johansen, S.E., Alves, T.M., Waldmann, N.D., 2018. Three-dimensional (3-D) seismic imaging of conduits and radial faults associated with hydrothermal vent complexes (Vøring Basin, Offshore Norway). Mar. Geol. 399, 115–134. https://doi.org/10.1016/j.margeo.2018.02.007

Omosanya, K.O., Johansen, S.E., Eruteya, O.E., Waldmann, N., 2017. Forced folding and complex overburden deformation associated with magmatic intrusion in the Vøring Basin, offshore Norway. Tectonophysics 706–707, 14–34. https://doi.org/10.1016/j.tecto.2017.03.026

Osmundsen, T., Sommaruga, A., Reidar, J., Odleiv, S.&, Osmundsen, O., Sommaruga, P.T., Olesen, J.R.&, 2002. Deep structure of the Mid Norwa y rifted margin, Norwegian journal of Geology.

Pakoksung, K., Suppasri, A., Imamura, F., Athanasius, C., Omang, A., Muhari, A., 2019. Simulation of the Submarine Landslide Tsunami on 28 September 2018 in Palu Bay, Sulawesi Island, Indonesia, Using a Two-Layer Model. Pure Appl. Geophys. 176, 3323–3350. https://doi.org/10.1007/s00024-019-02235-y

Palmer, A.C., Rice;, J.R., 1973. The growth of slip surfaces in the progressive failure of over-consolidated clay. Proc. R. Soc. London. A. Math. Phys. Sci. 332, 527–548. https://doi.org/10.1098/rspa.1973.0040

Paris, R., Ramalho, R.S., Madeira, J., Ávila, S., May, S.M., Rixhon, G., Engel, M., Brückner, H., Herzog, M., Schukraft, G., Perez-Torrado, F.J., Rodriguez-Gonzalez, A., Carracedo, J.C., Giachetti, T., 2018. Mega-tsunami conglomerates and flank collapses of ocean island volcanoes. Mar. Geol. 395, 168–187. https://doi.org/10.1016/j.margeo.2017.10.004

Paull, C.K., Ussler, W., Holbrook, W.S., Hill, T.M., Keaten, R., Mienert, J., Haflidason, H., Johnson, J.E., Winters, W.J., Lorenson, T.D., 2008. Origin of pockmarks and chimney structures on the flanks of the Storegga Slide, offshore Norway. Geo-Marine Lett. 28, 43–51. https://doi.org/10.1007/s00367-007-0088-9

Pawlowicz, R., 2013. Key physical variables in the ocean: temperature, salinity, and density. Nat. Educ. Knowl. 4, 13.

Peron-Pinvidic, G., Osmundsen, P.T., 2018. The Mid Norwegian - NE Greenland conjugate margins: Rifting evolution, margin segmentation, and breakup. Mar. Pet. Geol. 98, 162–184. https://doi.org/10.1016/j.marpetgeo.2018.08.011

Pigott, J.D., Kang, M.H., Han, H.C., 2013. First order seismic attributes for clastic seismic facies interpretation: Examples from the East China Sea. J. Asian Earth Sci. 66, 34–54. https://doi.org/10.1016/j.jseaes.2012.11.043

Piper, D.J.W., Cochonat, P., Morrison, M.L., 1999. The sequence of events around the epicentre of the 1929 Grand Banks earthquake: Initiation of debris flows and turbidity current inferred from sidescan sonar. Sedimentology 46, 79–97. https://doi.org/10.1046/j.1365-3091.1999.00204.x

Pittenger, A., Taylor, E., Bryant, W.R., 1989. The influence of biogenic silica on the geotechnical stratigraphy of the Voring Plateau, Norwegian Sea. Proc., Sci. results, ODP, Leg 104, Nor. Sea 104, 923–940. https://doi.org/10.2973/odp.proc.sr.104.145.1989

Planke, S., Rasmussen, T., Rey, S.S., Myklemust, R., Myklebust, R., 2005. Seismic characteristics and distribution of volcanic intrusions and hydrothermal vent complexes in the Vøring and Møre basins, in: Petroleum Geology Conference Proceedings. Geological Society of London, pp. 833–844. https://doi.org/10.1144/0060833

Planke, S., Svensen, H., Myklebust, R., Bannister, S., Manton, B., Lorenz, L., 2015. Geophysics and Remote Sensing. Springer, Cham, pp. 131–146. https://doi.org/10.1007/11157_2014_6

Plaza-Faverola, A., Bünz, S., Mienert, J., 2011. Repeated fluid expulsion through sub-seabed chimneys offshore Norway in response to glacial cycles. Earth Planet. Sci. Lett. 305, 297–308. https://doi.org/10.1016/j.epsl.2011.03.001

Pope, E.L., Talling, P.J., Carter, L., 2017. Which earthquakes trigger damaging submarine mass movements: Insights from a global record of submarine cable breaks? Mar. Geol. 384, 131–146. https://doi.org/10.1016/j.margeo.2016.01.009

Pope, E.L., Talling, P.J., Ó Cofaigh, C., 2018. The relationship between ice sheets and submarine mass movements in the Nordic Seas during the Quaternary. Earth-Science Rev. 178, 208–256. https://doi.org/10.1016/j.earscirev.2018.01.007

Puzrin, A.M., Gray, T.E., Hill, A.J., 2017. Retrogressive shear band propagation and spreading failure criteria for submarine landslides. Geotechnique 67, 95–105. https://doi.org/10.1680/jgeot.15.P.078

Quinn, P.E., Diederichs, M.S., Rowe, R.K., Hutchinson, D.J., 2011. A new model for large landslides in sensitive clay using a fracture mechanics approach. Can. Geotech. J. 48, 1151–1162. https://doi.org/10.1139/t11-025

Randolph, M.F., Gaudin, C., Gourvenec, S.M., White, D.J., Boylan, N., Cassidy, M.J., 2011. Recent advances in offshore geotechnics for deep water oil and gas developments. Ocean Eng. 38, 818–834. https://doi.org/10.1016/j.oceaneng.2010.10.021

Raymo, M.E., 1994. The initiation of Northern Hemisphere glaciation. Annu. Rev. Earth Planet. Sci. 22, 353–383. https://doi.org/10.1146/annurev.ea.22.050194.002033

Rebesco, M., Pedrosa, M.T., Camerlenghi, A., Lucchi, R.G., Sauli, C., De Mol, B., Madrussani, G., Urgeles, R., Rossi, G., Böhm, G., 2012. One Million Years of Climatic Generated Landslide Events on the Northwestern Barents Sea Continental Margin, in: Submarine Mass Movements and Their Consequences. Springer Netherlands, Dordrecht, pp. 747–756. https://doi.org/10.1007/978-94-007-2162-3_66

Reiche, S., Hjelstuen, B.O., Haflidason, H., 2011. High-resolution seismic stratigraphy, sedimentary processes and the origin of seabed cracks and pockmarks at Nyegga, mid-Norwegian margin. Mar. Geol. 284, 28–39. https://doi.org/10.1016/j.margeo.2011.03.006

Ren, S., Faleide, J.I., Eldholm, O., Skogseid, J., Gradstein, F., 2003. Late Cretaceous-Paleocene tectonic development of the NW Vøring Basin. Mar. Pet. Geol. 20, 177–206. https://doi.org/10.1016/S0264-8172(03)00005-9

Riis, F., Berg, K., Cartwright, J., Eidvin, T., Hansch, K., 2005. Formation of large, crater-like evacuation structures in ooze sediments in the Norwegian Sea. Possible implications for the development of the Storegga Slide. Mar. Pet. Geol. 22, 257–273. https://doi.org/10.1016/j.marpetgeo.2004.10.023

Rise, L., Chand, S., Hjelstuen, B.O., Haflidason, H., Bøe, R., 2010. Late Cenozoic geological development of the south Vøring margin, mid-Norway. Mar. Pet. Geol. 27, 1789–1803. https://doi.org/10.1016/j.marpetgeo.2010.09.001

Rise, L., Ottesen, D., Berg, K., Lundin, E., 2005. Large-scale development of the mid-Norwegian margin during the last 3 million years. Mar. Pet. Geol. 22, 33–44. https://doi.org/10.1016/j.marpetgeo.2004.10.010

Rise, L., Ottesen, D., Longva, O., Solheim, A., Andersen, E.S., Ayers, S., 2006. The Sklinnadjupet slide and its relation to the Elsterian glaciation on the mid-Norwegian margin. Mar. Pet. Geol. 23, 569–583. https://doi.org/10.1016/j.marpetgeo.2006.05.005

Roelofse, C., Alves, T.M., Gafeira, J., 2020. Structural controls on shallow fluid flow and associated pockmark fields in the East Breaks area, northern Gulf of Mexico. Mar. Pet. Geol. 112, 104074. https://doi.org/10.1016/j.marpetgeo.2019.104074

Roelofse, C., Alves, T.M., Omosanya, K.O., 2021. Reutilisation of hydrothermal vent complexes for focused fluid flow on continental margins (Modgunn Arch, Norwegian Sea). Basin Res. 33, 1111–1134. https://doi.org/10.1111/bre.12507

Rozhko, A.Y., Podladchikov, Y.Y., Renard, F., 2007. Failure patterns caused by localized rise in pore-fluid overpressure and effective strength of rocks. Geophys. Res. Lett. 34, 1–5. https://doi.org/10.1029/2007GL031696

Safronova, P.A., Laberg, J.S., Andreassen, K., Shlykova, V., Vorren, T.O., Chernikov, S., 2017. Late Pliocene–early Pleistocene deep-sea basin sedimentation at high-latitudes: mega-scale submarine slides of the north-western Barents Sea margin prior to the shelf-edge glaciations. Basin Res. 29, 537–555. https://doi.org/10.1111/bre.12161

Saint-Ange, F., Kuus, P., Blasco, S., Piper, D.J.W., Clarke, J.H., MacKillop, K., 2014.

Multiple failure styles related to shallow gas and fluid venting, upper slope Canadian Beaufort Sea, northern Canada. Mar. Geol. 355, 136–149. https://doi.org/10.1016/j.margeo.2014.05.014

Sanderson, D.J., 1991. Interpretation of Three-dimensional Seismic Data. J. Struct. Geol. 13, 121–122. https://doi.org/10.1016/0191-8141(91)90111-u

Sassa, S., Takagawa, T., 2019. Liquefied gravity flow-induced tsunami: first evidence and comparison from the 2018 Indonesia Sulawesi earthquake and tsunami disasters. Landslides 16, 195–200. https://doi.org/10.1007/s10346-018-1114-x

Saunders, A.D., Jones, S.M., Morgan, L.A., Pierce, K.L., Widdowson, M., Xu, Y.G., 2007. Regional uplift associated with continental large igneous provinces: The roles of mantle plumes and the lithosphere. Chem. Geol. 241, 282–318. https://doi.org/10.1016/j.chemgeo.2007.01.017

Sawyer, D.E., Flemings, P.B., Dugan, B., Germaine, J.T., 2009. Retrogressive failures recorded in mass transport deposits in the Ursa Basin, Northern Gulf of Mexico. J. Geophys. Res. Solid Earth 114, 1–20. https://doi.org/10.1029/2008JB006159

Scheck-Wenderoth, M., Raum, T., Faleide, J.I., Mjelde, R., Horsfield, B., 2007. The transition from the continent to the ocean: A deeper view on the Norwegian margin. J. Geol. Soc. London. 164, 855–868. https://doi.org/10.1144/0016-76492006-131

Schmiedel, T., Kjoberg, S., Planke, S., Magee, C., Galland, O., Schofield, N., Jackson, C.A.L., Jerram, D.A., 2017. Mechanisms of overburden deformation associated with the emplacement of the Tulipan sill, mid-Norwegian margin. Interpretation 5, SK23–SK38. https://doi.org/10.1190/INT-2016-0155.1

Schulten, I., Mosher, D.C., Krastel, S., Piper, D.J.W., Kienast, M., 2018. Surficial sediment failures due to the 1929 Grand Banks Earthquake, St Pierre Slope. Geol. Soc. London, Spec. Publ. 477, SP477.25. https://doi.org/10.1144/SP477.25

Sejrup, H.P., Hjelstuen, B.O., Dahlgren, K.I.T., Haflidason, H., Kuijpers, A., Nygård, A., Praeg, D., Stoker, M.S., Vorren, T.O., 2005. Pleistocene glacial history of the NW European continental margin. Mar. Pet. Geol. 22, 1111–1129.

https://doi.org/10.1016/j.marpetgeo.2004.09.007

Sejrup, H.P., Larsen, E., Landvik, J., King, E.L., Haflidason, H., Nesje, A., 2000. Quaternary glaciations in southern Fennoscandia: Evidence from southwestern Norway and the northern North Sea region. Quat. Sci. Rev. 19, 667–685. https://doi.org/10.1016/S0277-3791(99)00016-5

Shanmugam, G., 2021. Deep-Water Processes and Deposits, Encyclopedia of Geology. https://doi.org/10.1016/b978-0-12-409548-9.12541-2

Shanmugam, G., 1996. High-density turbidity currents; are they sandy debris flows? J. Sediment. Res. 66, 2–10. https://doi.org/10.1306/D426828E-2B26-11D7-8648000102C1865D

Shanmugam, G., Wang, Y., 2015. The landslide problem. J. Palaeogeogr. 4, 109–166. https://doi.org/10.3724/SP.J.1261.2015.00071

Sheriff, R.E., Geldart, L.P., 1995. Exploration seismology. Cambridge university press.

Shin, H., Santamarina, C.J., Cartwright, J.A., 2008. Contraction-driven shear failure in compacting uncemented sediments. Geology 36, 931–934. https://doi.org/10.1130/G24951A.1

Skogseid, J., Planke, S., Faleide, J.I., Pedersen, T., Eldholm, O., Neverdal, F., 2000. NE Atlantic continental rifting and volcanic margin formation, Geological Society Special Publication. https://doi.org/10.1144/GSL.SP.2000.167.01.12

Smallwood, J.R., Maresh, J., 2002. The properties, morphology and distribution of igneous sills: modelling, borehole data and 3D seismic from the Faroe-Shetland area. Geol. Soc. London, Spec. Publ. 197, 271–306. https://doi.org/10.1144/GSL.SP.2002.197.01.11

Smith, D.E., Shi, S., Cullingford, R.A., Dawson, A.G., Dawson, S., Firth, C.R., Foster, I.D.L., Fretwell, P.T., Haggart, B.A., Holloway, L.K., Long, D., 2004. The Holocene Storegga Slide tsunami in the United Kingdom. Quat. Sci. Rev. 23, 2291–2321. https://doi.org/10.1016/j.quascirev.2004.04.001

Soares, D.M., Alves, T.M., Terrinha, P., 2012. The breakup sequence and associated lithospheric breakup surface: Their significance in the context of rifted continental margins (West Iberia and Newfoundland margins, North Atlantic). Earth Planet. Sci. Lett. 355–356, 311–326. https://doi.org/10.1016/j.epsl.2012.08.036

Solheim, A., Berg, K., Forsberg, C.F., Bryn, P., 2005. The Storegga Slide complex: Repetitive large scale sliding with similar cause and development. Mar. Pet. Geol. 22, 97–107. https://doi.org/10.1016/j.marpetgeo.2004.10.013

Somoza, L., Medialdea, T., González, F.J., 2018. Giant mass-transport deposits in the southern Scotia Sea (Antarctica). 8th Int. Symp. Submar. Mass Movements Their Consequences, ISSMMTC 2018 195–205. https://doi.org/10.1144/SP477.2

Song, J., Alves, T.M., Omosanya, K.O., Hales, T.C., Ze, T., 2020. Tectonic evolution of strike-slip zones on continental margins and their impact on the development of submarine landslides (Storegga Slide, northeast Atlantic). Bull. Geol. Soc. Am. 132, 2397–2414. https://doi.org/10.1130/B35421.1

Srivastava, S.P., Roest, W.R., 1999. Extent of oceanic crust in the Labrador Sea. Mar. Pet. Geol. 16, 65–84. https://doi.org/10.1016/S0264-8172(98)00041-5

Steward, T., Sivakugan, N., Shukla, S.K., Das, B.M., 2011. Taylor's Slope Stability Charts Revisited. Int. J. Geomech. 11, 348–352. https://doi.org/10.1061/(ASCE)GM.1943-5622.0000093

Stewart, S.A., 2006. Implications of passive salt diapir kinematics for reservoir segmentation by radial and concentric faults. Mar. Pet. Geol. 23, 843–853. https://doi.org/10.1016/j.marpetgeo.2006.04.001

Strout, J.M., Tjelta, T.I., 2005. In situ pore pressures: What is their significance and how can they be reliably measured? Mar. Pet. Geol. 22, 275–285. https://doi.org/10.1016/j.marpetgeo.2004.10.024

Stuevold, L.M., Faerseth, R.B., Arnesen, L., Cartwright, J., Möller, N., 2003. Polygonal faults in the Ormen Lange Field, Møre Basin, offshore Mid Norway. Geol. Soc. Spec. Publ. 216, 263–281. https://doi.org/10.1144/GSL.SP.2003.216.01.17

Suess, E., Torres, M.E., Bohrmann, G., Collier, R.W., Greinert, J., Linke, P., Rehder, G., Trehu, A., Wallmann, K., Winckler, G., Zuleger, E., 1999. Gas hydrate destabilization: Enhanced dewatering, benthic material turnover and large methane plumes at the Cascadia convergent margin. Earth Planet. Sci. Lett. 170, 1–15. https://doi.org/10.1016/S0012-821X(99)00092-8

Sultan, N., Cochonat, P., Canals, M., Cattaneo, A., Dennielou, B., Haflidason, H., Laberg, J.S., Long, D., Mienert, J., Trincardi, F., Urgeles, R., Vorren, T.O., Wilson, C., 2004a. Triggering mechanisms of slope instability processes and sediment failures on continental margins: A geotechnical approach. Mar. Geol. 213, 291–321. https://doi.org/10.1016/j.margeo.2004.10.011

Sultan, N., Cochonat, P., Foucher, J.P., Mienert, J., 2004b. Effect of gas hydrates melting on seafloor slope instability. Mar. Geol. 213, 379–401. https://doi.org/10.1016/j.margeo.2004.10.015

Sun, Q., Alves, T., Xie, X., He, J., Li, W., Ni, X., Sun, Q., 2017. Free gas accumulations in basal shear zones of mass-transport deposits (Pearl River Mouth Basin, South China Sea): An important geohazard on continental slope basins. Mar. Pet. Geol. 81, 17–32. https://doi.org/10.1016/j.marpetgeo.2016.12.029

Sun, Q., Wu, S., Cartwright, J., Dong, D., 2012. Shallow gas and focused fluid flow systems in the Pearl River Mouth Basin, northern South China Sea. Mar. Geol. 315–318, 1–14. https://doi.org/10.1016/j.margeo.2012.05.003

Surlyk, F., 1990. Timing, style and sedimentary evolution of late Palaeozoic - Mesozoic extensional basins of east Greenland. Tecton. events responsible Britain’s oil gas Reserv. 107–125.

Surlyk, F., Clemmensen, L.B., Larsen, H.C., 1981. Post-Paleozoic evolution of the East Greenland continental margin. Can. Soc. Pet. Geol. Mem. 7, 487–510.

Sutra, E., Manatschal, G., Mohn, G., Unternehr, P., 2013. Quantification and restoration of extensional deformation along the Western Iberia and Newfoundland rifted margins. Geochemistry, Geophys. Geosystems 14, 2575–2597. https://doi.org/10.1002/ggge.20135

Svensen, H., Planke, S., Jamtveit, B., Pedersen, T., 2003. Seep carbonate formation controlled by hydrothermal vent complexes: A case study from the Vøring Basin, the Norwegian Sea. Geo-Marine Lett. 23, 351–358. https://doi.org/10.1007/s00367-003-0141-2

Svensen, H., Planke, S., Malthe-sørenssen, A., 2004. Svensen, Planke, Malthe-sørenssen - 2004 - Release of methane from a volcanic basin as a mechanism for initial Eocene global warming.pdf. Nature 429, 3–6. https://doi.org/10.1038/nature02575.1.

Talling, P.J., Clare, M., Urlaub, M., Pope, E., Hunt, J.E., Watt, S.F.L., 2014. Large submarine landslides on continental slopes: Geohazards, methane release, and climate change. Oceanography 27, 32–45. https://doi.org/10.5670/oceanog.2014.38

Talwani, M., Eldholm, O., 1977. Evolution of the Norwegian-Greenland Sea. Bull. Geol. Soc. Am. 88, 969–999. https://doi.org/10.1130/0016-7606(1977)88<969:EOTNS>2.0.CO;2

Tao, Z., Alves, T.M., 2019. Impacts of data sampling on the interpretation of normal fault propagation and segment linkage. Tectonophysics 762, 79–96. https://doi.org/10.1016/j.tecto.2019.03.013

Taylor, D.W., 1937. Stability of earth slopes. J. Bost. Soc. Civ. Eng. 24, 197–247.

ten Brink, U.S., Lee, H.J., Geist, E.L., Twichell, D., 2009. Assessment of tsunami hazard to the U.S. East Coast using relationships between submarine landslides and earthquakes. Mar. Geol. 264, 65–73. https://doi.org/10.1016/j.margeo.2008.05.011

Terzaghi, K., 1925. Erdbaumechanik auf bodenphysikalischer Grundlage. F. Deuticke.

Thiede, J., Myhre, A.M., 1996. The Paleoceanographic History of the North Atlantic-Arctic Gateways: Synthesis of the Leg 151 Drilling Results. Proc. Ocean Drill. Program, 151 Sci. Results. https://doi.org/10.2973/odp.proc.sr.151.147.1996

Thiede, Jörn, Myhre, A.M., 1996. The paleocenaographic history of the North Atlantic_arctic gateways: synthesis of leg 151 drilling results, Proceedings of the Ocean Drilling Program, Scientific Results. https://doi.org/10.2973/odp.proc.sr.151.147.1996

Torske, T., Prestvik, T., 1991. Mesozoic detachment faulting between Greenland and Norway: inferences from Jan Mayen fracture zone system and associated alkalic volcanic rocks. Geology 19, 481–484. https://doi.org/10.1130/0091-7613(1991)019<0481:MDFBGA>2.3.CO;2

Trincardi, F., Cattaneo, A., Correggiari, A., Ridente, D., 2004. Evidence of soft sediment deformation, fluid escape, sediment failure and regional weak layers within the late Quaternary mud deposits of the Adriatic Sea. Mar. Geol. 213, 91–119. https://doi.org/10.1016/j.margeo.2004.10.003

Tsikalas, F., Faleide, J.I., Eldholm, O., Wilson, J., 2005. Late Mesozoic-Cenozoic structural and stratigraphic correlations between the conjugate mid-Norway and NE Greenland continental margins, in: Petroleum Geology Conference Proceedings. pp. 785–801. https://doi.org/10.1144/0060785

Tsikalas, F., Faleide, J.I., Kusznir, N.J., 2008. Along-strike variations in rifted margin crustal architecture and lithosphere thinning between northern Vøring and Lofoten margin segments off mid-Norway. Tectonophysics 458, 68–81. https://doi.org/10.1016/j.tecto.2008.03.001

Turrini, L., Jackson, C.A.L., Thompson, P., 2017. Seal rock deformation by polygonal faulting, offshore Uruguay. Mar. Pet. Geol. 86, 892–907. https://doi.org/10.1016/j.marpetgeo.2017.06.038

Twichell, D.C., Chaytor, J.D., ten Brink, U.S., Buczkowski, B., 2009. Morphology of late Quaternary submarine landslides along the U.S. Atlantic continental margin. Mar. Geol. 264, 4–15. https://doi.org/10.1016/j.margeo.2009.01.009

Urlaub, M., Centre, H., 2007. Advances in natural and technological hazard research: Submarine mass movements and their consequences. Submar. Mass Movements Their Consequences 3rd Int. Symp. 27, 424. https://doi.org/10.1007/978-94-007-2162-3

Urlaub, M., Geersen, J., Krastel, S., Schwenk, T., 2018. Diatom ooze: Crucial for the generation of submarine mega-slides? Geology 46, 331–334. https://doi.org/10.1130/G39892.1

Urlaub, M., Hjelstuen, B.O., 2020. A numerical investigation of excess pore pressures and continental slope stability in response to ice-sheet dynamics. Geol. Soc. Spec. Publ. 500, 255–266. https://doi.org/10.1144/SP500-2019-185

Vachtman, D., Mitchell, N.C., Gawthorpe, R., 2013. Morphologic signatures in submarine canyons and gullies, central USA Atlantic continental margins. Mar. Pet. Geol. 41, 250–263. https://doi.org/10.1016/j.marpetgeo.2012.02.005

Vågnes, E., Gabrielsen, R.H., Haremo, P., 1998. Late Cretaceous-Cenozoic intraplate contractional deformation at the Norwegian continental shelf: Timing, magnitude and regional implications. Tectonophysics 300, 29–46. https://doi.org/10.1016/S0040-1951(98)00232-7

Vanneste, M., Mienert, J., Bünz, S., 2006. The Hinlopen Slide: A giant, submarine slope failure on the northern Svalbard margin, Arctic Ocean. Earth Planet. Sci. Lett. 245, 373–388. https://doi.org/10.1016/j.epsl.2006.02.045

Veeken, P., 2007. Seismic Stratigraphy, Basin Analysis and Reservoir Characterisation, Handbook of Geophysical Exploration: Seismic Exploration. Elsevier.

Vogt, P.R., 1997. Hummock fields in the Norway Basin and Eastern Iceland Plateau: Rayleigh-Taylor instabilities? Geology 25, 531–534. https://doi.org/10.1130/0091-7613(1997)025<0531:HFITNB>2.3.CO;2

Waghorn, K.A., Pecher, I., Strachan, L.J., Crutchley, G., Bialas, J., Coffin, R., Davy, B., Koch, S., Kroeger, K.F., Papenberg, C., Sarkar, S., 2018. Paleo-fluid expulsion and contouritic drift formation on the Chatham Rise, New Zealand. Basin Res. 30, 5–19. https://doi.org/10.1111/bre.12237

Ward, S.N., 2001. Landslide tsunami. J. Geophys. Res. Solid Earth 106, 11201–11215. https://doi.org/10.1029/2000JB900450

Wiemer, G., Moernaut, J., Stark, N., Kempf, P., De Batist, M., Pino, M., Urrutia, R., de Guevara, B.L., Strasser, M., Kopf, A., 2015. The role of sediment composition and behavior under dynamic loading conditions on slope failure initiation: a study of a subaqueous landslide in earthquake-prone South-Central Chile. Int. J. Earth Sci. 104, 1439–1457. https://doi.org/10.1007/s00531-015-1144-8

Wrona, T., Jackson, C.A.L., Huuse, M., Taylor, K.G., 2017a. Silica diagenesis in Cenozoic mudstones of the North Viking Graben: physical properties and basin modelling. Basin Res. 29, 556–575. https://doi.org/10.1111/bre.12168

Wrona, T., Magee, C., Jackson, C.A.L., Huuse, M., Taylor, K.G., 2017b. Kinematics of polygonal fault systems: Observations from the northern north sea. Front. Earth Sci. 5, 1–21. https://doi.org/10.3389/feart.2017.00101

Wu, N., Jackson, C.A.L., Johnson, H.D., Hodgson, D.M., Clare, M.A., Nugraha, H.D., Li, W., 2021. The formation and implications of giant blocks and fluid escape structures in submarine lateral spreads. Basin Res. 33, 1711–1730. https://doi.org/10.1111/bre.12532

Xu, W., Germanovich, L.N., 2006. Excess pore pressure resulting from methane hydrate dissociation in marine sediments: A theoretical approach. J. Geophys. Res. Solid Earth 111, 1–12. https://doi.org/10.1029/2004JB003600

Yamada, Y., Yamashita, Y., Yamamoto, Y., 2010. Submarine landslides at subduction margins: Insights from physical models. Tectonophysics 484, 156–167. https://doi.org/10.1016/j.tecto.2009.09.007

Yilmaz, Ö., 2001. Seismic Data Analysis, Journal of Sedimentary Research. Society of Exploration Geophysicists. https://doi.org/10.1190/1.9781560801580

Zachos, J., Pagani, H., Sloan, L., Thomas, E., Billups, K., 2001. Trends, rhythms, and aberrations in global climate 65 Ma to present. Science (80-.). 292, 686–693. https://doi.org/10.1126/science.1059412

Zhu, C., Cheng, S., Li, Q., Shan, H., Lu, J., Shen, Z., Liu, X., Jia, Y., 2019. Giant submarine landslide in the South China Sea: Evidence, causes, and implications. J. Mar. Sci. Eng. 7. https://doi.org/10.3390/jmse7050152